Application of satellite observations to improve nitrogen deposition estimates and the combined effects with drought on carbon sequestration in European forests

van der Graaf, Seline Caren

2022

document version
Publisher's PDF, also known as Version of record

VRIJE UNIVERSITEIT

Application of satellite observations to improve nitrogen deposition estimates and the combined effects with drought on carbon sequestration in European forests

ACADEMISCH PROEFSCHRIFT

ter verkrijging van de graad Doctor aan
de Vrije Universiteit Amsterdam,
op gezag van de rector magnificus
prof.dr. C.M. van Praag,
in het openbaar te verdedigen
ten overstaan van de promotiecommissie
van de Faculteit der Bètawetenschappen
op woensdag 12 januari 2022 om 13.45 uur
in een bijeenkomst van de universiteit,
De Boelelaan 1105

door

Seline Caren van der Graaf

geboren te Schiedam

promotoren:	prof.dr.ing. J.W. Erisman prof.dr. M. Schaap
promotiecommissie:	prof.dr. A.J. Dolman prof.dr.ir. S. Houweling prof.dr.ir. G. Velders prof.dr. M.C. Krol dr. F. Boersma

Cover: False-color image from the Spot-5 satellite on 28 September 2011 over central Belgium, capturing the capital city of Brussels. Darker blue areas throughout the image depict thick vegetation cover. © Cnes 2011, Distribution Airbus DS

English title: Application of satellite observations to improve nitrogen deposition estimates and the combined effects with drought on carbon sequestration in European forests. PhD thesis, VU University Amsterdam.

Nederlandse titel: Toepassing van satellietobservaties voor het verbeteren van stikstofdepositieschattingen en de gecombineerde effecten met droogte op koolstofvastlegging in Europese bossen. Academisch proefschrift, Vrije Universiteit Amsterdam.

Shelley van der Graaf, 2021

This research was funded by the Netherlands Organization for Scientific Research (NWO) under project number ALW-GO/16-05.

ISBN: 978-94-6421-584-7
Printed by Ipskamp Printing

TABLE OF CONTENTS

Chapter 1: Introduction

1.1 Introduction

1.1.1 Reactive nitrogen as a threat to the environment

The global nitrogen cycle is believed to be one of the three Earth subsystems or processes of which the planetary boundaries have been overstepped by human activity, alongside biodiversity loss and climate change (Rockström et al., 2009). These boundaries define a safe operating space for humanity, and breaching them causes unacceptable global environmental changes. Human interference with the global nitrogen cycle has led to enhanced losses of reactive nitrogen (N_r) to the environment. This extra input of N_r has led to a series of adverse effects, such as soil acidification, eutrophication, and biodiversity loss (De Vries et al., 2011), and poses a major threat to human and environmental health.

The Earth's atmosphere consists of nearly 80% dinitrogen gas (N_2). Most living organisms cannot use this inert form of nitrogen because of the strength of the triple bond that holds the two N atoms together. They require it to be converted into usable forms of nitrogen such as nitrogen dioxide (NO_2) or ammonia (NH_3), collectively known as reactive nitrogen compounds (N_r). Historically reactive nitrogen has only been available to nature in limited supply through the process of biological nitrogen fixation (Vitousek et al., 2002). In this biological process, N_2 gas is converted into NH_3 and other forms of N_r by nitrogenase enzymes. Biological nitrogen fixation is naturally carried out by microorganisms in soils, both free-living and in symbiosis, for instance, symbiotic bacteria associated with leguminous plants. Other natural sources of N_r include the formation of nitrogen oxides (NO_x) by lightning, or the release of NH_3 from the Earth's crust by volcanic eruptions (Galloway et al., 2003).

Nitrogen is a key component of amino acids, proteins, and DNA in living organisms and is therefore essential to life. By origin, N is the most limiting nutrient in the vast majority of natural ecosystems and almost all agricultural systems. Back in the day, farmers recycled organic waste (e.g., manure, guano) or planted leguminous, N_r fixing plants to enhance N_r inputs to their crops, and increase crop production. This all changed in 1908 when Fritz Haber discovered a way to synthesize NH_3 using an iron-based catalyst (Smil, 2001). Four years after his initial discovery, the process was commercialized by Germany's largest chemical company under engineer Carl Bosch. The newly discovered Haber-Bosch process made mass production of NH_3 from N_2 and H_2 under high pressures and temperatures possible, enabling humans to create large amounts of N_r inexpensively. Initially, the Haber-Bosch process was meant for the production of explosives. After the end of World War II, however, to meet the demand for food for a growing world population, the primary application of the process became the production of nitrogenous fertilizers. It is estimated that roughly half of the world's population is fed by synthetic fertilizers (Erisman et al., 2008), making the production of N_r vital for today's food security.

Today, over half of the existing N_r is created by humans. N_r fixation in agriculture is the largest source of human-created N_r and responsible for about 75% of the total anthropogenic N_r creation. The other 25% stems from the emissions of nitrogen oxides (NO_x). NO_x is a collective term for nitric oxide (NO) and nitrogen dioxide (NO_2) gas. NO_x is an oxidized form of N_r and is emitted as a byproduct from combustion processes, for instance from traffic, energy production or biomass burning. Over the past century, NO_x emissions have risen significantly together with the increase in fossil fuel consumption. Other forms of oxidized N_r are for example nitrates (NO_3^-), a common component of synthetic fertilizers, and nitrous oxide (N_2O) gas.

Another important form of N_r is ammonia (NH_3). Up to 50% of the global N_r emissions to the atmosphere consist of NH_3 (Reis et al., 2009). NH_3 is a reduced form of N_r and is mainly emitted from agricultural activities. The vast majority of the NH_3 emissions come from livestock housing and grazing and manure and synthetic fertilizer application to farm fields. Globally, around 40% of the NH_3 emissions directly follow from the volatilization of manure or synthetic fertilizers applied to farm fields (Sutton et al., 2013). Following the immense population growth of the previous century, NH_3 emissions have naturally increased substantially, too. Together with the increase in NO_x emissions, there has been almost a tripling of the global amounts of NO_x and NH_3 emissions to the atmosphere compared to pre-industrial levels (Erisman et al., 2015).

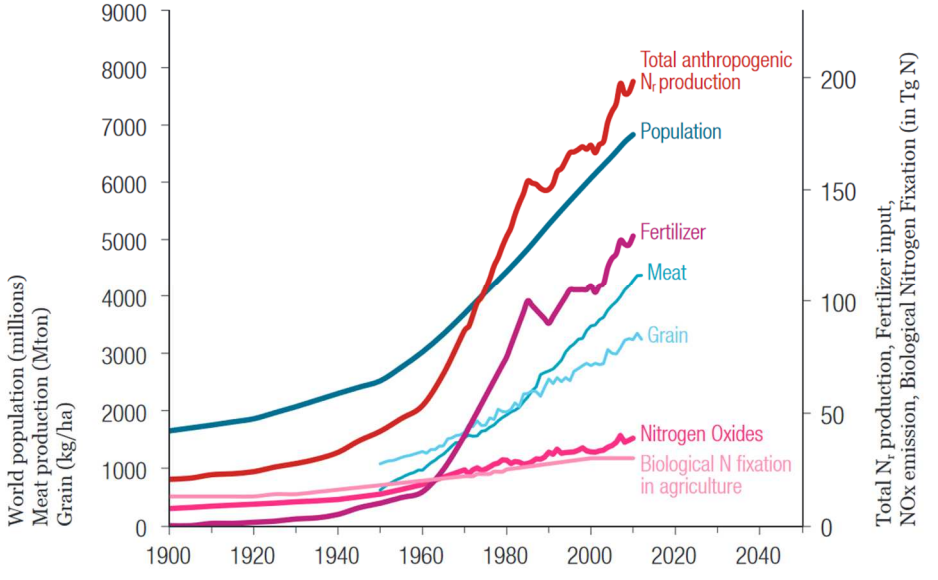

Figure 1.1. *Global trends in human population and total anthropogenic N_r creation throughout the 20th century. (Source: Erisman, 2015)*

1.1.2 Impacts of reactive nitrogen

After the creation of one atom of N_r, it may be chemically converted and transported through different pathways in the atmosphere, hydrosphere and biosphere. During its existence, the same atom of N_r may therefore have multiple consequences and contribute to several environmental and health impacts before being converted back to nonreactive N_2. This sequence of effects is called the *nitrogen cascade* (Galloway et al., 2003). As a result, whether it is related to the human production of food or energy, the origin of N_r becomes unimportant. To minimize the adverse effects of N_r, effective nitrogen management and policy development thus require consideration of all forms of N_r simultaneously.

To sustain the world's need for food and energy, the amount of N_r has tremendously increased over the past century. A large part of the created N_r is, however, lost to our environment and ends up as pollution. It is for instance estimated that approximately half of the N_r added to agricultural fields in Europe is either lost to the environment or converted back to N_2 and wasted (Sutton et al., 2011). N_r pollution either directly moves through the biosphere and hydrosphere, for instance

through leaching and run-off, or indirectly through N_r emissions to the atmosphere. Emitted N_r is transported through the atmosphere until it comes back down to terrestrial and aquatic surfaces through the process of nitrogen deposition. Through nitrogen deposition, large areas of the world receive N_r well above the natural background levels. All this extra input of N_r has caused unprecedented changes to the nitrogen cycle and comes with a series of unwanted negative impacts on our environment.

N_r is a significant driver of biodiversity loss through acidification and eutrophication. Nitrogen deposition is identified as the third most important driver of biodiversity loss, after habitat conversion and climate change (Sala et al., 2000). In the terrestrial biosphere, excessive N_r inputs on pristine surfaces can lead to acidification and biodiversity loss. High inputs of N_r accelerate the growth of certain nitrogen-loving species, well adapted to nutrient-rich conditions. Excessive amounts of ammonium (NH_4^+) and nitrate (NO_3^-) acidifies soils, favoring certain acid-tolerant species. The faster-growing plants (e.g., nettles, blackberries) outcompete other native species that were adapted to nutrient-poor conditions. Also, high concentrations of airborne N_r compounds can be harmful to plants. High concentrations of NH_3 gas, for instance, can be directly toxic to sensitive species such as lichens (Ashmore et al., 2010). Chronically elevated N_r inputs may even affect organisms higher on the food chain if their main source of food disappears (Erisman et al., 2013, WallisDeVries, 2014). Moreover, nitrogen deposition may enhance the susceptibility of plant species to stress and disturbance factors, such as drought, frost, or pathogens (Bobbink et al., 2010).

Nitrogen deposition, together with other forms of N_r pollution (e.g., through leaching and run-off), can lead to excess amounts of N_r in ground- and surface waters. High concentrations of nitrate in drinking water can be harmful to human health, and for instance increases the risk of bowel cancer (van Grinsven et al., 2010). In aquatic ecosystems, N_r enrichment stimulates the growth of algae and certain aquatic plants, a phenomenon known as eutrophication. Eutrophication can reduce species diversity in coastal and marine ecosystems (Smith and Schindler, 2009, Bauwman et al., 2010). The proliferation of algae can for instance inhibit coral reef growth by covering them. Ultimately, large inputs of N_r can lead to excessive biomass sedimentation and promote oxygen-consuming microbial decomposition. Severe eutrophication can lead to oxygen depletion, in the deeper water layers, i.e., hypoxia, and kill fish and invertebrates (Selman et al., 2008). In Europe, it is estimated that the N_r threshold for biodiversity risk is exceeded in around 80% of the fresh waters (Sutton et al., 2011).

In the atmosphere, N_r contributes to the formation of ground-level ozone (O_3) through the reaction of nitrogen oxides (NO_x) with volatile organic compounds (VOC) during daytime conditions. Moreover, NO_x and NH_3 are important precursors for the formation of particulate matter. In agriculture-intensive regions, NH_3 has been demonstrated to be one of the main precursors of inorganic secondary particulate matter and contributes substantially to fine particulate matter (PM2.5) concentrations (Erisman and Schaap, 2004, Wu et al., 2016). Fine particulate matter and ground-level ozone are associated with premature mortality by causing respiratory and cardiovascular disease (Pope et al., 2009, Lelieveld et al., 2015, Giannakis et al., 2019). Exposure to high concentrations of airborne particles is estimated to reduce the life expectancy of at least half of all Europeans by six months (Sutton et al., 2011). Moreover, fine particulate matter is not only harmful to human health, it also, directly and indirectly, impacts climate change (Erisman et al, 2011, Myhre et al., 2013).

Moreover, N_r contributes to climate change via several different processes. The most direct impact of N_r is through the formation of nitrous oxide (N_2O). The primary source of N_2O is agriculture, in particular the industrial production of fertilizers or microbial conversion of nitrogen-rich substrate after fertilizer or manure application on soils (Davidson et al., 2009). N_2O is a strong greenhouse gas that has a global warming potential of 265-298 CO_2-equivalents over 100 years (Myhre et al., 2013). Nitrogen oxides (NO_x) emissions also affect radiative forcing through their contribution to tropospheric ozone formation (O_3), which is the third most important greenhouse gas (Erisman et al., 2011). The production of these two powerful greenhouse gases (N_2O and O_3) results in a net warming effect. Moreover, N_r containing aerosols directly affects the radiative balance on Earth through the scattering of incoming sunlight, which results in a net cooling effect (Butterbach-Bahl et al., 2011).

N_r also indirectly affects climate through several pathways, mostly linked to alteration of the biosphere's exchange of greenhouse gases carbon dioxide (CO_2) and methane (CH_4). High levels of tropospheric O_3 following NO_x emissions are, for one, toxic to plants and damage crops and natural ecosystems, leading to a reduction of the biospheric CO_2 sink. For another, long-term exposure to enhanced nitrogen deposition on nutrient-poor wetlands likely increases vascular plant biomass, which increases CH_4 emissions and leads to a net warming effect (Bodelier et al., 2014). Nitrogen deposition can, to a certain extent, also have a positive effect on the biospheric CO_2 sink through enhancing vegetation productivity. Nitrogen deposition stimulates plant growth in areas where N_r is the limiting nutrient and herewith induces CO_2 sequestration in terrestrial ecosystems (Butterbach-Bahl et al., 2011). Globally, it is estimated that about 10% more CO_2 is sequestered due to nitrogen deposition compared to natural conditions (de Vries et al., 2014). This additional storage of CO_2, i.e., carbon sequestration, has a mitigating effect on climate change and results in a net cooling effect (Erisman et al., 2011). Carbon sequestration predominantly takes place in forest ecosystems (Pan et al., 2011), and forest are therefore vital drivers of the biospheric CO_2 sink. The effect of N_r on carbon sequestration in forests is, however, uncertain. In the next section, the important processes and determining factors are discussed.

1.1.3 Nitrogen deposition and carbon sequestration in forest ecosystems

Nitrogen deposition is thus an important driver of carbon sequestration in terrestrial ecosystems. On the global scale, it is currently estimated that N_r deposition increases the forest carbon sink by around 276 to 448 Tg C yr^{-1} (De Vries et al., 2014). Most of this extra carbon sequestration takes place in boreal and temperate forests that are N_r limited. Excessive amounts of nitrogen deposition, on the other hand, can also cause chemical imbalances if the N_r demands are exceeded and damage ecosystem health and functioning (Aber et al., 1998). Long-term exposure to excess N_r may ultimately lead to growth reductions by nitrogen saturation (Bobbink et al., 2010), which may lead to a reduction of the biospheric CO_2 sink on the long term.

Besides nitrogen deposition, there are many other stressors that influence growth and carbon sequestration in forest ecosystems (e.g., CO_2 fertilization, O_3 exposure, forest management, climatic and edaphic conditions, herbivore and pathogen outbreaks). As most studies focus on the effect of one of these stressors at the time, the effect of multiple, interacting stressors is often less understood. An example of this is the interplay between nitrogen deposition and drought. In the coming century, nitrogen deposition is projected to increase (Lamarque et al., 2013). Furthermore, climate change effects are becoming more apparent (e.g., increased atmospheric CO_2 levels,

elevated temperatures, and changes in water availability) and, as a result, the frequency and intensity of droughts will likely be exacerbated (Seneviratne et al., 2012). The effects of N deposition in terrestrial ecosystems strongly depend on water availability and therefore on drought. The current state of knowledge, however, limits the satisfactory coupling of the co-effects of nitrogen deposition and drought on quantification of terrestrial carbon sequestration in forest ecosystems (e.g., Fleischer et al., 2013, Erisman et al., 2011). So far, estimates of nitrogen deposition have been too coarse in space and time with substantial uncertainty. To tackle this, our main objective in this thesis is to provide more accurate estimates of nitrogen deposition by making the best out of the synergistic use of state-of-the-art chemical transport models and satellite observations.

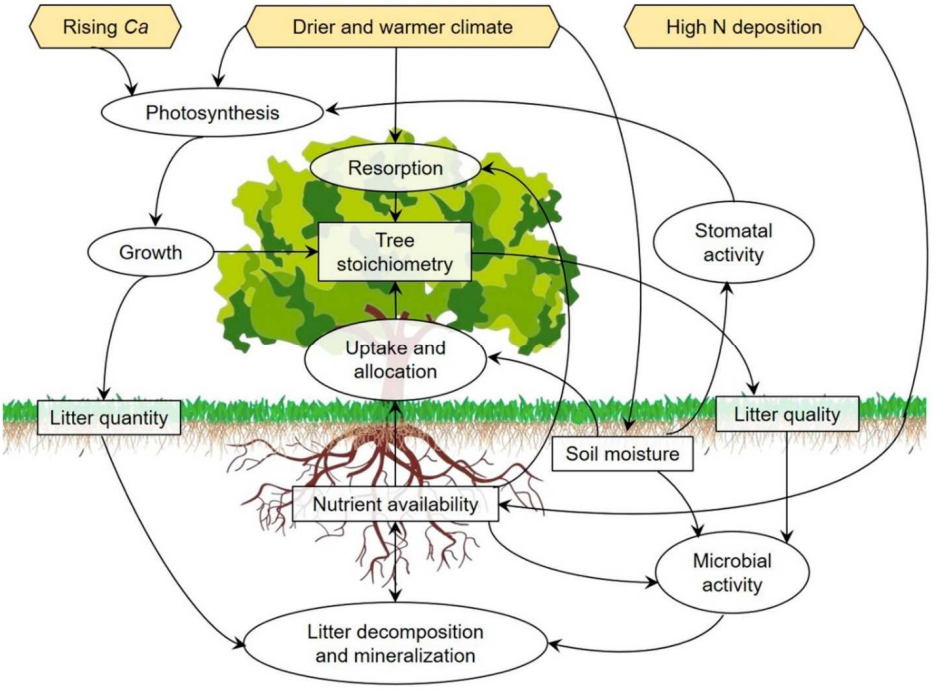

Figure 1.2. *Conceptual diagram of the impacts of global change on processes controlling the stoichiometry of trees. Yellow hexagons are global change drivers: increasing atmospheric CO_2 concentration (Rising Ca); climate change leading to drier and warmer conditions and high rates of atmospheric nitrogen (N) deposition; rectangles represent nutrient pools; and ellipses indicate biogeochemical processes (Source: González de Andrés, 2019).*

1.1.4 Modelling the fate of reactive nitrogen

Models are important tools to understand the fate of N_r emissions, and the subsequent consequences for human health and environmental quality. With the scarceness of available ground observations for N_r and their limited representativeness, together with the large spatial and temporal variation in source strength, concentrations and deposition of N_r, models are commonly used to estimate N_r fields on a regional scale. The mechanisms that govern the atmospheric composition are summarized in so-called chemistry transport models (CTMs). CTMs are used to

simulate the various chemical and physical processes that take place (emissions, transport, chemical conversion, deposition processes), using different sources of information and mathematical approximations (parameterizations). CTMs are equipped with several input variables, such as emission inventories and land use and meteorological data. Emission inventories provide estimates of the amounts of air pollutants that are discharged into the atmosphere over a longer period, usually a year, and can be translated to hourly input emissions using time profiles. The dispersion and transport of the emitted species are then computed using meteorological data, for instance from the European Centre for Medium-Range Weather Forecasts (ECMWF). Air pollutants that are transported through the atmosphere may undergo chemical transformations or may be deposited back to the surface, which is also simulated in CTMs. The transport distance of each N_r component depends on its susceptibility for chemical conversion and deposition. NH_3, for instance, has a very short atmospheric lifetime of a few hours (e.g., Dammers et al., 2019) because it readily reacts with other components and is deposited relatively rapidly. Once converted to its particulate form ammonium (NH_4^+), however, which has a lifetime of about a week (e.g., John et al., 2016), it can be transported much farther away from its source. Because of the reactive nature of N_r components, the use of CTMs is thus especially important. To understand the impacts of N_r deposition, reduced (NH_x) and oxidized (NO_y) forms cannot be addressed separately. Moreover, the atmospheric concentrations of other trace gases (e.g., O_3, SO_2) are also important because of their chemical interactions in the atmosphere and their effect on deposition processes. For a correct representation of the composition of the troposphere, and the chemical conversion that takes place in it, multiple atmospheric species need to be considered simultaneously. The most relevant chemical reactions and deposition processes for N_r are discussed in more detail in the next sections.

Chemical conversion

Chemical conversion in the troposphere is one of the removal processes of atmospheric N_r. The main chemical reactions involving NH_3 are discussed here. In the atmosphere nitric acid (HNO_3) and sulfuric acid (H_2SO_4) are formed through the oxidation of NO_x and SO_2, respectively. Reaction of these acids with sea salt cause the release of a third acid, hydrochloric acid (HCl). When atmospheric NH_3 comes into contact with sulfuric acid, nitric acid or hydrochloric acid the following chemical reactions take place:

$$H_2SO_4 + 2\,NH_3 \rightarrow (NH_4)_2SO_4$$

$$HNO_3 + NH_3 \leftrightarrow NH_4NO_3$$

$$HCl + NH_3 \leftrightarrow NH_4Cl$$

In these chemical reactions, ammonium sulfate ($(NH_4)_2SO_4$), ammonium nitrate (NH_4NO_3) and ammonium chloride (NH_4Cl) aerosol particles are formed. The reaction to $(NH_4)_2SO_4$ is one-sided and permanently removes gaseous NH_3 from the atmosphere (Seinfeld, 1986). The gas-aerosol partitioning of nitric acid and hydrochloric acid, on the other hand, are equilibria, meaning that after formation they may decompose and release NH_3 again (Behera et al, 2013). For nitric acid, the rate and direction of this balance depend on equilibrium constant $K = [NH_3][HNO_3]$, which is dependent on the ambient conditions (temperature, relative humidity) and NH_3 and HNO_3 concentrations (Erisman et al., 1988, West et al., 1999). Hence, the effectiveness in which ammonium forms depends on the relative abundance of both reactants and meteorological

conditions. The balance shifts towards the aerosol phase during low temperatures, for instance during winter, and relatively humid conditions. At a given ammonia level, the nitrate formation depends on the nitric acid production and thus the amount of NO_2. The chemical reactions involving the formation of nitric acid are different during day- and nighttime (see Hertel et al., 2012). During the daytime, the formation of nitric acid is dependent on the available amount of free hydroxyl radicals (OH·). Under influence of light (photons) tropospheric ozone (O_3) is photochemically broken down to excited oxygen atoms (O·), which in turn can react with water to form free hydroxyl radicals:

$$O_3 + hv \rightarrow O\cdot + O_2$$

$$O\cdot + H_2O \rightarrow 2\,OH\cdot$$

The generated hydroxyl radicals react with volatile organic compounds leading to ozone formation when nitrogen monoxide is oxidized by peroxides. $OH\cdot$ also reacts directly with gaseous NO_2, forming HNO_3:

$$NO_2 + OH\cdot \rightarrow HNO_3$$

During nighttime, nitric acid is formed from dinitrogen pentoxide (N_2O_5), which is generated from the following reaction pathway:

$$NO_2 + O_3 \rightarrow NO_3\cdot + O_2$$

$$NO_3\cdot + NO_2 \leftrightarrow N_2O_5$$

$$N_2O_5 + H_2O \rightarrow 2\,HNO_3$$

These reactions only occur during the night, because both NO_3 and N_2O_5 decompose during daylight conditions. In Europe, most of the nitric acid is formed through the night time reaction (Schaap et al., 2004)

Atmospheric deposition

N_r molecules, both in gaseous and particle form, can be removed from the atmosphere through the process of deposition. There are two forms of deposition: wet- and dry deposition. Wet deposition is the removal of atmospheric gases and particles by precipitation events (Fowler et al., 1990, Erisman and Draaijers, 1995). The two main wet deposition processes are in-cloud and below-cloud scavenging. In-cloud scavenging, also called rain-out, is the process where condensation of humid air forms cloud droplets on aerosol particles. Subsequently, water soluble gases may solute into the cloud water. This mostly happens with particles that can act as a nucleation core, such as aerosols. In below-cloud scavenging, also called wash-out, gases and particles in the air column below clouds are incorporated into droplets due to impaction (particles) or dissolution (gases) (Banzhaf et al., 2012). This is an effective way to remove highly soluble gases like NH_3 from the atmosphere. Another type of wet deposition is the removal of gases or particles via early morning dew or fog (Fowler et al., 1989). This process is called occult deposition and is normally neglected in CTMs. Direct deposition of cloud water on mountain ridges is also included in this process.

Dry deposition is the direct removal of atmospheric gases and particles by vegetation, soils, or surface waters (Farquhar et al., 1980, Nemitz et al., 2001). The dry deposition flux of trace gases depends on the surface concentrations and the dry deposition velocity. A common way to parameterize the dry deposition velocity is the use of a resistance analogy. In a resistance model, the most important pathways along which trace gases are taken up by the surface are parameterized. The dry deposition velocity can be represented as the reciprocal sum of the aerodynamic resistance, the quasi-laminar resistance and the canopy resistance (Van Zanten et al., 2010). Here, the aerodynamic resistance describes the resistance to turbulent transport close to the surface. The quasi-laminar resistance accounts for transport by molecular diffusion through the laminar layer close to the surface. Lastly, the canopy resistance accounts for the uptake at the surface (e.g., through leaves and stomata). For NH_3, the surface-atmosphere exchange is bi-directional, i.e., NH_3 can be re-emitted from surfaces to the atmosphere. Plants, for instance, can act as a source of NH_3 when the NH_3 concentrations in their stomata exceed the ambient atmospheric NH_3 concentrations. The direction of the NH_3 flux depends on the so-called compensation point. The compensation point is defined as the NH_3 concentration at which no net NH_3 exchange takes place between the surface and the atmosphere (Nemitz et al., 2000, Wichink Kruit et al., 2012). For plants, the compensation point is determined by the temperature, pH, and the ammonium (NH_4^+) concentration inside the stomata (Massad et al, 2008).

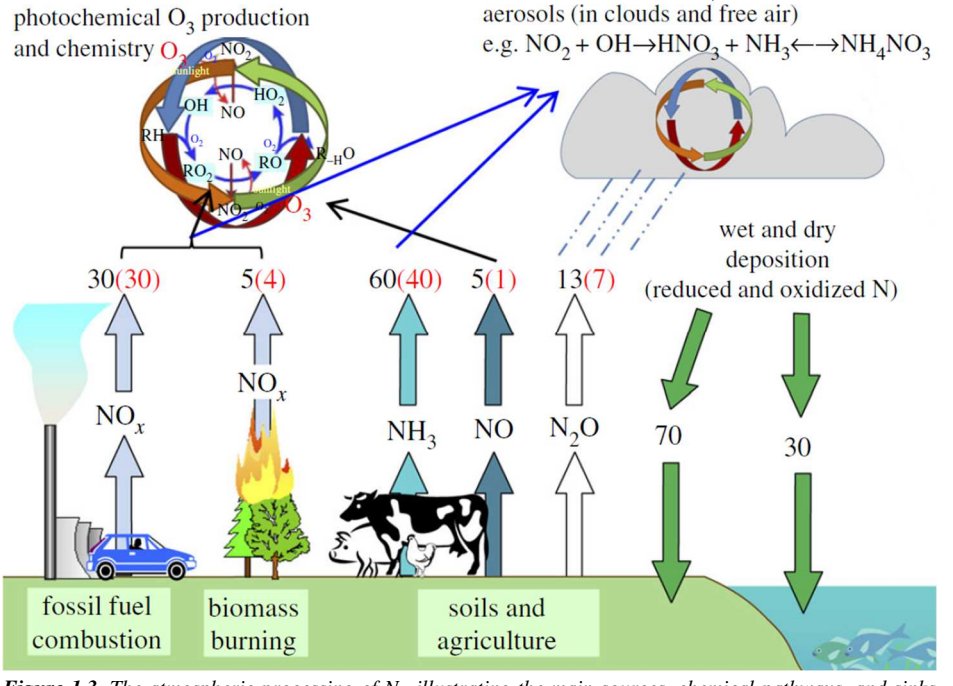

Figure 1.3. *The atmospheric processing of N_r, illustrating the main sources, chemical pathways, and sinks. The black values indicate the total emissions (in Tg yr^{-1}), the red values the anthropogenic contribution. (Adapted from Fowler et al., 2013)*

1.1.5 Satellite measurements for reactive nitrogen

After the launch of the first artificial satellite to be put into outer space in 1957, the Sputnik 1, many satellites followed. The primary purpose of the earliest Earth observational satellites was to study weather from space. As of April 2020, 446 operational Earth observational satellites are in orbit (UCS, 2021), collecting not only weather-related variables (e.g., precipitation, relative humidity, temperature, cloud structure), but all sorts of information (e.g., surface elevation, vegetation types and parameters, snow cover, ice thickness, mineral composition of the Earth's surface, ocean waves, tectonic movement, atmospheric composition). The main advantage of satellites is that they provide global observations, which is especially advantageous for remote locations, in a uniform way, i.e., with the same sensors. Moreover, most satellite measurements provide long time series on a regular basis, making them ideal for monitoring (Rees, 2013).

The vast majority of satellite instruments measure electromagnetic radiation. Active sensors provide their own source of radiation and detect the amount of emitted radiation that is reflected or scattered by the targets of interest. Passive sensors, on the other hand, make use of naturally existing radiation. The source of electromagnetic radiation can be either the sun, i.e., solar energy reflected from the Earth, radiation emitted by the Earth itself, or a combination of both (Toth and Jóźków, 2016, Zhu et al., 2018). Electromagnetic radiation interacts with the Earth's surface and atmosphere, where it can be scattered, absorbed, or emitted. Each molecule has its specific way of interacting with electromagnetic waves. This behavior can be used to recognize or discriminate between certain molecules, or on a larger scale, everything that's made up of these molecules. The amount of electromagnetic radiation that is reflected by a surface as a function of wavelength, its spectral signature, can for example be used to differentiate between different types of soils or vegetation (Zhu et al., 2018).

Broadly speaking, Earth observational satellites either target the Earth's surface or the atmosphere. The atmosphere, a thin sheet of air around the Earth, is in between the satellites and the Earth's surface. The molecules in the Earth's atmosphere, in particular water vapor (H_2O), absorb large proportions of incoming and outgoing radiation. Only the part of the electromagnetic radiation that is transmitted through the atmosphere can be observed by satellites. Satellites aimed at monitoring the variability of the Earth's surface typically measure in spectral regions with high atmospheric transmittance, so-called atmospheric windows (Rees, 2013). These satellites typically observe the reflected radiation at certain wavelength ranges within these atmospheric windows. These wavelength ranges are called spectral bands and are usually located somewhere within the visible light (VIS), near-infrared (NIR), or short-wave infrared (SWIR) part of the electromagnetic spectrum. Satellite sensors with relatively more, and narrower spectral bands (e.g., hyperspectral sensors) can extract more detailed spectral signatures and can detect more subtle differences (Zhu et al., 2018).

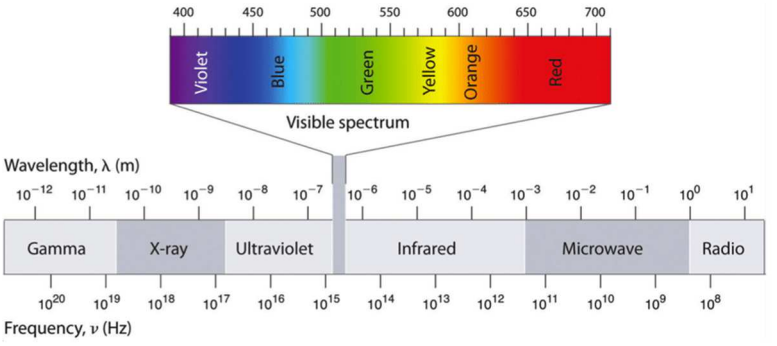

Figure 1.4. *The electromagnetic spectrum. (Source: Averill and Eldredge, 2011)*

Atmospheric sounders interested in the composition of the atmosphere focus on wavelength ranges where certain molecules in the atmosphere absorb (or emit) radiation. Usually, this is in either the ultraviolet (UV) or infrared regions (IR) of the electromagnetic spectrum. Atmospheric sounders typically have a high spectral resolution (narrow wavelength intervals) so that they can distinguish absorption lines from various molecules. The intensity and shape of the absorption lines can be used to infer the concentrations of atmospheric species (Rees, 2013). In this work, observations from two different satellite instruments that measure NH_3 concentrations in the atmosphere are used. The Infrared Atmospheric Sounder Interferometer (IASI) (e.g., Whitburn et al., 2016, Van Damme et al., 2015, Van Damme et al., 2017) and the Cross-track Infrared Sounder (CrIS) (e.g., Shephard et al., 2015, Shephard et al., 2020) instruments both provide global distributions of atmospheric NH_3 at a twice-daily resolution. Both instruments measure infrared radiation coming from the Earth's surface with interferometers. An example of the atmospheric NH_3 concentrations observed by CrIS is shown in Figure 1.5. The two main differences between these two instruments are the used retrieval strategies and their overpass times. A detailed description of the IASI-NH_3 and CrIS-NH_3 products is given in Chapter 2 and Chapter 4 of this work, respectively.

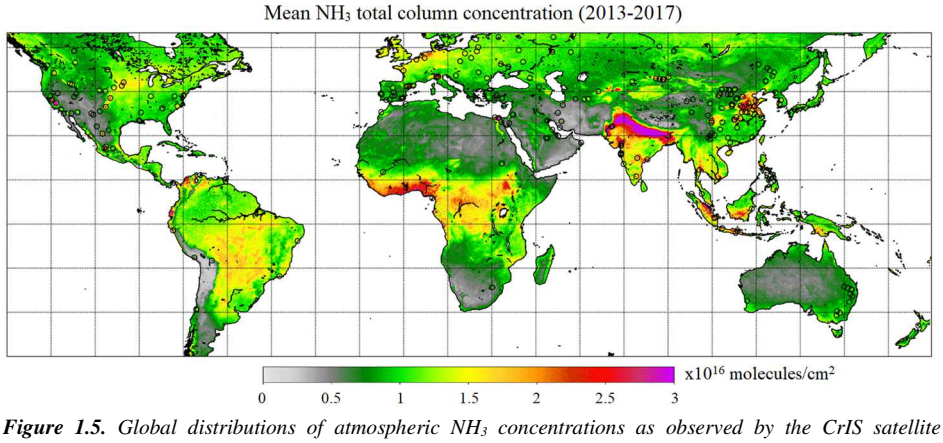

Figure 1.5. *Global distributions of atmospheric NH_3 concentrations as observed by the CrIS satellite instrument. The circles indicate large NH_3 point sources at which NH_3 emissions could be successfully estimated from satellite data. (Source: Dammers et al., 2019)*

1.2 Outline

1.2.1 Motivation and research aims

The nitrogen cycle has been severely disturbed by human activity. Several studies have shown that increased nitrogen deposition on natural ecosystems influences the carbon cycle and the response of vegetation to drought. With the occurrence and severity of droughts likely to be exacerbated by climate change, nitrogen deposition – drought interactions remain one of the key uncertainties in climate models to date. The coupling of nitrogen deposition and drought, however, is currently hampered by the relatively high uncertainty in the modelled nitrogen deposition estimates. Nitrogen deposition is highly variable in space and time and is difficult to estimate and model accurately. At this moment, nitrogen deposition estimates are too coarse in space and time to effectively link to carbon exchange and drought. To tackle this, the following questions were pre-defined in the original research proposal:

- How do nitrogen deposition rates in terrestrial systems vary spatially and temporally?
- What is the influence of N deposition on C-exchange at FLUXNET sites, both under normal and under drought conditions? What is the effect of N deposition and drought on carbon interactions in terrestrial systems?

This research was funded by the Netherlands Organization for Scientific Research (NWO) under project number ALW-GO/16-05. A major part of this work is devoted to answering the first question. The primary focus of this research is hence to reduce the uncertainty in nitrogen deposition estimates through synergetic use of satellite observations and atmospheric transport models. Multiple types of satellite measurements are used in combination with the modelling infrastructure of the LOTOS-EUROS chemical transport model to quantitively estimate the spatial and temporal variability of nitrogen deposition. Two types of satellite observations are differentiated: atmospheric satellite observations of NH_3 concentrations (IASI-NH_3, CrIS-NH_3) and vegetation remote sensing products (e.g., MODIS). In addition, one of the chapters of this work is devoted to answering the second question**.** Here, the aim is to contribute to the understanding of nitrogen deposition and drought dynamics on C-exchange specifically in forest ecosystems. The abovementioned questions are translated and split up into several research questions, each of which is described in the next section.

1.2.2 Research questions

With the scarceness of available observations, large-scale dry deposition estimates usually come from models such as CTMs. Dry deposition fields in CTMs are computed from air concentrations of trace gases or particles through inferential modelling. The modelled air concentrations in CTMs, however, are relatively uncertain, particularly for NH_3. Satellite observations from IASI provide us with the daily distribution of atmospheric NH_3 concentrations, but in itself lack information about the temporal evolution of atmospheric NH_3. Synergistic use of IASI-NH_3 observations and information from CTMs (e.g., vertical distribution, diurnal cycle, deposition velocities) may help to improve dry deposition estimates. Satellite observed NH_3 total columns can be translated to NH_3 surface concentrations and dry deposition fluxes with the help of the LOTOS-EUROS chemical transport model. This brings us to the first research question of this thesis:

- How can NH_3 dry deposition estimates be improved through synergistic use of the LOTOS-EUROS model and NH_3 satellite observations?

In the next chapter of this thesis, Chapter 2, a relatively simple, satellite-data driven method is applied to derive NH_3 surface concentrations and dry deposition fluxes. This method has previously been demonstrated to improve on modelled dry deposition fluxes of NO_2 and SO_2 (Nowlan et al., 2014) by combining information from a chemical transport model and satellite-observed atmospheric concentrations. Here, the LOTOS-EUROS chemical transport model and NH_3 total column concentrations of the Infrared Atmospheric Sounding Interferometer (IASI) instrument are used. The applicability and limitation of this method specifically for NH_3 are discussed, focusing on Europe, where in-situ observations of NH_3 surface concentrations are plentily available and used as a proxy for validation.

Deposition schemes for trace gases and particles in CTMs are often pragmatic and include relatively simple empirical functions. Two important input values that are used to compute deposition velocities in CTMs are the leaf area index (LAI), a quantity that describes the amount of plant canopy per unit ground area, and the surface roughness length (z_0), a measure for surface roughness. The assumed values and seasonality of the LAI and the z_0 input values in CTMs are typically fixed values, dependent on land use classification maps only. In reality, however, these values are dynamic, i.e., they vary spatially and show seasonal variation. Optical remote sensing data can be used to derive more realistic, dynamic LAI and z_0 values. The integration of these satellite-derived values potentially improves their representativeness in CTMs, and could herewith improve the estimated nitrogen deposition fields. This brings us to the next research question:

- How does the integration of satellite-derived LAI and z_0 values improve the modelled N_r deposition fields in LOTOS-EUROS?

In Chapter 3 of this work, a combination of multiple satellite products is used to derive dynamic LAI and z_0 input maps for the LOTOS-EUROS chemical transport model. An approach to derive monthly z_0 maps using data from satellite sensors MODIS (Moderate Resolution Imaging Spectroradiometer) and GLAS (Geoscience Laser Altimeter System) is presented and the derived z_0 values are validated with z_0 values computed from FLUXNET observations. The satellite-derived LAI and z_0 values are integrated into LOTOS-EUROS, and the sensitivity of the modelled N_r deposition fields to these values is evaluated. Here, the impact on both the total N_r deposition as well as the subpixel N_r deposition per land-use class (e.g., deciduous forest, coniferous forest, arable land) is looked into. Moreover, focusing on a region in western Europe (Germany, the Netherlands, and Belgium), the modelled NH_4^+ and NO_3^- wet deposition and NH_3 and NO_2 surface concentration fields are compared to in-situ observations.

The modelled NH_3 concentration and deposition fields are strongly determined by the emission distributions used in a CTM. Due to the large spatiotemporal variability stemming from the diverse nature of agricultural sources, NH_3 emission inputs are especially uncertain compared to those of other air pollutants. Recently, satellite observations have successfully been used for deriving emission estimates of various atmospheric species, either directly or indirectly through inverse modelling or data assimilation. Data assimilation is a way to link simulations to actual observations

and can be used to optimally combine information from models and satellites. Currently, CrIS is the newest satellite instrument that observes NH_3 concentrations globally at twice-daily resolution. The satellite-observed NH_3 concentrations from CrIS can serve as an important "reality check" for modelled NH_3 concentrations and can be used to update the NH_3 input emissions from CTMs, for instance using data assimilation. This way, by reducing the uncertainty related to NH_3 emission inputs, the modelled NH_3 concentrations and deposition fields would improve as well. This leads us to the next research question:

- How can integration and assimilation of NH_3 satellite observations improve the spatio-temporal distribution of modelled NH_3 fields in LOTOS-EUROS?

Chapter 4 of this work describes two methods to update NH_3 input emissions from the LOTOS-EUROS chemistry transport model using CrIS-NH_3 observations. The first method uses CrIS-NH_3 observations to derive a set of a-priori, observation-based NH_3 time factors for agricultural emission sources. The second method uses a Local Ensemble Transform Kalman Filter (LETKF) to assimilate CrIS-NH_3 observation into the LOTOS-EUROS model. The two methods are tested, individually and combined, focusing on a low-to-high NH_3 emission area within western Europe (The Netherlands, Germany, Belgium). The impact on the simulated NH_3 emissions, concentration and deposition fields is evaluated. The modelled fields are validated against in-situ observations of NH_3 surface concentrations and NH_4^+ wet deposition to see if they improve.
Nitrogen deposition is an important driver of carbon sequestration in forest ecosystems. Although previous studies have focused on nitrogen-carbon interaction in forest ecosystems, relatively little is known about the impact of nitrogen deposition on ecosystem carbon cycling during climate extremes such as droughts. Nitrogen deposition and drought effects on forest growth are found to be interdependent and non-additive, but to date, their joint effect is barely researched. With the frequency and intensity of droughts likely exacerbated by climate change and nitrogen deposition projected to increase the coming century, understanding the co-effects of N deposition and drought on the carbon exchange of forests, the most important terrestrial carbon sink, becomes increasingly important. This brings us to the next and last research question of this work:

- What is the effect of nitrogen deposition on the drought response of gross primary production at European FLUXNET forest sites?

In Chapter 5 of this work, several soil water availability indicators (Standardized Precipitation Evapotranspiration Index, soil volumetric water) are used to quantify the effect of drought on gross primary production at the European forest sites, using high-quality measurements from the FLUXNET database. The computed drought responses were linked to ecosystem-specific nitrogen deposition estimates from the LOTOS-EUROS chemical transport model for varying edaphic, physiological, and climatic conditions.

Chapter 2: How are NH_3 dry deposition estimates affected by combining the LOTOS-EUROS model with IASI-NH_3 satellite observations?

Abstract. Atmospheric levels of reactive nitrogen have increased substantially during the last century resulting in increased nitrogen deposition to ecosystems, causing harmful effects such as soil acidification, reduction in plant biodiversity and eutrophication in lakes and the ocean. Recent developments in the use of atmospheric remote sensing enabled us to resolve concentration fields of NH_3 with larger spatial coverage. These observations may be used to improve the quantification of NH_3 deposition. In this paper, we use a relatively simple, data-driven method to derive dry deposition fluxes and surface concentrations of NH_3 for Europe and for the Netherlands. The aim of this paper is to determine the applicability and the limitations of this method for NH_3. Space-born observations of the Infrared Atmospheric Sounding Interferometer (IASI) and the LOTOS-EUROS atmospheric transport model are used. The original modelled dry NH_3 deposition flux from LOTOS-EUROS and the flux inferred from IASI are compared to indicate areas with large discrepancies between the two. In these areas, potential model or emission improvements are needed. The largest differences in derived dry deposition fluxes occur in large parts of central Europe, where the satellite-observed NH_3 concentrations are higher than the modelled ones, and in Switzerland, northern Italy (Po Valley) and southern Turkey, where the modelled NH_3 concentrations are higher than the satellite-observed ones. A sensitivity analysis of eight model input parameters important for NH_3 dry deposition modelling showed that the IASI-derived dry NH_3 deposition fluxes may vary from ~ 20 % up to ~50 % throughout Europe. Variations in the NH_3 dry deposition velocity led to the largest deviations in the IASI-derived dry NH_3 deposition flux and should be focused on in the future. A comparison of NH_3 surface concentrations with in situ measurements of several established networks – the European Monitoring and Evaluation Programme (EMEP), Meetnet Ammoniak in Natuurgebieden (MAN) and Landelijk Meetnet Luchtkwaliteit (LML) – showed no significant or consistent improvement in the IASI-derived NH_3 surface concentrations compared to the originally modelled NH_3 surface concentrations from LOTOS-EUROS. It is concluded that the IASI-derived NH_3 deposition fluxes do not show strong improvements compared to modelled NH_3 deposition fluxes and there is a future need for better, more robust, methods to derive NH_3 dry deposition fluxes.

Published as: van der Graaf, S. C., Dammers, E., Schaap, M., and Erisman, J. W.: Technical note: How are NH_3 dry deposition estimates affected by combining the LOTOS-EUROS model with IASI-NH_3 satellite observations?, Atmos. Chem. Phys., 18, 13173–13196, https://doi.org/10.5194/acp-18-13173-2018, 2018.

2.1 Introduction

Reactive nitrogen (N_r) emissions have substantially increased during the last century to around 4 times the pre-industrial levels (Erisman et al., 2008; Fowler et al., 2013). As a result, atmospheric deposition of reactive nitrogen to both terrestrial and aquatic ecosystems has also increased (Dentener et al., 2006b). Excessive nitrogen deposition to sensitive ecosystems can cause harming effects such as soil acidification, reduction in plant biodiversity and eutrophication in water bodies (Erisman et al., 2015). One molecule of reactive nitrogen may even contribute to a number of these environmental impacts through different pathways and chemical transportation in the biosphere, the so-called nitrogen cascade (Galloway et al., 2003). Ammonia (NH_3) is one form of reactive nitrogen and constitutes an important part of the total amount of N_r emissions. Up to 50 % of global reactive nitrogen emissions consist of NH_3 (Reis et al., 2009), and therefore NH_3 contributes significantly to these adverse effects. Atmospheric ammonia is deposited to surfaces by two processes: dry and wet deposition.

Dry deposition may comprise a large part of the total deposition. Earlier modelling studies showed that dry deposition of NH_x even constitutes to over 60 % of the total deposition (Dentener et al., 2006a). The modelled fraction of dry deposition, however, ranges hugely depending on the used model. Deposition models in general are known to involve large uncertainties regarding the chemistry behind NH_4 formation and the NH_3 dry deposition velocities (Dentener et al., 2006a). At the same time, large-scale assessment of NH_3 dry deposition is hindered by the extremely limited number of dry deposition observations and their sparse distribution in space and time. Measurements of NH_3 dry deposition fluxes largely remain experimental and are limited to a few research sites and measurement campaigns of short durations (e.g. Zoll et al., 2016; Spindler et al., 2001). These measurements typically are representative of a confined area and a specific ecosystem. Dry deposition has so far been estimated on a regional scale through mainly two methods: geostatistical approaches and atmospheric chemistry models. Geostatistical approaches include geospatial interpolation of, or generating statistical models based on, existing in situ observations (e.g. Erisman and Draaijers, 1995). Atmospheric chemistry models use known and modelled inputs (i.a. emissions) to derive dry deposition fluxes (e.g. Dentener et al., 2006a; Wichink Kruit et al., 2012; Van der Swaluw et al., 2017). Both methods depend strongly on the quality and availability of reliable input information, which is often limited or even absent.

Recent developments in the use of atmospheric remote sensing to measure NH_3 distributions with large spatial coverage and daily resolution (Van Damme et al., 2014a) allow us to examine their development in space and time in more detail. Information from satellites can be of help to strengthen our understanding of the complex chain of processes of atmospheric deposition, emissions, dispersion and chemistry, especially when complemented with information from atmospheric chemistry models. Atmospheric chemistry models may, for example, help to fill in missing information on NH_3 concentrations close to the Earth's surface, arising from low sensitivities of NH_3 measuring instruments, or may, for instance, supplement satellite data with information on diurnal cycles. Nowlan et al. (2014) estimated surface concentrations and dry deposition of NO_2 and SO_2 by combining satellite observations of the Ozone Monitoring Instrument (OMI) and the GEOS-Chem model. The resulting estimates compared reasonably well with in situ measurements, thus providing a relatively simple, data-driven method to estimate surface concentrations and dry deposition fluxes on a worldwide scale. More recently, Kharol et

al. (2017) derived NH_3 dry deposition fluxes over North America using a similar method with NH_3 observations of the Cross-track Infrared Sounder (CrIS) satellite and the GEM-MACH model. The aim of this paper is to search for the applicability and the limitations of this method for NH_3 over Europe using space-born observations of the Infrared Atmospheric Sounding Interferometer (IASI) and the LOTOS-EUROS atmospheric transport model. This paper shows the first use of the IASI-NH_3 product for the derivation of NH_3 dry deposition fluxes, together with validation of the derived NH_3 surface concentrations with in situ measurements. The latter serve as a direct proxy for the validity of the derived NH_3 dry deposition fluxes. Also, this paper is the first to estimate the effect of modelling errors on the satellite-derived NH_3 dry deposition fluxes by performing a model sensitivity study.

Table 2.1. *Type of instruments used to measure ambient NH_3 concentrations and associated uncertainty estimates.*

Network	Instrument(s)	Uncertainty
EMEP	Filter packs, denuders	~ 20 %–25 % (yearly means)
MAN	Passive samplers	20 %–41 % (monthly means) (Lolkema et al., 2015)
LML	Continuous-flow denuders (AMORs)	> 9 % (hourly measurement), > 7 % (observed annual means) (Blank, 2001)

We start this paper with a description of the used models and datasets and their associated uncertainties. This is followed by a description of the methodology that is used to determine the NH_3 surface concentrations and dry deposition fluxes. Here, we also describe the design of the sensitivity study of the LOTOS-EUROS model. The resulting estimates of the NH_3 surface concentrations and dry deposition fluxes are given. The NH_3 surface concentrations are compared to in situ measurements from the European Monitoring and Evaluation Programme (EMEP) network in Europe. In a special case study for the Netherlands, they are compared to in situ measurements from the Meetnet Ammoniak in Natuurgebieden (MAN) and Landelijk Meetnet Luchtkwaliteit (LML) networks. Moreover, a sensitivity study of the LOTOS-EUROS model is evaluated to estimate the effect of model input uncertainties on the results that are obtained in the same section. The study is then concluded with a discussion.

2.2 Models and datasets

2.2.1 IASI NH_3 product

The Infrared Atmospheric Sounding Interferometer (IASI) is a passive remote-sensing instrument that measures infrared radiation emitted by the Earth's surface and atmosphere within the spectral range of 645–2769 cm^{-1} (Clerbaux et al., 2009). The IASI-A instrument is aboard the MetOp-A satellite that was launched in 2006 and circles in a polar Sun-synchronous orbit. In this study, we used NH_3 total column measurements from the morning overpass, as these are more sensitive to NH_3 than the nighttime observations (Van Damme et al., 2015). The morning overpass passes over Europe once a day in the morning around 09:30 LT. The NH_3 product has an elliptical spatial footprint of approximately 12 by 12 km and a detection limit of 2.5 ppbv (Van Damme et al., 2015). The retrieval uses a neural network to derive NH_3 columns based on the calculation of the hyperspectral range index (HRI), e.g. the spectral index (Van Damme et al., 2017). The retrieval

algorithm combines information on the temperature, humidity and pressure profiles to represent the atmospheric state closely (Whitburn et al., 2016). The retrieval uses a fixed profile in time, based on the profiles described by Van Damme et al. (2015). The IASI-NN (neural network) retrievals have been validated in Dammers et al. (2016) and Dammers et al. (2017b). In these papers, they compared the IASI-NN and Fourier-transform infrared spectrometer (FTIR) total columns and showed that the two compare reasonably well with a systematic underestimation by the IASI-NN product of around 30 %. In this paper, the NH_3 total columns observed during the warmer season (April to September) of 2013 and 2014 are used. The warm season was chosen because considerably fewer observations are available during the cold months. Moreover, the observations in the cold months generally have a higher relative uncertainty (Van Damme, 2014a). A filter has been applied after (Van Damme et al., 2014b). This filter leaves out observations with a relative error of <100 % unless the absolute error is smaller than 5×10^{15} molecules cm^{-2}. Fig. 2.1 shows the mean IASI NH_3 total column concentration over Europe and the Netherlands.

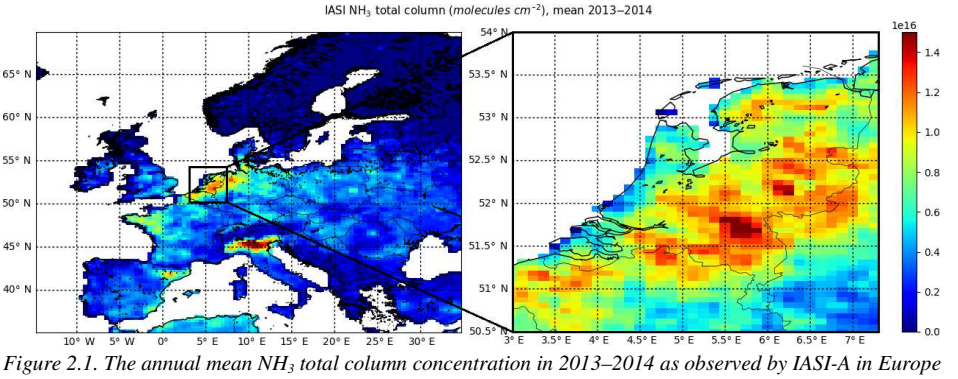

Figure 2.1. The annual mean NH_3 total column concentration in 2013–2014 as observed by IASI-A in Europe (regridded to 0.50° longitude by 0.25° latitude) and the Netherlands (regridded to 0.125° longitude by 0.0625° latitude).

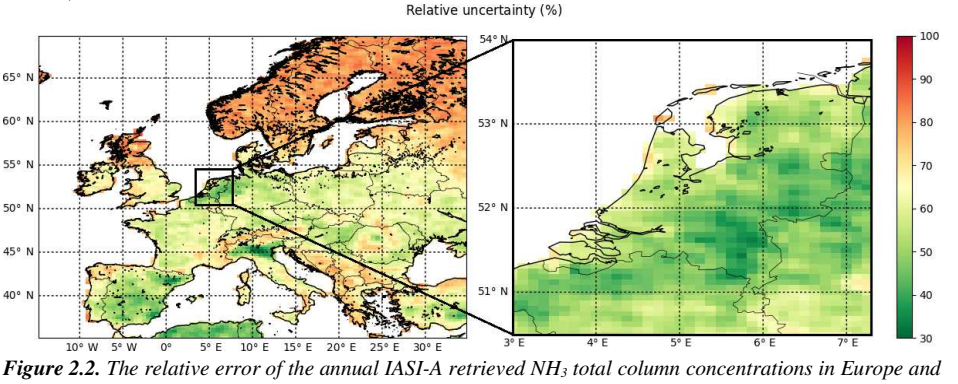

***Figure 2.2.** The relative error of the annual IASI-A retrieved NH_3 total column concentrations in Europe and the Netherlands in 2013–2014.*

2.2.2 IASI NH_3 uncertainties

The retrieval algorithm (Whitburn et al., 2016) allows estimation of quantitative errors of each observation. The error estimate depends on a combination of the thermal contrast (the temperature difference between Earth's surface and atmosphere at 1.5 km) and the HRI, i.e. the spectral

footprint. The estimate also includes error terms for the uncertainty in the profile shape and error terms arising from the used temperature and water vapour profiles. The uncertainty estimate for each retrieved NH_3 total column is an error propagation of the individual parameter uncertainties. Whitburn et al. (2016) showed in an error characterization that individual retrieved NH_3 columns hold the smallest errors (~25 %) in the situation of a high NH_3 concentration combined with a high thermal contrast. The error increases progressively when either of these lowers. In the case of a low NH_3 concentration and a low thermal contrast, the errors can be as high as ~270 %. More information on how the IASI-NN retrieval works and how the relative errors are derived can be found in Whitburn et al. (2016). Fig. 2.2 shows the relative uncertainty of the IASI-A NH_3 total column concentrations in 2013–2014 over Europe and the Netherlands. The relative uncertainty ranges from ~90 % in remote areas with little emissions to ~30 % in high emissions areas.

2.2.3 NH_3 ground measurements

Ground measurements of NH_3 surface concentrations from three air quality networks were used to validate the LOTOS-EUROS and IASI-derived NH_3 surface concentrations on a monthly and a yearly basis. To do this, observations of ambient NH_3 concentrations of the EMEP network are used for Europe (EMEP, 2016). For the case study of the Netherlands, observations from two established networks are used, the LML (RIVM, Netherlands National Institute for Public Health and the Environment) and MAN (Lolkema et al., 2015). NH_3 is challenging to measure reliably because of potential adsorption to parts of the measurement device, leading to slow response times (von Bobrutzki et al., 2010). The uncertainties of the measurements may differ significantly per instruments design. Table 2.1 gives an overview of the instruments used by each of these networks and their uncertainties.

2.2.3.1 EMEP network

The main measurement network for reactive nitrogen concentrations on a European scale is the EMEP network (Tørseth et al., 2012). NH_3 measurements from 35 stations were available to validate the results of 2013 and 46 stations for the results of 2014. Different types of measurement devices are used to measure NH_3 within the EMEP network. The majority of the EMEP sites use filter packs, of which the results are relatively uncertain. In a field intercomparison of different NH_3 measurement techniques, von Bobrutzki et al. (2010) found that different instruments have an overall bias varying from −31.1 % to +10.9 % for the entire data range (~ 2 weeks), demonstrating that there is a need for a standardized approach. For smaller concentrations (<10 ppbv) the bias is even larger, from −22.0 % to +54.5 %.

2.2.3.2 LML network

The LML has monitored hourly NH_3 concentrations in the Netherlands since 1993 (van Zanten et al., 2017). Since 2014, only six stations have been left in operation; before that, there were eight stations. The locations of the monitoring stations were carefully selected to cover regions with high, moderate and low emission densities equally. The measurements are performed with AMOR instruments, which are continuous-flow denuders. Airflow passes through a wetted rotating denuder tube in the AMOR instrument and the NH_3 absorbs into this fluid. The electric conductivity is then determined and used as a measure for the NH_3 concentration (van Zanten et al., 2017). The measurements have a reported uncertainty of at least 9 % for hourly concentrations and at least 7 % for yearly averages (van Zanten et al., 2017; Blank, 2001).

2.2.3.3 MAN network

The MAN network has provided monthly mean ambient NH_3 concentrations in nature areas in the Netherlands since 2005. The network has 236 sampling points as of 2014, spread over 60 different nature areas. The measurements are performed with low-cost passive samplers from Gradko. The measurements are calibrated against the measurements of the LML (Lolkema et al., 2015). The bottom of the passive sampler is an open cap with a porous filter through which NH_3 in the air can enter. In the top end of the tube, the NH_3 is adsorbed by an acid to form NH_4^+. The NH_4^+ concentrations in the samplers are analysed in a laboratory every month to compute the monthly mean NH_3 concentrations. The uncertainty of the MAN measurements depends on the NH_3 concentration and varies between 20 % for high concentrations (10–20 $\mu g\ m^{-3}$) and 41 % for low concentrations (1 $\mu g\ m^{-3}$) (Lolkema et al., 2015).

2.2.4 The LOTOS-EUROS model

2.2.4.1 Model description

LOTOS-EUROS is an Eulerian chemistry transport model (CTM) (Manders et al., 2017) that simulates air pollution in the lower troposphere. A horizontal resolution of 0.50° longitude by 0.25° latitude, corresponding to approximately 28 by 28 km^2, is used to perform simulations for Europe (35–70° N, 15° W–35° E). Secondly, for the case study of the Netherlands, the horizontal resolution is set to 0.125° longitude by 0.0625° latitude, approximately 7 by 7 km (50.5–54° N, 3–7.5° E). The vertical resolution of the model is a four-layer vertical grid that extends up to 3.5 km above sea level. The bottom layer is the surface layer and has a fixed height of 25 m. On top of this layer, there is a mixing layer, followed by two equally thick dynamic reservoir layers with time-varying thicknesses. The model follows the mixed layer approach. LOTOS-EUROS performs hourly calculations using meteorology provided by ECMWF (ECMWF, 2016). Gas-phase chemistry is described using the Netherlands Organisation for Applied Scientific Research (TNO) CBM-IV (carbon bond mechanism) scheme (Schaap et al., 2009), which is an updated version of the original scheme by (Whitten et al., 1980). Anthropogenic emissions used in LOTOS-EUROS are taken from the TNO Monitoring Atmospheric Composition and Climate (MACC) III emission database (Kuenen et al., 2014). LOTOS-EUROS uses a set of temporal factors (monthly, daily and hourly) to break down annual total emissions into hourly emissions. The time profile of a particular pollutant is an aggregation of the time-dependent emission strengths from different Selected Nomenclature for Sources of Air Pollution (SNAP) sources. The monthly NH_3 emissions peak in March and then decrease, followed by another smaller peak in September. The daily NH_3 emission strengths are redistributed more or less evenly over the week. The hourly NH_3 emission peak is reached at 13:00 LT (Denier van der Gon et al., 2011).

2.2.4.2 Dry deposition parameterization

The dry deposition fluxes in LOTOS-EUROS are calculated with the Deposition of Acidifying Compounds (DEPAC) 3.11 module, following the resistance approach (van Zanten et al., 2010). In this approach, the deposition velocity is the reciprocal sum of the aerodynamic resistance, the quasi-laminar layer resistance and the surface resistance. A canopy compensation point for simulation of the bi-directional flux of NH_3 is included in the implementation of the DEPAC3.11 module, following the approach presented in Wichink Kruit et al. (2012). The compensation point is computed dynamically using modelling results from the last month. The model uses the CORINE/Smiatek land use map converted to the DEPAC land use classes to determine the

exchange velocities for different land use classes. More information on the LOTOS-EUROS model can be found in Manders et al. (2017).

2.2.4.3 Model performance

The LOTOS-EUROS model has participated in multiple model intercomparison studies (e.g. Colette et al., 2017; Wichink Kruit, 2013; Bessagnet et al., 2016; Vivanco et al., 2018), showing an overall good model performance. LOTOS-EUROS also showed a good correspondence with yearly NH_3 concentrations with a slight underestimation in agricultural areas and overestimation in nature areas in the Netherlands (Wichink Kruit, 2013). The inferential method that we use here heavily relies on results from LOTOS-EUROS. The model therefore has to closely represent reality, if we wish to obtain reasonable results. As in any model, there are, however, uncertainties associated with every part of the total chain of modelled processes. The uncertainties related to emissions and to dry and wet deposition are expected to impact the results the most and are discussed below.

2.2.4.4 Uncertainties related to emission input

Emissions are the most important input for any CTM and are, at the same time, a source of substantial uncertainties (Reis et al., 2009; Behera et al., 2013). NH_3 emissions are relatively uncertain due to the diverse nature of agricultural sources leading to large spatial and temporal variations in emissions. The uncertainty of the European reported annual totals is estimated to be around ±30 % (EMEP, 2016). The uncertainty is larger for countries that have limited research on their emission inventory and carry out a few emission measurement activities.

The presence of other gaseous components such as SO_2 and NO_x may have a high impact on the modelled NH_3 concentrations, as NH_3 in the atmosphere reacts readily with sulfuric acid (H_2SO_4) and nitric acid (HNO_3) to form particulate ammonium (e.g. $(NH_4)_2SO_4$ or NH_4NO_3). It is therefore also important to consider the errors in the SO_2 and NO_x emissions. The SO_2 emissions are relatively well known per source category and thus hold a relatively low uncertainty of about ±10 % on reported annual totals. The uncertainty in the NO_x emissions is higher, of around ±20 % on reported annual totals. However, due to interpolation to account for missing data for some countries, the final uncertainty of the annual totals of both SO_2 and NO_x is estimated to be higher (Kuenen et al., 2014). Needless to say, one single emission at a certain time may have a much higher error due to the large uncertainty related to redistribution and the timing of emissions (Hendriks et al., 2016; Skjøth et al., 2011). More information on the quality data ratings of NH_3, SO_2 and NO_x per source category and per country can be found in the report of the European Environment Agency (EEA, 2016).

2.2.4.5 Uncertainties regarding dry and wet deposition

The second source of uncertainties originates from the model parameterization of both dry and wet deposition. Several multi-model studies (e.g. Dentener et al., 2006a; Colette et al., 2017; Wichink Kruit, 2013; Flechard et al., 2011; Vivanco et al., 2018) have shown that there is quite a large discrepancy in the implementation of dry and wet deposition in different CTMs. A fundamental input for estimating dry deposition fluxes in CTMs is the uncertainty in the deposition velocity. Schrader and Brummer (2014) compiled a database of the NH_3 deposition velocities per land use category that have been used in several deposition models from 2004 to 2013. The results showed

quite a large variation in the V_d values for different land use classes. Some classes (e.g. water, urban) showed only a small variation in V_d of an interquartile range of ~5 to 10 % for 50 % of the data. Other classes (e.g. coniferous, agriculture) showed a much larger interquartile range in V_d of ~30 to 40 %. Flechard et al. (2011) compared four existing dry deposition routines across 55 N_r monitoring sites and found that the differences between models reach a factor 2–3 and are often larger than differences between monitoring sites. Erisman (1993) estimated the dry and wet deposition fluxes of acidifying substances in the Netherlands from measured and modelled concentrations. The estimated uncertainty in the average NH_3 fluxes in this paper was estimated to be 30 %, with a systematic error of 30 % in the used V_d for NH_3. Dentener et al. (2006a) calculated the deposition of N_r with 23 atmospheric chemistry transport models in a multi-model evaluation. Although there were quite large differences between the different models, the paper showed that 71.7 % of the model-calculated mean wet deposition rates in Europe agreed to within ±50 % with NH_4^+ wet deposition measurements from the EMEP network.

2.3 Methodology

The NH_3 surface concentrations and dry deposition fluxes are estimated by combining the observations of the IASI-A satellite instrument and the modelling results from LOTOS-EUROS. The method is an adapted version of the approach for NO_2 and SO_2 presented by Nowlan et al. (2014). The IASI-A instrument only observes the NH_3 total column at overpass time. We use the modelling results of LOTOS-EUROS to account for the diurnal variation in the atmospheric concentrations of NH_3. The vertical NH_3 profiles in LOTOS-EUROS are also used to deduce the ground-level NH_3 concentrations from IASI. The computation of the IASI-derived NH_3 surface concentrations and dry deposition fluxes is described in detail in the following sections.

2.3.1 Surface concentration computation

The NH_3 total column observations from IASI are first regridded onto the LOTOS-EUROS model grid. The monthly mean NH_3 total column concentrations are then calculated for each pixel. We use the vertical profile of NH_3 per grid cell in LOTOS-EUROS to relate the IASI NH_3 total column to NH_3 surface concentrations. The IASI-derived NH_3 surface concentrations ($\mathbf{C^{IASI}}$) are computed following Eq. (2.1):

$$\mathrm{C}^{\mathrm{IASI}} = \frac{\Omega^{\mathrm{IASI}}}{\Omega^{\mathrm{LE}}_{\mathrm{overpass}}} \cdot \mathrm{C}^{\mathrm{LE}} \qquad \text{(Eq. 2.1)}$$

Here Ω^{IASI} represents the monthly mean NH_3 total column concentration from IASI (molecules cm^{-2}), $\Omega^{\mathrm{LE}}_{\mathrm{overpass}}$ represents the modelled NH_3 total column at overpass time in LOTOS-EUROS (molecules cm^{-2}) and C^{LE} is the modelled mean surface concentration (μg m^{-3}), the concentration in the down-most layer in LOTOS-EUROS.

2.3.2 Dry deposition flux computation

The hourly NH_3 dry deposition fluxes are modelled in LOTOS-EUROS. The modelled NH_3 dry deposition fluxes are then adjusted based on actual observations from IASI. The modelled and the IASI-derived NH_3 concentrations share the same vertical profile. The ratio of the observed and the modelled total column concentrations, rather than the surface concentrations, is therefore directly

used to alter the modelled NH_3 dry deposition flux. The NH_3 dry deposition flux (kg N ha^{-1} yr^{-1}) inferred from IASI, F^{IASI}, is computed following Eq. (2.2):

$$F^{IASI} = \frac{\Omega^{IASI}}{\Omega^{LE}_{overpass}} \cdot F^{LE}_{daily} \qquad \text{(Eq. 2.2)}$$

Here Ω^{IASI} denotes the NH_3 total column concentration from IASI, $\Omega^{LE}_{overpass}$ the modelled NH_3 total column at overpass time in LOTOS-EUROS (molecules cm^{-2}) and F^{LE}_{daily} the total daily NH_3 dry deposition flux in LOTOS-EUROS (kg N $ha^{-1}yr^{-1}$). F^{LE}_{daily} is the sum of the hourly NH_3 dry deposition fluxes, as shown in Eq. (2.3):

$$F^{LE}_{daily} = \sum_{h=1}^{24} F^{LE}_{h} = \sum_{h=1}^{24} V_d \, (C^{LE}_{h} - \chi^{LE}_{tot,h}) \qquad \text{(Eq. 2.3)}$$

The hourly NH_3 dry deposition flux is the product of the dry deposition velocity V_d and the difference between the hourly NH_3 surface concentration, C^{LE}_{h}, and the total compensation point of NH_3, $\chi^{LE}_{tot,h}$. To account for the high variability of atmospheric NH_3 and the limiting amount of available IASI observations, monthly means of these values are used rather than daily values.

2.3.3 Sensitivity analysis

The main sources of model uncertainties that are relevant for deposition modelling arise from uncertainties in the emission input and the deposition parameterizations (see Sect. 2.2.3). A total of four input fields were varied in LOTOS-EUROS: the MACC-III NH_3 emissions, the MACC-III NO_x and SO_2 emissions, the dry deposition velocity, V_d, of NH_3 and the wet deposition of NH_3. The wet deposition is varied by adjustment of the gas scavenging constant, G_{scav}, for NH_3. The wet scavenging constant G_{scav} linearly influences the amount of NH_3 wet deposition. This results in changes in the wet NH_3 deposition flux of +30 % and −30 %, too. The objective of these eight sensitivity runs is to assess the uncertainty ranges on the estimated dry NH_3 deposition fluxes resulting from modelling errors. Table 2.2 gives an overview of the parameters that are varied. We chose to apply a constant perturbation of +30 % and −30 % to one field at the time to see their individual effect and to improve the comparability of the results, too. Moreover, perturbations of ±30 % are reasonable ranges since they correspond to the estimated uncertainties in the MACC-III emission fields' annual totals and the uncertainties in the wet and dry deposition fluxes of NH_3.

Table 2.2. *Perturbations on input fields that have been used for the sensitivity analysis of the method.*

Perturbed parameter	Perturbations
MACC-III NH_3 emissions	+30 %, −30 %
MACC-III NO_x and SO_2 emissions	+30 %, −30 %
NH_3 dry deposition velocity, $V_d^{NH_3}$	+30 %, −30 %
NH_3 gas scavenging coefficient, $G_{scav}^{NH_3}$	+30 %, −30 %

2.4 Results

2.4.1 NH_3 surface concentrations

2.4.1.1 Europe

Fig. 2.3 shows the warm season (April–September) mean NH_3 surface concentrations in 2013 and 2014. Fig. 2.3a, c, e, g show the modelled concentrations from LOTOS-EUROS (which we will refer to as the "modelled concentrations") and concentrations that are derived from IASI in combination with LOTOS-EUROS (which we will refer to as "IASI-derived concentrations"). The dots represent the corresponding measurements from the EMEP stations. Fig. 2.3b, d, f, h show the absolute differences between the EMEP measurements and the modelled and IASI-derived concentrations. In general, the pattern of the EMEP measurements and the modelled and IASI-derived concentrations matches quite well. The majority of the EMEP measurements agree with the modelled and IASI-derived concentrations to −0.75 to +0.75 µg m^{-3}. The sum of the absolute differences between the warm season mean NH_3 surface concentrations in a cubic metre from EMEP and LOTOS-EUROS was 23.0 µg in 2013 and 32.5 µg in 2014. The sum of the absolute differences between the warm season mean NH_3 surface concentrations from EMEP and IASI was slightly lower: 22.6 µg in 2013 and 28.0 µg in 2014.

Fig. 2.4 shows scatterplots of the monthly mean (Fig. 2.4a, b, e, f) and the warm season mean (Fig. 2.4c, d, g, h) NH_3 surface concentrations. The *x* axis represents concentrations measured by the EMEP stations. The *y* axis represents either the modelled concentrations (blue) or the IASI-derived concentrations (orange). The monthly mean modelled concentrations and the EMEP measurements show a reasonably strong linear relationship in 2013 (r=0.71). The correlation between the two was weaker (r=0.39) in 2014. The correlation between the IASI-derived concentrations and the EMEP measurements was similar in 2013 (r=0.71) and was higher in 2014 (r=0.46). The warm season mean IASI-derived concentrations and the EMEP measurements have a slightly stronger correlation coefficient and an improved slope compared to the modelled concentrations.

Fig. 2.5 shows the mean NH_3 surface concentration of all EMEP stations per month and the corresponding modelled and IASI-derived concentrations at the same locations. The absolute differences per month are plotted in the same figure in blue (LOTOS-EUROS vs. EMEP) and orange (IASI-derived vs. EMEP). All concentration time profiles show a peak value in April, resulting from spring fertilization. The LOTOS-EUROS time profile at the EMEP locations decreases from April to May and starts to increase towards the end of the year. The time profile of the EMEP stations follows the same pattern from April to June but decreases towards the end of the year. The IASI-derived time profile shows a decreasing pattern, except in August, where there is a small peak. The IASI-derived time profile shows a relatively better comparison with the EMEP measurements in April and July to September in 2013 and in April and September in 2014. The sum of the absolute differences of the mean NH_3 surface concentrations in a cubic metre at all EMEP locations between LOTOS-EUROS and EMEP amounts to 3.1 µg in 2013 and 2.5 µg in 2014. The sum of the absolute differences between IASI and EMEP was somewhat smaller in 2013, amounting to 1.7 µg, and somewhat higher in 2014, amounting to 3.0 µg. In summary, the majority of the IASI-derived concentrations showed a slightly stronger correlation with the EMEP measurements than modelled concentrations on a monthly basis. The correlation became more pronounced on a seasonal basis (mean of April–September).

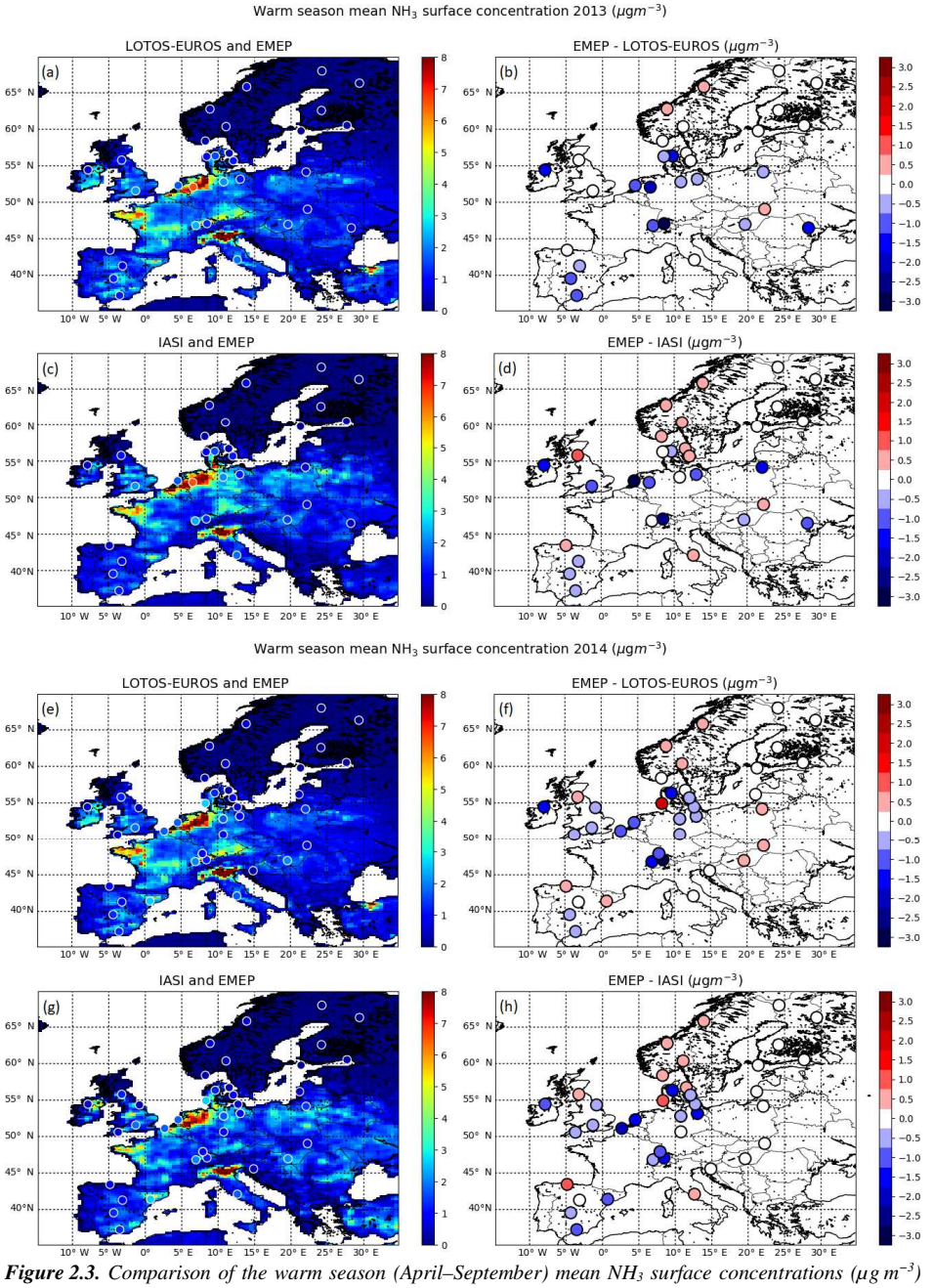

Figure 2.3. *Comparison of the warm season (April–September) mean NH_3 surface concentrations ($\mu g\, m^{-3}$) from LOTOS-EUROS and derived from IASI and the warm season mean NH_3 surface concentrations measured by the EMEP stations in 2013* ***(a, b, c, d)*** *and 2014* ***(e, f, g, h)****. The absolute differences between the two are shown in the right figures.*

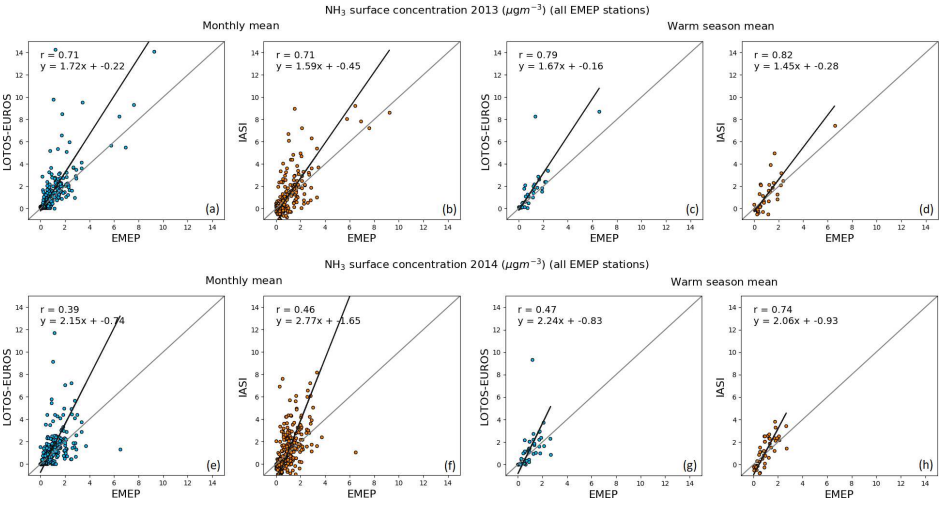

Figure 2.4. *Comparison of the monthly mean* ***(a, b, e, f)*** *and warm season (April–September) mean* ***(c, d, g, h)*** *NH_3 surface concentrations measured by the EMEP stations and the corresponding NH_3 surface concentrations from LOTOS-EUROS (blue dots) and inferred from IASI (orange dots) in 2013 (top) and 2014 (bottom).*

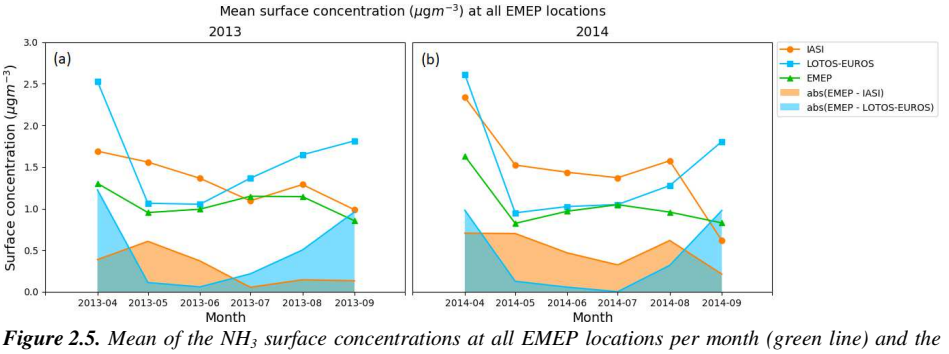

Figure 2.5. *Mean of the NH_3 surface concentrations at all EMEP locations per month (green line) and the coinciding NH_3 surface concentrations from LOTOS-EUROS (blue line) and derived from IASI (orange line) in 2013* ***(a)*** *and 2014* ***(b)****. The absolute differences between EMEP and LOTOS-EUROS are shown in blue and the absolute differences between EMEP and IASI are shown in orange.*

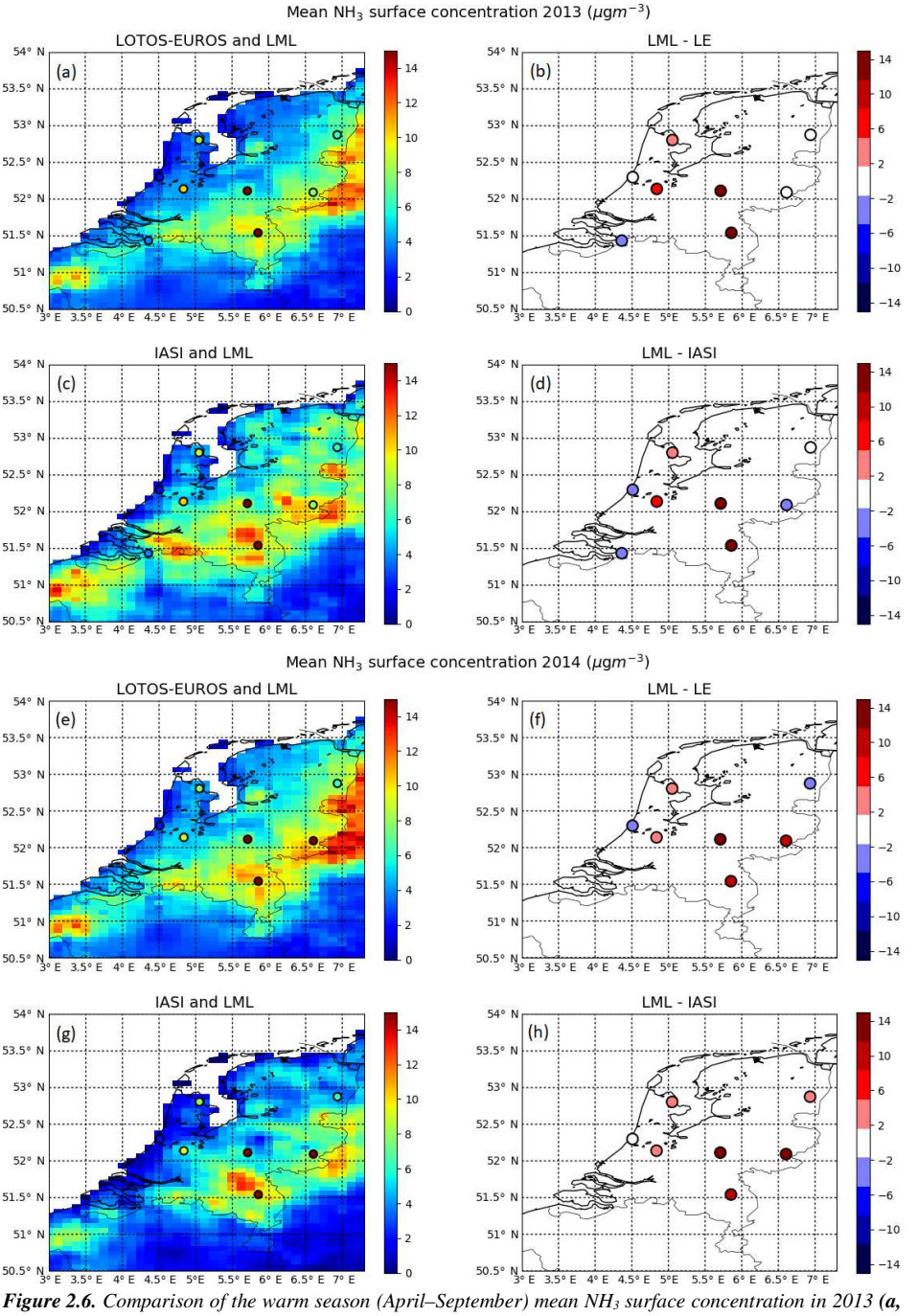

Figure 2.6. *Comparison of the warm season (April–September) mean NH_3 surface concentration in 2013* ***(a, b, c, d)*** *and in 2014* ***(e, f, g, h)*** *from LOTOS-EUROS and derived using IASI. The corresponding warm season mean NH_3 surface concentrations measured by the LML stations are plotted on top of the left figures. The right figures depict the differences between the two.*

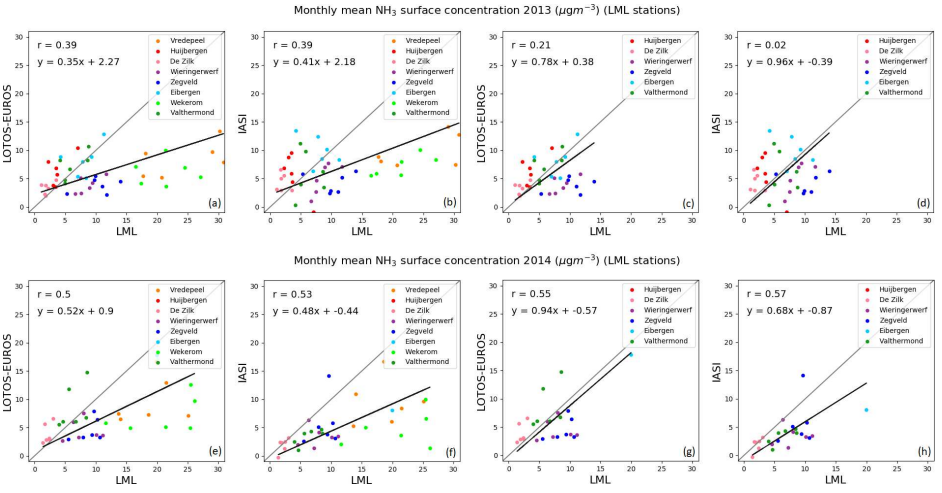

Figure 2.7. *Comparison of the monthly mean NH_3 surface concentrations measured by the LML stations and the corresponding LOTOS-EUROS and IASI-derived NH_3 surface concentrations during the warm season (April–September) of 2013 (top) and 2014 (bottom). The high-concentration stations (Vredepeel and Wekerom) are eliminated from the right figures* ***(c, d, g, h)****.*

2.4.1.2 The Netherlands

Comparison with LML measurements

Fig. 2.6 shows the warm season (April–September) mean NH_3 surface concentrations (µg m^{-3}) in the Netherlands in 2013 and 2014. The corresponding LML measurements are plotted on top of the modelled and IASI-derived concentrations. LOTOS-EUROS seems to capture the general pattern of the LML measurements fairly well in both 2013 and 2014. The sum of the absolute differences between the warm season mean NH_3 surface concentrations in a cubic metre from LML and LOTOS-EUROS was 47.3 µg in 2013 and 44.8 µg in 2014. The sum of the absolute differences between the warm season mean NH_3 surface concentrations from LML and IASI was slightly lower in 2013, namely 44.9 µg, and somewhat higher in 2014, namely 48.5 µg.

Fig. 2.7 shows scatterplots of the monthly mean NH_3 surface concentrations (µg m^{-3}). The *x* axis depicts the LML measured concentrations. The *y* axis depicts the corresponding modelled and IASI-derived concentrations. The modelled concentrations and the LML measurements show a moderate linear relationship (r=0.39 in 2013, r=0.50 in 2014). The high NH_3 concentration stations (Vredepeel and Wekerom) are underestimated by LOTOS-EUROS. The other stations are closer to the 1:1 line and appear to match quite well. The correlation coefficient of the IASI-derived concentrations and the LML measurements is r=0.39 in 2013 and r=0.53 in 2014. The IASI-derived concentrations also underestimate the high-concentration LML stations (Vredepeel and Wekerom) in both years. The majority of the low-concentration LML stations are overestimated by the IASI-derived concentrations in 2013 and underestimated by the IASI-derived concentrations in 2014. In general, both high and low LML measurements were reproduced inadequately by the IASI-derived concentrations. The elimination of the high-concentration stations (Vredepeel and Wekerom) does not lead to a better comparison of the LML measurements to the IASI-derived concentrations.

Table 2.3 gives a month-by-month comparison of the correlation coefficient, the slope and the intercept of the monthly mean NH_3 surface concentrations of all LML stations vs. the corresponding modelled and IASI-derived concentrations. In 5 out of 12 months, the IASI-derived concentrations and the LML measurements have a better correlation coefficient and slope compared to the modelled concentrations and the LML measurements. The modelled concentrations are consistently lower than the LML measurements. In short, the IASI-derived concentrations do not show a better comparability with the LML measurements compared to the modelled concentrations.

Comparison with MAN measurements

Fig. 2.8 shows the warm season mean NH_3 surface concentrations in the Netherlands in 2013 and 2014. The dots represent the corresponding MAN measurements. The patterns of the MAN measurements are captured quite well by the modelled concentrations, with low NH_3 surface concentrations near the coast and increasing values towards the east of the Netherlands. The sum of the absolute differences between the warm season mean NH_3 surface concentrations in a cubic metre from MAN and LOTOS-EUROS was 444.7 µg in 2013 and 494.3 µg in 2014. The sum of the absolute differences between the warm season mean NH_3 surface concentrations from MAN and IASI was slightly higher in both years, amounting to 512.1 µg in 2013 and 513.6 µg in 2014.

Fig. 2.9 shows scatterplots of the monthly mean (Fig. 2.9a, b, e, f) and warm season mean (Fig. 2.9c, d, g, h) NH_3 surface concentrations. The *x* axis depicts the MAN measurements. The *y* axis depicts the corresponding modelled or IASI-derived concentrations. The modelled concentrations and the MAN measurements show a moderate positive linear relationship (r=0.5 in 2013, r=0.46 in 2014). The correlation of the IASI-derived concentrations and the MAN measurements is somewhat weaker in both years (r=0.40 in 2013, r=0.38 in 2014). The IASI-derived concentrations and the MAN measurements show a similar to slightly stronger correlation (r=0.59 in 2013, r=0.54 in 2014) compared to the modelled concentrations and the MAN measurements for the warm season (r=0.54 in 2013, r=0.54 in 2014).

Fig. 2.10 shows the mean NH_3 surface concentration of all MAN stations per month and the corresponding modelled and IASI-derived concentrations at the same locations. The absolute differences per month are plotted in blue (LOTOS-EUROS vs. MAN) and orange (IASI-derived vs. MAN). The mean of all MAN stations peaks in April in both years. In 2013, the mean of all MAN stations increases from May on, peaks in July and then decreases towards the end of the year. In 2014, there is an additional peak in July, followed by another decrease.

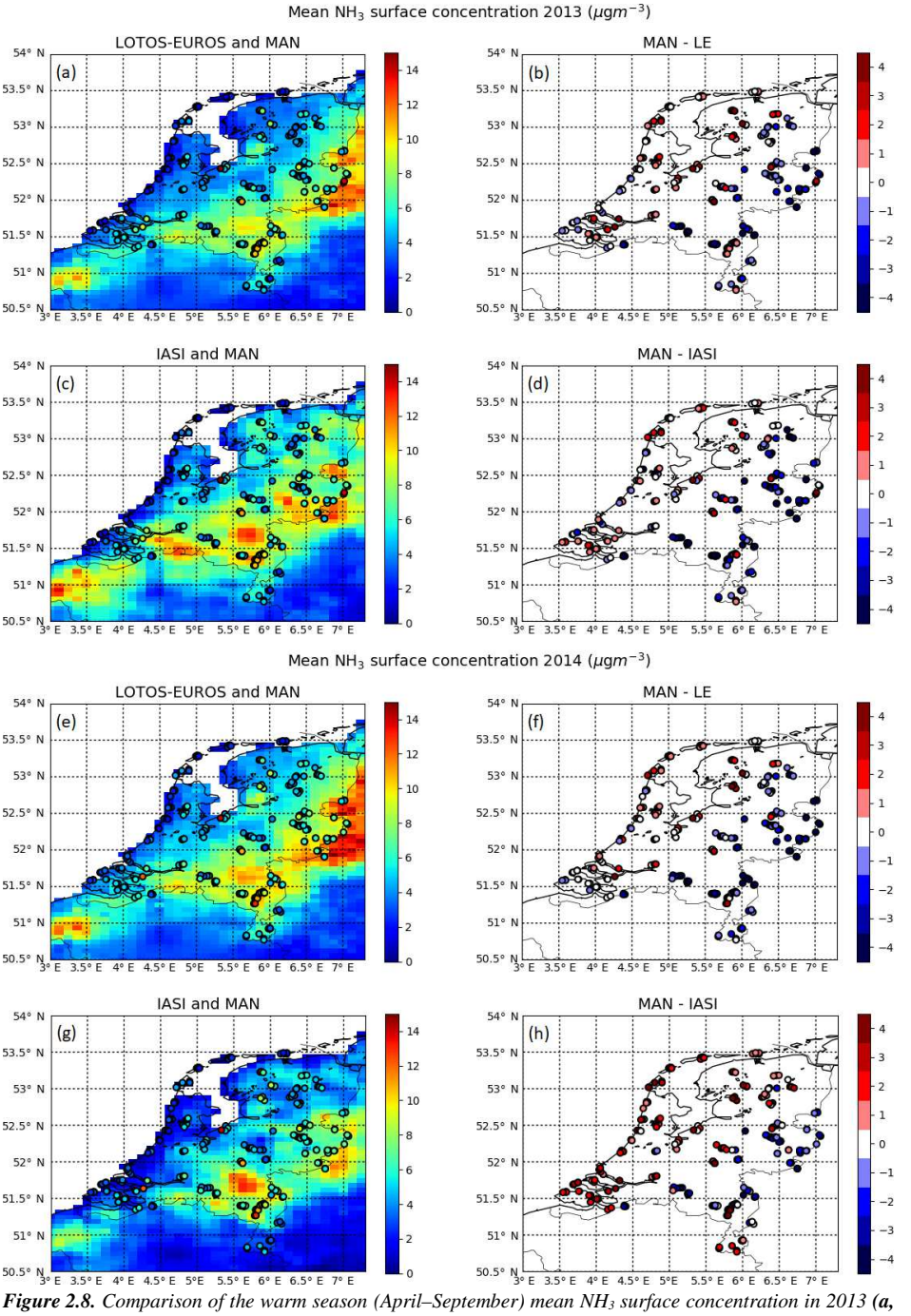

Figure 2.8. *Comparison of the warm season (April–September) mean NH_3 surface concentration in 2013* ***(a, b, c, d)*** *and in 2014* ***(e, f, g, h)*** *from LOTOS-EUROS and derived using IASI. The corresponding warm season mean NH_3 surface concentrations measured by the MAN stations are plotted on top of the left figures. The right figures depict the differences between the two.*

Table 2.3. *Month-by-month comparison of the correlation coefficient (r), slope and intercept of the monthly mean NH_3 surface concentrations of the LML stations (x axis) and the coinciding monthly mean LOTOS-EUROS and IASI-derived NH_3 surface concentrations (y axis). The arrows denote which of the two (LOTOS-EUROS or IASI) gives the most desirable value. The arrows are attributed to either LOTOS-EUROS or IASI based on the following criteria: highest r, slope closest to 1, intercept closest to 0 and smallest RMSD.*

	Month	LOTOS-EUROS				IASI-derived			
		r	Slope	Intercept	RMSD	*r*	Slope	Intercept	RMSD
LML	Apr 2013	0.57	0.39 ↑	4.12	7.78 ↑	0.57	0.36	0.01 ↑	10.80
	May 2013	0.49 ↑	0.19 ↑	2.16 ↑	7.53	−0.21	−0.30	9.61	7.20 ↑
	Jun 2013	0.38	0.19	1.73 ↑	8.58	0.44 ↑	0.45 ↑	1.74	6.80 ↑
	Jul 2013	0.36	0.18	3.31 ↑	11.67	0.46 ↑	0.34 ↑	3.74	10.00 ↑
	Aug 2013	0.49	0.23	3.82	10.10	0.86 ↑	0.35 ↑	3.63 ↑	7.93 ↑
	Sep 2013	0.27 ↑	0.33	4.28	5.79 ↑	0.04	0.65 ↑	0.38 ↑	7.31
	Apr 2014	0.69 ↑	0.56 ↑	4.36	5.81 ↑	0.21	0.46	0.44 ↑	10.32
	May 2014	0.39	0.29	1.90 ↑	6.35	0.76 ↑	0.72 ↑	−2.79	6.15 ↑
	Jun 2014	0.63	0.20	2.31	9.65	0.85 ↑	0.66 ↑	−0.99 ↑	6.60 ↑
	Jul 2014	0.70 ↑	0.19	2.27	10.53	0.68	0.29 ↑	1.22 ↑	10.19 ↑
	Aug 2014	0.68 ↑	0.47 ↑	0.75	4.97 ↑	0.46	0.31	0.69 ↑	6.50
	Sep 2014	0.55 ↑	0.33 ↑	4.84	8.20 ↑	0.04	0.27	1.49 ↑	11.59

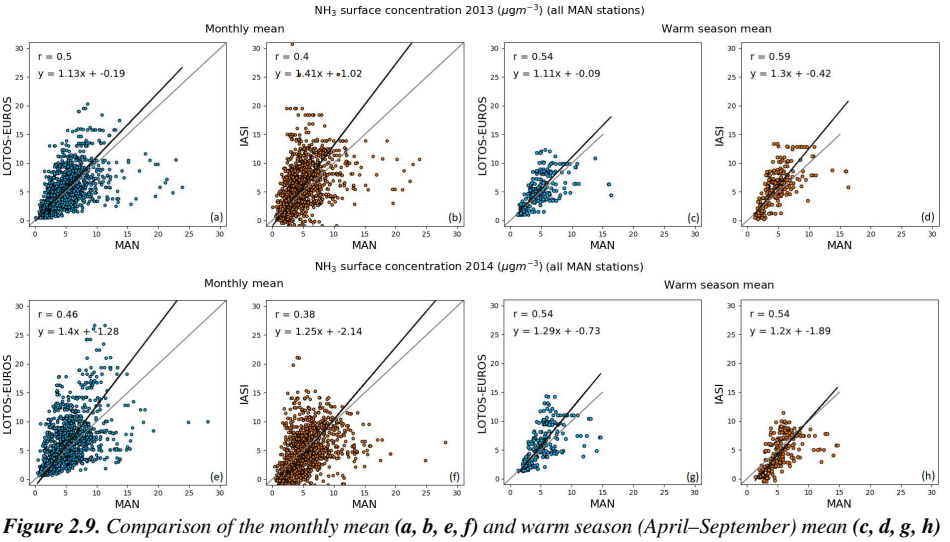

Figure 2.9. *Comparison of the monthly mean* ***(a, b, e, f)*** *and warm season (April–September) mean* ***(c, d, g, h)*** *NH_3 surface concentrations measured by the MAN stations and the corresponding NH_3 surface concentrations from LOTOS-EUROS (blue dots) and inferred from IASI (orange dots) in 2013 (top) and 2014 (bottom).*

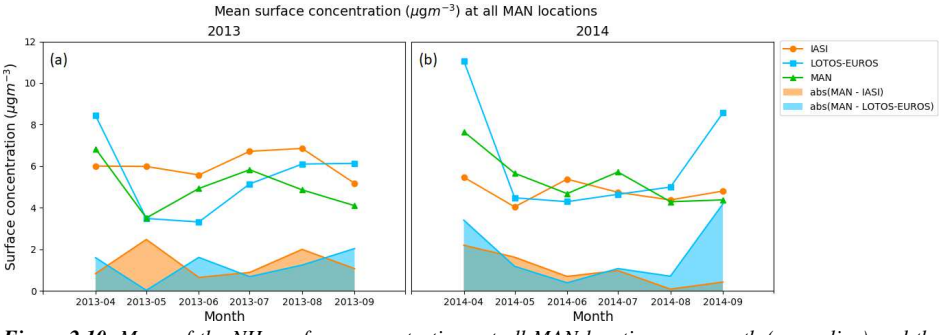

Figure 2.10. *Mean of the NH_3 surface concentrations at all MAN locations per month (green line) and the coinciding NH_3 surface concentrations from LOTOS-EUROS (blue line) and IASI (orange line) in 2013* ***(a)*** *and 2014* ***(b)****. The absolute differences between MAN and LOTOS-EUROS are shown in blue and the absolute differences between MAN and IASI are shown in orange.*

The sum of the absolute differences of the mean NH_3 surface concentrations in a cubic metre at all MAN locations between LOTOS-EUROS and MAN amounts to 7.2 µg in 2013 and 10.9 µg in 2014. The sum of the absolute differences between IASI and MAN was somewhat larger in 2013, amounting to 7.9 µg, but considerably smaller in 2014, amounting to 6.0 µg.

Table 2.4 shows the correlation coefficient, the slope and the intercept of the MAN measurements vs. the modelled and IASI-derived concentrations for the warm months in 2013 and 2014. In 2013, the IASI-derived concentrations show a weaker correlation with the MAN measurements than the modelled concentrations in all months. Only in May and June in 2014, the IASI-derived concentrations compared slightly better to the MAN measurements than the modelled concentrations.

The data are grouped into different MAN NH_3 surface concentration ranges to test the performance of the modelled and IASI-derived concentrations as a function of concentration level. Fig. 2.11 shows the grouped absolute differences between the monthly mean NH_3 surface concentrations measured by the MAN stations and the corresponding modelled (blue) and IASI-derived (orange) concentrations. For low MAN concentration ranges (0–10 µg m^{-3}), the modelled concentrations agree fairly well with the MAN measurements in both years. For higher MAN concentration ranges (>10 µg m^{-3}), the model seems to underestimate the monthly mean NH_3 surface concentrations. The IASI-derived concentrations were relatively higher than the modelled concentrations for all concentration levels in 2013. The opposite is true in 2014, where the IASI-derived concentrations were relatively lower than the modelled concentrations. We conclude that the differences between modelled and IASI-derived concentrations in the Netherlands cannot be assigned to specific concentration levels. In summary, the comparison with the MAN measurements does also not show any significant or consistent improvement in the IASI-derived concentrations compared to the modelled concentrations.

Table 2.4. *Month-by-month comparison of the correlation coefficient (r), slope and intercept of the monthly mean NH_3 surface concentrations of the MAN stations (x axis) and the coinciding monthly mean LOTOS-EUROS and IASI-derived NH_3 surface concentrations (y axis). The arrows denote which of the two (LOTOS-EUROS or IASI) gives the most desirable values. The arrows are attributed to either LOTOS-EUROS or IASI based on the following criteria: highest r, slope closest to 1, intercept closest to 0 and smallest RMSD.*

	Month	LOTOS-EUROS				IASI-derived			
		r	Slope	Intercept	RMSD	*r*	Slope	Intercept	RMSD
MAN	Apr 2013	0.53 ↑	1.48	−1.41	4.33	0.46	1.05 ↑	−1.08 ↑	3.37 ↑
	May 2013	0.48 ↑	0.92 ↑	0.30	1.95 ↑	0.44	1.69	0.04 ↑	3.94
	Jun 2013	0.59	0.70 ↑	−0.06 ↑	2.66 ↑	0.59	1.42	−1.19	3.23
	Jul 2013	0.48 ↑	0.71	0.94	3.32 ↑	0.44	1.15 ↑	−0.06 ↑	4.18
	Aug 2013	0.49	0.89 ↑	1.67	3.37 ↑	0.49	1.15	1.11 ↑	4.03
	Sep 2013	0.40 ↑	1.45 ↑	0.15 ↑	3.47 ↑	0.25	3.05	−7.48	6.09
	Apr 2014	0.52 ↑	1.75	−2.80	5.66	0.35	0.98 ↑	−2.03 ↑	4.24 ↑
	May 2014	0.39	0.80	−0.10 ↑	2.78 ↑	0.46 ↑	1.08 ↑	−2.12	3.17
	Jun 2014	0.70	0.87 ↑	0.12 ↑	2.08 ↑	0.71 ↑	1.41	−1.44	2.74
	Jul 2014	0.56	0.76	0.18 ↑	2.74 ↑	0.56	1.08 ↑	−1.79	3.13
	Aug 2014	0.47	1.31 ↑	−0.57 ↑	2.44 ↑	0.47	1.50	−2.09	2.58
	Sep 2014	0.28 ↑	1.22 ↑	3.42 ↑	6.03 ↑	0.12	1.87	−3.73	6.23

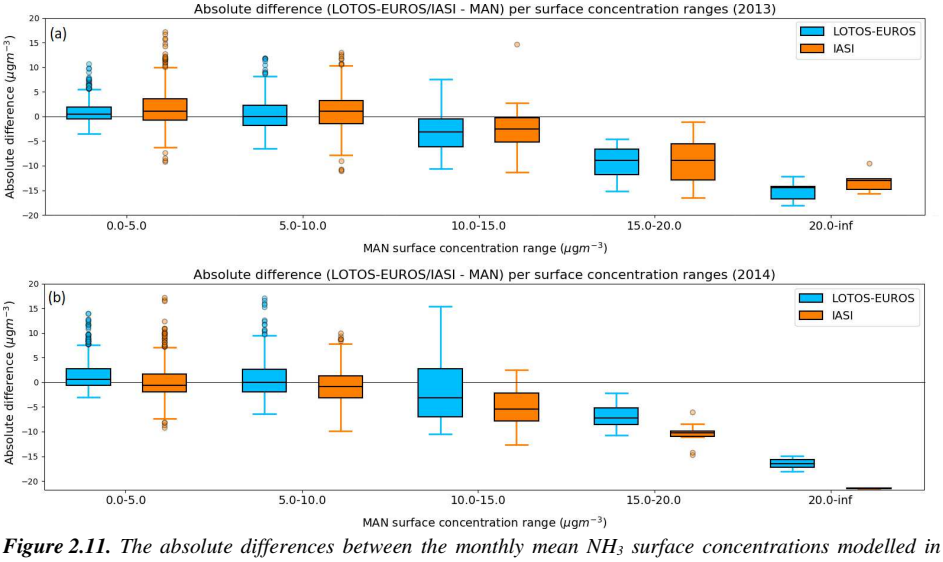

Figure 2.11. *The absolute differences between the monthly mean NH_3 surface concentrations modelled in LOTOS-EUROS (blue) and derived from IASI (orange) and the monthly mean NH_3 surface concentrations measured by the MAN stations in the warm season (April–September) in 2013* ***(a)*** *and 2014* ***(b)****, grouped as function of the MAN monthly mean NH_3 surface concentrations. The black line indicates the median, the edges of the boxes indicate the 25th and the 75th percentiles (Q1 and Q2), the whiskers indicate the full range of the absolute differences (Q1 − 1.5*IQR and Q3 + 1.5*IQR), and the dots indicate the outliers values that lie outside the whiskers.*

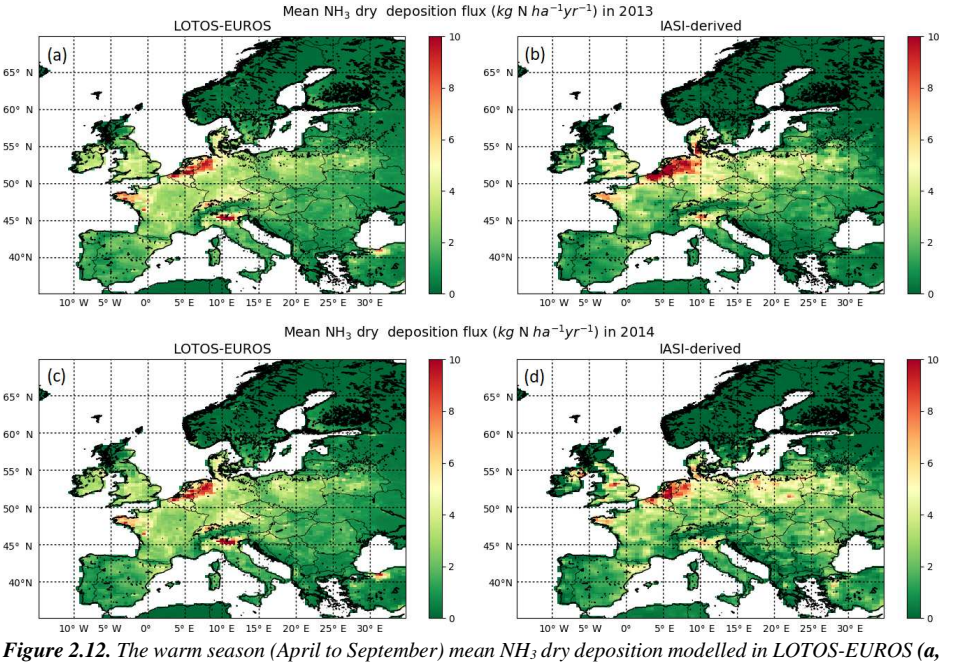

Figure 2.12. *The warm season (April to September) mean NH_3 dry deposition modelled in LOTOS-EUROS* ***(a, c)*** *and inferred from IASI* ***(b, d)*** *in kg N ha^{-1} yr^{-1} in 2013* ***(a, b)*** *and 2014* ***(c, d)****.*

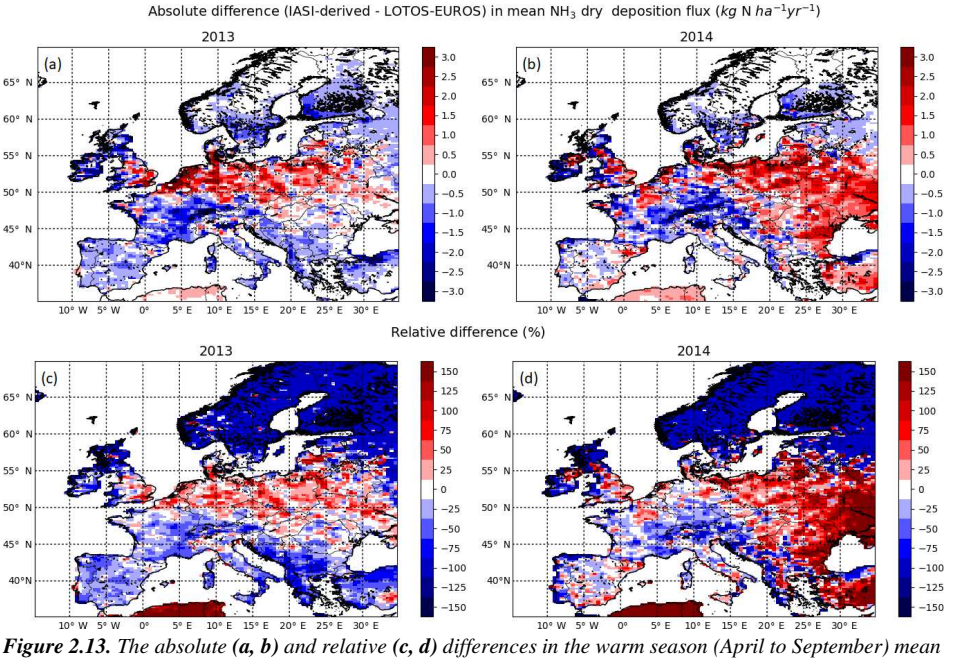

Figure 2.13. *The absolute* ***(a, b)*** *and relative* ***(c, d)*** *differences in the warm season (April to September) mean NH_3 dry deposition modelled in LOTOS-EUROS and inferred from IASI in 2013* ***(a, c)*** *and 2014* ***(b, d)****.*

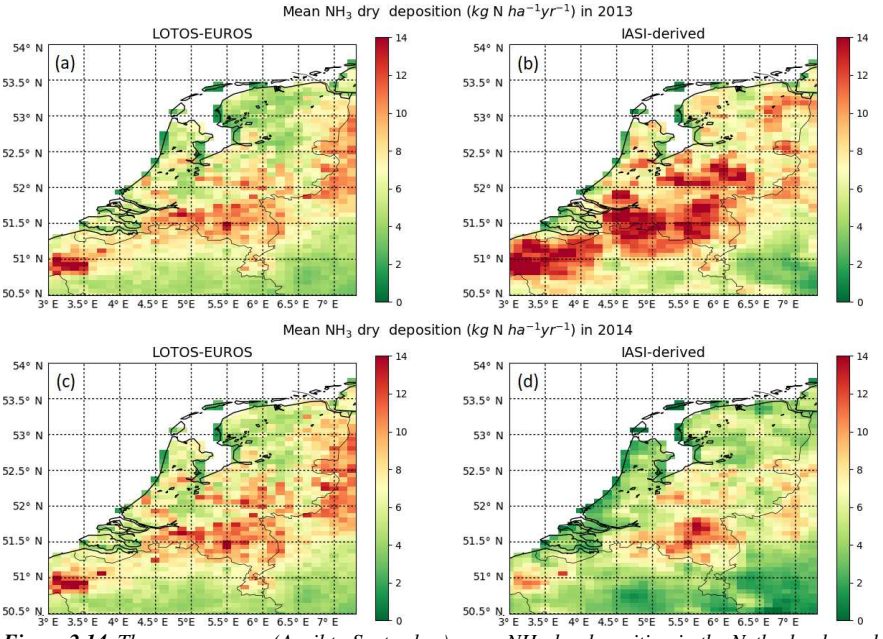

Figure 2.14. *The warm season (April to September) mean NH_3 dry deposition in the Netherlands modelled in LOTOS-EUROS* ***(a, c)*** *and inferred from IASI* ***(b, d)*** *in kg N ha^{-1} yr^{-1} in 2013* ***(a, b)*** *and 2014* ***(c, d)****.*

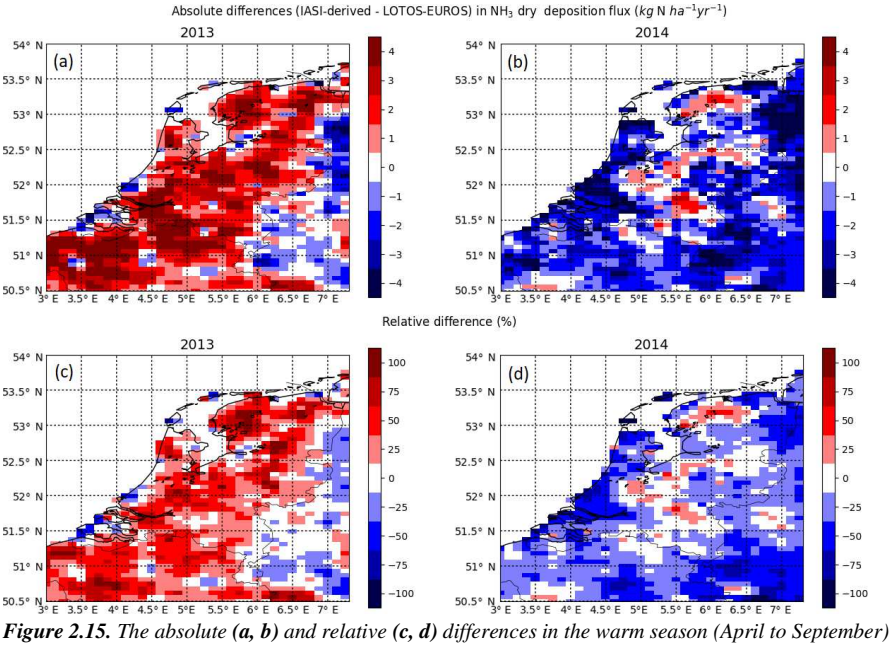

Figure 2.15. *The absolute* ***(a, b)*** *and relative* ***(c, d)*** *differences in the warm season (April to September) mean NH_3 dry deposition in the Netherlands modelled in LOTOS-EUROS and inferred from IASI in 2013* ***(a, c)*** *and 2014* ***(b, d)****.*

2.4.1.3 Summary of the comparison with in situ measurements

We compared the modelled and IASI-derived concentrations to measurements of the European EMEP network. The IASI-derived concentrations showed in general a slightly stronger correlation with the EMEP measurements than modelled concentrations on a monthly basis. Moreover, the correlation became more pronounced on a seasonal basis (mean of April–September). We then compared the modelled and the IASI-derived concentrations to measurements of Dutch MAN and LML networks. This comparison, on the other hand, did not show any significant or consistent improvement in the IASI-derived concentrations compared to the modelled concentrations.

In general, both the modelled and the IASI-derived concentrations seem to be overestimated in emission areas. This could potentially be related to the overpass time of the satellite. In high emission areas, the NH_3 concentrations are more variable in time, and the IASI observations might have an uncertain representativeness. Moreover, the measurements in high emission areas are generally more uncertain with regard to their spatial representativeness. Overall, these measurements can be more affected by local rather than regional sources.

Generally, the modelled and the observed NH_3 total columns match quite well. This means that the LOTOS-EUROS model represents the spatial distribution of NH_3 rather well. There are some areas with large discrepancies between the two where we see considerable deviations in the modelled and the IASI-derived concentrations. Most of these areas, however, cannot be validated against measurements, because of the lack of measurements here. The changes in the comparison of the available measurements with modelled vs. IASI-derived concentrations are therefore relativity small. Based on the measurements we have, we conclude that we do not see any significant improvement in the IASI-derived concentrations compared to the modelled concentrations.

The differences between Europe and the Netherlands could be explained by the location of the ground measurements. The majority of the European-scale stations are located in background regions, with relatively well-mixed and low NH_3 concentrations. Most stations in the Netherlands, on the other hand, are located in, or nearby, regions with relatively higher NH_3 concentrations. As a result, the vertical profile shapes in LOTOS-EUROS in the Netherlands are more complex and variable in time, as this region is influenced by a constantly changing combination of transport, emission and deposition. The use of an inadequate vertical profile to derive NH_3 surface concentrations from IASI could lead to an erroneous redistribution of the total amount of measured NH_3, therewith worsening the comparability with in situ measurements. On the contrary, the vertical profile shapes in background regions are more stable and constant in time, and therefore more likely to be described adequately by the LOTOS-EUROS model.

Side note on validation with in situ measurements

The differences between the in situ measurement and the modelled and IASI-derived concentrations can partially be explained by their discrepancy in terms of spatial representation, which limits their comparability to some extent. The footprint of the in situ measurements is relatively small and easily influenced by local factors, whereas the model and the satellite provide us with a mean value over a much larger area. The two high-concentration stations of the LML

network in the Netherlands, Vredepeel and Wekerom, are, for instance, influenced by nearby emission sources which cannot be resolved by regional models at the current resolution.

2.4.2 NH_3 dry deposition flux

2.4.2.1 Europe

The monthly mean dry NH_3 deposition flux has been computed for the warm season (April to September) in 2013 and 2014. Fig. 2.12 shows the warm season mean dry NH_3 deposition flux (kg N ha^{-1} yr^{-1}). Fig. 2.12a, c show the original, modelled flux from LOTOS-EUROS (which will be referred to as the "modelled flux"). Fig. 2.12b, d show the modelled flux adjusted by the IASI satellite observations (which will be referred to as "IASI-derived flux"). The modelled fluxes were very similar in both years. Fig. 2.13 shows the absolute and relative differences between the modelled and the IASI-derived flux. In 2013, the IASI-derived fluxes were higher than the modelled fluxes in the Netherlands and Belgium. This depicts that the IASI-observed NH_3 total columns here were higher than the modelled total columns in LOTOS-EUROS. The IASI-derived fluxes were higher than the modelled fluxes in other areas such as Germany and large parts of central Europe, mainly in Poland, Belarus and Romania. In 2014, the IASI-derived fluxes were much higher than the modelled flux in parts of central Europe, mainly in Poland and the Czech Republic, and in parts of the United Kingdom, for instance, Northern Ireland. In both years, the IASI-derived fluxes were much lower than modelled fluxes in Switzerland, the Po Valley in Italy and the northern part of Turkey. Here, the IASI-observed NH_3 total columns were thus consistently lower than the modelled total columns in LOTOS-EUROS. Inadequate emission input data could explain the differences at these locations. Another possible cause is incorrect modelling of the atmospheric transport and/or stability of NH_3 in LOTOS-EUROS.

2.4.2.2 The Netherlands

The modelled and IASI-derived fluxes in the Netherlands are shown in Fig. 2.14. Fig. 2.14 shows that the modelled fluxes were similar in both years, whereas the IASI-derived flux varied quite a lot. The IASI-derived flux was higher than the modelled flux in 2013 and lower than the modelled flux in 2014. The IASI-observed NH_3 total columns in the Netherlands were thus in general somewhat higher than the modelled NH_3 columns in 2013 and somewhat lower than the modelled NH_3 columns in 2014.

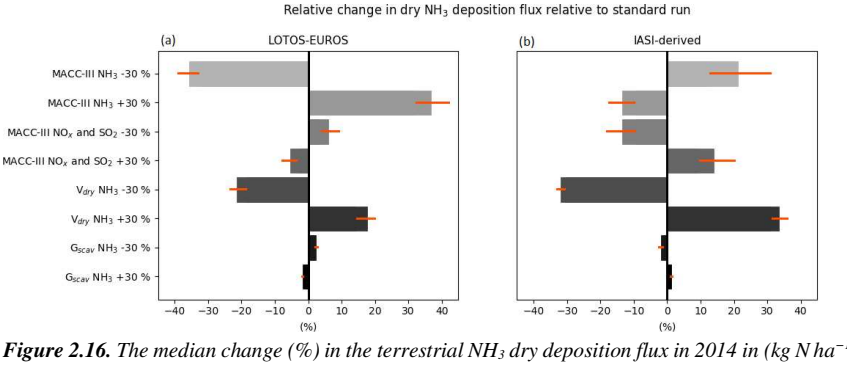

Figure 2.16. *The median change (%) in the terrestrial NH_3 dry deposition flux in 2014 in (kg N ha^{-1} yr^{-1}) from LOTOS-EUROS* ***(a)*** *and IASI-derived fluxes* ***(b)****, resulting from different perturbations of model inputs of LOTOS-EUROS. The orange lines indicate the 25th and the 75th quartiles.*

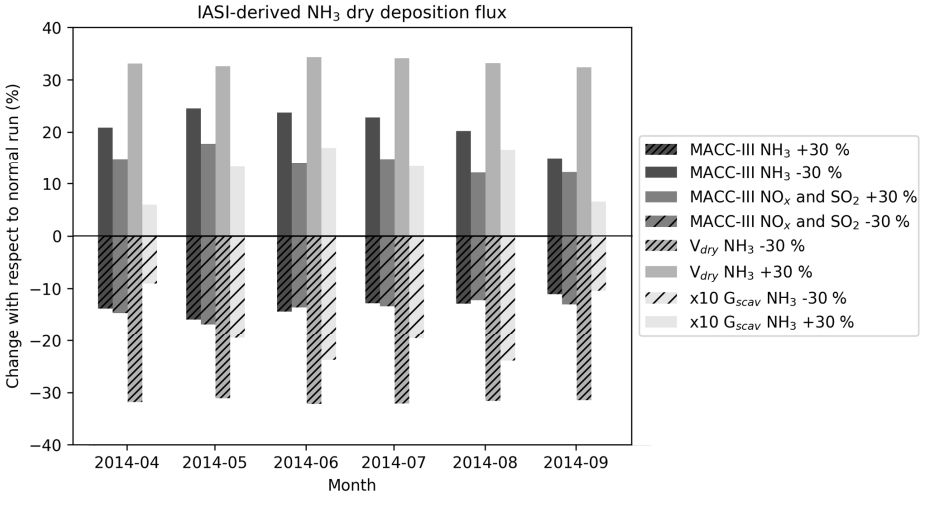

Figure 2.17. *The change (%) in the monthly mean IASI-derived NH_3 dry deposition flux resulting from different perturbations of the LOTOS-EUROS model.*

Fig. 2.15 depicts the absolute and relative differences between the modelled and IASI-derived fluxes. In 2013, the main differences occurred in the central and northernmost parts of the Netherlands, where the IASI-derived fluxes were clearly higher than the modelled ones. Furthermore, the IASI-derived fluxes were higher than the modelled fluxes for the largest part of the Netherlands. In 2014, the IASI-derived fluxes were lower than the modelled fluxes for the largest part of the Netherlands, except for the centre and the northernmost part.

2.4.2.3 Interannual differences

The interannual variations of the modelled and IASI-derived flux differences (see Figs. 2.13 and 2.15) could be related to different meteorological conditions. The annual global climate reports from the National Oceanic and Atmosphere Administration (NOAA) show that the mean temperatures in Europe were higher in 2014 than in 2013, especially in western Europe. This might have had an effect on the actual emissions and their variability, which is only limited taken into account by the model. The annual precipitation in both years was near average for Europe as a whole. However, if we zoom in to a more regional scale, we see that it was much wetter than average during the warm season in nearly all parts of the Balkan peninsula and Turkey (NOAA, 2014, 2015). Fig. 2.13 shows that the largest interannual variations on a European scale occur around the Black Sea: in Ukraine but also in the eastern parts of the Balkan peninsula and Turkey. Some of these regions thus coincide with regions that experienced heavy rainfall in 2014 and might have affected emission and deposition processes which are not taken into account by the model. This suggests that meteorological effects might indeed influence our results. However, the examined period of two warm seasons only is too short to draw a conclusion.

2.4.3 LOTOS-EUROS sensitivity study

The results of the sensitivity runs are summarized in Figs. 2.16, 2.17 and 2.18. Fig. 2.16 shows the relative changes in the warm season mean terrestrial dry NH_3 deposition flux over Europe modelled in LOTOS-EUROS (Fig. 2.16a) and derived from IASI (Fig. 2.16b) in 2014 for different model runs. The mean LOTOS-EUROS dry NH_3 deposition over the land cells in the modelling grid in 2014 was 1.76 kg N ha^{-1} yr^{-1}. The mean IASI-derived dry NH_3 deposition flux was somewhat higher, namely 2.20 kg N ha^{-2} yr^{-1}.

Variations in the MACC-III NH_3 emissions caused the largest changes in the modelled flux. The smallest change was obtained by variation of the wet deposition scavenging coefficient G_{scav}. The variations in the dry deposition velocity V_d led to the biggest changes in the IASI-derived flux. The effect appears to be amplified compared to the effect on the modelled flux. The effect of the MACC-III NH_3 emissions is dampened. On the other hand, the effect of the MACC-III NO_x and SO_2 emissions is also amplified. The signs of the changes in the IASI-derived flux have flipped because of the changes in MACC-III NH_3, MACC-III NO_x and SO_2 and G_{scav}. The modelled flux is 1:1 sensitive to emission changes in NH_3, whereas for IASI-derived flux this is much lower. The IASI-derived flux, in turn, changes 1:1 with the V_d. The variations in the modelled flux are a result of daily and monthly variations in emissions. The variations in the IASI-derived flux are also a result of these variations, but on top of this they also include an effect of the overpass time of the satellite.

Fig. 2.17 shows the changes (%) of monthly mean IASI-derived fluxes in 2014 resulting from the different LOTOS-EUROS sensitivity runs. Note that the effect of the runs with changes in wet deposition through variations of the gas scavenging coefficient for NH_3 is enlarged by a factor of 10. We see that the changes with respect to the standard LOTOS-EUROS run are in general constant over the months. The least variation is observed for the runs with changed V_{dry} values, that all resulted in a change of ∼31 % per month. The runs with adjusted MACC-III emissions of NH_3 and emissions of NO_x and SO_2 led to largest changes in May and the smallest changes in September. The maximum differences between months are 9.5 % and 5.6 %, respectively, for the runs with adjusted NH_3 and the runs with adjusted NO_x and SO_2 values. The runs with changed values of G_{scav} for NH_3 seem to be affected most by changing weather conditions, which resulted in the relatively largest variation per month. However, because the changes in the IASI-derived flux are small (−2.4 % to +1.7 %), we now continue to look at yearly changes.

Fig. 2.18 shows the relative standard deviation (%) of all eight sensitivity runs for Europe. Fig. 2.18d shows the relative standard deviation of the final IASI-derived flux. The relative standard deviation varies from ∼20 % to ∼50 % throughout Europe. The smallest variations can be seen in the southwestern and central parts of Europe. The highest variations, of ∼40 %–50 %, are mainly found in long-distance transport areas with low NH_3 concentrations and deposition fluxes, such as Scandinavia, and in areas with high aerosol precursor emissions, such as the Balkans.

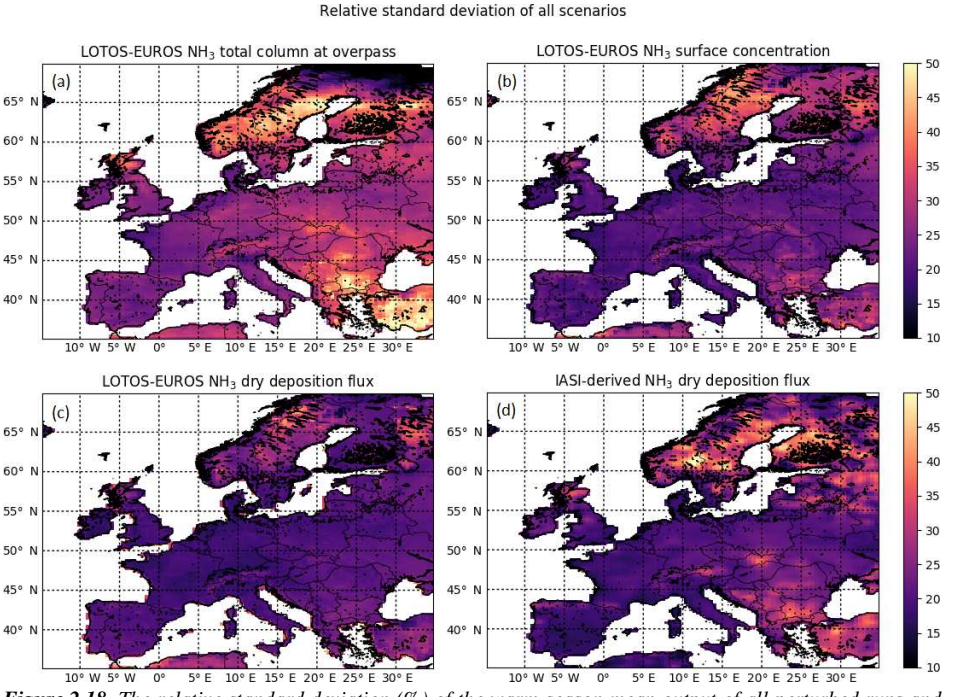

Figure 2.18. *The relative standard deviation (%) of the warm season mean output of all perturbed runs and the associated dry deposition estimate inferred from IASI in 2014. Panel* ***(a)*** *shows the LOTOS-EUROS NH_3 total column concentration at overpass time,* ***(b)*** *the LOTOS-EUROS NH_3 surface concentration,* ***(c)*** *the NH_3 dry deposition flux in LOTOS-EUROS and* ***(d)*** *the resulting IASI-derived NH_3 dry deposition flux.*

2.5 Discussion

In this paper, we examined the applicability and the limitations of the method suggested by Nowlan et al. (2014) for the derivation of NH_3 surface concentrations and dry deposition fluxes across Europe. A comparison of the LOTOS-EUROS modelled and IASI-derived NH_3 surface concentrations with in situ measurements of the EMEP network on a European scale and the LML and MAN networks in the Netherlands has been made. Although there appeared to be some improvements in the IASI-derived NH_3 surface concentrations compared to the modelled LOTOS-EUROS NH_3 surface concentrations, mainly in background regions, there did not seem to be any significant, consistent improvement. In addition, the timing of the IASI-derived NH_3 surface concentrations did not show better correspondence with the in situ observations than the modelled NH_3 surface concentrations. Consequently, as the dry NH_3 deposition fluxes are directly derived from the NH_3 surface concentrations, no significant improvement is expected here either. On top of this, the sensitivity study using eight input parameters important for NH_3 dry deposition modelling showed that the effect of model uncertainties on the IASI-derived dry NH_3 deposition fluxes is amplified by the estimation procedure compared to the effect on the model simulations itself. The final IASI-derived dry NH_3 deposition fluxes can vary ~20 % up to ~50 % throughout Europe as a result of model uncertainties.

The method used to derive the NH_3 surface concentrations and dry deposition fluxes from IASI observations is based on various assumptions. For one, the method assumes that the relationship between the NH_3 concentration and the dry deposition flux is linear, whereas this relationship is in reality non-linear. In fact, these quantities can even be anti-correlated with highest surface concentrations during the night when the atmosphere is stable and the exchange is limited. The compensation point of NH_3 further enhances the non-linearity. For our purpose, we focus on a single time of the day using monthly data; however, approximating this concentration–flux relationship by a linear curve may seem reasonable for concentration regimes below the saturation point. For higher NH_3 surface concentrations the current approach will likely lead to overestimated dry deposition fluxes. Moreover, this study includes the impact of the compensation point of NH_3 through the dry deposition scheme in LOTOS-EUROS. Although the uncertainties are relatively large as the used compensation points are based on relatively few observations (e.g. Wichink Kruit et al., 2007), we feel that the inclusion of the compensation point is a strong point of this study.

Moreover, the approach by Nowlan also assumes that the NH_3 total column concentrations measured by IASI serve as a direct proxy of the NH_3 surface concentrations. In reality, however, the relationship between the two is influenced by various different factors, including the vertical distribution of NH_3 and the satellite's sensitivity. There are already quite some uncertainties involved with the vertical distribution of NH_3, and therefore tower measurement campaigns (Dammers et al., 2017a; Li et al., 2017a) are very important to strengthen our understanding. Dammers et al. (2017a), for instance, showed that the daytime boundary layer is well mixed, which supports the choice of a model that uses the mixed layer approach such as LOTOS-EUROS. Li et al. (2017b) showed that there is a clear seasonal variation in the vertical distribution of NH_3 and that the slope of the NH_3 concentration gradient varies throughout the year. During winter, Li et al. (2017b) observed relatively high NH_3 ground concentrations due to potential trapping of NH_3 emissions in a shallow winter boundary layer and reduced NH_3 concentrations higher up the column. In these types of situations, the IASI satellite instrument potentially misses high NH_3 ground concentrations because of the lack of sensitivity to the lower parts of the boundary layer. The computation of averaging kernels for IASI could help to indicate more precisely where the sensitivity lies and how the measured total columns are distributed. Moreover, further development and validation of the IASI retrieval may help to improve our understanding of the satellite's product, therewith also increasing its applicability.

The method also assumes that the timing and distribution of the emissions in the LOTOS-EUROS model closely represent reality, as the ratio between the retrieved and the modelled ammonia burden is used at overpass time. The accuracy of the seasonal variation in the NH_3 emissions in LOTOS-EUROS is therefore of great importance. The reliability of yearly dry NH_3 deposition estimates using our method is limited by the lack of high-quality IASI observations during the cold season. As a result, derivation of yearly IASI-derived NH_3 dry deposition estimates may differ substantially depending on whether or not the spring maximum peak occurs in the satellite-observed months (April–September). Skjøth et al. (2011) presented the seasonal variation and the distribution of NH_3 emissions for different European countries per agricultural source. They showed, for instance, that approximately half of the NH_3 emissions from spring fertilization are usually emitted in March. As the spring fertilization amounts to ~20 %–50 % of the yearly total NH_3 emissions, this may result in a variation of the same magnitude on the subsequent deposition

estimates. Improvement of the seasonal variation in NH_3 emissions in LOTOS-EUROS could be used to fill in this gap and lead to a more accurate representation of reality. Skjøth et al. (2011) showed that the implementation of a dynamic NH_3 emission model for different agricultural sources may result in considerable model performance improvements when high-quality activity data and information on spatial distributions of emissions are available. Furthermore, Hendriks et al. (2016) showed that the use of manure transport data for NH_3 emission time profiles leads to additional model improvements and a better representation of the spring maximum.

Moreover, mismatches between the actual and modelled diurnal variations in NH_3 emission could also easily lead to large differences in the IASI-derived dry NH_3 deposition estimates. As an illustration, Sintermann et al. (2016), for instance, measured NH_3 emissions from an agricultural surface after slurry application and showed that ~80 % of the total NH_3 was emitted within 2 h. Combined with the short lifetime of NH_3, there is a possibility that the IASI instrument completely misses these kinds of events if they occur after its overpass. A possible way to reduce the impact of the diurnal variation is to combine information from IASI with other satellites that have different overpass times. NH_3 observations from the CrIS satellite instrument could, for instance, be used (Shephard and Cady-Pereira, 2015).

At this stage, we can conclude that the IASI-derived NH_3 deposition fluxes do not show strong improvements compared to modelled NH_3 deposition fluxes and there is a future need for better, more robust, methods to derive NH_3 dry deposition fluxes. This could potentially be achieved by further integration of existing in situ and satellite data into models with special attention to data representativeness, for instance, by means of data assimilation. In addition, there is a need for a better understanding of the surface exchange of NH_3 for different land use types. Model parameterizations of the surface exchange of NH_3 are now based on a limited number of direct flux measurements, and more measurements could definitely improve this. Also, a better understanding of the timing and distribution of NH_3 emissions could lead to considerable improvements in modelled emission fields and consequently deposition fields from CTMs.

Acknowledgements. The authors acknowledge the Nederlandse Organisatie voor Wetenschappelijk Onderzoek (NWO). This project was funded by the NWO under project number ALW-GO/16-05. The authors would like to thank the “Centre National d'Etudes Spatiales” (CNES, France) for building and developing IASI and for sharing their products. The MetOp satellites are part of the EUMETSAT Polar System. We acknowledge the Aeris website (https://iasi.aeris-data.fr/nh3/, last access: 10 January 2018) for providing access to the IASI-NH_3 dataset. Moreover, we would like to thank RIVM and EMEP for maintaining, collecting and sharing data from their NH_3 ground networks.

Chapter 3: Satellite-derived leaf area index and roughness length information for surface–atmosphere exchange modelling: a case study for reactive nitrogen deposition in north-western Europe using LOTOS-EUROS v2.0.

Abstract. The nitrogen cycle has been continuously disrupted by human activity over the past century, resulting in almost a tripling of the total reactive nitrogen fixation in Europe. Consequently, excessive amounts of reactive nitrogen (N_r) have manifested in the environment, leading to a cascade of adverse effects, such as acidification and eutrophication of terrestrial and aquatic ecosystems, and particulate matter formation. Chemistry transport models (CTMs) are frequently used as tools to simulate the complex chain of processes that determine atmospheric N_r flows. In these models, the parameterization of the atmosphere–biosphere exchange of N_r is largely based on few surface exchange measurements and is therefore known to be highly uncertain. In addition to this, the input parameters that are used here are often fixed values, only linked to specific land use classes. In an attempt to improve this, a combination of multiple satellite products is used to derive updated, time-variant leaf area index (LAI) and roughness length (z_0) input maps. As LAI, we use the Moderate Resolution Imaging Spectroradiometer (MODIS) MCD15A2H product. The monthly z_0 input maps presented in this paper are a function of satellite-derived normalized difference vegetation index (NDVI) values (MYD13A3 product) for short vegetation types (such as grass and arable land) and a combination of satellite-derived forest canopy height and LAI for forests. The use of these growth-dependent satellite products allows us to represent the growing season more realistically. For urban areas, the z_0 values are updated, too, and linked to a population density map. The approach to derive these dynamic z_0 estimates can be linked to any land use map and is as such transferable to other models. We evaluated the sensitivity of the modelled N_r deposition fields in LOng Term Ozone Simulation – EURopean Operational Smog (LOTOS-EUROS) v2.0 to the abovementioned changes in LAI and z_0 inputs, focusing on Germany, the Netherlands and Belgium. We computed z_0 values from FLUXNET sites and compared these to the default and updated z_0 values in LOTOS-EUROS. The root mean square difference (RMSD) for both short vegetation and forest sites improved. Comparing all sites, the RMSD decreased from 0.76 (default z_0) to 0.60 (updated z_0). The implementation of these updated LAI and z_0 input maps led to local changes in the total N_r deposition of up to ∼30 % and a general shift from wet to dry deposition. The most distinct changes are observed in land-use-specific deposition fluxes. These fluxes may show relatively large deviations, locally affecting estimated critical load exceedances for specific natural ecosystems.

Published as: van der Graaf, S. C., Kranenburg, R., Segers, A. J., Schaap, M., and Erisman, J. W.: Satellite-derived leaf area index and roughness length information for surface–atmosphere exchange modelling: a case study for reactive nitrogen deposition in north-western Europe using LOTOS-EUROS v2.0, Geosci. Model Dev., 13, 2451–2474, https://doi.org/10.5194/gmd-13-2451-2020, 2020.

3.1 Introduction

The nitrogen (N) cycle has been continuously disrupted by human activity over the past century (Fowler et al., 2015; Galloway et al., 2004, 2008), resulting in a doubling of the total reactive nitrogen (N_r) fixation globally and even a tripling in Europe. As a result, excessive amounts of N_r, defined as all N compounds except N_2, have manifested in the environment contributing to acidification and eutrophication of sensitive terrestrial and aquatic ecosystems (Bobbink et al., 2010a; Paerl et al., 2014). NO_x and NH_3 affect air quality through their significant role in the formation of particulate matter, impacting human health and life expectancy (Lelieveld et al., 2015; Bauer et al., 2016; Erisman and Schaap, 2004). N_r also influences climate change through its impact on greenhouse gas emissions and radiative forcing (Erisman et al., 2011; Butterbach-Bahl et al., 2011). As N_r forms are linked through chemical and biological conversion in one another within the environmental compartments, one atom of N may even take part in a cascade of N_r forms and effects (Galloway et al., 2003). To minimize these adverse effects, effective nitrogen management and policy development therefore require consideration of all N_r forms simultaneously.

With the scarceness and inadequate distribution of available ground measurements, especially for reduced N_r, the most important method to assess and quantify total N_r budgets on a larger spatial scale to date remains the use of models. Models – chemistry transport models, in particular – are used for understanding the atmospheric transport and the atmosphere–biosphere exchange of nitrogen compounds. Most chemistry transport models compare reasonably with observations for oxidized forms of N_r but need improvement when it comes to the reduced forms of N_r (Colette et al., 2017). Modelled NH_3 fields are in general uncertain due to the highly reactive nature and the uncertain lifetime of NH_3 in the atmosphere. More importantly, NH_3 emissions that are used as model input are very complex to estimate and remain highly uncertain (Reis et al., 2009; Behera et al., 2013), for example, due to the diversity in NH_3 volatilization rates originating from different agricultural practices. Recently, a lot of effort has been made to improve the spatiotemporal distributions of bottom-up NH_3 emissions (e.g. Hendriks et al., 2016; Skjøth et al., 2011). Emissions can also be estimated top-down through the usage of data assimilation and inversion techniques. Optimally combining observations and chemistry transport models has already enabled us to create large-scale emission estimates for various pollutants (e.g. Curier et al., 2014; Abida et al., 2017), for instance, for NO_2 and will likely also be used for large-scale NH_3 emission estimates in the future.

Most data assimilation and inversion methods rely on the assumption that sink terms in the model hold a negligible uncertainty. To obtain reasonable top-down emission estimates, we must thus also aim to reduce the uncertainty involved on this side of models. The sink strengths of trace gases and particles in chemistry transport models are often pragmatic and computed with relatively simple empirical functions (e.g. following Wesely, 1989; Emberson et al., 2000; Erisman et al., 1994), mostly linked to land use classification maps. The parameterization of the atmosphere–biosphere exchange of N_r components that is used in models is largely based on surface exchange measurements and is therefore very uncertain, especially for NH_3 (Schrader et al., 2016). The deposition strengths in models may vary tremendously depending on the used deposition parameterization and velocities (Wu et al., 2018; Schrader and Brummer, 2014; Flechard et al., 2013). Moreover, inter-model discrepancies in deposition fluxes may also arise from differences

in the used input variables. Here, we focus on the leaf area index (LAI) and the roughness length (z_0) input values. The deposition velocity is often parameterized using both the LAI and the z_0. Currently, most models use fixed, land-use-specific values for both parameters. In practice, however, spatial as well as seasonal variation is observed. In this paper, we aim to improve the deposition flux modelling by using more realistic, space- and time-variant LAI and z_0 values that are derived from optical remote sensors.

The LAI is defined as the one-sided green leaf area per unit surface area (Watson, 1947). The LAI serves as a measure for the amount of plant canopy and herewith directly related to energy and mass exchange processes. As a result, the LAI is nowadays used as one of the main parameters in many ecological models. In deposition modelling, stomatal uptake is often parameterized using the LAI. The LAI can be determined in the field using either direct methods, such as leaf traps, or indirect methods, such as hemispherical photography (Jonckheere et al., 2004). For larger areas, the LAI can be simulated using land surface or biosphere models. Another group of indirect methods to estimate the LAI for large regions is the use of optical remote sensing. The LAI can, for instance, be estimated using empirical relationships between LAI and vegetation indices (e.g. Soudani et al., 2006; Davi et al., 2006; Turner et al., 1999) or by inversion of canopy reflectance models (e.g. Houborg and Boegh, 2008; Myneni et al., 2015). A well-known example of the latter is the LAI product from the Moderate Resolution Imaging Spectroradiometer (MODIS) instrument, which we will use in this study.

The z_0 is used to describe the surface roughness. The surface roughness serves as a momentum sink for atmospheric flow and is therefore an important term in atmospheric modelling. The interaction between the boundary layer and the roughness of the Earth's surface results in shear stress that affects the wind speed profile. Under neutral conditions, the resulting wind profile can be approximated using a logarithmic profile:

$$U(z) = \frac{u_*}{k} ln\left(\frac{z}{z_0}\right) \qquad \text{(Eq. 3.1)}$$

U(z) represents the mean wind speed, u_* the friction velocity and k the von Kármán constant. Here, z_0 is a constant that represents the height at which the wind speed theoretically becomes zero. The z_0 can be estimated from in situ wind speed measurements using bulk transfer equations. More recently, several studies have shown that z_0 for specific, uniform land cover types can also be estimated from optical remote sensing measurements, for instance, using vegetation indices (e.g. Xing et al., 2017; Yu et al., 2016; Bolle and Streckenbach, 1993; Hatfield, 1988; Moran, 1990). The z_0 can also be estimated using (satellite-derived) vegetation height (e.g. Raupach, 1994; Plate, 1971; Brutsaert, 2013; Schaudt and Dickinson, 2000).

The use of optical remote sensing data holds large potential for improvements to the representativeness of the surface characterization in chemistry transport models. Here, we present an approach to derive monthly z_0 input maps using satellite-derived normalized difference vegetation index (NDVI) values (MYD13A3 product) for short vegetation types and a combination of satellite-derived forest canopy height and LAI for forests. We validate these z_0 values by comparing them to z_0 values computed from FLUXNET observations. We also update the z_0 values

for urban areas, using a population density map. We use the updated z_0 values, as well as the MODIS LAI, as input in LOng Term Ozone Simulation – EURopean Operational Smog (LOTOS-EUROS) to illustrate the effect on transport and deposition modelling of N_r components. We evaluate the sensitivity of the N_r deposition fields to these input parameters, focusing on Germany, the Netherlands and Belgium. Moreover, we quantify and present the implications for land-use-specific fluxes on a model subpixel level. Also, we compare our model outputs with wet deposition measurements of NH_4^+ and NO_3^- and surface concentration measurements of NH_3 and NO_2.

3.2 Model and datasets

3.2.1 LOTOS-EUROS

3.2.1.1 Model description

The LOTOS-EUROS model is a Eulerian chemistry transport model that simulates air pollution in the lower troposphere (Manders et al., 2017). In this study, the horizontal resolution is set to 0.125° by 0.0625°, corresponding to pixels of approximately 7 by 7 km in size. The model uses a five-layer vertical grid that extends up 5 km above sea level, starting with a surface layer with a fixed height of 25 m. The next layer is a mixing layer, followed by two time-varying dynamic reservoir layers of equal thickness and a top layer up to 5 km. LOTOS-EUROS follows the mixed layer approach and performs hourly results using European Centre for Medium-Range Weather Forecasts (ECMWF) meteorology. The gas-phase chemistry uses the Netherlands Organisation for Applied Scientific Research (TNO) carbon bond mechanism (CBM) IV scheme (Schaap et al., 2009) and the anthropogenic emissions from the TNO Monitoring Atmospheric Composition and Climate (MACC) III emission database (Kuenen et al., 2014). The wet deposition parameterization is based on the Comprehensive Air Quality Model with Extensions (CAMx) approach and includes both in-cloud and below-cloud scavenging (Banzhaf et al., 2012). LOTOS-EUROS makes use of the Coordination of Information on the Environment (CORINE)/Smiatek land use map to determine input values for surface variables.

3.2.1.2 Dry deposition

The dry deposition flux of gases is computed following the resistance approach, in which the exchange velocity V_d is equal to the reciprocal sum of the aerodynamic resistance R_a, the quasi-laminar boundary layer resistance R_b and the canopy resistance R_c:

$$V_d = \frac{1}{R_a + R_b + R_c} \quad \text{(Eq. 3.2)}$$

R_a and R_b are both influenced by the wind profile, which is computed with (Eq. 3.1). The wind profile, in turn, depends on roughness length z_0 associated with different land use classes. The aerodynamic resistance R_a is computed as follows:

$$R_a = \int_{z_0}^{h} \frac{\Phi\left(\frac{z}{L}\right)}{\kappa u_* z} dz \quad \text{(Eq. 3.3)}$$

Here, h is the canopy height, which is pre-defined per land use class. The empirical function $\Phi\left(\frac{z}{L}\right)$ is taken from Businger et al. (1971) and depends on the state of the atmosphere. Depending on the value of Monin-Obukhov length L, the following stability equations are used:

- for a stable atmosphere ($L > 0$):

$$\Phi_s\left(\frac{z}{L}\right) = 1 + 4.7\left(\frac{z}{L}\right) \qquad \text{(Eq. 3.4)}$$

- for an unstable atmosphere ($L < 0$):

$$\Phi_u\left(\frac{z}{L}\right) = \left(1 - 15\left(\frac{z}{L}\right)\right)^{-0.25} \qquad \text{(Eq. 3.5)}$$

For a neutral atmosphere is it equal to unity. The Monin-Obukhov length L is dependent on z_0, and is computed using the following empirical equation (Majumbar and Ricklin, 2010):

$$\frac{1}{L} = S\,(a_1 + a_2 S^2)\, z_0^{(b_1 + b_2|S| + b_3 S^2)} \qquad \text{(Eq. 3.6)}$$

Here, a_1, a_2, b_1, b_2 and b_3 are constants (0.004349, 0.003724, -0.5034, 0.2310 and -0.0325 respectively) and empirical factor $S = -0.5\,(3.0 - 0.5\,u_s|CE|)$ with near-surface wind speed u_s and exposure factor CE , depending on cloud cover and solar zenith angle. The wind speed at a reference height (10 meters) is used to obtain the friction velocity u_*:

$$u_* = \kappa u_{10m} / \ln\left(\frac{z_{10m}}{z_0}\right) \qquad \text{(Eq. 3.7)}$$

The quasi-laminar boundary layer resistance R_b is a function of the cross-wind leaf dimension L_d and the wind speed at canopy top, $u(h)$, following the parameterisation presented in McNaughton and Van Den Hurk, 1995:

$$R_b = 1.3 * 150 * \sqrt{\frac{L_d}{u(h)}} \qquad \text{(Eq. 3.8)}$$

L_d is set to 0.02 m for arable land and permanent crops, and to 0.04 m for deciduous and coniferous forests. For other land use classes L_d, and subsequently, the R_b, is equal to zero. The canopy resistance R_c is computed using the DEPAC3.11 (Deposition of Acidifying Compounds) module (van Zanten et al., 2010). R_c is a parallel system of the resistances of three different pathways, the external leaf surface or cuticular resistance R_w, the effective soil resistance $R_{soil,eff}$ and the stomatal resistance R_s, and is defined as:

$$R_c = \left(\frac{1}{R_w} + \frac{1}{R_{soil,eff}} + \frac{1}{R_s}\right)^{-1} \qquad \text{(Eq. 3.9)}$$

The external leaf surface resistance R_w is a function of the surface area index (SAI) and the relative humidity. The SAI is a function of the LAI. The effective soil resistance $R_{soil,eff}$ is the sum of the in-canopy resistance R_{inc} and the soil resistance R_{soil}. Soil resistance R_{soil} has a fixed value, depending on the land use class and conditions (frozen, wet or dry). In case of $u_* > 0$ the in-canopy resistance for arable land, permanent crops and forest is computed as follows:

$$R_{inc} = \frac{14\ h\ SAI}{u_*} \qquad \text{(Eq. 3.10)}$$

For $u_* < 0$ and other land use classes a fixed value is used. The stomatal conductance for optimal conditions is the product of the LAI and the maximum leaf resistance from (Emberson et al., 2000). This maximum value is reduced by correction factors for photoactive radiation, temperature and vapor pressure deficit to obtain the stomatal conductance G_S. The R_S is then equal to $1/G_S$. The resistance parameterizations differ with land us type. A total of nine different land use classes are used in DEPAC. LOTOS-EUROS uses a fixed z_0 value for each of these land use classes. The default LAI values are also linked to the DEPAC classes, and follow a fixed temporal behaviour that describes the growing season of each land use class (Emberson et al., 2000). The bi-directional exchange of NH_3 is included in the implementation of the DEPAC3.11 module (Wichink Kruit et al., 2012), allowing emissions of NH_3 under certain atmospheric conditions. More information about the most recent version of the model can be found in Manders et al. (2017).

3.2.2 Datasets

The following section gives a short description of all the datasets that are used in this study. Firstly, a description of the LAI dataset is given. Subsequently, the datasets that are used to derive the updated z_0 maps are described. Finally, the in-situ observations used for validation are discussed in the last paragraphs.

3.2.2.1 MCD15A2H leaf area index

The satellite-derived LAI is a combined product of the MODIS instruments aboard the Terra and Aqua satellites (Myneni et al., 2015). The LAI algorithm compares bidirectional spectral reflectances observed by MODIS to values evaluated with a vegetation canopy radiative transfer model that are stored in a look-up table. The algorithm then archives the mean and the standard deviation of the derived LAI distribution functions. We used the sixth version of the product, MCD15A2H, which has a temporal resolution of 8 d and a spatial resolution of 500 m.

3.2.2.2 MYD13A3 NDVI

NDVI is a vegetation index computed with reflectances observed by the MODIS instrument aboard the Aqua satellite (Didan, 2015). The NDVI is the normalized transform of the near infrared to the red reflectance and is expressed by

$$\mathrm{NDVI} = \frac{\rho_{\mathrm{NIR}} - \rho_{\mathrm{red}}}{\rho_{\mathrm{NIR}} + \rho_{\mathrm{red}}} \quad \text{(Eq. 3.11)}$$

We used the MYD13A3 product, which is the monthly NDVI product with a spatial resolution of 1 km.

Table 3.1. *Overview of eddy covariance sites used to compute z_0. The following abbreviations for land use types are used: DBF – deciduous broadleaf forest, ENF – evergreen needleleaf coniferous forest, MF – mixed forest, CRO – croplands, WET – permanent wetlands, GRA – grasslands.*

Site ID	Site name	Latitude (°)	Longitude (°)	Land use	z (m)	FLUXNET2015 DOI
BE-Bra	Brasschaat	51.30761	4.51984	MF	41.0	https://doi.org/10.18140/FLX/1440128
BE-Lon	Lonzée	50.5516	4.74613	CRO	2.7	https://doi.org/10.18140/FLX/1440129
BE-Vie	Vielsalm	50.30496	5.99808	MF	51.0	https://doi.org/10.18140/FLX/1440130
DE-Akm	Anklam	53.86617	13.68342	WET	9.5	https://doi.org/10.18140/FLX/1440213
DE-Geb	Gebesee	51.1001	10.9143	CRO	3.5	https://doi.org/10.18140/FLX/1440146
DE-Gri	Grillenburg	50.95004	13.51259	GRA	3.0	https://doi.org/10.18140/FLX/1440147
DE-Hai (2012)	Hainich	51.07917	10.4530	DBF	42.0	https://doi.org/10.18140/FLX/1440148
DE-Kli	Klingenberg	50.89306	13.52238	CRO	3.5	https://doi.org/10.18140/FLX/1440149
DE-Obe	Oberbärenburg	50.78666	13.72129	ENF	30.0	https://doi.org/10.18140/FLX/1440151
DE-RuR	Rollesbroich	50.62191	6.30413	GRA	2.6	https://doi.org/10.18140/FLX/1440215
DE-RuS	Selhausen Juelich	50.86591	6.44717	CRO	2.5	https://doi.org/10.18140/FLX/1440216
DE-Seh (2010)	Selhausen	50.87062	6.44965	CRO	2.0	https://doi.org/10.18140/FLX/1440217
DE-SfN	Schechenfilz Nord	47.80639	11.3275	WET	6.7	https://doi.org/10.18140/FLX/1440219
DE-Tha	Tharandt	50.96235	13.56516	ENF	42.0	https://doi.org/10.18140/FLX/1440152
NL-Hor (2011)	Horstermeer	52.24035	5.0713	GRA	4.3	https://doi.org/10.18140/FLX/1440177
NL-Loo (2013)	Loobos	52.16658	5.74356	ENF	26	https://doi.org/10.18140/FLX/1440178
FR-Fon	Fontainebleau-Barbeau	48.47636	2.7801	DBF	37	https://doi.org/10.18140/FLX/1440161
CH-Cha	Chamau	47.21022	8.41044	GRA	2.4	https://doi.org/10.18140/FLX/1440131
CH-Fru	Früebüel	47.11583	8.53778	GRA	2.5	https://doi.org/10.18140/FLX/1440133
CH-Lae	Lägern	47.47808	8.3650	MF	47	https://doi.org/10.18140/FLX/1440134
CH-Oe1 (2008)	Oensingen grassland	47.28583	7.73194	GRA	1.2	https://doi.org/10.18140/FLX/1440135
CH-Oe2	Oensingen crop	47.28631	7.73433	CRO	2.25	https://doi.org/10.18140/FLX/1440136
CZ-wet	Třeboň	49.02465	14.77035	WET	2.6	https://doi.org/10.18140/FLX/1440145

References for each Site ID: BE-Bra: Janssens (2016); BE-Lon: De Ligne et al. (2016a); BE-Vie: De Ligne et al. (2016b); DE-Akm: Bernhofer et al. (2016a); DE-Geb: Brümmer et al. (2016); DE-Gri: Bernhofer et al. (2016b); DE-Hai: Knohl et al. (2016); DE-Kli: Bernhofer et al. (2016c); DE-Obe: Bernhofer et al. (2016d); DE-RuR: Schmidt and Graf (2016a); DE-RuS: Schmidt and Graf (2016b); DE-Seh: Schneider and Schmidt (2016); DE-SfN: Klatt et al. (2016); DE-Tha: Bernhofer et al. (2016e); NL-Hor: Dolman et al. (2016); NL-Loo: Moors and Elbers (2016); FR-Fon: Berveiller et al. (2016); CH-Cha: Hörtnagl et al. (2016a); CH-Fru: Hörtnagl et al. (2016b); CH-Lae: Hörtnagl et al. (2016c); CH-Oe1: Ammann (2016); CH-Oe2: Hörtnagl et al. (2016d); CZ-wet: Dušek et al. (2016).

3.2.2.3 Forest canopy height

The forest canopy height is derived from lidar (light detection and ranging) data acquired by the GLAS (Geoscience Laser Altimeter System) instrument aboard the ICESat (Ice, Cloud, and land Elevation Satellite) satellite (Zwally et al., 2002). This instrument was an altimeter that transmitted a light pulse of 1024 nm and recorded the reflected waveform. We used the global forest canopy height product developed by Simard et al. (2011), which has a spatial resolution of 1 km.

3.2.2.4 Population density map

The population density grid used in this study available for all European countries and provided by the European Environmental Agency (Gallego, 2010). The population density is disaggregated with the CORINE Land Cover inventory of 2000, using data on population per commune. The resulting population density grid is downscaled to a spatial resolution of 100 m.

3.2.2.5 CORINE Land Cover

The CORINE Land Cover (CLC) is a land use inventory that consists of 44 classes (European Environmental Agency, 2014). The CLC is produced by computer-assisted visual interpretation of a collection of high-resolution satellite images. The CLC has a minimum mapping unit of 25 ha

and a thematic accuracy of >85 %. We used the latest version of the product, CLC2012, in this study.

Table 3.2. *An overview of the datasets that are used to derive z_0 input values for each DEPAC land use category.*

DEPAC class	Dataset
1 – Grass	MODIS NDVI
2 – Arable land	MODIS NDVI
3 – Permanent crops	MODIS NDVI
4 – Coniferous forest	GLAS forest canopy height
5 – Deciduous forest	GLAS forest canopy height, MODIS LAI
6 – Water	–
7 – Urban	Population density
8 – Other	MODIS NDVI
9 – Desert	–

3.2.2.6 In situ reactive nitrogen observations

The modelled NH_4^+ and NO_3^- wet deposition fluxes are compared to observations of wet-only samplers. We used observation from the Dutch Landelijk Meetnet Regenwatersamenstelling (LMRe) network (Van Zanten et al., 2017) and the German lander network (Schaap et al., 2017). The location of the stations can be found in Fig. 3.16. The modelled NH_3 surface concentrations are compared to observation from the Dutch MAN network (Lolkema et al., 2015) and the European Monitoring and Evaluation Programme (EMEP) network (EMEP, 2016). The modelled NO_2 surface concentrations are compared to observation from AirBase (EEA, 2019). We only used background stations. The location of these stations can be found in Fig. 3.14.

3.2.2.7 Eddy covariance data

FLUXNET is a global network of micrometeorological towers that measure biosphere–atmosphere exchange fluxes using the eddy covariance (EC) method. We used half-hourly observations from the FLUXNET2015 dataset (Pastorello et al., 2017) to validate the z_0 values. We use observations of the mean wind speed, the friction velocity, the sensible heat flux, precipitation and air temperature to determine z_0 values. The sites used in this study are shown in Table 3.1.

Table 3.3. *Studies that relate the aerodynamic roughness length (z_0) to satellite-derived NDVI values for specific land cover types and conditions.*

Function	Vegetation type(s)	Reference
$z_0 = \begin{cases} -0.173 + 1.168 \cdot \text{NDVI} \lvert - 1.125 \cdot \text{NDVI}^2 & \text{for NDVI} < 0.6 \\ 0.1 & \text{for NDVI} \geq 0.6 \end{cases}$ (Eq. 14)	Partial cover cotton and wheat canopies	Hatfield (1988)
$z_0 = e^{-5.2+5.3 \cdot \text{NDVI}}$ (Eq. 15)	Alfalfa (Arizona)	Moran (1990)
$z_0 = e^{-5.5+5.8 \cdot \text{NDVI}}$ (Eq. 16)	Mixed, non-irrigated agricultural land (Mediterranean)	Bolle and Streckenbach (1993)
$z_0 = 0.2255 \cdot \text{NDVI} + 0.0087$ (Eq. 17)	Spring maize	Yu et al. (2016)
$z_0 = 0.2476 \cdot \text{NDVI} + 0.0615$ (Eq. 18)	Winter wheat	Yu et al. (2016)
$z_0 = 0.2858 \cdot \text{NDVI} + 0.1017$ (Eq. 19)	Summer maize	Yu et al. (2016)
$z_0 = 0.0203 \cdot \text{NDVI}^{0.9547}$ (Eq. 20)	Grassland	Xing et al. (2017)

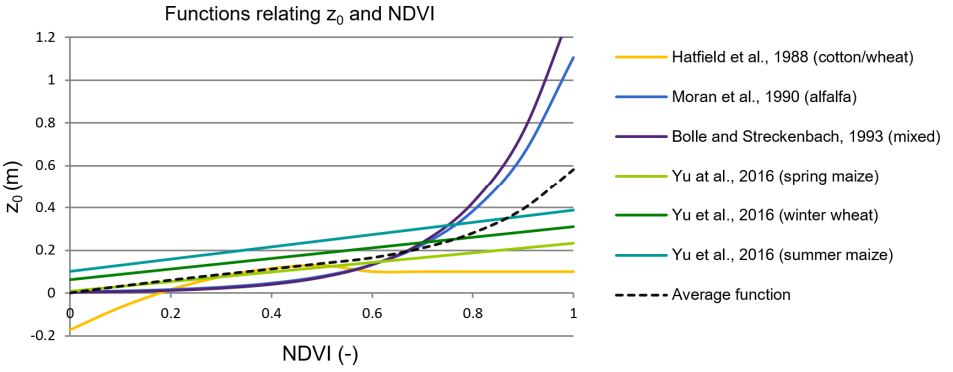

Figure 3.1. *Several functions that relate the roughness length z_0 (m) to the normalized difference vegetation index (NDVI). The dotted line shows the average of all the functions. This function is used to compute NDVI-dependent z_0 values for the subcategories within DEPAC classes "arable", "other" and "permanent crops".*

3.3 Methodology

3.3.1 Updated z_0 maps

The updated z_0 maps are a composition of z_0 values derived using different methods. We distinguish three different main approaches: (1) z_0 values that depend on forest canopy height, (2) z_0 values that depend on the NDVI and (3) new z_0 values for urban areas that depend on the population density map. In addition to these three approaches, the z_0 values of some urban classes were set to new default values. An overview of the datasets that are used for each DEPAC land use class is given in Table 3.2.

The MODIS NDVI, the MODIS LAI and the GLAS forest canopy height had to be pre-processed and homogenized in order to obtain consistent input maps that can be read into the LOTOS-EUROS model. To achieve this, we created input maps for each DEPAC class on the coordinate grid of the CORINE/Smiatek land use map in LOTOS-EUROS.

First of all, the original datasets were re-projected to geographic coordinates. The following approach is used to deal with the different horizontal resolutions of the datasets. We used the CLC2012 map, having the highest horizontal resolution, as a basis for the computation of the updated z_0 values. For each of the other datasets, we first computed the percentages of each CORINE land cover class within every pixel. We define homogeneous pixels, consisting of nearly one CORINE land cover class, for which we will use a threshold value of 85 % of the pixels area. Then we isolate and use only these (nearly) homogeneous pixels to compute z_0 values for each CORINE land cover class. The methods that were applied are described in the subsequent section.

3.3.1.1 Forest-canopy-height-derived z_0 values

The forest canopy height dataset derived from GLAS lidar observations is used to compute the z_0 values for each CLC2012 forest land cover class (broadleaved forest, coniferous forest and mixed forest) that corresponds to one of the DEPAC forest land use classes (4: coniferous forest and 5: deciduous forest). Several publications relate vegetation height to z_0 (e.g. Raupach, 1994; Plate, 1971; Brutsaert, 2013). Here, we used the often-used equation from Brutsaert (2013):

$$z_0 = 0.136 * h \quad \text{(Eq. 3.12)}$$

The vegetation height is the most important parameter influencing turbulence near the surface, and for this reason, the used parameterization gives a reasonable estimate of z_0, even though it ignores many other aspects that influence z_0 (e.g. density, vertical distribution of foliage). Multiple studies have illustrated that there is a seasonal variation in z_0/h for different types of forests (e.g. Yang and Friedl, 2003; Nakai, 2008). The z_0 of deciduous trees is therefore additionally linked to the leaf area index to account for changes in tree foliage. The following formula is used to compute the monthly z_0 value for each deciduous forest pixel:

$$z_0(\mathrm{LAI}) = z_{0,\min} + \frac{\mathrm{LAI} - \mathrm{LAI,min}}{\mathrm{LAI,max} - \mathrm{LAI,min}} (z_{0,\max} - z_{0,\min}) \quad \text{(Eq. 3.13)}$$

Here, the maximum roughness length $z_{0,max}$ is set to the lidar-derived z_0 from (Eq. 3.12). The minimum roughness length $z_{0,min}$ represents the z_0 of leafless deciduous trees. Following the dependence of z_0/h on LAI presented in Nakai (2008) and Yang and Friedl (2003), we set the $z_{0,min}$ to 80 % of $z_{0,max}$.

Table 3.4. *An overview of the default and the adjusted roughness length of each DEPAC class used in LOTOS-EUROS for Germany, the Netherlands and Belgium. The datasets that are used to derive the updated z_0 values are given in the last column. The mean z_0 value of the DEPAC classes computed using the MODIS NDVI product is the yearly mean of all monthly z_0 values.*

DEPAC class	Default z_0	New mean z_0 (σ)
1 – Grass	0.03	0.013 (0.002)
2 – Arable land	0.1	0.19 (0.04)
3 – Permanent crops	0.25	0.20 (0.04)
4 – Coniferous forest	2	2.91 (0.56)
5 – Deciduous forest	2	2.55 (0.51)
6 – Water	0.002	–
7 – Urban	2	0.92 (0.20)
8 – Other	0.05	0.19 (0.05)
9 – Desert	0.013	–

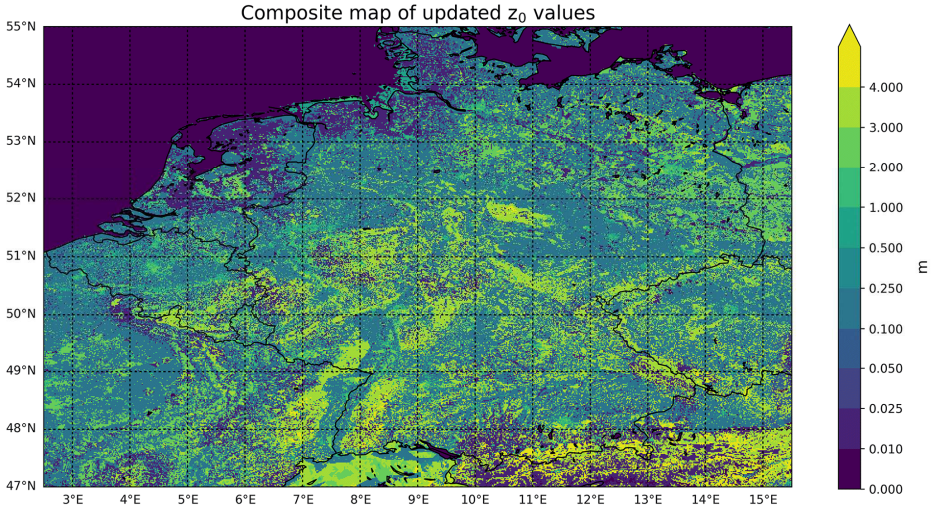

Figure 3.2. *Composite map of the new z_0 values. The yearly mean is displayed for land use classes with time-variant z_0 values.*

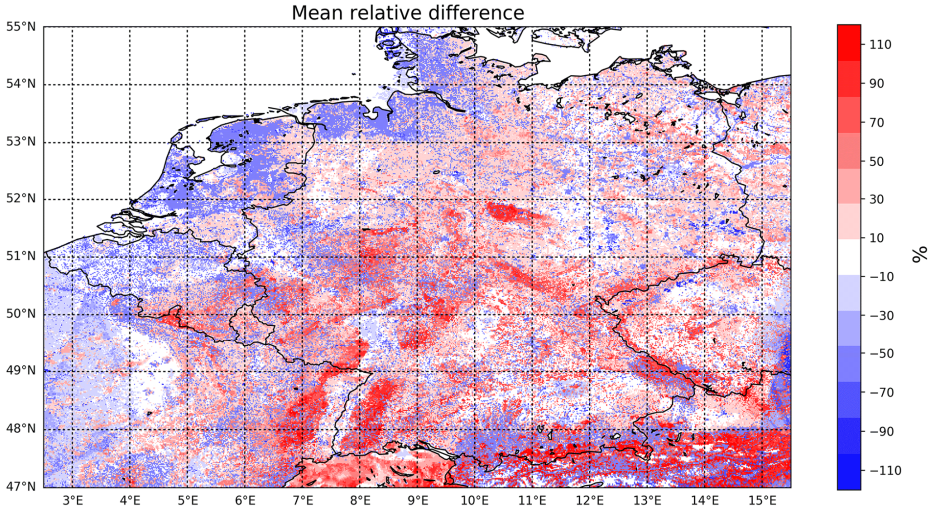

Figure 3.3. *Mean relative difference (%) of the updated z_0 values with respect to the default z_0 values.*

3.3.1.2 NDVI-derived z_0 values

Table 3.3 gives an overview of several studies that relate the z_0 value to the NDVI. The functions are derived for different vegetation types under specific conditions. Equations (3.12)–(3.20) are derived for different types of agricultural land. These equations are all within a reasonable range from one another for NDVI values below ~0.8. Therefore, we chose to use the average function of Eqs. (3.12)–(3.19) to compute z_0 values for all CLC subcategories of the following DEPAC classes: "arable", "other" and "permanent crops". Fig. 3.1 is a visualization of Eqs. (3.12)–(3.19) and the used mean function. Fig. S3.1 in the Supplement shows a histogram of all NDVI values in our study area in 2014. We computed that 7.4 % of all NDVI values have a NDVI >0.8, 1.3 % have a NDVI >0.85 and only 0.04 % have a NDVI >0.9. Virtually all NDVI values thus fall within the range where the average function does not differ much from the individual functions. The z_0 value of grasslands is in general lower than other vegetation types. The last equation, Eq. (3.20), is specifically derived for grassland and is therefore used for all CLC subcategories that fall under the DEPAC class "grass".

3.3.1.3 z_0 values for urban areas

The default z_0 of urban areas in LOTOS-EUROS was set to 2 m. We have updated the z_0 values for urban areas to avoid possible overestimation of z_0 in sparsely populated urban areas. The updated z_0 values for CLC2012 classes 1 and 2, "1: continuous urban fabric" and "2: discontinuous urban fabric" are time-invariant and coupled to the EEA population density map. The z_0 values are set to 2 m in areas with a population density higher than 5000 inhabitants km^{-2} and to 1 m in areas with a population density lower than 5000 inhabitants km^{-2}. The z_0 values of the other urban subcategories, CLC2012 classes 3 to 9, are updated to the proposed values for CLC classes in Silva et al. (2007). Fig. S3.2 shows the resulting updated z_0 values for urban areas.

3.3.2 LAI and z_0 in LOTOS-EUROS

After the computation of the z_0 values, the maps for each CLC class were merged and converted into DEPAC classes using a pre-defined conversion table. As multiple CORINE land covers may translate to a single DEPAC class, the weighted average based on the respective percentage of each CORINE land cover class was computed for each pixel. We then used linear interpolation to obtain continuous z_0 maps for each DEPAC class. Finally, the maps were regridded unto the CORINE/Smiatek grid and saved into one file per month.

The default parameterization of the LAI in LOTOS-EUROS is replaced by the MCD15A2H LAI product from MODIS. First, we applied a coordinate transformation to obtain the data in geographical coordinates. The data were then regridded unto the grid of the CORINE/Smiatek land use map using linear interpolation. The quality tags were evaluated to identify pixels with default fill values from the MCD15A2H product. These fill values were replaced by the default LAI values in LOTOS-EUROS, to avoid modelling discrepancies resulting from sudden jumps in LAI values. Finally, the values were sorted per DEPAC land use class and individual fields were created for each class as new input for LOTOS-EUROS.

Table 3.5. *Roughness length values from different types of studies. The first column states the global land use category of the z_0 values. The second column states the (range of) z_0 values, as well as the specific type of land use they are derived for. The third column shows the reference. [1]Literature study. [2] Model input (EMEP Meteorological Synthesizing Centre – West; MSC-W). [3]Model input (CHIMERE).*

Land use categories	Proposed z_0 values (type name)	Reference
Grass	0.008–0.03 (short grass, moss)	Wieringa (1993)[1]
	0.02–0.06 (long grass, heather)	
	0.03–0.6 (DEPAC class 1)	Silva et al. (2007)
	0.022 (short grassland)	Gallagher et al. (2002)
	0.063 (long grassland)	
	0.01 (mown grass)	Troen and Petersen (1989)
	0.03	Simpson et al. (2012)[2]
	0.1 (grassland)	Mailler et al. (2017)[3]
	0.013 (mean DEPAC 1)	This study
Arable land/permanent crops	0.04–0.09 (low mature crops)	Wieringa (1993)[1]
	0.12–0.18 (high mature crops)	
	0.05–0.5 (DEPAC class 2)	Silva et al. (2007)
	0.1–0.5 (DEPAC class 3)	
	0.12 (arable crop)	Gallagher et al. (2002)
	0.03–0.1 (farmland)	Troen and Petersen (1989)
	0.1–0.2 (different types of crops)	Simpson et al. (2012)[2]
	0.05–0.15 (agriculture)	Mailler et al. (2017)[3]
	0.19 (mean DEPAC 2)	This study
	0.20 (mean DEPAC 3)	
Forests	0.8–1.6 (mature pine forests)	Wieringa (1993)[1]
	0.6–1.2 (DEPAC class 4 & 5)	Silva et al. (2007)
	1	Troen and Petersen (1989)
	0.8–1	Simpson et al. (2012)[2]
	1	Mailler et al. (2017)[3]
	2.5	Gallagher et al. (2002)
	1.71–1.9 (oak and pine trees)	Lankreijer et al. (1993)
	1.70–2.29 (spruce and pine trees)	Yang and Friedl (2003)
	2.91 (mean DEPAC 4)	This study
	2.55 (mean DEPAC 5)	
Urban	0.4–0.7 (dense low buildings)	Wieringa (1993)[1]
	0.7–1.5 (regularly built town)	
	0.005–1.3 (DEPAC class 7)	Silva et al. (2007)
	0.5–1 (suburbs, city)	Troen and Petersen (1989)
	1	Simpson et al. (2012)[2]
	1	Mailler et al. (2017)[3]
	0.92 (mean DEPAC 7)	This study
Other	0.35–0.45 (continuous bushland)	Wieringa (1993)[1]
	0.03–0.1 (DEPAC class 8)	Silva et al. (2007)[1]
	0.01 (heathland)	Gallagher et al. (2002)
	0.05–0.2 (moorland, scrubs, wetlands)	Simpson et al. (2012)[2]
	0.15 (scrubs)	Mailler et al. (2017)[3]
	0.19 (mean DEPAC 8)	This study

3.4 Results

3.4.1 Comparison of the default and updated z_0 values

We used the CORINE/Smiatek land use map to combine all the updated z_0 values into a single map. The resulting composite map has a horizontal resolution of 500 by 500 m and is shown in Fig. 3.2. The mean relative difference (MRD) between the default and updated z_0 values is presented in Fig. 3.3. The largest positive differences occur in forested areas, meaning that the default z_0 values are lower than the updated z_0 values. The largest negative deviations occur in urban areas and areas with "grass". The updated z_0 values are generally lower in the Netherlands and Belgium, and mostly higher in Germany. Table 3.4 gives an overview of the default z_0 values in LOTOS-EUROS and the mean and standard deviation of the new z_0 values for each of the DEPAC land use classes. The updated z_0 values for "arable land", "coniferous forest", "deciduous forest" and "other" are on average higher than the default z_0 values in LOTOS-EUROS. The updated z_0 values for "grass", "permanent crops" and "urban" are on average lower than the default z_0 values in LOTOS-EUROS.

Table 3.6. *Comparison of the computed z_0 values from FLUXNET observations and the corresponding satellite-derived z_0 values. The table shows the mean and standard deviation of all z_0 values in 1 year. For forest, only the maximum z_0 value is given.*

Site ID	Land use	Computed z_0	Satellite-derived z_0
DE-Hai	DBF	2.3 (0.88)	3.5
FR-Fon	DBF	2.9 (0.53)	2.6
DE-Obe	ENF	1.9 (0.52)	3.4
DE-Tha	ENF	2.6 (0.72)	3.1
NL-Loo	ENF	2.8 (0.43)	2.3
BE-Bra	MF	2.8 (0.69)	2.4
BE-Vie	MF	4.7 (1.5)	3.0
CH-Lae	MF	3.5 (0.92)	3.8
DE-Akm	WET	0.72 (0.21)	0.14 (0.033)
DE-SfN	WET	0.46 (0.13)	0.22 (0.033)
CZ-wet	WET	0.16 (0.075)	0.18 (0.040)
BE-Lon	CRO	0.013 (0.018)	0.16 (0.029)
DE-Geb	CRO	0.020 (0.020)	0.17 (0.025)
DE-Kli	CRO	0.043 (0.043)	0.18 (0.030)
DE-RuS	CRO	0.066 (0.048)	0.15 (0.015)
DE-Seh	CRO	0.034 (0.028)	0.16 (0.015)
CH-Oe2	CRO	0.084 (0.065)	0.19 (0.019)
DE-RuR	GRA	0.035 (0.019)	0.014 (0.0016)
NL-Hor	GRA	0.14 (0.076)	0.014 (0.0019)
CH-Cha	GRA	0.078 (0.038)	0.015 (0.00099)
CH-Fru	GRA	0.13 (0.086)	0.015 (0.0024)
CH-Oe1	GRA	0.0064 (0.0035)	0.014 (0.00088)

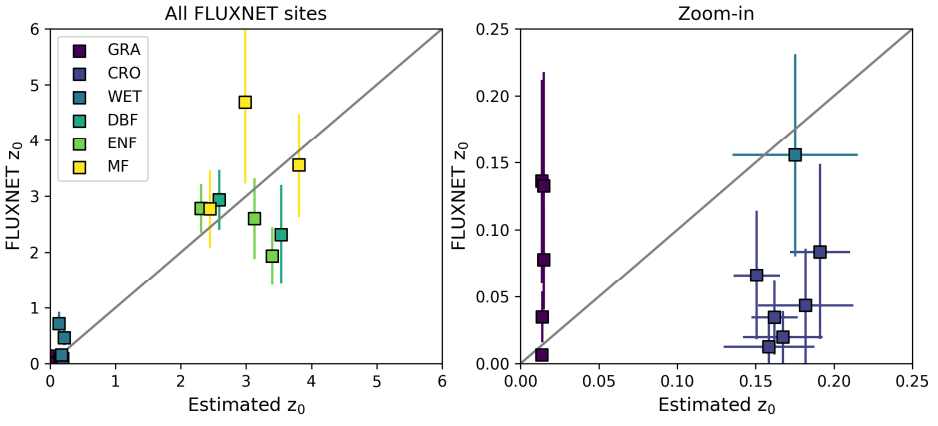

Figure 3.4. *Comparison of the updated z_0 values (x axis) to the z_0 values derived from EC measurements (y axis). The error bars indicate the standard deviation.*

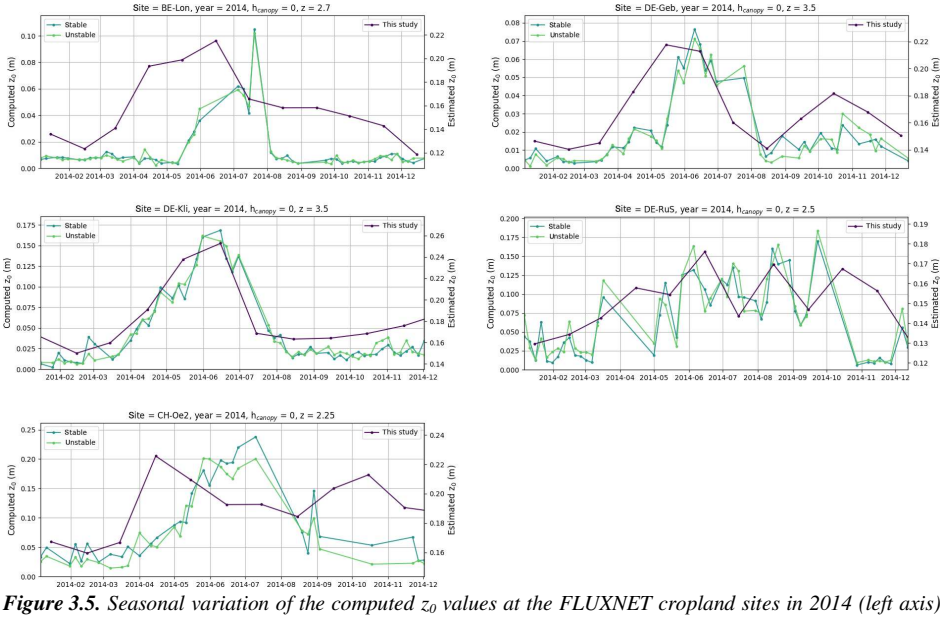

Figure 3.5. *Seasonal variation of the computed z_0 values at the FLUXNET cropland sites in 2014 (left axis) and the corresponding z_0 values estimated from NDVI values (right axis). The green lines indicate the estimated z_0 values derived from FLUXNET measurements and the purple lines indicate the z_0 values derived from NDVI values. The assumptions used to compute the z_0 values are shown in the titles of the figures.*

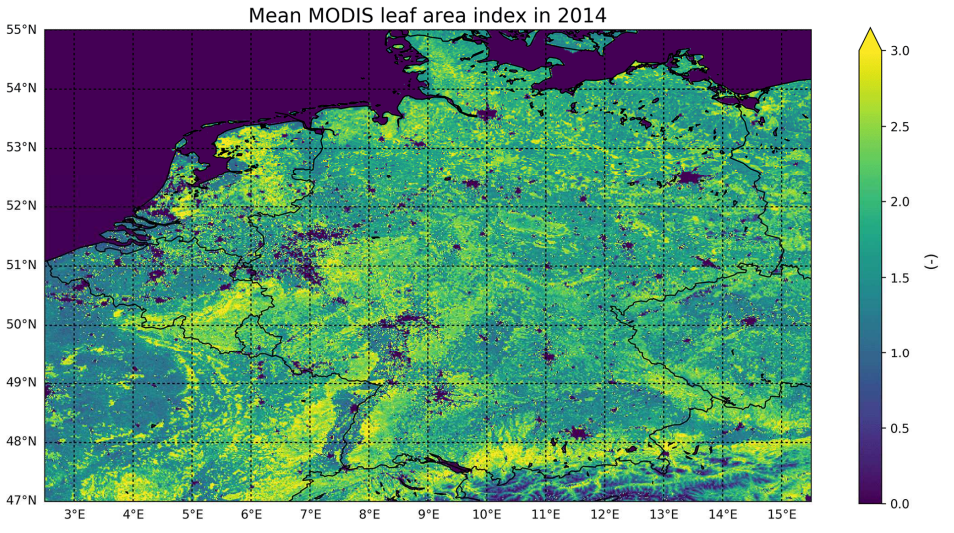

Figure 3.6. *The yearly mean MODIS leaf area index in 2014.*

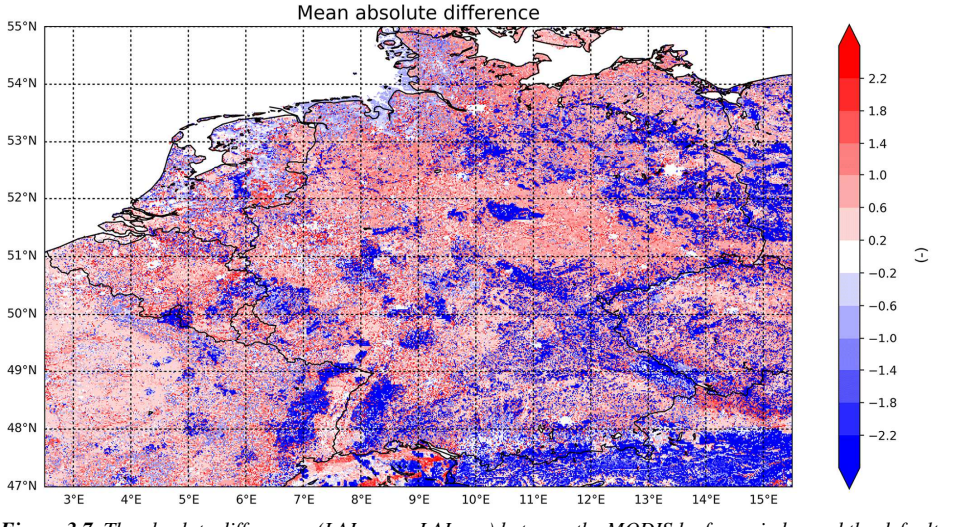

Figure 3.7. *The absolute differences ($LAI_{MODIS} - LAI_{default}$) between the MODIS leaf area index and the default leaf area index in LOTOS-EUROS.*

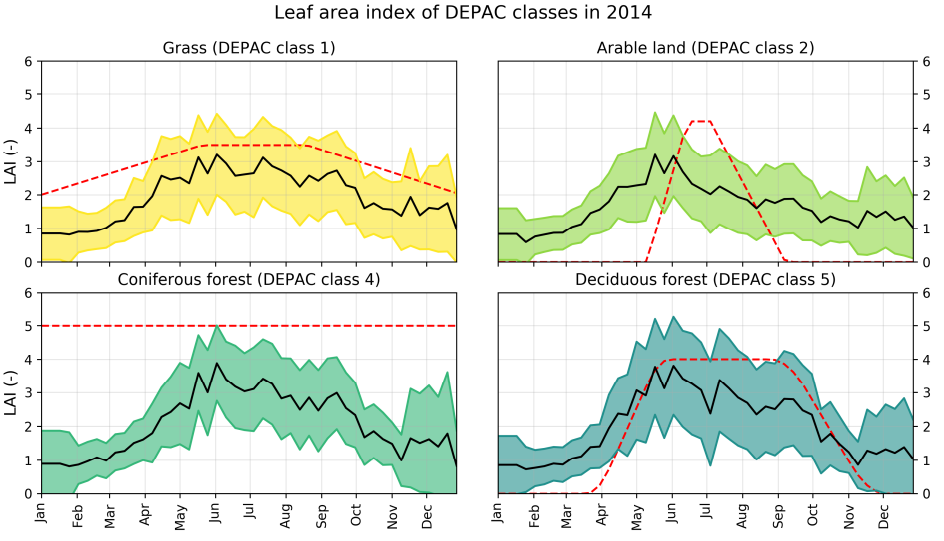

Figure 3.8. *Seasonal variation of the default and MODIS LAI values per DEPAC class. The black line represents the mean MODIS LAI of all pixels within the modelled grid for that particular DEPAC class; the ranges represent the mean plus and minus the standard deviation of the MODIS LAI. The red line depicts the default LAI values in LOTOS-EUROS.*

3.4.2 Comparison to z_0 values from other studies

We compared the updated z_0 values to z_0 values from several studies (Wieringa, 1993; Silva et al., 2007; Troen and Petersen, 1989; Lankreijer et al., 1993; Yang and Friedl, 2003) and z_0 values used in other CTMs (Simpson et al., 2012; Mailler et al., 2017). Table 3.5 gives an overview of these z_0 values. There is in general good agreement with these z_0 values, and the updated z_0 values mostly fall within the stated ranges. The updated z_0 values for coniferous and deciduous forest are on the high side compared to these studies. A histogram of the forest canopy heights derived from GLAS within our study area is given in Fig. S3.1 in the Supplement. These differences can in part be explained by the occurrence of relatively tall forest canopy (~30 m) in the dataset, especially in forests in southern Germany, whereas most of these studies either assumed or studied shorter trees. Another possible explanation lies in the fact that we used a relatively large conversion factor of 0.136 (Eq. 3.12), whereas a factor of 0.10 is also used quite often.

3.4.3 Comparison to z_0 values derived from EC measurement sites

We computed the z_0 values of the EC sites, and we refer to Sect. S1 in the Supplement for a description of the methodology that is used to derive these values. We compared the z_0 values based on their land use stated by FLUXNET to avoid issues arising from discrepancies in land use classifications. The forest sites (DBF, ENF and MF) are compared to z_0 values derived from GLAS. The cropland and wetland sites (CRO and WET) are compared to the NDVI-dependent z_0 values derived using the mean function shown in Fig. 3.1. The grassland sites (GRA) are compared to the NDVI-dependent z_0 values for grassland specifically. The results per site are given in Table 3.6. Fig. 3.4 shows the comparison of the z_0 values from EC measurements and the updated z_0 values for different land use classes. The z_0 values for forests match quite well. Differences between the two can in part be explained by the influence of topography, which is not accounted for in the z_0

values that are derived using forest canopy height only. The z_0 values for short vegetation seem to be overestimated for crops and underestimated for grassland and wetland sites. The underestimation of some grassland and wetland sites can be explained by the large inter-site differences in vegetation cover. Some of the FLUXNET sites classified as grasslands are, for instance, mostly covered with short grass only (for instance, Oensingen), while other sites are covered with relatively tall herbaceous vegetation, such as reeds (for instance, Horstermeer). Compared to the default z_0 values in LOTOS-EUROS, the root mean square difference (RMSD) improved from 0.76 (default z_0) to 0.60 (updated z_0). For forest, the RMSD improved from 1.23 (default z_0) to 0.96 (updated z_0). For short vegetation, the RMSD also decreased, from 0.22 (default z_0) to 0.19 (updated z_0). Fig. 3.5 shows the comparison of the seasonal variation in computed and satellite-derived z_0 values for the FLUXNET sites classified as crops in 2014. We can once more observe a clear offset between the two. The FLUXNET z_0 values go to near-zero values in wintertime, whereas the satellite-derived z_0 values never drop below 0.12 m. This seems to be due to the distribution of the NDVI values (Fig. S3.1), which shows that the NDVI >0.4 most of the time. The seasonal patterns, on the other hand, seem to match well in general, even though the satellite-derived z_0 values rise somewhat earlier in the year.

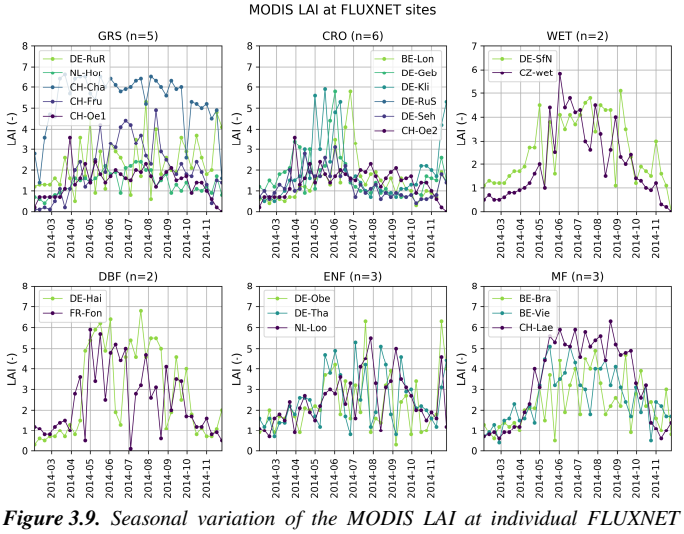

Figure 3.9. *Seasonal variation of the MODIS LAI at individual FLUXNET sites with different land use classifications.*

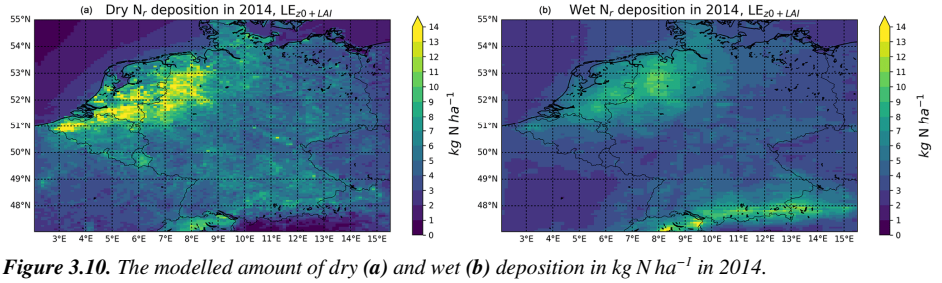

Figure 3.10. *The modelled amount of dry* ***(a)*** *and wet* ***(b)*** *deposition in kg N ha^{-1} in 2014.*

3.4.4 Comparison of the default and MODIS LAI

The yearly mean MODIS LAI values are shown in Fig. 3.6. The mean differences between the MODIS and the default LAI values are presented in Fig. 3.7. The largest positive differences occur in areas with "arable land", where the mean default LAI values are lower than the MODIS LAI values. The largest negative deviations occur in areas with forest, especially for "coniferous forest". The seasonal variations of the MODIS and the default LAI values are shown in Fig. 3.8. The default LAI of "grass" and "deciduous forest" seems to fit the yearly variation of the MODIS LAI quite well. We matched the MODIS LAI with the locations of the FLUXNET sites to take a closer look at the pattern for different land use classes. Figures 3.9 and S3.3 show the seasonal variation of the MODIS LAI at FLUXNET sites with different land use classifications. The LAI of the grassland sites seems to vary the most, which corresponds to the large inter-site differences in vegetation cover as explained in Sect. 3.4.3. For the cropland sites, we can recognize the growing season and the apparent harvest, where the LAI values drop again. Of all the different land use classes, deciduous broadleaf forest sites reach the highest LAI values in the growing season. There is less variation in the LAI for evergreen needleleaf forest sites. However, the wintertime LAI values seem to be unrealistically low.

3.4.5 Implications for modelled N_r deposition fields

In the following section, the impact of the updated LAI and z_0 values on modelled N_r deposition fields in LOTOS-EUROS is discussed. A total of four different LOTOS-EUROS runs are compared to examine the individual effect of the updated LAI and z_0 values on the modelled N_r distributions and deposition fields. The first run, named "$LE_{default}$", is the standard run using default LAI and z_0 values. The second run, named "LE_{LAI}", uses updated LAI values and the default z_0 values. The third run, named "LE_{z0}", uses updated z_0 values and the default LAI values. The fourth run, named "LE_{z0+LAI}", uses both updated LAI and z_0 values. From now on, we will refer to the outputs of these different runs using the abovementioned abbreviations.

3.4.5.1 Effect on total N_r deposition

Fig. S3.4 shows the division of the total terrestrial N_r deposition over Germany, the Netherlands and Belgium into different N_r compounds for each of the model runs. A relatively larger portion of the total N_r deposition is attributed to oxidized forms of N_r in Germany. The reduced forms of N_r predominate in the Netherlands and Belgium. The largest change in total N_r deposition occurs in Belgium (+6.19 %) due to the inclusion of the MODIS LAI. This corresponds to the relative increase in LAI values here. The inclusion of the updated z_0 values led to a minor decrease in total N_r deposition in the Netherlands (−1.45 %) and Belgium (−1.13 %), and a minor increase in Germany (+0.44 %).

3.4.5.2 Effect on wet and dry N_r deposition

We examined the direct effect of the updated LAI and z_0 values on the modelled dry N_r deposition, as well as the related indirect effect in modelled wet N_r deposition. Fig. 3.10 shows the dry and wet N_r deposition in kg N ha^{-1} in 2014, modelled with the updated LAI and z_0 values as input in LOTOS-EUROS. Fig. 3.11 shows the relative changes in the total amount of dry and wet N_r deposition of the different runs with respect to the default run. The combined effect shows an increase of the amount of dry N_r deposition over most parts of Belgium and Germany. The amount of wet N_r deposition decreases over most parts of Germany and eastern Belgium but remains

unchanged in north-western parts of Germany. We observe a decrease in total N_r deposition in the Netherlands. In general, we observe changes ranging from approximately −20 % to +30 % in the total amount of dry N_r deposition. The changes in wet N_r deposition are smaller in magnitude and range from approximately −3 % to +3 %.

3.4.5.3 Effect on reduced and oxidized N_r deposition

We split up the total N_r deposition into NH_x (NH_3 and NH_4^+) and NO_y (NO and NO_2 and NO_3^- and HNO_3) deposition to look at the effect of the updated LAI and z_0 input maps on the deposition of reduced and oxidized forms of N_r, respectively. Fig. 3.12 shows the modelled NH_x and NO_y deposition in kg N ha^{-1} in 2014, including the updated LAI and z_0 input values. Fig. 3.13 shows the relative changes (%) in the total NH_x and NO_y of the different runs with respect to the default run of LOTOS-EUROS. The updated z_0 values have a larger impact on the NH_x deposition than on the NO_y deposition. The implementation of the updated z_0 values has led to a decrease in NH_x deposition over most of the Netherlands and western Belgium, driven by the large fraction of grassland here. The updated LAI values led to relatively more NH_x deposition in Belgium. The updated LAI values led to an increase of NO_y deposition in almost all areas within the modelled region, except for some urban areas. Moreover, the impact seems to be limited in large forests located in background areas.

Table 3.7. *Relative change (%) in total N_r deposition with respect to the default run over Germany, the Netherlands and Belgium in 2014 per land use class.*

	LE_{LAI}	LE_{z0}	LE_{z0+LAI}
Grass (1)	−5.34	−3.95	−8.05
Arable land (2)	9.53	3.27	12.88
Permanent crops (3)	0.22	−3.17	−2.78
Coniferous forest (4)	−9.36	−0.86	−7.36
Deciduous forest (5)	1.15	1.93	1.83
Urban (7)	16.62	−0.37	6.53
Other (6, 8, 9)	3.45	0.58	3.31

3.4.5.4 Effect on land-use-specific fluxes

Table 3.7 gives an overview of changes in the distribution of the land-use-specific fluxes in the whole study area (Germany, the Netherlands and Belgium combined) for the different runs. The most distinct changes in N_r deposition are due to the updated LAI values ("LE_{LAI}"), where we observe an increase in total N_r deposition on urban areas (+16.62 %) and arable land (+9.53 %), and a decrease on coniferous forests (−9.36 %). This coincides with the categories where we observe the largest changes in LAI values. The default LAI values in urban areas were first set to zero for all urban DEPAC categories. The MODIS LAI values, however, are only zero in densely populated areas and areas with industry. The main effects of the updated z_0 values ("LE_{z0}") can be observed for grass (−3.95 %), permanent crops (+3.27) and arable land (−3.17 %). In the combined run, "LE_{z0+LAI}", we observe an amplified effect in total N_r deposition over grass (−8.05 %) and arable land (+12.88 %). The impact of the individual parameters on the remaining land use categories is attenuated in this run.

3.4.6 Implications for N_r distributions

The changes in N_r deposition amounts induce an effect in the modelled distribution of nitrogen components. Here, we look at the effect of the updated LAI and z_0 values on NH_3 and NO_2 surface concentrations. Fig. 3.14 shows the updated modelled NH_3 and NO_2 surface concentrations in 2014. The dots on top of the figures represent the stations that are used for validation and their observed mean NH_3 and NO_2 surface concentrations. Fig. 3.15 shows the relative change in yearly mean NH_3 and NO_2 surface concentrations in 2014 of the different runs with respect to the default run of LOTOS-EUROS.

The first column represents the changes in NH_3 and NO_2 surface concentrations due to the updated z_0 values. The NH_3 surface concentration in the Netherlands has increased by up to ~8 %. The NH_3 surface concentration in almost all of Germany has decreased by up to ~10 %. The changes in the NO_2 surface concentration are less distinct and changed approximately minus to plus 4 % in most areas. The middle column represents the changes in NH_3 and NO_2 surface concentrations due to the inclusion of the MODIS LAI only. The NH_3 surface concentration has increased with up to ~10 % in the Netherlands, western Belgium and north-western and southern Germany. The NH_3 surface concentration has decreased in eastern Belgium and central Germany. The NO_2 surface concentrations have decreased with up to ~6 % in almost all of the modelled area.

3.4.7 Comparison to in situ measurements

To analyse the effect of the updated LAI and z_0 values, we compared our model output to the available in situ observations. Due to the lack of available dry deposition measurements, we decided to use NH_4^+ and NO_3^- wet deposition and NH_3 and NO_2 surface concentrations measurements instead. The distribution of the wet deposition stations is shown in Fig. 3.16, as well as the modelled mean NH_4^+ (left) and NO_3^- (right) wet deposition in 2014. The locations of the stations that measure the NH_3 and NO_2 surface concentrations are shown in Fig. 3.14.

The relationships between the modelled and observed fields are evaluated using the Pearson correlation coefficient (r), the RMSD and the coefficients (slope, intercept) of simple linear regression. Table S3.1 shows these measures for the comparison with monthly mean NO_3^- wet deposition, NH_4^+ wet deposition and the monthly mean NH_3 and NO_2 surface concentrations in 2014. Table S3.1 shows the same statistics but computed per DEPAC land use class. Overall, we do not observe large changes in the shown measures due to the inclusion of the updated LAI and z_0 values on a yearly basis. The model underestimates NO_3^- wet deposition, and NH_4^+ to a lesser extent, too. The modelled NH_3 surface concentrations are in general higher than observed concentrations. The opposite is true for NO_2; here, the modelled surface concentrations are lower than the observed concentrations. The computed measures did not change drastically due to the inclusion of the updated z_0 and LAI values.

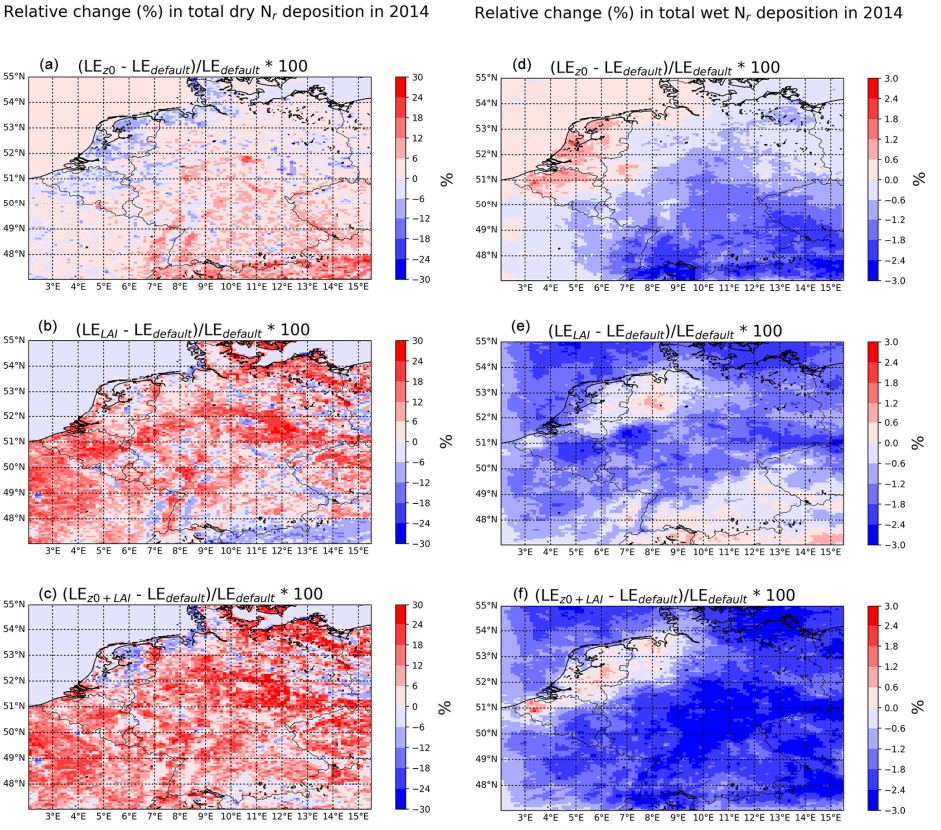

Figure 3.11. *The relative change in total dry* ***(a, b, c)*** *and wet* ***(d, e, f)*** N_r *deposition in 2014 for the different model runs relative to the default LOTOS-EUROS run. The first row indicates the changes related to the implementation of the updated* z_0 *values. The second row indicates the changes related to the implementation of the MODIS LAI values. The third row shows the combined effect of both these updates.*

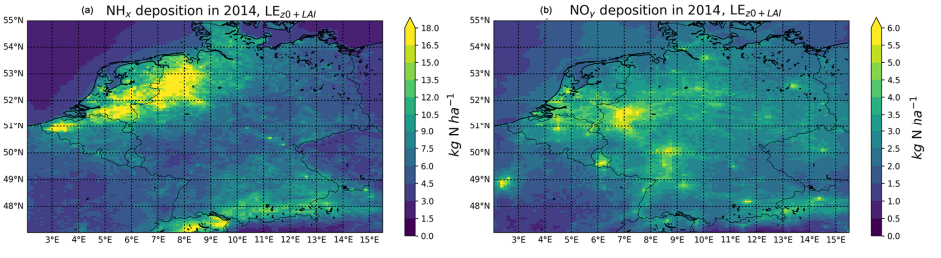

Figure 3.12. *NH_x deposition* ***(a)*** *and NO_y deposition* ***(b)*** *in kg N ha^{-1} in 2014.*

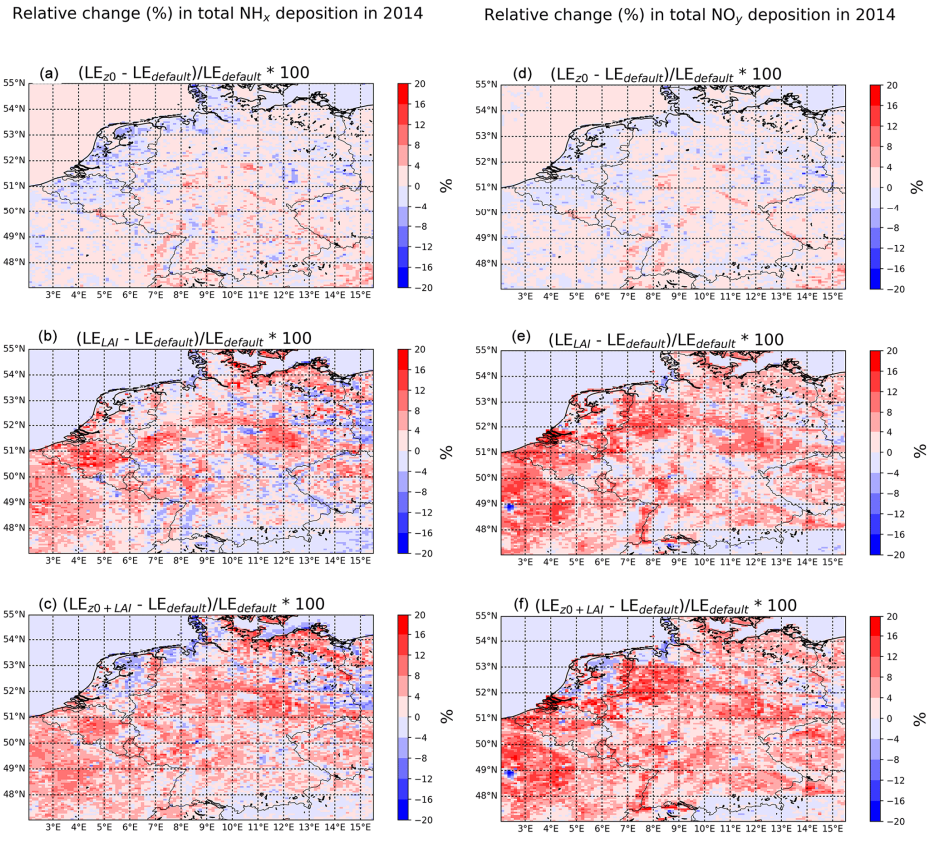

Figure 3.13. *The relative change in total NH_x* ***(a, d)*** *and NO_y* ***(c, f)*** *deposition in 2014 for the different model runs relative to the default LOTOS-EUROS run. The first row indicates the changes related to the implementation of the updated z_0 values. The second row indicates the changes related to the implementation of the MODIS LAI values. The third row shows the combined effect of both these updates.*

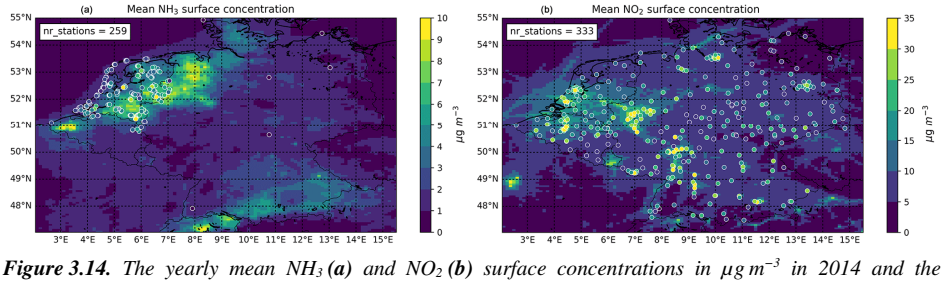

Figure 3.14. *The yearly mean NH_3* ***(a)*** *and NO_2* ***(b)*** *surface concentrations in $\mu g\, m^{-3}$ in 2014 and the corresponding mean surface concentrations measured at the in-situ stations.*

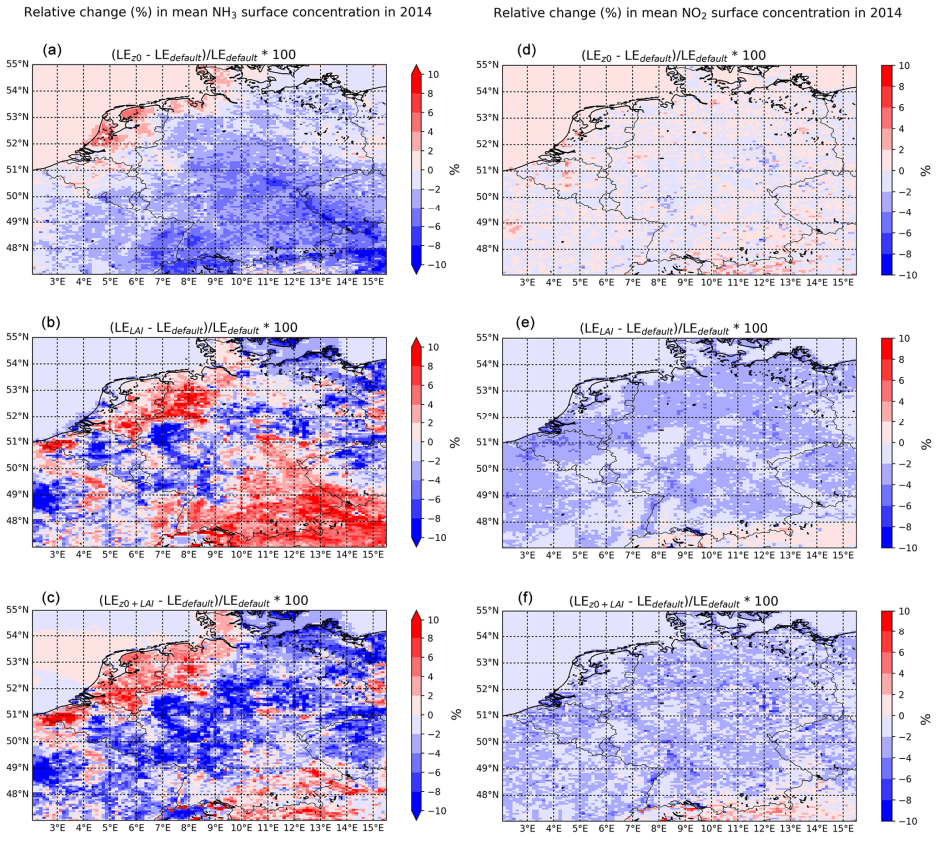

Figure 3.15. *The relative change (%) in mean NH_3* ***(a, b, c)*** *and NO_2* ***(d, e, f)*** *surface concentration in 2014 for the different model runs relative to the default LOTOS-EUROS run. The first row indicates the changes related to the implementation of the updated z_0 values. The second row indicates the changes related to the implementation of the MODIS LAI values. The third row shows the combined effect of both these updates.*

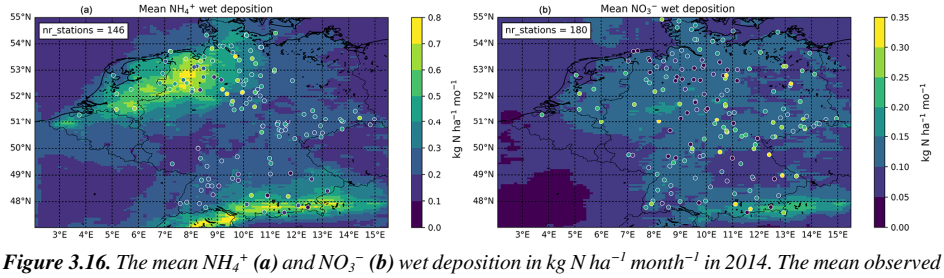

Figure 3.16. *The mean NH_4^+* ***(a)*** *and NO_3^-* ***(b)*** *wet deposition in kg N ha^{-1} $month^{-1}$ in 2014. The mean observed wet deposition observed at the stations is plotted on top.*

Fig. S3.5 shows the monthly mean NO_3^- wet deposition, NH_4^+ wet deposition, NH_3 surface concentration and NO_2 surface concentrations for the different model runs and the mean of the corresponding in situ observations. The relative changes with respect to the default model run are shown in the bottom figures. For NH_4^+, the model captures the observed pattern quite well, although the mean spring peak has slightly shifted. The model captures the monthly variation of NO_3^- well in general, too. There appears to be an underestimation during the winter, especially in December. The observed NH_3 surface concentrations are lower than the modelled concentrations at the beginning of spring and higher during summer. The measured NO_2 surface concentrations are continuously higher than the modelled values. A potential reason for this might be the spread of the NO_2 stations. Unlike NH_3, NO_2 is not only measured in nature areas but all types of locations. Even the selected background stations may therefore be located relatively closer to emission sources, leading to higher observed NO_2 surface concentrations. The changes due to the inclusion of either the MODIS LAI or the updated z_0 values in our model are limited. Both Tables S3.1 and S3.2, and Fig. 3.16 illustrate that the comparability of the modelled wet deposition and surface concentration fields to the available in situ measurements did not change significantly. The impact of the updated LAI and z_0 values on these fields is largely an indirect effect of the more distinct changes in the dry deposition and thus too small to lead to any drastic changes. We conclude that we are unable to demonstrate any major improvements with the use of the currently available in situ measurements.

3.5 Discussion

This paper aimed to improve the surface characterization of LOTOS-EUROS through the inclusion of satellite-derived LAI and roughness length (z_0) values. We used empirical functions to derive z_0 values for different land use classes. The updated z_0 values are compared to literature values, showing a good agreement in general. We also compared our z_0 values to z_0 values computed from FLUXNET sites. The z_0 values for forests seemed to match well, but the z_0 values for short vegetation seem to be overestimated for crops and underestimated for grassland and wetland sites. The differences for short vegetation types can be partially explained by the large inter-site variability in vegetation types within each classified land use (e.g. reeds versus short grass). The equation for short vegetation used here seems to work best for short grasslands. For our current study area, this does not pose a problem, since most grasslands in Germany, Belgium and the Netherlands are managed and grazed upon. We found an improved RMSD value of 0.60, compared to RMSD of 0.76 with default z_0 values. Even though there is an offset between the satellite-derived and computed FLUXNET z_0 values for crops, the seasonal pattern seemed to match well. The offset can be explained by the absence of low NDVI (<0.4) values.

The z_0 is closely related to the geometric features and distributions of the roughness elements in a certain area. In reality, it is not only dependent on vegetation properties but, for instance, also the topography of the area. The updated z_0 values are linked to specific land use pixels and are therefore assumed reasonable estimates for moderately homogeneous areas with this specific land use type. There are various approaches to combine these z_0 values into an “effective” roughness for larger, mixed areas (e.g. Claussen, 1990; Mason, 1988). The LOTOS-EUROS model uses logarithmic averaging to compute an effective roughness for an entire model pixel. This averaging step seems to be one of the reasons why the effect of our updated z_0 values on the deposition fields is limited. To illustrate this, the relative change in total dry NH_3 deposition due to the updated z_0 values were

computed and shown in Fig. 3.17. We used increasing threshold percentages to sort the NH_3 deposition on a model pixel level per land use type and fraction. Fig. 3.17 shows that the differences in total NH_3 deposition between the two runs increase with increasing land use fraction. The model pixels that mostly consist of one type of land use seem to show the largest change in NH_3 deposition. The change thus appears to be less distinct in pixels that have a higher degree of mixing. Most of the model pixels largely contain mixtures of different land uses on the current model resolution. As a result, averaging of z_0 on a model pixel level is thus likely to cause a levelling effect on the current model resolution. The impact of the updated z_0 values is therefore expected to be larger at a higher model resolution. The use of another approach for computing the "effective" roughness could potentially lead to stronger changes in the modelled deposition fields.

Moreover, we should also consider the limitations of the datasets used in this study. The forest canopy height map used in this study has been validated against 66 FLUXNET sites (Simard et al., 2011). The results showed that root mean square error (RMSE) was 4.4 m and R^2 was 0.7 after removal of seven outliers. For the FLUXNET forest sites used in this study, we compared the forest canopy heights from GLAS to the maximum forest canopy height at the FLUXNET sites taken from (Flechard et al., 2020). For all but one site (DE-Hai), the forest canopy heights from GLAS were lower than this value (Table S3.3). This method could potentially be improved by using another product with either a higher precision or resolution. For modelling studies on a national level, one could or instance consider the use of airborne lidar point clouds to retrieve forest canopy heights. This procedure, although it is computationally expensive, would allow us to create high-resolution z_0 maps.

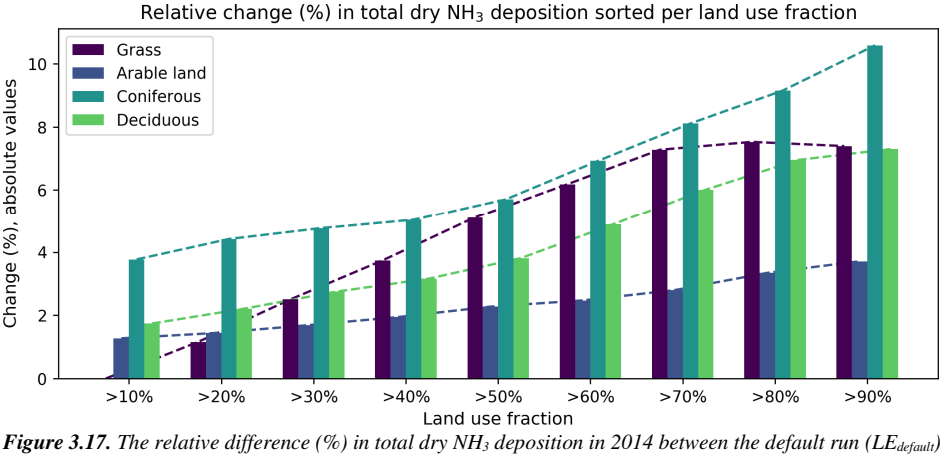

Figure 3.17. *The relative difference (%) in total dry NH_3 deposition in 2014 between the default run ($LE_{default}$) and the run with the updated z_0 values (LE_{z0}), sorted by increasing land use fraction.*

The MODIS LAI at the FLUXNET sites showed realistic seasonal variations for most land use classifications, except for relatively low wintertime values for evergreen needleleaf forests. The previous versions of the MODIS LAI have been validated in many studies (e.g. Fang et al., 2012; Wang et al., 2004; Kobayashi et al., 2010), showing an overall good agreement with ground-observed LAI values and other LAI products. The seasonality in LAI is properly captured for most biomes, but unrealistic temporal variability is observed for forest due to infrequent observations.

Also, the previous versions overestimate LAI for forests (Fang et al., 2012; Kobayashi et al., 2010; Wang et al., 2004). The MODIS LAI products have been gradually improving with each update; however, these issues still exist in the newer versions of the product. For the most recent version of the MODIS LAI, version 6, Yan et al. (2016) found an overall RMSE of 0.66 and a R^2 of 0.77 in comparison with LAI ground observation. More recently, using a different approach, Xu et al. (2018) found a slightly higher RMSE of 0.93 and a R^2 of 0.77. Some studies (e.g. Tian et al., 2004) have reported an underestimation of the MODIS LAI in presence of snow cover, particularly affecting evergreen forests. With only limited amounts of snowfall, the regions in our study did not suffer from this problem. However, this issue should be carefully considered when using the MODIS LAI for regions with frequent snow cover, like Scandinavia. LOTOS-EUROS uses meteorological data to determine what regions are covered with snow and for these regions the standard parameterization for the canopy resistance is not used. LOTOS-EUROS uses a pre-defined value for the canopy resistance instead. As such, these low MODIS LAI values do not affect the modelled deposition in LOTOS-EUROS during snow cover.

Though the issues with the MODIS LAI should be considered with care, the spatial and temporal distributions of these LAI values are more realistic than those of the default LAI values used in LOTOS-EUROS. The same holds for the updated, time-variant z_0 values. The representation of the growing season is now more realistic due to their dependence on NDVI and LAI values. Moreover, the z_0 values for forests now also have a clear spatial variation, such as a latitudinal gradient with increasing z_0 values towards the south of Germany. These types of patterns can simply not be captured by fixed values.

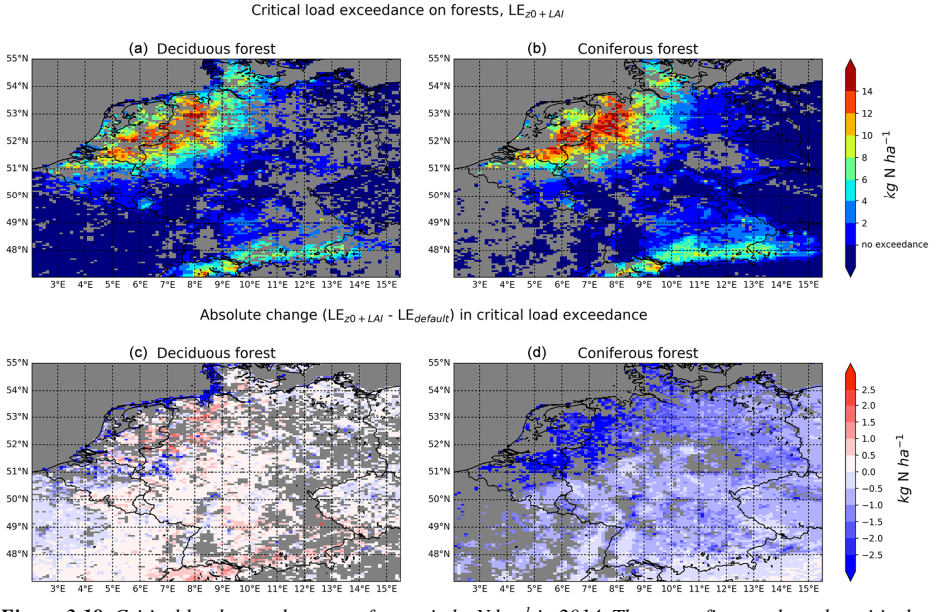

Figure 3.18. *Critical load exceedances on forests in kg N ha^{-1} in 2014. The upper figures show the critical on deciduous* ***(a)*** *and coniferous* ***(b)*** *forest, as modelled with the updated z_0 and LAI values. The lower figures show the absolute differences in critical load exceedance on deciduous* ***(c)*** *and coniferous* ***(d)*** *between the new and the default LOTOS-EUROS run.*

We evaluated the effect of updated z_0 and LAI values on modelled N_r distribution and deposition fields. The distribution of the relative changes in deposition of the reduced and oxidized forms of reactive nitrogen showed a similar pattern. Here, the updated z_0 values led to a variation of ∼±8 %, and the updated LAI values led to variations of ∼±30 % in both fields. The dry deposition fields were most sensitive to changes in z_0 and LAI, as these varied from approximately −20 % to +20 % with the updated z_0 map, and from −20 % even up to +30 % with the MODIS LAI values. As a result, we observed a shift from wet to dry deposition, except for the Netherlands, where we observe an opposite shift from dry to wet deposition. Moreover, we observed a redistribution of N_r deposition over different land use classes on a subgrid level. To illustrate the potential consequences on a local scale, we computed the critical load exceedances for deciduous and coniferous forest (Fig. 3.18) using critical loads of 10 kg following Bobbink et al. (2010b). Compared to the default run, the changes may be sizable locally, ranging from approximately −3 up to +2 kg for deciduous forest and even over −3 kg for coniferous forest.

The uncertainties of the LAI and z_0 input data are but one aspect of the model uncertainty of CTMs. The model uncertainty has several other origins, like the physical parameterizations (e.g. deposition velocities) and the numerical approximations (e.g. grid size). Two of the most important uncertainties related to deposition modelling are the emissions and the surface exchange parameterization. The emission inventories for reactive nitrogen hold a relatively large uncertainty. The uncertainty of the reported annual total NH_3 emissions is estimated to be at least ±30 %. This is mainly due to the diverse nature of agricultural emission sources, leading to large spatiotemporal variations. The annual NO_x emissions total hold a lower uncertainty, of approximately ±20 % (Kuenen et al., 2014). Emissions at specific locations, especially for NH_3, are even more uncertain due to assumptions made in the redistribution and timing of emissions. A recent paper of Dammers et al. (2019), for instance, found that satellite-derived NH_3 emissions of large point sources are a factor of 2.5 higher than those given in emission N inventories. The surface exchange parameterization is another source of uncertainty. The complexity of the NH_3 surface exchange schemes in CTMs is usually low compared to the current level of process understanding (Flechard et al., 2013). Moreover, large discrepancies exist between deposition schemes. Flechard et al. (2011), for instance, showed that the differences between four dry deposition schemes for reactive nitrogen can be as large as a factor of 2–3.

This work has shown that changes in two of the main deposition parameters (LAI, z_0) can already lead to distinct, systematic changes (∼30 %) in the modelled deposition fields. This demonstrates the model's sensitivity toward these input values, especially the LAI. In addition to the known uncertainty involved with the surface exchange parameterization itself, this further stresses the need for further research. Another important aspect that should receive more attention is the validation of the dry deposition fields with in situ dry deposition measurements. Here, we illustrated the need for direct validation methods, as relatively large changes in modelled dry deposition field cannot be verified sufficiently by surface concentration and wet deposition measurements.

The surface–atmosphere exchange remains one of the most important uncertainties in deposition modelling. The use of satellite products to derive LAI and z_0 values can help us to represent the surface characterization in models more accurately, which in turn might help us to minimize the

uncertainty in deposition modelling. The approach to derive high-resolution, dynamic z_0 estimates presented here can be linked to any land use map and is as such transferable to many different models and geographical areas.

Acknowledgements. The authors acknowledge the Nederlandse Organisatie voor Wetenschappelijk Onderzoek (NWO). This project was funded by the NWO under project number ALW-GO/16-05. We would like to thank the Umweltbundesamt (UBA), the German monitoring networks, as well as the European Monitoring and Evaluation Programme (EMEP) and the Rijksinstituut voor Volksgezondheid en Milieu (RIVM) for providing the in situ observations used for validation. This work used eddy covariance data acquired and shared by the FLUXNET community, including these networks: AmeriFlux, AfriFlux, AsiaFlux, CarboAfrica, CarboEuropeIP, CarboItaly, CarboMont, ChinaFlux, Fluxnet-Canada, GreenGrass, ICOS, KoFlux, LBA, NECC, OzFlux-TERN, TCOS-Siberia and USCCC. We would like to thank Dario Papale for providing us the measurement heights of the FLUXNET towers. The ERA-Interim reanalysis data are provided by ECMWF and processed by LSCE. The FLUXNET eddy covariance data processing and harmonization were carried out by the European Fluxes Database Cluster, AmeriFlux Management Project and Fluxdata project of FLUXNET, with the support of CDIAC and ICOS Ecosystem Thematic Center, and the OzFlux, ChinaFlux and AsiaFlux offices.

Chapter 4: Data assimilation of CrIS-NH_3 satellite observations for improving spatiotemporal NH_3 distributions in LOTOS-EUROS.

Abstract. Atmospheric levels of ammonia (NH_3) have substantially increased during the last century, posing a hazard to both human health and environmental quality. The atmospheric budget of NH_3, however, is still highly uncertain due to an overall lack of observations. Satellite observations of atmospheric NH_3 may help us in the current observational and knowledge gaps. Recent observations of the Cross-track Infrared Sounder (CrIS) provide us with daily, global distributions of NH_3. In this study, the CrIS-NH_3 product is assimilated into the LOTOS-EUROS chemistry transport model using two different methods aimed at improving the modelled spatio-temporal NH_3 distributions. In the first method NH_3 surface concentrations from CrIS are used to fit spatially varying NH_3 emission time factors to redistribute model input NH_3 emissions over the year. The second method uses the CrIS-NH_3 profile to adjust the NH_3 emissions using a Local Ensemble Transform Kalman Filter (LETKF) in a top-down approach. The two methods are tested separately and combined, focusing on a region in western Europe (Germany, Belgium, and the Netherlands). In this region, the mean CrIS-NH_3 total columns were up to a factor 2 higher than the simulated NH_3 columns between 2014 and 2018, which, after assimilating the CrIS-NH_3 columns using the LETKF algorithm, led to an increase of the total NH_3 emissions of up to approximately 30%. Our results illustrate that CrIS-NH_3 observations can be used successfully to estimate spatially variable NH_3 time factors, and improve NH_3 emission distributions temporally, especially in spring (March to May). Moreover, the use of the CrIS-based NH_3 time factors resulted in an improved comparison with the onset and duration of the NH_3 spring peak observed at observation sites at hourly resolution in the Netherlands. Assimilation of the CrIS-NH_3 columns with the LETKF algorithm is mainly advantageous for improving the spatial concentration distribution of the modelled NH_3 fields. Compared to in-situ observations, a combination of both methods led to the most significant improvements in modelled monthly NH_3 surface concentration and NH_4^+ wet deposition fields, illustrating the usefulness of the CrIS-NH_3 products to improve the temporal representativity of the model and better constrain the budget in agricultural areas.

This chapter is under review for publication in Atmospheric Chemistry and Physics: van der Graaf, S.C., Dammers, E., Segers, A., Kranenburg, R., Schaap, M., Shephard, M.W., and Erisman, J. W.: Data assimilation of CrIS-NH_3 satellite observations for improving spatiotemporal NH_3 distributions in LOTOS-EUROS, Atmos. Chem. Phys. Discuss. [preprint], https://doi.org/10.5194/acp-2021-473, in review, 2021.

4.1 Introduction

Ammonia (NH_3) is an alkaline gas in the Earth's atmosphere. NH_3 is highly reactive and readily reacts with available acids, forming aerosol components harmful to human health (Pope et al., 2009, Lelieveld et al., 2015, Giannakis et al., 2019) and, directly and indirectly, impacting global climate change (Erisman et al, 2011, Myhre et al., 2013). NH_3 is emitted from a large number of sources, including agriculture, natural nitrogen fixation in oceans and plants, volcanic eruptions, and biomass-, industrial- and fossil fuel burning (Erisman et al., 2015). Globally, agriculture is the largest source of NH_3. Agricultural emissions of NH_3 consist of, among others, volatilized NH_3 after manure and chemical fertilizer application, livestock housing and grazing and harvesting of crops. About 40% of the total global NH_3 emissions follow directly from volatilization of animal manure and chemical fertilizer, a spatially variable process highly controlled by the temperature and acidity of soils (Sutton et al., 2013). In western Europe, for instance, agriculture is an even more dominant source of NH_3 and contributes to 85-100% of all NH_3 emissions (Hertel et al., 2011). After the emitted NH_3 is transported through the atmosphere, it is deposited back to the Earth's surface through the processes of wet and dry deposition. Excess amounts of reactive nitrogen deposition can cause several adverse effects, such as eutrophication in aquatic ecosystems and soil acidification (Erisman et al., 2007) and biodiversity loss in terrestrial ecosystems (Bobbink et al., 2010).

Even though NH_3 at its current levels is an important threat to human health and environmental quality, its atmospheric budget is still very uncertain. NH_3 concentrations are highly variable in space and time and are difficult to be reliably measured in-situ due to the sticky nature of NH_3 leading to potential adsorption to parts of the measurement devices (von Bobrutzki et al, 2010). Globally, only a few NH_3 measurement networks exist, most of which contain only a small number of locations. Moreover, most measurements are performed at a coarse temporal resolution (weeks to months), while most atmospheric processes occur on much shorter time scales. Due to the lack of dense and precise measurement networks, measures for NH_3 emission controls currently rely mostly on estimates from models, for instance from chemical transport models (CTMs). CTMs simulate atmospheric processes such as emissions, transport, deposition and chemical conversion to estimate the spatial and temporal distribution of atmospheric NH_3. However, these models involve large uncertainties. On the one hand, model assumptions and parameterizations are uncertain due to insufficient or lack of knowledge of some of the processes, for instance, the limited understanding of bi-directional fluxes of NH_3 (Schrader and Brümmer, 2014, Schrader et al., 2018) or the direct effect of meteorology on NH_3 emissions (Sutton et al., 2013). On the other hand, uncertainties stem from the underlying input data and the spatial and temporal variation in emissions. Compared to other air pollutants, NH_3 emission inputs are especially uncertain due to their large spatiotemporal variability resulting from the diverse nature of agricultural sources (Behera et al., 2013). In Europe, the uncertainty of the total annual reported NH_3 emissions on a country level is for instance already estimated to be at least round ~30% (EEA, 2019). Naturally, NH_3 emissions from individual sources have a much higher uncertainty due to errors related to spatial and temporal distribution. So as to reduce the uncertainty in modelled NH_3 fields from CTMs, it is vital to better understand both the spatiotemporal distribution of NH_3 emissions.

With the scarceness of in-situ measurements and uncertainties in existing models, the atmospheric NH_3 budget remains among the least known parts of the nitrogen cycle (Erisman et al., 2007). Recent satellite observations of NH_3 in the lower troposphere can help us to fill in both observational and knowledge gaps. Satellite instruments, such as the NASA Tropospheric Emission Spectrometer (TES) (Beer et al., 2008), ESA's Infrared Atmospheric Sounder Interferometers (IASI) (Clarisse et al., 2009), the NASA Atmospheric Infrared Sounder (AIRS) (Warner et al., 2016), the Thermal And Near-infrared Spectrometer for Observation-Fourier Transform Spectrometer (TANSO-FTS) (Someya et al., 2020) and the NASA/NOAA Cross-track Infrared Sounder (CrIS) (Shephard and Cady-Pereira, 2015) provide global observations of atmospheric NH_3. Out of the operational satellites that observe NH_3 with twice daily global coverage, CrIS is the newest instrument and has the lowest radiometric noise in the spectral region used for NH_3 (Zavyalov et al., 2013). Moreover, CrIS has greater vertical sensitivity to near-surface NH_3, and provides retrievals of the vertical distribution of NH_3 (Shephard et al., 2020).

These atmospheric trace gas measurements with satellites have opened up new ways to study the atmospheric budget. Recently, satellite observations have successfully been used for direct estimates of emissions and lifetimes of various other atmospheric species (e.g., SO_2, NO_2, CO_2) of single anthropogenic or natural point sources (e.g., Fioletov et al., 2015, Nassar et al., 2017) or even multiple sources at a time (Fioletov et al.,2017, Beirle et al., 2019). For NH_3 specifically, multiple studies have reported emissions and atmospheric lifetime estimates either based on satellite data (e.g., Zhu et al., 2013, Whitburn et al., 2015, Van Damme et al., 2018, Zhang et al., 2018, Cao et al., 2020, Evangeliou et al., 2021) or directly estimated from satellite data (e.g., Van Damme et al., 2018, Adams et al., 2019, Dammers et al., 2019). Here, also different forms of model inversions have been used. Overall, these studies indicate an underestimation of both anthropogenic and natural NH_3 emissions in the current emission inventories. In addition to estimating NH_3 emissions, various studies used satellite observations to estimate dry deposition fluxes of NH_3 (Kharol et al., 2018, Van der Graaf et al., 2018, Lui et al., 2020).

In this manuscript, we describe two methods to improve both the temporal and spatial variation of NH_3 emissions in the LOTOS-EUROS chemistry transport model with CrIS-NH_3 observations. The first method aims at deriving an improved set of a-priori, observation-based NH_3 time factors to be used for the temporal distribution of agricultural emission sources within LOTOS-EUROS. In this method, the NH_3 surface concentrations from CrIS are used to fit daily NH_3 time factors. The second method is used to assimilate the CrIS-NH_3 observations into the LOTOS-EUROS model, using a Local Ensemble Transform Kalman Filter (LETKF) approach as data-assimilation system. The impact of the two methods, both individually and combined, on the simulated NH_3 emissions, concentration and deposition fields is then evaluated. The focus region of the study is a low-to-high NH_3 emission area within western Europe (The Netherlands, Germany, Belgium), which is representative for other intense agricultural regions in the world. Moreover, the NH_3 emissions within this region are relatively well known and in-situ observations are sufficiently available.

4.2 Methodology

4.2.1 LOTOS EUROS

LOTOS-EUROS is an Eulerian chemistry transport model (Manders et al., 2017) that could be used to simulate trace gas and aerosol concentrations in the lower troposphere. The model has an intermediate complexity with limited run time, allowing ensemble-based simulations and assimilation studies. LOTOS-EUROS uses meteorological data as input, which in this study is taken from the using European Centre for Medium-Range Weather Forecasts (ECMWF). The gas-phase chemistry follows a carbon-bond mechanism (Schaap et al., 2008). The dry deposition fluxes are calculated with the Deposition of Acidifying Compounds (DEPAC) 3.11 module, following the resistance approach and it includes a calculation of bi-directional NH_3 fluxes (Van Zanten et al., 2010, Wichink Kruit et al., 2012). The wet deposition fluxes are computed using the CAMx (Comprehensive Air quality Model with Xtensions) approach, which includes both in-cloud and below-cloud scavenging (Banzhaf et al., 2012). The anthropogenic emissions are taken from CAMS-REG-AP (Copernicus Atmospheric Monitoring Services Regional Air Pollutants) emissions dataset v2.2 (Granier et al., 2019). For Germany, high resolution gridded NH_3 emission inputs (GRETA) are used (Schaap et al., 2018). In this study, a region in Western Europe (47°N-56°N, 2°E-16°E) is modelled, which includes all of Germany, the Netherlands and Belgium (Fig. 4.2). A spatial resolution of 0.20° longitude by 0.10° latitude is used, corresponding to approximately 12 by 12 square kilometers, which is also roughly the footprint size of CrIS (14 by 14 km^2 at nadir). The vertical grid extends up to 200 hPa and is split up into 13 vertical layers. This captures the largest part of atmospheric NH_3, as it is a relatively short-lived species mainly located in the boundary layer. The interfaces of the vertical layers are based on the pressure layers used in the ECMWF meteorological input data. LOTOS-EUROS is part of the operational Copernicus Atmosphere Monitoring Service (CAMS) ensemble forecasts and analysis for Europe (Marécal et al., 2015). The model has participated in multiple model intercomparison studies (e.g., Bessagnet et al., 2016, Colette et al., 2017, Vivanco et al., 2018), showing overall good performance.

4.2.2 Datasets

4.2.2.1 CrIS NH_3

The Cross-Track Infrared Sounder (CrIS) is an instrument aboard NASA's sun-synchronous, Earth orbiting Suomi NPP satellite with an equatorial overpass at 13:30 and 1:30 LST. The CrIS sensor has a spectral resolution of 0.625 cm^{-1} (Shephard et al., 2015) and a detection limit of 0.3-0.5 ppbv under favorable conditions (Shephard et al., 2020). The instrument has a wide swath of up to 2200 km with pixels of approximately 14 km in size at nadir. Compared to other NH_3 satellite sounders (e.g., AIRS, IASI), CrIS has greater vertical sensitivity to NH_3 close to the surface due to its low spectral noise of approximately 0.04K at 280K in the NH_3 spectral region (Zavyalov et al., 2013). Moreover, CrIS has a relatively high near-surface sensitivity and an overpass time around 1:30 LST which coincides with the time of the day with the highest thermal contrast. The peak sensitivity of the instrument is typically between 900 and 700 hPa, which corresponds to approximately 1 to 3 km (Shephard et al., 2020). The CrIS NH_3 total columns have an estimated total random measurement error of around 10-15%, and an estimated random total error of ~30%. Due to the limited vertical resolution, the NH_3 concentrations at individual retrieval levels have a higher random measurement error of about 10-30% and a total error of ~60-100% (Shephard et al., 2020). Version 1.3 of the CrIS-NH_3 product has been evaluated against in-situ Fourier Transform

Infrared (FTIR) measurements (Dammers et al., 2017) showing an overall good performance and high correlations of r~0.8. In this study, we used version 1.5 of the CrIS fast physical retrieval (FPR)-NH_3 product, which is based on the optimal estimation method (Rodgers, 2000). More details about the CrIS FPR-NH_3 product can be found in (Shephard et al., 2020). Here, we used daytime observations of NH_3 (partial) column concentrations and surface concentrations made between January 2014 and December 2018 from the first CrIS sensor, which has the longest observing period. During this 5-year period, a virtually continuous timeseries of CrIS observations was available. More recent observations were not used due to the technical issues of the CrIS instrument during the summertime in 2019, and the potentially anomalous situation resulting from the COVID-19 outbreak in 2020.

4.2.2.2 In-situ observations

Several measurement networks were used to evaluate the simulated concentration and deposition fields. The NH_3 surface concentrations are evaluated against observations from the Dutch Meetnet Ammoniak in Natuurgebieden (MAN) network (Lolkema et al., 2015), the Dutch Landelijk Meetnet Luchtkwaliteit (LML) network (van Zanten et al., 2017), the Belgium Flanders Environment Agency (VMM) network (den Bril et al., 2011) and the German Environment Agency (UBA) network (Schaap et al., 2018). The locations of these sites are shown in Fig. 4.1. The MAN network provides monthly mean NH_3 surface concentrations since 2005, spread over 80 mostly low NH_3 emission nature areas in the Netherlands. The measurements are performed with low-cost passive samplers from Gradko and have an estimated uncertainty of ~20% for high concentrations and ~41% for low concentrations (Lolkema et al., 2015). The NH_3 concentrations in Flanders are measured with passive samplers from Radiëllo and IVL samplers (den Bril et al., 2011). The LML network observes hourly NH_3 concentrations at six different locations in the Netherlands with different emission regimes (high, moderate, low). Initially, continuous flow denuders from AMOR were used, which have a reported uncertainty of at least 9% for hourly concentrations (Blank et al., 2001). Around 2016, the AMOR instruments were replaced by miniDOAS instruments (Berkhout et al., 2017), which are active differential optical absorption spectroscopes. For evaluation of the wet deposition fields, observations from wet-only samplers from the Dutch Landelijk Meetnet Regenwatersamenstelling (LMRe) network (van Zanten et al., 2017), whose locations largely overlap with the LML network, and the UBA network (Schaap et al., 2018) are used. The locations of the wet-only samplers are shown in Fig. S4.1.

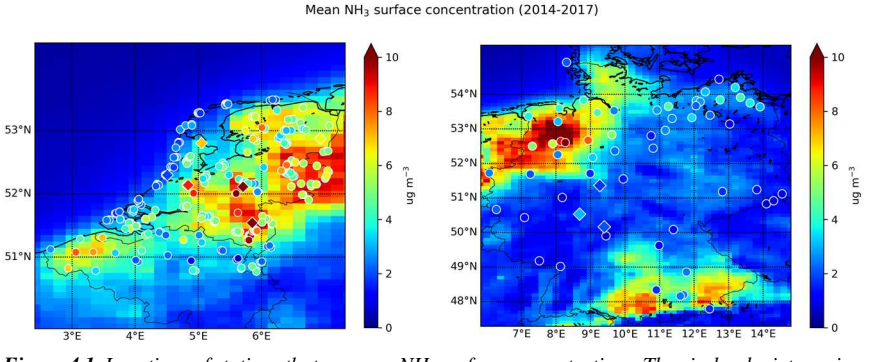

Figure 4.1. *Locations of stations that measure NH_3 surface concentrations. The circles depict passive samplers and the diamonds hourly observations stations.*

4.2.3 Fitting method for deriving CrIS-based NH_3 time factors

A non-linear least squares method is used to fit a trimodal gaussian curve to the scaled NH_3 surface concentrations (see section 4.2.3.3.) from CrIS in each grid cell. The Trust Region Reflective algorithm is used to perform the minimization (Conn et al., 2000). The minimalization algorithm is restrained with initial parameter guesses and bounds for three fitted gaussians. The three gaussians represent the spring (μ_1, σ_1, and A_1), autumn (μ_2, σ_2, and A_2) and summer peak (μ_3, σ_3, and A_3) in NH_3 emissions, respectively. The initial parameter guesses are based on the standard MACC-III (Kuenen et al., 2014) NH_3 emission time profiles. The bounds are defined as follows:

• the mean values ($\mu_{1,2,3}$) are permitted to shift by one month (30 days) to cover the most probable emission peaks
• the standard deviations ($\sigma_{1,2,3}$) are permitted to vary by half their initial value guess (i.e., $\pm 0.5\sigma$)
• the fitted amplitude of the spring peak (A_1) is allowed to be between 0.1 and 1.0 and amplitudes of the autumn and summer gaussians ($A_{2,3}$) between 0.1 and 0.8

An overview of the permitted parameter bounds is given in Table 4.1. The range in permitted $A_{1,2,3}$ values is quite large, allowing the minimization algorithm to fit meaningful trimodal curves for different types of time variant NH_3 emission sources simultaneously (e.g., flatter peaks for emissions that mainly dependent of temperature and specific periods, such as open stables, a sharper more distinct spring and autumn peaks for emissions following fertilizer or manure application).

Table 4.1. *Initial parameter guesses and parameter bounds used in the trimodal fit algorithm.*

	Spring peak			**Autumn peak**			**Summer peak**		
	μ_1 (doty)	σ_1 (days)	A_1 (-)	μ_2 (doty)	σ_2 (days)	A_2 (-)	μ_3 (doty)	σ_3 (days)	A_3 (-)
Lower bound	47.4	13.1	0.1	222.8	11.6	0.1	148.9	26.9	0.1
First guess (MACC-III)	77.4	26.1	0.96	252.8	23.2	0.26	178.9	53.7	0.21
Upper bound	107.4	39.1	1.0	282.8	34.8	0.8	208.9	107.4	0.8

After the daily NH_3 time factors are fitted, the diurnal variation from the MACC-III NH_3 time factors is added to obtain hourly time factors. The resulting hourly CrIS-based time factors are used as input for all time-variant NH_3 sources from agriculture subcategories in LOTOS-EUROS, i.e., continuous NH_3 point sources emissions remain time-invariant.

4.2.3.2 Data selection

The CrIS NH_3 concentrations in the lowest retrieval level, i.e., closest to the surface, are used to adjust the daily variability in the NH_3 time profiles spatially on a regular 0.1° by 0.05° grid. First, to collect a sufficient number of observations for the fitting algorithm, the CrIS NH_3 surface concentrations with a quality flag of at least 3 and within a selection radius of 1° around the center points of each grid cell are selected. The daily average NH_3 concentrations throughout the year are computed after application of a simple outlier filter (>99th percentile excluded given more than 3 observations). Due to the lower number of observations during winter, and to avoid a bias towards

higher values due to lower thermal contrast, observations in January, November and December are ignored. During these months it is anyway prohibited to apply fertilizer or spread manure in parts of the regions (for the Netherlands, see RVO, 2021), and in combination with the colder temperatures, NH_3 concentrations are expected to be low due to low volatilization rates (e.g., Søgaard et al., 2002).

4.2.3.3 Correction for local emission to concentration ratio

The relationship between NH_3 emissions and surface concentrations differs by region and changes throughout the year due to changes in the meteorological and chemical conditions. To correct for this, the following adjustment factor is applied to the daily CrIS NH_3 surface concentrations. The factor is derived from the NH_3 emission and simulated surface concentration fields from LOTOS-EUROS, which are used to compute the local ratio of the smoothed daily total NH_3 emissions to the NH_3 surface concentrations at the CrIS overpass time per grid cell. These are used as a first order approximation for the relation between the emission and concentration. The ratios are rescaled by the mean annual values for each grid cell to obtain a unitless daily scaling factor (Fig. S4.2). After multiplying the daily averaged CrIS NH_3 surface concentrations with this scaling factor, a $\pm 1\sigma$ filter is used to smoothen out the daily time series. To avoid too much flattening of the spring emission peak, a separate filter is applied for the spring period. NH_3 emissions originating from the application of synthetic or manure fertilizer are mainly found during this period, at the beginning of the growing season. This may lead to an increase in observed NH_3 concentrations, that would be filtered out when the same filter is applied for the entire year. Finally, the scaled NH_3 surface concentrations are normalized for each grid cell.

4.2.4 Data assimilation system

4.2.4.1 Local Ensemble Transform Kalman Filter

The Ensemble Kalman Filter (Evensen, 2003) is a sequential data assimilation method that could be used to combine model simulations with observation. In this study, the Local Ensemble Transform Kalman Filter (LETKF) formulation is used (Hunt et al, 2007) following the implementation by (Shin et al., 2016). The LETKF performs an analysis per grid cell based on nearby observations only and it therefore computationally advantageous compared to the regular implementation of the Ensemble Transform Kalman Filter. The basic idea behind an Ensemble Kalman Filter is to express the probability function of the state in terms of an ensemble with N possible states $\boldsymbol{x_1}$, $\boldsymbol{x_2}$, ... $\boldsymbol{x_N}$, each considered to be a possible sample out of the distribution of the true state. In this study, the state contains the NH_3 concentrations in a three-dimensional grid and two-dimensional NH_3 emission perturbation factors β. The perturbation factors describe the uncertainty in the emissions, and are modelled as samples out of normal distribution with zero mean and standard deviation σ. Spatial variations are initially not defined, but are introduced by a localization length scale that is described below. The temporal variation in the emission factors is described by temporal correlation coefficient α, that depends on temporal length scale τ (Lopez-Restrepo et al., 2020, Barbu et al., 2009):

$$\alpha_k = e^{-|t_k - t_{k-1}|/\tau} \quad \text{(Eq. 4.1)}$$

An initial ensemble is created by generating random samples of the perturbation factors. The ensemble is then propagated in time in what is called the *forecast* step between consecutive

analysis times for which observations are available. In the *forecast* step, the model propagates the *analysed* ensemble members from time t_{k-1} to time t_k following, with integer value k that describes steps in time:

$$\mathbf{x_i}(\mathrm{k}) = \mathbf{M_{k-1}}(\mathbf{x_i^a}(\mathrm{k}-1)) \quad \text{(Eq. 4.2)}$$

where operator $\mathbf{M_{k-1}}$ describes the model simulation, including application of the perturbation factors that are present in $\mathbf{x}$. The ensemble mean x and forecast error covariance $\mathbf{P}$ at time k are expressed as:

$$\mathrm{x} = \frac{1}{\mathrm{N}}\sum_{\mathrm{i}=1}^{\mathrm{N}} \mathrm{x_i} \quad \text{(Eq. 4.3)}$$

$$\mathbf{P} = \frac{1}{\mathrm{N}-1}\sum_{\mathrm{i}=1}^{\mathrm{N}} (\mathrm{x_i}-\mathrm{x})(\mathrm{x_i}-\mathrm{x})^{\mathrm{T}} \quad \text{(Eq. 4.4)}$$

When CrIS observations ($\mathbf{y^{CrIS}}$) are available (at time t_k), the LETKF algorithm *analyses* the ensemble by incorporating the observations to reduce the ensemble spread. The *analysed* ensemble members are computed from:

$$\mathbf{x_i^a} = \mathbf{x_i} + \mathbf{P^a H^T R^{-1}}\,(\mathbf{y^{CrIS}} - \mathbf{h}(\mathrm{x_i}) + \mathbf{v_i}) \quad \text{(Eq. 4.5)}$$

In here, $\mathbf{h}(\mathrm{x_i})$ represents the simulated retrieval from the state $\mathbf{x_i}$, or in particular from the concentration array in $\mathbf{x_i}$ and error $\mathbf{v_i}$. Operator $\mathbf{H}$ is a linearization of $\mathbf{h}(\mathrm{x})$ to x (see section 4.2.4.4.). The matrix $\mathbf{R}$ is the *observation representation error covariance*, which describes the difference between the simulation and the observation due to measurement and representation errors:

$$\mathbf{y^{CrIS}} - \mathbf{h}(\mathrm{x_i}) \sim \mathrm{N}(0, \mathbf{R}) \quad \text{(Eq. 4.6)}$$

The actual implementation of $\mathbf{h}$, $\mathbf{H}$, and $\mathbf{R}$ are described below. The *analysis covariance* $\mathbf{P^a}$ is computed from:

$$\mathbf{P^a} = [\mathbf{P H^T R^{-1} H} + \mathbf{I}]^{-1}\,\mathbf{P} \quad \text{(Eq. 4.7)}$$

4.2.4.2 Observation simulation

The simulated observation vector $\mathbf{h}(\mathbf{x_i})$, representing the simulated retrieval, which is what the satellite observes from the concentrations described in 3-dimensional grid $\mathrm{x_i}$, and is computed from:

$$\mathbf{h}(\mathrm{x_i}) = \mathbf{y_a} - \mathbf{A y_a} + \mathbf{A G}\mathrm{x_i} \quad \text{(Eq. 4.8)}$$

Here, matrix $\mathbf{G}$, the gridding operator, is applied to horizontally and vertically match the simulated partial NH_3 columns in LOTOS-EUROS with the retrieval CrIS pressure levels. Here, air-mass weighted averaging is used to average the model layers to the retrieval levels. The relationship between the true and the retrieved atmospheric NH_3 profiles, i.e., the vertical sensitivity of the CrIS measurements, is described by averaging kernel $\mathbf{A}$. The full relationship between the true and the

observed state is given by $\mathbf{y^{true}} = \mathbf{h}(\mathbf{x^{true}}) + \mathbf{v}$, which can be rewritten to (Eq. 4.9) (Rodgers and Connor, 2003):

$$\mathbf{y^{true}} = \mathbf{y_a} + \mathbf{A}\,(\mathbf{G}\,\mathbf{x^{true}} - \mathbf{y_a}) + \mathbf{v} \qquad \text{(Eq. 4.9)}$$

with $\mathbf{y_a}$ the a-priori profile that is part of the CrIS retrieval product. The error $\boldsymbol{\nu}$ is a sample of the *observation representation error*, taken from a normal distribution, that describes the possible differences between simulation and retrieval:

$$\mathbf{v} \sim N(0,\mathbf{R}) \qquad \text{(Eq. 10)}$$

In this study, $\mathbf{R}$ is set to the retrieval error covariance that is part of the CrIS product. The linearized observation operator becomes:

$$\mathbf{H} = \mathbf{A}\,\mathbf{G} \quad \text{(Eq. 4.11)}$$

4.2.4.3 Analysis per grid cell

The analysis described above is applied per model grid cell; for the exact implementation we refer to Shin et al. (2016). First, the simulated observation vectors $\mathbf{h}(\mathbf{x_i})$ are computed for all ensemble members. For the grid cell to be analyzed, all simulations are collected that are within 3.5ρ distance, where ρ is called the localization length scale as well as the matching actual observations $\mathbf{y^{CrIS}}$. The state elements corresponding to the grid cell are then analyzed using the collected observations and simulations, where the weight of observations further away is limited using Gaussian correlation that decays with distance and that uses the same correlation length scale ρ that is used for collection.

4.2.4.4 Observation selection

CrIS observations with the highest quality flag, QF = 5, were used. These observations have a relatively higher impact because of their low uncertainty. As the assumed vertical NH_3 profile shape in background areas used in the CrIS retrieval and in LOTOS-EUROS differ, CrIS retrievals with "unpolluted" a-priori profiles were filtered out. The original CrIS retrieval is performed in the log domain and therefore either the averaging kernels A from CrIS need to be linearized or the LOTOS-EUROS profiles transformed to the log-domain. Linearization of the kernel is only accurate for higher concentrations, and since this is the case for the selected "polluted" retrievals, this option was found to be suitable.

4.2.4.5 Parameter calibration

In this study, we used a localization radius of ρ = 15 km, a standard deviation of σ = 0.5 and a temporal correlation length of τ = 3 days. Two experiments were performed to study the effect of ρ, σ and τ in more detail. A description of the experiments can be found in section S1 of the supplementary materials. A limited ensemble size of N=12 was found to be sufficient to describe the imposed model uncertainty, which is not too complicated due to short life-time of NH_3 and therefore strong relation between concentrations and nearby emissions.

4.3 Results

4.3.1 Direct comparison of NH_3 concentrations from CrIS and LOTOS-EUROS

Before looking at the effects of assimilating the CrIS observations, a direct comparison of the modelled and observed NH_3 column densities was made. The simulated NH_3 concentrations from the default run in LOTOS-EUROS were sampled at the locations of the CrIS observations, and after application of the averaging kernels compared with the retrievals. The observed and simulated NH_3 total columns averaged over all years are shown in Fig. 4.2. Similar maps per year are available in Fig. S4.3 of the supplementary materials. The general pattern of the NH_3 total column densities matches quite well. For instance, the observed and simulated NH_3 columns are very similar in southwestern Germany, and close to the Dutch border. The CrIS NH_3 total columns are generally higher than the simulated NH_3 total columns. This is for instance found in large parts of northeastern Germany, along the Belgium coast and in the south of the Netherlands. Here, the observed NH_3 columns were on average approximately a factor 2 higher than the simulated NH_3 columns. Moreover, the observed NH_3 total columns are consistently higher than the simulated NH_3 columns in background areas, with a bias between the observed and modelled concentrations of approximately ~0.5×10^{16} molecules/cm^2.

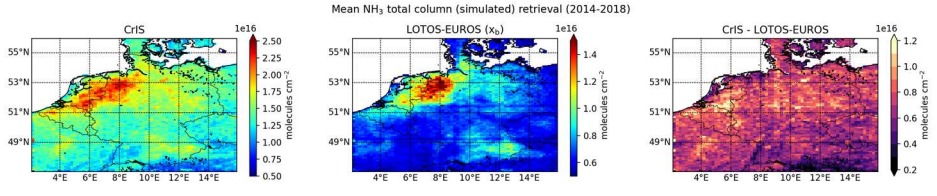

Figure 4.2. *Mean retrieved* ***(left)*** *and simulated* ***(center)*** *NH_3 total column from 2014-2018, and their absolute difference* ***(right)****.*

4.3.2 CrIS-based NH_3 time factors

4.3.2.1 Effect on NH_3 emissions in LOTOS-EUROS

Following the method described in section 4.2.3, temporal profiles for the NH_3 have been obtained per grid cell. Compared to the original model, the new time profiles vary spatially. Fig. 4.3 shows a comparison of the daily grid-averaged NH_3 emissions between the default background model run (x_b) and the background run with the CrIS-based NH_3 time factors ($x_{b,CrIS}$), using a different color for each month. The default NH_3 time factors from MACC-III provide more intra-annual variation than the CrIS-based NH_3 time factors. The default time factors include a very high peak in spring and much lower peaks during summer and autumn (i.e., $A_1/A_3 = 4.57$, $A_1/A_2 = 3.70$). Fig. S4.4 shows the fitted spring parameters (μ_1, σ_1 and A_1). The NH_3 spring peak present in the CrIS-NH_3 surface concentrations is generally lower than the default NH_3 spring peak. In large parts of the model region, the CrIS-observed NH_3 spring peak is subsequently lower and less sharp. Compared to the default NH_3 time factors, the amplitude of the spring peak in the CrIS-based NH_3 time factors is now generally much lower. The amplitude of the spring peak differs almost by a factor 2 on average. As a result, there is a decrease in springtime NH_3 emissions, especially in March and April. The CrIS-based NH_3 time factors, and consequently the NH_3 emissions, are, on the other hand, generally higher later in the year. The NH_3 emissions are on average approximately 50% higher in summer and the beginning of autumn (June to September), and approximately twice as high in October.

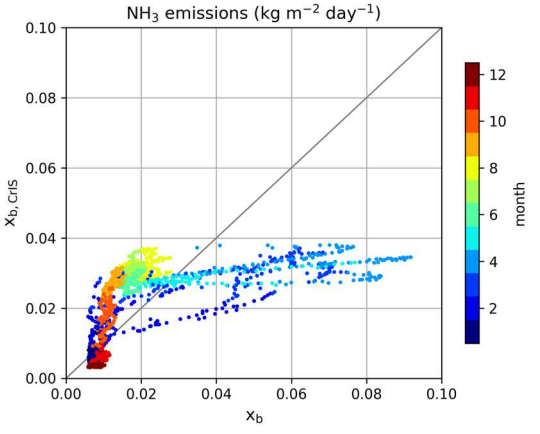

Figure 4.3. *Daily grid-average NH_3 emission, colored per month. Here, x_b represents the default background run and $x_{b,CrIS}$ the background run with CrIS-based NH_3 time factors.*

4.3.2.2 Effect on NH_3 concentrations and deposition fields in LOTOS-EUROS

The changes in modelled NH_3 surface concentration, total column concentrations and NH_x total deposition from 2014 to 2018 related to the use of the CrIS-based NH_3 time factors alone are shown in Fig. 4.4, Fig. S4.5 in the supplementary materials and Fig. 4.5. Here, x_b represents the default background run and $x_{b,CrIS}$ the background run with the CrIS-based NH_3 time factors. The use of the CrIS-based emission time profiles led to an overall increase in mean NH_3 surface concentrations. The absolute change is largest in areas with already relatively high NH_3 surface concentrations, for instance in northwestern Germany, where the mean NH_3 surface concentrations increased with up to 2 $\mu g/m^3$. The mean NH_3 surface concentrations increased with up to ~25% due to the change in NH_3 time factors. The effect of the CrIS-based NH_3 time factors on the NH_3 total column concentrations is smaller, with minor changes from minus ~5% up to 5%. The mean NH_3 total column concentrations generally increase in areas with already high NH_3 concentrations, such as large parts of the Netherlands, and decrease in background areas with little NH_3 emissions, for instance in central Germany. The use of the CrIS-based NH_3 time factors led to ~10% less total NH_X deposition along the northwestern coast, including agricultural hotspots such as the Netherlands and northwestern Germany, and an increase of up to ~10% in background areas.

Fig. S4.6 compares the daily, grid averaged, NH_3 surface concentrations, total column concentrations and NH_x wet and dry deposition, with different colors per month. Here, a similar redistribution is observed for the NH_3 concentration and deposition fields as seen earlier for the NH_3 emission fields. Compared to the default background run (x_b), the NH_3 concentration fields were up to a factor 2 lower during March and April. The NH_3 total columns decreased in spring, the largest decrease occurring in April (up to ~60%). The NH_3 surface concentrations increased during the summer and the beginning of autumn, up to ~50% in September. During these months, a similar but slightly lower increase in the NH_3 total column concentrations is observed.

Because the CrIS-based NH_3 time factors vary per year, the interannual variation in the modelled NH_3 fields is much larger. Fig. S4.7 shows the relative changes in NH_3 surface concentration, total column concentration and NH_x deposition fields per year. Overall, the mean NH_3 surface concentration increases by up to ~30% per year. The largest increases occurred in 2016 and 2018, years with relatively high summer temperatures (Copernicus Climate Change Service, 2021). The variation in the annual mean NH_3 total column concentrations is much smaller (-15 to +15%). The relative change in NH_x budget shows much more variation, with the most prominent increase occurring in 2014 (+25%) and decreases occurring in 2018 (-25%).

The temporal redistribution of the NH_3 emissions thus significantly impacts the modelled NH_3 concentration and deposition fields, too. Generally, a part of the initial spring NH_3 emissions is now attributed to the summer and autumn months. Depending on the degree of redistribution, there are distinct changes in the NH_x budget. Looking at the fitted spring peak parameters (Fig. S4.4) and the matching CrIS-based NH_3 factors at hourly measurement sites (Fig. S4.8), clear interannual differences are observed. For instance, a relatively sharp spring peak was observed over the Netherlands in 2014. In 2018, on the other hand, the fitted spring peak had a distinctly lower amplitude and started later in the year. Moreover, a relatively large rise in NH_3 time factors was observed again in late summer and autumn (July to September). Compared to 2014, this resulted in a relatively larger redistribution of the NH_3 emissions towards warmer months. The higher temperatures resulted in lower dry deposition velocities and more vertical mixing and transport of NH_3, leading to an overall decrease in NH_X deposition over the Netherlands. Moreover, the summer of 2018 was relatively dry, also leading to higher NH_3 total column concentrations and a decrease in wet NH_x deposition.

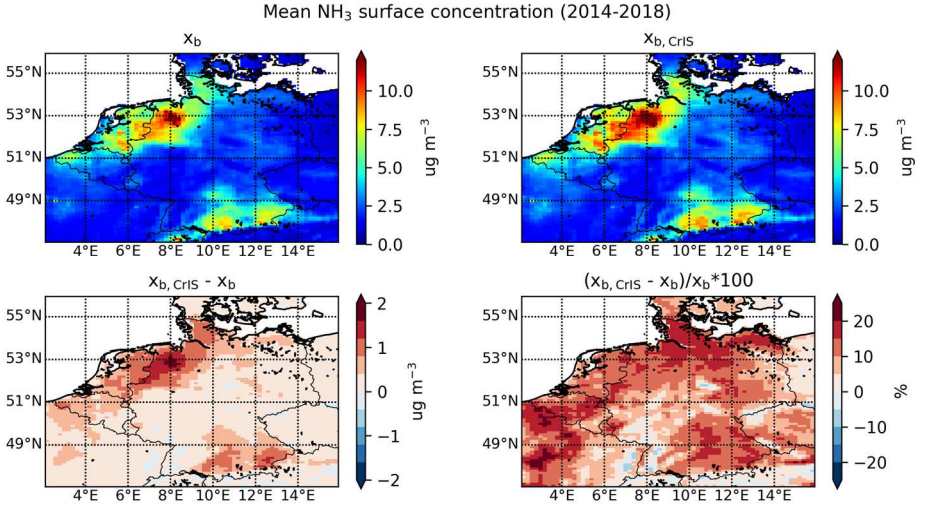

Figure 4.4. *The mean NH_3 surface concentration over 2014 to 2018 from the* ***(top left)*** *default background run (x_b) and the* ***(top right)*** *background run with CrIS-based NH_3 time factors ($x_{b,CrIS}$) and their* ***(bottom left)*** *absolute and* ***(bottom right)*** *relative difference.*

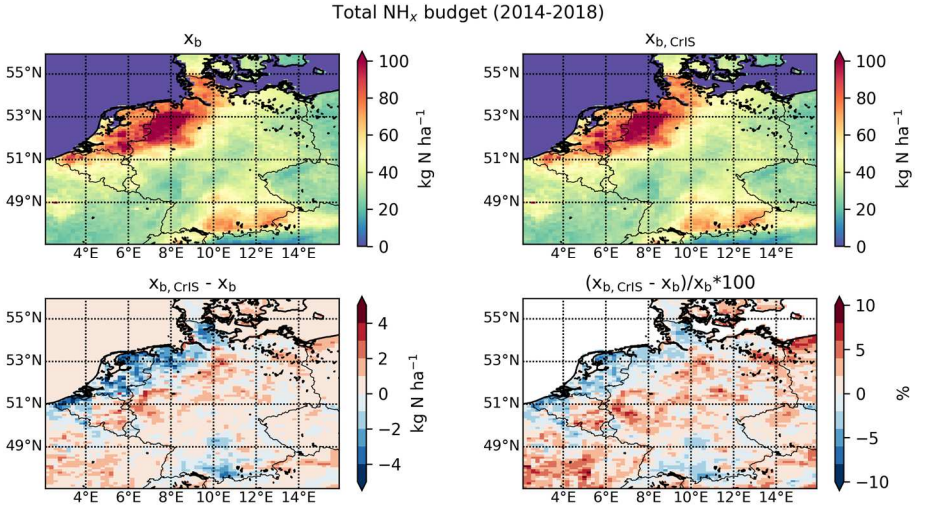

Figure 4.5. *The total NH_x deposition from 2014 to 2018 from the* ***(top left)*** *default background run (x_b) and the* ***(top right)*** *background run with CrIS-based NH_3 time factors ($x_{b,CrIS}$) and their* ***(bottom left)*** *absolute and* ***(bottom right)*** *relative difference.*

4.3.3 Local Ensemble Transform Kalman Filter

4.3.3.1 Effect on NH_3 emissions and concentrations in LOTOS-EUROS

The CrIS-NH_3 columns were assimilated using the Local Ensemble Transform Kalman Filter (LETKF) described in section 4.2.4. Assimilations were performed using either the default emission time profiles (x_a), or using the CrIS-based profiles ($x_{a,CrIS}$). The total NH_3 emissions from 2014 to 2018 and the relative and absolute changes compared to background simulations x_b and $x_{b,CrIS}$ are shown in Fig. 4.6. The corresponding mean NH_3 surface and total column concentrations are shown in Fig. S4.9 and Fig. S4.10 of the supplementary materials. The absolute NH_3 emission updates by the LETKF are, as expected, largest in regions with already high NH_3 emissions. There is a maximum increase of ~30% in total NH_3 emission by the LETKF over the entire period for some grid cells. Relatively, the largest changes are found in the southern parts of the Netherlands (province of Noord-Brabant), the west coast of Belgium (province of West-Vlaanderen), the northeastern parts of Germany and France. Compared to the analysis run using default emission time profiles (x_a), the analysis runs with the CrIS-based NH_3 profiles ($x_{a,CrIS}$) generally have more NH_3 emission and consequently higher NH_3 surface and total column concentrations. The long-term spatial patterns of the emission updates by the LETKF, however, remained very similar.

To study the effect of the LETKF in more detail, the daily grid average NH_3 emissions of the background runs (x_b and $x_{b,CrIS}$) are plotted against analysis runs (x_a and $x_{a,CrIS}$) in Fig. 4.7. Similarly, the NH_3 surface and total column concentrations are plotted in Fig. S4.11 of the supplement. In the runs with the default NH_3 time factors (x_b and x_a), data assimilation of the CrIS-NH_3 columns led to both positive and negative emission updates in spring. In the summer, on the contrary, it mostly resulted in an increase in NH_3 emissions. In the runs with the CrIS-based NH_3 time factors ($x_{b,CrIS}$ and $x_{a,CrIS}$), the pattern is distinctly different. Compared to the default runs, the

NH_3 emission updates in spring are now smaller and largely positive, with the largest updates occurring in April. Moreover, the NH_3 emission updates were generally smaller during summer, too. This is related to the fact that the CrIS-NH_3 surface concentrations were used to fit the NH_3 time factors, which resulted in the model being closer to the CrIS observations already.

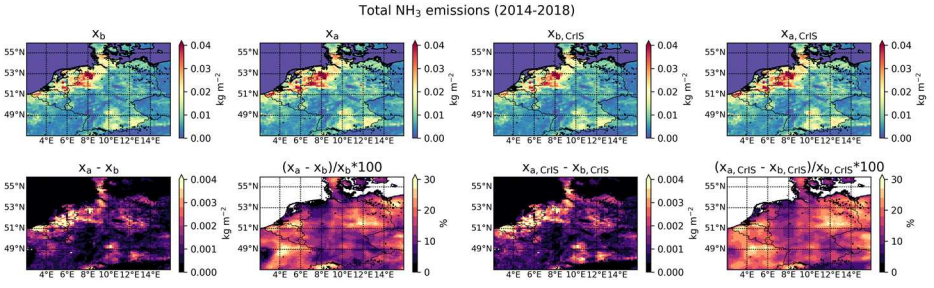

Figure 4.6. *The total NH_3 emissions in 2014-2018 in the background runs x_b and $x_{b,\,CrIS}$ and in analysis runs x_a and $x_{a,CrIS}$* ***(top panels)****, as well as their absolute and relative difference* ***(bottom panels)****.*

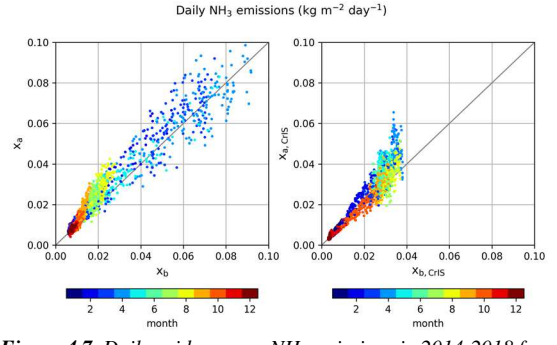

Figure 4.7. *Daily grid average NH_3 emissions in 2014-2018 from the* ***(left)*** *default background run (x_b) versus analysis run (x_a), and from the* ***(right)*** *background run with the CrIS-based NH_3 time factors ($x_{b,\,CrIS}$) versus analysis run $x_{a,CrIS}$, colored per month.*

Perturbation factor β is the computed multiplication factor by which the initial input NH_3 emissions are updated in the LETKF. The mean perturbation factors β per year are shown in Fig. S4.12 of the supplementary materials. The pattern of the NH_3 emission updates does not change drastically between years, which points to a consistent, spatial misdistribution of the emissions in the current inventory. By far the largest mean NH_3 emission updates took place in 2018, followed by 2015. Fig. 4.8 shows timeseries of the daily grid average NH_3 emissions in both background runs x_b and $x_{b,CrIS}$ and analysis runs x_a and $x_{a,CrIS}$. Fig. 4.9 and S4.13 show the corresponding timeseries and changes in NH_3 surface and total column concentrations. The NH_3 emissions in the default background run (x_b) have a strong, annually reoccurring spring peak. After this peak, the NH_3 emissions decrease steeply and then slightly increase again in late summer and autumn (August and September). In analysis run x_a, the spring NH_3 emissions are both positively and negatively adjusted. Later in the year, almost only positive emission updates are found. The largest positive NH_3 emission updates occurred around August and September, which suggests an underestimation of the autumn NH_3 peak in the default runs.

In the background runs with the CrIS-based NH_3 time factors ($x_{b,CrIS}$), the NH_3 emissions are much more evenly distributed over the year. In contrast to the default runs, practically only positive NH_3 emission updates occurred in the analysis run ($x_{a,CrIS}$). The largest NH_3 updates took place during spring (March to May). The flattening of the NH_3 emissions led to a flattening in NH_3 concentration fields, too. Compared to default runs (x_b and x_a), there is much less interannual variation in the NH_3 surface and total column concentrations. As a result, the NH_3 concentrations during summer and autumn could be at the same level or even higher than the springtime concentrations. During the warm summer of 2018 (Copernicus Climate Change Service, 2021), for instance, the NH_3 concentrations in August even clearly exceed the spring NH_3 concentrations.

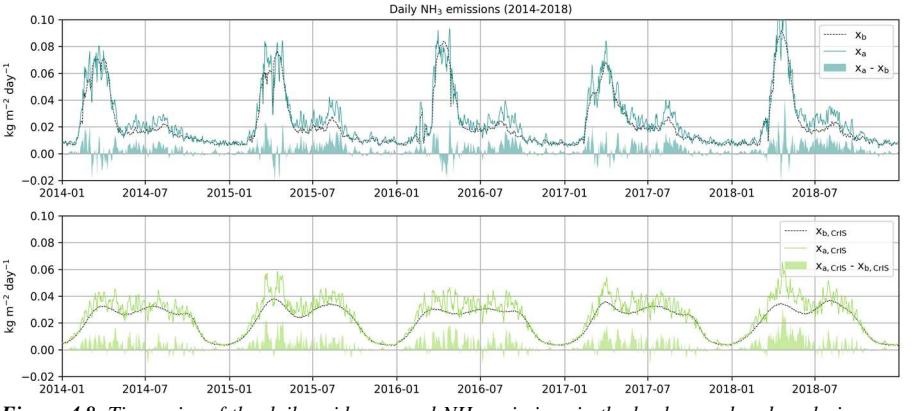

Figure 4.8. *Timeseries of the daily grid-averaged NH_3 emissions in the background and analysis runs, and their absolute difference. The top figure (blue) represents the default background (x_b) and analysis run (x_a). The bottom figure (green) the background ($x_{b,CrIS}$) and analysis run ($x_{a,CrIS}$) with the CrIS-based NH_3 time factors.*

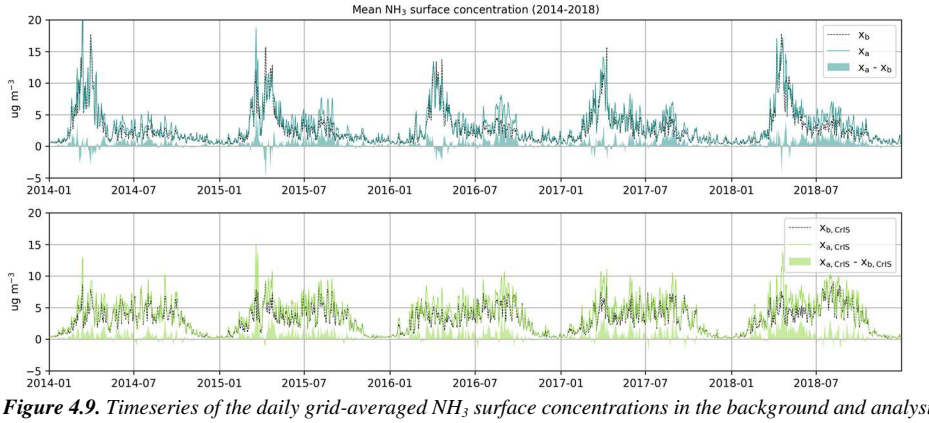

Figure 4.9. *Timeseries of the daily grid-averaged NH_3 surface concentrations in the background and analysis runs, and their absolute difference. The top figure (blue) represents the default background (x_b) and analysis run (x_a). The bottom figure (green) the background ($x_{b,CrIS}$) and analysis run ($x_{a,CrIS}$) with the CrIS-based NH_3 time factors.*

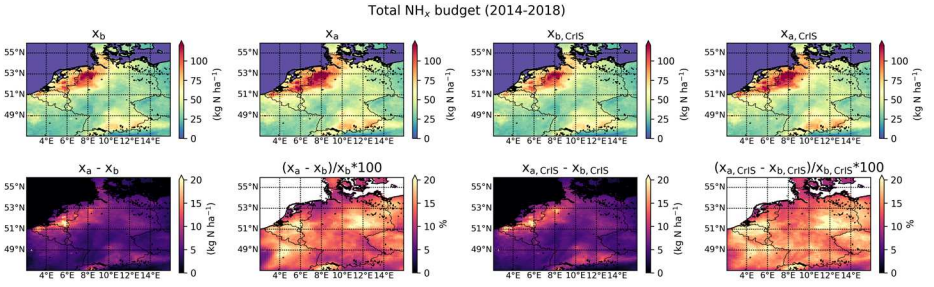

Figure 4.10. *The total NH_x budget from 2014-2018 in the background (x_b and $x_{b,\ CrIS}$) and analysis (x_a and $x_{a,CrIS}$) model runs in LOTOS-EUROS, and their absolute and relative difference.*

4.3.3.2 Effect on NH_x deposition in LOTOS-EUROS

The modelled total NH_x budgets from 2014 to 2018 from the two background runs (x_b and $x_{b,CrIS}$) and analysis runs (x_a and $x_{a,CrIS}$) are shown in Fig. 4.10. Overall, the modelled NHX budget shows the same spatial pattern as the NH_3 emissions. Like the NH_3 emissions, the relatively largest spatial differences between the background and analysis runs took place in the south of the Netherlands, the west of Belgium and northeast Germany. Compared to the default runs, the relative changes in total NH_x budget were slightly larger in the runs with the CrIS-based NH_3 time factors ($x_{b,CrIS}$ and $x_{a,CrIS}$).

The modelled NH_x deposition follows the temporal distribution of the NH_3 emissions, too. Timeseries of the daily wet and dry deposition amounts in the domain are shown in Fig. 4.11. The wet and dry deposition in the default runs (x_b and $x_{b,CrIS}$) versus the analysis runs (x_a and $x_{a,CrIS}$) per month is shown in Fig. S4.14 in the supplement. In the default background run (x_b), the total NH_x deposition peaks in March and April. In the analysis run (x_a), the dry and wet deposition both increased and decreased during spring (March to May). Later in the year, the wet and dry NH_x deposition mostly increased in the analysis run, particularly in August and September. In the background runs with the CrIS-based NH_3 time factors ($x_{b,CrIS}$ and $x_{a,CrIS}$), the modelled dry and wet deposition fields are much less variable. Following the NH_3 emission updates, both the dry and wet deposition mostly increased in the analysis run, especially in March and April. Moreover, the use of the CrIS-based NH_3 time factors resulted in a redistribution of the ratio of wet and dry deposition over the year. As a result of the relatively lower spring NH_3 surface concentrations, there is a reduction of the dry deposition during spring. The relatively higher summer NH_3 total column concentrations led to a shift in wet deposition, too, from spring to summer.

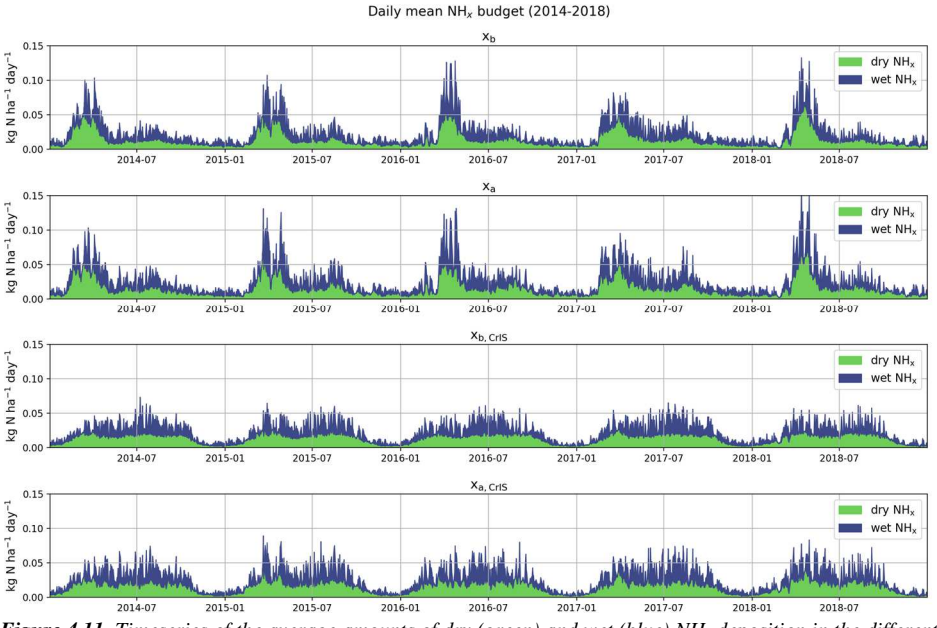

Figure 4.11. *Timeseries of the average amounts of dry (green) and wet (blue) NH_x deposition in the different model runs. The top two figures represent the default background (x_b) and analysis (x_a) run and the bottom two figures the background ($x_{b,CrIS}$) and analysis ($x_{a,CrIS}$) run with the CrIS-based NH_3 time factors.*

4.3.4 Comparison to in-situ observations

The modelled NH_3 surface concentration and NH_4^+ wet deposition fields are compared with in-situ observations. First, the spatial distribution is evaluated by comparing the modelled NH_3 surface concentration and NH_4^+ wet deposition fields to the observed annual averages per measurement site. Second, the temporal distribution is evaluated by comparing the modelled NH_3 surface concentration and NH_4^+ wet deposition fields to the same set of observations, but on a monthly basis. The comparisons are done per type of observation, e.g., all available wet-only measurements simultaneously. To differentiate between different NH_3 emission regimes, the results are plotted separately for either all hourly observations or for the passive samplers. The results are shown in Fig. 4.12 and 4.13. The Dutch site with the highest NH_3 surface concentrations, Vredepeel, is excluded from this comparison because of the large model-observation discrepancies here (see Fig. S4.18). This site is located near agricultural emission sources and therefore less representative of a larger region. In these figures, the first column shows the comparison for the default background run (x_b), the second column shows the background run with CrIS-based NH_3 time factors ($x_{b,CrIS}$), the third column shows the analysis run with the default NH_3 time factors (x_a) and, finally, the fourth column shows the analysis run with CrIS-based NH_3 time factors ($x_{a,CrIS}$).

4.3.4.1 Spatial distribution

Fig. 4.12 shows the scatterplots of the annual averages per site per year. The annual average NH_3 surface concentrations (top row) in the default run x_b show a strong correlation (r = 0.88) with the observed concentrations at the hourly observation sites (LML and UBA). Here, the NH_3 surface concentrations are generally underestimated (slope = 0.61). The annual average NH_3 surface

concentrations (middle row) at the passive sampler sites (MAN, VVM and UBA) are generally overestimated (slope = 1.17), with a lower, but still relatively strong correlation is observed (r = 0.69). The modelled annual average NH_4^+ wet deposition budgets (bottom row) are moderately correlated with the observations from wet-only samplers (r = 0.45), and are generally lower than the observed wet deposition (slope = 0.81). When using the CrIS-based NH_3 time factors, the annual average NH_3 surface concentrations and NH_4^+ wet deposition budgets are slightly increased. This led to a slight, overall increase in slope between all observations and the background run with the CrIS-based NH_3 time factors ($x_{b,CrIS}$). As the annual totals, and herewith the spatial distribution of the NH_3 emissions, remained the same in this run, the other measures (r, RMSE, MAD, MRD, NMB) didn't change drastically on a yearly basis.

The comparison with annual average NH_3 surface concentrations from the passive sampler networks from both analysis runs (x_a and $x_{a,CrIS}$) slightly worsened compared to the background runs (x_b and $x_{b,CrIS}$). The comparison at the hourly observation and wet-only sampler sites, on the other hand, showed clear improvements. Here, virtually all statistical measures improved, illustrating an overall improvement in modelled NH_3 surface concentration and NH_4^+ wet deposition field spatially. Of all runs, the analysis run with the CrIS-based NH_3 time factors ($x_{a,CrIS}$) compared the best with the hourly observation and wet-only sampler network. The differences between the modelled and observed NH_3 surface concentrations at the hourly observation were distinctly smaller, compared to the default background run (x_b: {RMSE = 2.79, MAD = 1.96, MRD = -0.15, NMB = -0.28} versus $x_{a,CrIS}$: {RMSE = 2.2, MAD = 1.69, MRD = -0.11, NMB = -0.08}). Here, also the slope largely improved (x_b: slope = 0.61 versus $x_{a,CrIS}$: slope = 0.76). The same is observed for the modelled NH_4 wet deposition fields, where the slope improved particularly (x_b: {RMSE = 0.95, MAD = 0.63, MRD = -0.13, NMB = -0.22, slope = 0.81} versus $x_{a,CrIS}$: {RMSE = 0.92, MAD = 0.61, MRD = -0.02, NMB = -0.11, slope = 0.95}).

4.3.4.2 Temporal distribution

Fig. 4.13 shows the scatterplots of the monthly means per site. The modelled monthly NH_3 surface concentrations from the default background run (x_b) are strongly correlated with the hourly observation network (r = 0.73), and with the passive sampler network (r = 0.63). Both comparisons show a distinct overestimation of the NH_3 surface concentration in March and April. The observed NH_3 surface concentrations at the hourly observation sites are higher than the modelled ones during the rest of the year. At the passive sampler sites, the observed versus modelled monthly NH_3 surface concentrations during the rest of the year lie more around the one-on-one line. Here, too, the modelled NH_3 surface concentrations are slightly underestimated at the beginning of summer (June and July). The NH_4^+ wet deposition is moderately correlated with monthly observations from wet-only samplers (r = 0.44). At these sites, a similar pattern is observed. The modelled NH_4^+ wet deposition is overestimated in spring (especially March and April), and underestimated during the rest of the year. In general, this comparison indicates an overestimation of the NH_3 spring peak emissions in the default model runs, particularly in March and April, and an underestimation of the NH_3 emission during the rest of the year, mainly during summer (June, July, August).

The use of the CrIS-based NH_3 time factors ($x_{b,CrIS}$) led to an overall improvement at the hourly observation and wet-only sampler sites. Compared to the default background run (x_b), higher correlations and lower differences (RMSE, MAD, MRD, NMB) are observed. At the hourly observation sites, the comparison improved the most (x_b: {r = 0.73, RMSE = 3.67, MAD = 2.67, MRD = -0.22, NMB = -0.27, slope = 0.84} versus $x_{b,CrIS}$:{r = 0.82, RMSE = 2.98, MAD = 2.24, MRD = -0.12, NMB = -0.20, slope = 0.88}). Compared to observations from the passive sampler and wet-only sampler networks, the modelled monthly NH_3 surface concentration and NH_4^+ wet deposition fields now generally lie around the one-on-one line during spring (March, April, May). There is, on the other hand, an overestimation in July and August now. Moreover, as a result of the decrease in CrIS-based NH_3 time factors to zero during winter, the NH_3 surface concentration and NH_4^+ wet deposition in December is underestimated in the $x_{b,CrIS}$ run.

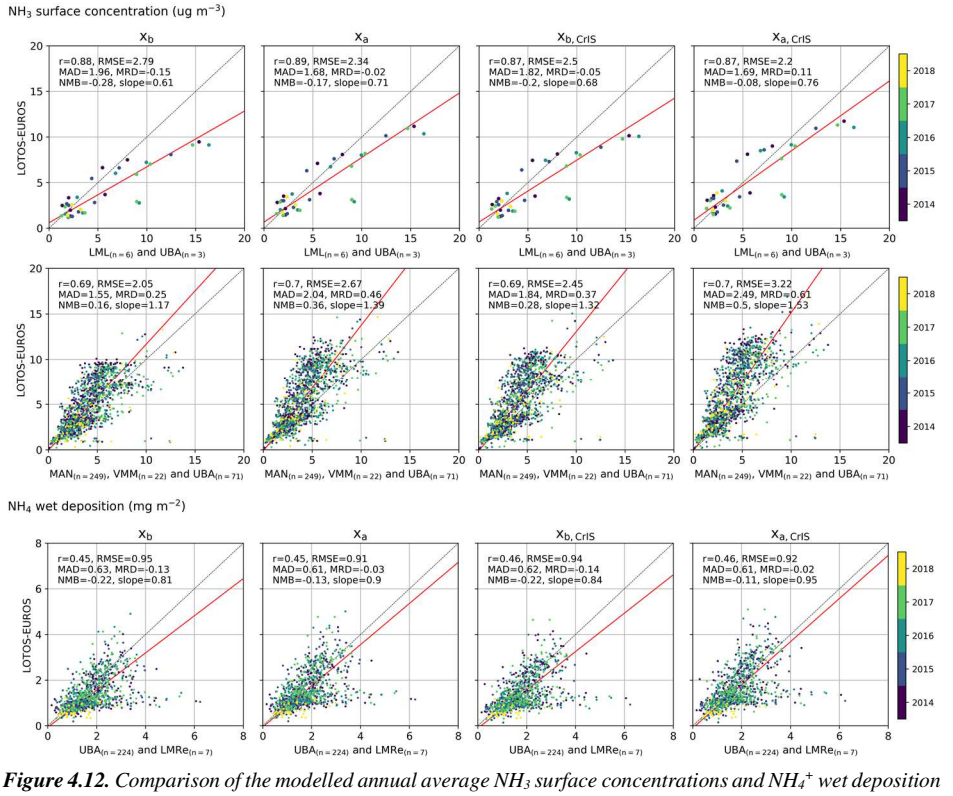

Figure 4.12. *Comparison of the modelled annual average NH_3 surface concentrations and NH_4^+ wet deposition fields to in-situ observations.*

Compared to the background runs (x_b and $x_{b,CrIS}$), the two analysis runs (x_a and $x_{a,CrIS}$) show higher correlations with all types of measurements. The differences (RMSE, MAD, MRD, NMB) between the observed and modelled monthly NH_3 surface concentrations at the passive sampler sites are now, on the other hand, larger in the two analysis runs (x_a and $x_{a,CrIS}$), illustrating an overall overestimation of the NH_3 concentrations in background regions. Although a large shift in the temporal distribution of the monthly NH_4^+ wet deposition is observed, the differences between the observed and modelled values remained similar. At the hourly observation sites, the comparison

improved the most in the analysis run with the CrIS-based NH_3 time factors ($x_{a,CrIS}$). Here, compared to the default background run (x_b), higher correlations and smaller differences were found (x_b: {r = 0.73, RMSE = 3.67, MAD = 2.67, MRD = -0.22, NMB = -0.27, slope = 0.84} versus $x_{a,CrIS}$:{r = 0.83, RMSE = 2.83, MAD = 2.21, MRD = 0.03, NMB = -0.07, slope = 1.0}).

4.3.4.3 Regional patterns

The modelled NH_3 surface concentrations were compared to observations from each passive sampler network separately. Fig. S4.15, S4.16 and S4.17 show comparison with the MAN network in the Netherlands, the UBA network in Germany and the VMM network in Belgium, respectively. In the default background run (x_b), the Dutch sites with relatively higher NH_3 surface concentrations are overestimated, most of which are located along the eastern border of the Netherlands. The highest correlation coefficients and lowest differences (RMSE, MAD) are found at the VMM network in Belgium. Here, the lower NH_3 surface concentration sites are overestimated and the higher NH_3 concentrations sites are underestimated in the default background run (x_b). At the German UBA stations, the comparison lies more around the one-on-one line. The mean NH_3 surface concentrations at the sites close to the western border of Germany are generally overestimated in the default background run (x_b). The use of the CrIS-based NH_3 time factors ($x_{b,CrIS}$) led to an overall increase in modelled mean NH_3 surface concentrations compared to the default background run (x_b). This led to a slight, overall increase in differences (RMSE and MAD) at all networks. Furthermore, steeper slopes were found at all three networks, i.e., the modelled NH_3 surface concentrations increased relatively more at sites with already higher concentrations. The same is observed in the two analysis runs (x_a and $x_{a,CrIS}$), but to a greater extend. Compared to background runs (x_b and $x_{b,CrIS}$), the differences (RMSE, MAD) between the modelled and observed concentrations were relatively higher at all networks. At the Dutch MAN network, a slightly higher correlation coefficient is observed.

Fig. S4.18 of the supplementary materials shows another comparison of the modelled and observed NH_3 surface concentrations at the hourly observation stations at daily resolution. Here, the correlation coefficient, root-mean-squared error RMSE, the mean difference MD and the slope are shown per site. The stations are located in different NH_3 emission regimes and are sorted by increasing NH_3 surface concentrations. The modelled NH_3 surface concentrations in the default background run (x_b) are generally overestimated at stations with low NH_3 emission regimes and underestimated at stations with medium to high NH_3 emission regimes. The use of the CrIS-based NH_3 time factors ($x_{b,CrIS}$) led to an improved comparison (higher correlation coefficient and lower RMSE) at the Dutch stations, but a worse comparison at the German stations. On a monthly basis, the comparison to the German UBA sites slightly worsened after the use of the CrIS-based NH_3 time factors ($x_{b,CrIS}$) (Fig. S4.19). The modelled NH_3 surface concentrations in the background run with the CrIS-based NH_3 time factors ($x_{b,CrIS}$) were, on the other hand, closer to the observations of the Dutch LML network in most months, with a lower differences (RMSE, MD) and slopes closer to 1. Here, the largest increase in correlation coefficients were found in March and April. In both analysis runs (x_a and $x_{a,CrIS}$), the correlation coefficient improved and lower model-observation differences were found at all sites. Here, no clear distinction between sites located in different NH_3 emission regimes can be seen.

Compared to the default background run (x_b), the modelled NH_3 surface concentrations in the background run with the CrIS-based NH_3 time factors ($x_{b,CrIS}$) thus improved the most at Dutch stations located in medium to high NH_3 emission regimes. Most of the Dutch stations are located in the proximity of agricultural hotspots. The German stations, on the other hand, are located in background areas in central Germany, further away from major agricultural hotspots for NH_3. Fig. S4.8 of the supplementary materials shows the fitted CrIS-based NH_3 time factors at each site. The fitted NH_3 time factors at the majority of the Dutch stations show clear, identifiable peaks, in particular the spring peak. Moreover, most Dutch sites show clear year-to-year variations. For the German stations, on the other hand, the fitted NH_3 time factors are much flatter and show much less interannual variation. This indicates that the observed CrIS-NH_3 surface concentrations at these locations remained around the same level, and thus that no clear (inter)annual patterns were present in the CrIS data.

In the Netherlands, the CrIS-based NH_3 time factors led to an improvement in the representation of the NH_3 spring peak. A time-series of the observed daily NH_3 surface concentrations at LML sites Valthermond and Zegveld are plotted in Fig. S4.20 of the supplementary materials. The modelled NH_3 surface concentrations in the default background run (x_b) start to rise too early in the year, particularly in 2014. In the background run with the CrIS-based NH_3 time factors ($x_{b,CrIS}$), both the start and the duration of the spring peak in NH_3 concentration improve. Here, the onset of the spring peak is delayed, better matching the observed NH_3 timeseries.

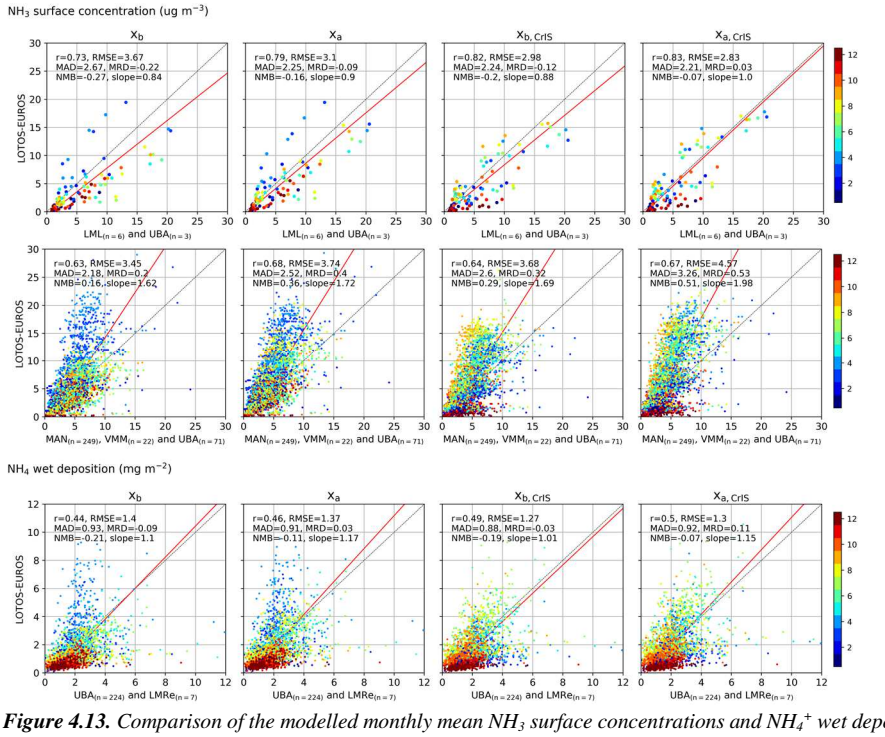

Figure 4.13. *Comparison of the modelled monthly mean NH_3 surface concentrations and NH_4^+ wet deposition fields to in-situ observations. The colors indicate the month.*

4.4 Summary and discussion

4.4.1 Summary

In this study, the CrIS-NH_3 product is integrated into the LOTOS-EUROS chemical transport model using two different methods. In the first method, the CrIS-NH_3 surface concentrations were used to fit spatially varying NH_3 time factors to redistribute the NH_3 emission inputs in LOTOS-EUROS over the year. In the second method, the CrIS-NH_3 columns were assimilated to adjust NH_3 emissions through local Ensemble Transform Kalman filtering in a top-down approach.

The fitted NH_3 time factors based on the CrIS-NH_3 surface concentrations led to a major temporal redistribution of the NH_3 emissions. In most regions, the updated NH_3 time profiles became flatter, with an overall decrease in spring (March to May) NH_3 emissions and an increase in NH_3 emissions in June to October. As a result, the mean modelled NH_3 fields between 2014 and 2018 spatially changed by up to +25% in NH_3 surface concentrations, -5 to +5% in NH_3 total column concentrations and -5 to +5% in NH_x budget. The CrIS-based NH_3 time factors added an extra interannual variation of up to ±25% in the annual mean NH_3 concentrations and deposition fields. Data assimilation of the CrIS-NH_3 columns with the LETKF led to a unanimous increase in total NH_3 emissions. The modelled NH_3 fields between 2014 and 2018 changed with up to +30% in NH_3 surface concentrations, up to +20% in NH_3 total column concentrations and +10 to +25% in NH_x budget. The largest increases in NH_3 emissions (+30%) were found over the south of the Netherlands (Brabant), the west of Belgium (West-Vlaanderen) and a large region in northeastern Germany. The temporal distribution of the NH_3 emissions wasn't largely adjusted by the LETKF. The largest positive NH_3 emission updates took place in late summer and the beginning of autumn (July to September) and both increases and decreases in NH_3 emissions were observed in spring (March to May).

The modelled NH_3 surface concentration and NH_4^+ deposition fields were compared to in-situ observations. The statistics are summarized in Table 4.2. Our results illustrate that the strength of the first method, i.e., CrIS-based NH_3 time factors, primarily lies in improving the temporal distribution of the NH_3 emissions. Compared to in-situ networks, an overall increase in correlation coefficient and clear decrease in differences (RMSE, MAD, MRD, NMB) at the hourly observation and the wet-only sampler sites was observed. Moreover, time-series of observed daily NH_3 surface concentrations illustrate that using the CrIS-based NH_3 time factors resulted in a better representation of both the onset and duration of the spring NH_3 peak in the Netherlands. The second method, data assimilation of the CrIS-NH_3 columns with the LETKF, improved the comparability to in-situ observation both spatially and temporally. Here, higher correlations with both annual and monthly observed mean NH_3 surface concentrations and NH_4^+ wet deposition were observed. This method also led to a decrease in differences (RMSE, MAD, MRD, NMB) at the hourly observation and the wet-only sampler sites. The mean NH_3 surface concentrations at the passive sampler sites, on the other hand, were more strongly overestimated in both methods. The comparison to in-situ observations improved the most, both spatially and temporally, in the run where both methods are combined ($x_{a,CrIS}$). This illustrates that an initial, observation-based, rescaling of the NH_3 emissions enhances the adaptability of the LETKF, herewith thus improving the modelled NH_3 surface concentration and NH_4^+ wet deposition fields.

Table 4.2. *Summary of the computed statistics (correlation coefficient (r), root mean square error (RMSE), mean absolute difference (MAD), mean relative difference (MRD), normalized mean bias (NMB) and slope) for each type of instruments from Figure 4.12 and 4.13.*

		hourly observations				**passive samplers**				**wet-only samplers**			
		x_b	x_a	$x_{b,cris}$	$x_{a,cris}$	x_b	x_a	$x_{b,cris}$	$x_{a,cris}$	x_b	x_a	$x_{b,cris}$	$x_{a,cris}$
annual mean	r	0.88	**0.89**	0.87	0.87	0.69	**0.70**	0.69	**0.70**	0.45	0.45	**0.46**	**0.46**
	RMSE	2.79	**2.34**	2.50	2.20	**2.05**	2.67	2.45	3.22	0.95	**0.91**	0.94	0.92
	MAD	1.96	**1.68**	1.82	1.69	**1.55**	2.05	1.84	2.49	0.63	**0.61**	0.62	**0.61**
	MRD	-0.15	**-0.02**	-0.05	0.11	**0.25**	0.46	0.37	0.61	-0.13	-0.03	-0.14	**-0.02**
	NMB	-0.28	-0.17	-0.20	**-0.08**	**0.16**	0.36	0.28	0.50	-0.22	-0.13	-0.22	**-0.11**
	slope	0.61	0.71	0.68	**0.76**	**1.17**	1.39	1.32	1.53	0.81	0.90	0.84	**0.95**
monthly mean	r	0.73	0.79	0.82	**0.83**	0.63	**0.68**	0.64	0.67	0.44	0.46	0.49	**0.50**
	RMSE	3.67	3.10	2.98	**2.83**	**3.45**	3.74	3.68	4.57	1.40	1.37	**1.27**	1.30
	MAD	2.67	2.25	2.24	**2.21**	**2.18**	2.52	2.60	3.26	0.93	0.91	**0.88**	0.92
	MRD	-0.22	-0.09	-0.12	**0.03**	**0.20**	0.40	0.32	0.53	-0.09	**0.03**	**-0.03**	0.11
	NMB	-0.27	-0.16	-0.20	**-0.07**	**0.16**	0.36	0.29	0.51	-0.21	-0.11	-0.19	**-0.07**
	slope	0.84	0.90	0.88	**1.00**	**1.62**	1.72	1.69	1.98	1.10	1.17	**1.01**	1.15

4.4.2 Discussion

4.4.2.1 CrIS-based NH_3 time factors

The temporal redistribution of the NH_3 emissions after using the fitted CrIS-based NH_3 time factors led to a significantly better representation of the temporal variation in NH_3 emissions, especially the spring peak. Compared to in-situ observations, however, the NH_3 surface concentrations were overestimated in late summer and autumn (August to October). Further fine-tuning of the fitting algorithm could help to reduce the current overestimation and potentially improve the fitted NH_3 time factors. For example, data filtering and selection criteria could be adapted. Narrowing the selection radius used for selecting the CrIS-NH_3 observations could for instance lead to a better representation of the NH_3 concentrations locally. This, however, may not always be possible, as a minimum number of observations is needed for a converging fit. Furthermore, the fitting algorithm currently doesn't allow for NH_3 area emissions during winter, because of the limited number of available CrIS observations at this time. As a result, the fitted NH_3 time factors show a relatively steep increase at the beginning of spring and a decrease at the beginning of winter. This could lead to step-like functions in areas where clear NH_3 peaks in the CrIS-NH_3 data are absent. However, as this mainly occurs in areas with little to no NH_3 emissions, this shouldn't severely impact the modelled NH_3 concentrations in this study.

4.4.2.2 Local Ensemble Transform Kalman Filter

The NH_3 emission updates computed by the Local Ensemble Transform Kalman Filter (LETKF) always remain tied to the initial model fields by a certain uncertainty range. As such, data assimilation of the CrIS-NH_3 columns with the LETKF is mainly suitable for fine-tuning NH_3 emissions in regions where the NH_3 emissions are already relatively well known. The chosen

LETKF configuration is for instance not able to correct for missing NH_3 emissions in areas where little or no initial NH_3 emissions are present. Furthermore, the LETKF is unable to resolve temporal patterns well without sensible input, as was illustrated in an experiment with homogeneous NH_3 emission fields (supplement section S1).

The LETKF filter settings used in this modelling setup (ρ = 15 km, σ = 0.5, τ = 3 days) led to a maximum emission increase of roughly ~30% on the initial NH_3 emissions for long-term simulations. The choice of these filter settings affects the adaptability of the LETKF, i.e., the achievable emission adjustments by correction factors. In this study, a temporal length scale τ of 3 days was chosen as a compromise between short time scales needed for irregular emissions (e.g., fertilizer application) and longer time scales needed for regular emissions (e.g., stables and other point sources). Moreover, it matches the average satellite revisiting time per grid cell given the number of CrIS-NH_3 observations left after data selection (Fig. S4.21). A spatial correlation of ρ = 15 km was chosen because it matches the footprint size of the satellite. Furthermore, as shown in section S1 in the supplement, increasing standard deviation σ leads to larger, positive β factors. To prevent further overestimations in background regions, a σ of 0.5 was used for this region.

The current LETKF settings could for instance be improved by using spatially varying τ values. The choice of τ could be optimized for each emission category in the model. Locations with fertilizer application as dominant NH_3 emission source could for instance be set to lower τ values than locations with predominantly regular NH_3 sources. Another way to optimize the filter settings would be to study timeseries of the model-satellite discrepancies in more detail and base the choice of τ on this. A more apparent memory effect (i.e., higher τ) would be useful in areas with consistent model-satellite discrepancies, whereas in areas with incidental differences a lower τ would be more appropriate. Similarly, statistical analysis of the already computed emission perturbation factors β could be performed. In this study, the model uncertainty follows a normal distribution in the current model setup. The distribution of the NH_3 concentrations, however, is, in reality, better approximated by a log-normal distribution. It would therefore be more realistic to use a log-normal distribution for the model uncertainty as well. This would incidentally allow for larger correction factors when high NH_3 peaks are observed, for instance after fertilizer application. In the current LETKF model setup, only the NH_3 emissions are perturbed. Thus, the discrepancies between the observed and modelled NH_3 concentrations are currently thus fully assigned to errors in the underlying model NH_3 emissions. However, other model uncertainties could also cause these discrepancies, for instance uncertainties in other model inputs (e.g., other trace gas emissions) or parameterizations (e.g., deposition routines). In a follow-up study, it would be interesting to further investigate to the effect of an inverted LETKF setup, where model sink terms are perturbed instead of the source terms. However, the current setup is the most obvious as the NH_3 emissions are likely the largest source of model uncertainty in this area. It would also be interesting to assimilate in-situ observations and/or other satellite products (for instance IASI-NH_3) simultaneously in a follow-up study.

4.4.2.3 Data products

Direct comparison of the observed and simulated NH_3 columns showed distinctly lower NH_3 total column concentrations in LOTOS-EUROS. This discrepancy could be the result of a systematic underestimation of the input NH_3 emission in LOTOS-EUROS, or other model uncertainties. It could, on the other hand, also be partially related to the CrIS observations themselves. Here, only

CrIS observations with the highest quality flag (QF=5) were used, which for instance could have resulted in a bias towards observations with higher NH_3 concentrations or during good weather (e.g., no clouds), as these observations usually have a lower uncertainty. Moreover, an offset of approximately ~$0.5x10^{16}$ molecules/cm^2 is observed. This seems to be the effect of the detection limit of the CrIS instrument, which is unable to detect very low NH_3 concentrations. Furthermore, this, too, could be enhanced by the relatively strict data selection criteria used in this study, which favors higher NH_3 concentrations that usually have a lower uncertainty. In the next version of the CrIS-NH_3 product, which was not yet available for this study, these non-detects are addressed. This might lead to lower NH_3 concentrations in background regions and partially solve this discrepancy. Moreover, this could also result in a better comparison with observations of the passive sampler networks.

The differences between the modelled and observed NH_3 concentrations and NH_4^+ wet deposition fields are partially related to limitations in the spatial representativeness of the in-situ observations. The comparison of the different model runs to in-situ observations showed an overall overestimation at the passive sampler sites. These sites are mainly located in nature areas and therefore assumed to be representative of background regions with little to no NH_3 emissions. However, especially in the Netherlands, the landscape layout is very heterogenous and the nature areas are relatively small. As a result, at the current model grid size, each model pixel is likely to include other landscape elements than nature alone. The larger model scale averages out the small-scale effects, thus leading to an overestimation. The opposite is true for the hourly observation sites located in medium to high NH_3 emission regimes. Especially at sites close to NH_3 emission sources, an underestimation is expected.

4.4.2.4 Conclusions

To conclude, satellite observed CrIS-NH_3 timeseries are helpful in improving NH_3 emissions, both spatially and temporally. Our results illustrated that CrIS-NH_3 surface concentrations can be successfully used to fit spatially variable NH_3 time factors, which allows us to improve temporal NH_3 emission distributions relatively easy in a forward modelling setup. Comparison with in-situ NH_3 surface concentrations and NH_4^+ wet deposition observations showed that the fitted CrIS-based NH_3 time factors were particularly useful for adjusting the timing and duration of the NH_3 spring peak in medium to high NH_3 regimes. Moreover, the comparison showed that the CrIS-based NH_3 time factors improve the temporal distribution of the modelled NH_3 surface concentrations and NH_4^+ wet deposition fields. Our results show that data assimilation of the CrIS-NH_3 columns data with the Local Ensemble Transform Kalman Filter (LETKF) improves the comparability with in-situ observations both spatially and, to a lesser extent, temporally, too. As the adaptability of the LETKF is limited by the uncertainty in the modelled fields, the strength of this method primarily lies in fine-tuning pre-existing NH_3 emission patterns. As a result, this method proved particularly useful for improving spatial NH_3 distributions in long-term simulations. Moreover, our results illustrated that combining both methods enhanced the adaptability of the LETKF, and led to the largest improvements in modelled NH_3 surface concentration and NH_4^+ wet deposition fields compared to in-situ observations.

Acknowledgements. The authors acknowledge the Nederlandse Organisatie voor Wetenschappelijk Onderzoek (NWO). This project was funded by the NWO under project number ALW-GO/16-05 The authors would like to thank the Rijksinstituut voor Volksgezondheid en Milieu (RIVM), the Vlaamse Milieumaatschappij (VVM) and the Umweltbundesambt (UBA) for providing observations of the NH_3 surface concentrations and NH_4^+ wet deposition.

Chapter 5: Nitrogen deposition shows no consistent negative nor positive effect on the response of forest productivity to drought across European FLUXNET forest sites.

Abstract. Atmospheric reactive nitrogen (N) deposition is an important driver of carbon (C) sequestration in forest ecosystems. Previous studies have focused on N-C interactions in various ecosystems; however, relatively little is known about the impact of N deposition on ecosystem C cycling during climate extremes such as droughts. With the occurrence and severity of droughts likely to be exacerbated by climate change, N deposition – drought interactions remain one of the key uncertainties in process-based models to date. This study aims to contribute to the understanding of N deposition-drought dynamics on gross primary production (GPP) in European forest ecosystems. To do so, different soil water availability indicators (*Standardized Precipitation Evapotranspiration Index (SPEI), soil volumetric water*) and GPP measurements from European FLUXNET forest sites were used to quantify the response of forest GPP to drought. The computed drought responses of the forest GPP to drought were linked to modelled N deposition estimates for varying edaphic, physiological, and climatic conditions. Our result showed a differential response of forest ecosystems to the drought indicators. Although all FLUXNET forest sites showed a coherent dependence of GPP on N deposition, no consistent or significant N deposition effect on the response of forest GPP to drought could be isolated. The mean response of forest GPP to drought could be predicted for forests with *Pinus* trees as dominant species (R^2 = 0.85, *RMSE* = 8.1). After extracting the influence of the most prominent parameters (*mean annual temperature and precipitation, forest age*), however, the variability remained too large to significantly substantiate hypothesized N deposition effects. These results suggest that, while N deposition clearly affects forest productivity, N deposition is not a major nor consistent driver of forest productivity responses to drought in European forest ecosystems.

A revised version of this chapter is accepted for publication: van der Graaf, S.C., Janssen, T.A. J., Schaap, M., and Erisman, J.W.: Nitrogen deposition shows no consistent negative nor positive effect on the response of forest productivity to drought across European FLUXNET forest sites, Environ. Res. Commun., in press, https://doi.org/10.1088/2515-7620/ac2b7d, 2021.

5.1 Introduction

5.1.1 Nitrogen-carbon interactions

Terrestrial ecosystems have the potential to take up significant amounts of carbon dioxide from the atmosphere through photosynthesis and growth and thereby mitigate climate change. As the sequestration of carbon (C) in terrestrial ecosystems predominantly occurs in forest ecosystems (Pan et al., 2011), forests largely drive the terrestrial C balance. The compound effect of many interacting drivers determines whether a forest is a net sink of C (i.e., taking up C from the atmosphere over multi-year timescales) or a net source of C (i.e., releasing C to the atmosphere over multi-year timescales). These drivers include edaphic and climatic factors such as soil nutrient and moisture conditions and air temperature and humidity. Drought, fires and outbreaks of insect herbivores and fungal pathogens can reduce forest productivity for many years and can also cause widespread forest mortality (e.g., Anderegg et al. 2020). On the other hand, some factors can potentially increase ecosystem carbon storage, such as CO_2 fertilization, ozone exposure, nitrogen (N) deposition and forest management.

Earth system models (ESMs) can be used to quantify and predict ecosystem responses to a changing climate and the feedbacks involved. However, ESMs are known to involve large uncertainties in terrestrial C feedbacks (Friedlingstein et al, 2014). These uncertainties partially result from a lack of knowledge of the physical and biogeochemical processes responsible for these C cycle feedbacks. Furthermore, we know relatively little about ecosystem responses to multiple, simultaneous stressors and their interactions, as most studies to date focus on the effect of one single stressor on plant growth. The impact of co-stressors is highly variable across ecosystems and, currently, ESMs are ill-equipped to model these interactions (Drewniak and Gonzalez-Meler, 2017). One key example is the interplay between increased nitrogen (N) deposition and drought. With the frequency and intensity of droughts likely to increase globally as a result of climate change (Seneviratne et al., 2012), and N deposition projected to increase to 88 Tg N yr^{-1} by 2100 under representative concentration pathway (RCP) 8.5 scenario (Lamarque et al., 2013), understanding the effects of N deposition-drought interactions on forest productivity becomes increasingly important. N deposition-drought interactions are found to be interdependent and non-additive and remain one of the least quantified processes that vary locally and therewith one of the major uncertainties in ESMs to date (Drewniak and Gonzalez-Meler, 2017).

Our objective is to contribute to understanding the variability of combined N deposition – drought interactions on C dynamics in forest ecosystems by (1) quantifying the effect of different types of drought on the gross primary production (GPP) from FLUXNET observations at European forest sites, and (2) linking these responses to different levels of N deposition for different forest types, climate zones and soil types.

5.1.2 Forest response to N deposition

Nitrogen (N) is an important nutrient in ecosystems and critical for driving photosynthesis and growth (Evans 1989; Fernández-Martínez, M. et al. 2014; Oren, R. et al. 2001). Forest growth in temperate and boreal forest ecosystems is generally limited by N availability (Fischer et al, 2012), and N deposition is, therefore, an important driver of forest growth in these ecosystems. The three main effects of N deposition on ecosystems are changes in foliar or leaf N, changes in biomass partitioning and increases in biomass N (Bobbink et al., 2010). Reactive nitrogen (N) emissions have substantially increased during the last century, causing enhanced atmospheric N deposition

on forest ecosystems (Dentener et al., 2006; Lamarque et al. 2013). With most forest ecosystems being N limited, this has resulted in significantly increased net primary production (NPP) and subsequently carbon (C) sequestration in trees (e.g. (Thomas et al., 2010; De Vries et al., 2009)).

Several studies have found increases in foliar N and, as a consequence, decreases in C:N ratios in leaves under elevated N deposition (e.g. (Pregitzer et al., 2008; Elvir et al., 2005; Boggs et al., 2005)). Increases in foliar N are often associated with increases in aboveground net primary production (ANPP) (Pregitzer et al., 2008) as foliar N is generally found to be linearly and positively related to leaf photosynthetic capacity (Xue et al. 2016). Under elevated N availability, the ANPP may also increase because of reductions in N use efficiency and C allocation shifts away from mycorrhizae, leaving more C available for growth (Talhelm et al., 2011).

Gains in forest productivity from increased N deposition may lead to an increase in litter production, which may ultimately lead to an increase of N mineralization in soils. Moreover, increased productivity in trees may result in higher C sequestration in soil due to higher soil C inputs by litterfall and reduction of organic matter decomposition (Lu et al, 2011, Janssens et al., 2010). The increase in forest productivity is often correlated with an increase in aboveground biomass (e.g. (Pregitzer et al., 2008; Quinn Thomas et al, 2010)), resulting from changes in C partitioning in trees. Most of this increase in aboveground biomass is allocated to stems (Pregitzer et al., 2008; de Vries et al., 2014), and generally resulting in faster biomass accumulation and taller, thinner trees. However, the increase in growth varies largely among different tree species. Needle-leaved boreal forests, for instance, have higher C/N ratios in all compartments and show a lower C-N response and N use efficiency than deciduous and evergreen broadleaved forests in temperate regions (de Vries et al., 2014).

The C-N responses of forest ecosystems are non-linear and vary with N input level and time. At high and chronic N deposition rates, forest ecosystems will become N saturated. N loss rates by leaching, runoff and denitrification will increase, leading to a decrease in N retention (de Vries et al., 2014). Forest growth is initially stimulated by low levels of N deposition, as N limitations for growth diminish. At higher N deposition levels, when the ecosystem starts to become N saturated, the stimulating effect may decline and even reverse due to soil acidification and nutrient imbalances (Aber et al., 1998).

N deposition can also lead to an increase in forest biomass N. Eventually, this extra N will flow from the canopy into the litter pool, where it can cause faster decomposition (Zhu et al., 2015) and enhanced N mineralization to the forest floor. At low external N inputs, the breakdown of organic C due to microbial activity is stimulated, increasing respiration. This stimulating effect diminishes completely, however, after ecosystems start to become N saturated, due to N-induced microbial community and decomposing enzyme shifts, resulting in a reduction of forest soil respiration (Janssens et al., 2010).

Modelling studies estimated that approximately 24% of the global historical C sink (between 1900–2006) was driven by N deposition effects (Fleischer et al., 2015) and that N deposition accounts for the additional storage of approximately 175 Pg C in forests since pre-industrial times (Bala et al., 2013). It is estimated that N deposition currently increases the global forest C sink by around 276 to 448 Tg C yr^{-1} (De Vries et al., 2014). Quantification of stimulation of forest growth

as the result of nitrogen deposition, is still under discussion (Ehtesham and Bengtson, 2017), with estimates of net ecosystem production (NEP) being simulated at rates of 30–75 kg C per kg N down to 16 kg C per kg N (e.g. Butterbach-Bahl et al. 2011). A recent meta-analysis showed the difference between old and younger forest with a factor of 5 for the stimulation of aboveground woody production, but also low productivity forests respond more strongly than high productivity forests, (Schulte-Uebbing and de Vries, 2017).

Excess amounts of N deposition, on the other hand, can also cause nitrate leaching, reductions in forest biodiversity and may ultimately lead to growth reductions by N saturation (Bobbink at al., 2010). N deposition thus significantly influences the response of forest ecosystems, and consequently plays a vital role in understanding the long-term response of forests to the effects of climate change (increased CO_2 levels, elevated temperatures and changes in water availability) (De Vries et al., 2009).

5.1.3 Forest response to drought

The response of forest ecosystems to drought depends on various factors, including the sensitivity of dominant tree species to drought, soil characteristics -especially those related to soil water retention and rooting depth-, the climatic zone and the severity of the particular drought (e.g. (Schwalm et al., 2010; von Buttlar et al., 2017)). Generally, two mechanisms are identified through which plants are negatively impacted by drought, carbon starvation and hydraulic failure. Carbon starvation and hydraulic failure can co-occur and both mechanisms generally result in lower C assimilation and may ultimately lead to tree mortality (Sevanto et al. 2011). Carbon starvation can occur when leaf stomata close to constrain water losses, also impairing the diffusion of CO_2 into the leaf and thereby limiting C assimilation. Reduced C assimilation results in fewer carbohydrates available for growth and maintenance and may ultimately lead to serious tissue damage if existing C reserves are insufficient to sustain plant maintenance requirements. Hydraulic failure occurs when xylem functioning is partially or completely lost through xylem embolism, which inhibits water and nutrient transport from the roots to the leaves and leads to tissue desiccation (Adams et al., 2017, McDowell et al., 2008).

The drought tolerance of trees depends on many morphological and physiological traits and drought response mechanisms, such as stomatal control, hydraulic redistribution, tissue desiccation tolerance or allometric plasticity (Baker et al., 2008). To withstand droughts, trees may also reduce C demand for instance by leaf senescence or down-regulation of respiration (Sala et al., 2010). The effects forest may experience under droughts include changes in C availability, mobilization and transport, increases in N limitation and changes in biomass partitioning (Drewniak and Gonzalez-Meler, 2017).

Stomatal closure or leaf senescence during droughts may lead to lower C availability and a higher N limitation. Stomata closure reduces photosynthesis and may lead to lower litter production and N mineralization in the soil over long periods, which in turn may lead to additional N limitations (Schimel et al., 2007). Moreover, low soil moisture levels during droughts reduce nutrient flow and diffusion in soils, resulting in additional nutrient limitations, which may reduce photosynthesis levels even further. As a response to the early stages of drought, trees have shown to increase the root-to-shoot ratio to maintain transpiration. Several studies have found changes in C partitioning in trees following droughts, such as translocation of carbohydrates to roots and increases in root-

to-leaf biomass production (e.g. (Hanson et al., 2007; Hertel et al., 2013)). Trees may also alter morphological traits of their roots to help fulfil water demands in response to drought (Meier et al., 2008). Furthermore, certain trees can extend root systems to deep soil layers or to redistribute water through the soil column via hydraulic redistribution (Hanson et al., 2007). Hydraulic redistribution can effectively transfer water upwards into dry soil layers, and even move water deeper into the soil to be protected from evaporation or competition. These mechanisms may prevent hydraulic failure in trees by maintaining water potential above the failure limits.

The frequency, severity and timing of a drought plays an important role in the magnitude of a forest productivity response to drought. Over shorter time scales, stomata regulate water loss and can result in a decline of photosynthesis. Over longer time scales, frequent but less severe droughts may on the other hand increase forest drought tolerance as changes in tree physiology may occur that optimize hydraulic conductance (Martin-StPaul et al., 2013). The time scale at which forest growth responds to drought reflects its ability to cope with water deficits and is a proxy for drought vulnerability. The period between water shortage and impact on growth differ among different forest types and climate zones. For example, forests located in semi-arid and sub-humid areas tend to respond over longer time-scales than forests located in humid areas. Some forests may not respond to drought at all, for example, forests located in very cold and humid areas (Vicente-Serrano et al., 2014). The timing of drought also plays a key role in forest response. Droughts coinciding with peak growth periods will for instance likely result in a stronger response of forest C uptake and higher tree mortality.

The response to drought varies strongly among different tree species. For example, in angiosperms, European beech (*Fagus sylvatica*) is generally found to be more vulnerable to drought-induced growth reductions compared to European oak (*Quercus robur*) (van der Werf et al., 2007, Scharnweber et al, 2011). In gymnosperms, Norway spruce (*Picea abies*) is found to be more drought vulnerable in terms of radial growth compared to black pine (*Pinus nigra*) and Douglas fir (*Pseudotsuga menziesii*) due to its relatively shallow rooting depth (Lévesque et al., 2014). Pine species (*Pinus spp.*), for example, Scots pine (*Pinus sylvestris*) and the Maritime pine (*Pinus pinaster*) are generally considered more drought-tolerant, although the Maritime pine shows a strong stomatal response (decline in stomatal conductance and photosynthesis) to drought (Picon et al., 1996). In addition to species-specific drought tolerance, angiosperms and gymnosperms also have fundamental differences in their drought response strategies. A recent study, for instance, found that angiosperms, initially, have lower resistance to droughts, while gymnosperms generally show reduced recovery after droughts (DeSoto et al., 2020).

5.1.4 N deposition and drought interactions

The interactions between N deposition and drought are not always straightforward and vary with climate zone, forest type, as well as drought severity and duration. Furthermore, N deposition and drought may have counteracting effects on forest growth on different time scales. Where N deposition tends to increase photosynthetic capacity, photosynthesis is generally limited by drought. As a result, drought could negate increases in forest productivity resulting from increased N deposition (Wang et al., 2012, Lui et al., 2013). However, experiments have also shown that N addition may also partially alleviate drought impacts on growth (Wang et al., 2012).

N deposition and droughts both affect nutrient availability in forest ecosystems. Reduced soil

moisture content during drought may lead to a decrease in organic matter decomposition, and immobilize nutrients in the soil. However, extra N available from N deposition may help reduce N limitations (Hanson et al., 2000). Very low N deposition rates may also lead to a lack of N reserves, impairing the trees ability to sustain drought stress (Gessler et al., 2017). Excessive N deposition, on the other hand, may result in nutrients imbalance within the soil and plants tissue, and cause a reduction of available cations (Mg, Ca and K), that play an important role in physiological drought defense mechanisms (Schulze, 1989). Furthermore, excess nitrogen leads to an increase in the shoot – root ratio and a shallower rooting system and decreasing fine root biomass increasing the risk of drought (e.g., Li et al. 2015). Therefore, we would expect an optimum value of N deposition where N deposition alleviates drought stress.

The anatomical and physiological traits of trees are also influenced by N deposition and drought. Chronic, elevated N deposition levels may lead to lower root to shoot ratios, a shallower rooting system and decreasing fine root biomass increasing the risk of drought (e.g., Li et al. 2015). Reduction in root biomass under combined N deposition and drought appear to be more severe for younger trees than for older trees (Palátová et al., 2002), as trees tend to allocate more biomass to roots as they age (Meyer-Grünefeldt et al., 2015). Trees that allocated more C to stems under elevated N deposition may, on the other hand, initially experience less water stress during droughts due to extra water storage (Albuquerque et al., 2013).

5.1.5 Paper setup

A global network of eddy-covariance measurements allows us to look at CO_2 fluxes between the atmosphere and biosphere on an ecosystem level. The FLUXNET2015 dataset provides an estimate of the net CO_2 balance of an ecosystem, as well as partitioning into upward- and downward CO_2 fluxes. Here we focus on the European forest sites because of the availability of more detailed nitrogen deposition data. One important component of the ecosystem C cycle is the net ecosystem exchange (NEE), which is the net CO_2 flux from the ecosystem to the atmosphere (Chapin et al., 2006). The NEE corresponds to the difference of photosynthetic C uptake, or the gross primary production (GPP), and the total ecosystem respiration (R_{eco}), which includes both autotrophic and heterotrophic respiration (Papale et al., 2006). So far, accurate estimates of nitrogen deposition are lacking for these sites. Flechard et al. (2019) used the inferential method and the EMEP model with a coarse grid to provide estimates of nitrogen deposition. Here, we used the recent updated LOTOS-EUROS model to provide site-specific estimates using more detailed local estimates. Furthermore, we use multiple methods to quantify the response of GPP at European forest eddy-covariance sites to drought. Several drought indices and soil water availability products (Standardized Precipitation Evapotranspiration Index, soil volumetric water layer) were used, indicating different types and durations of droughts. The computed responses of forest GPP to drought were then linked to the modelled N deposition estimates to assess potential N-drought interactions. In doing so, the across-site variability in circumstances, such as different dominant forest type, soil types and climate zones is taken into account.

We hypothesize that the response of forest GPP to droughts is smallest at an intermediate level of N deposition of max 10 kg ha^{-1} yr^{-1}, which is generally accepted as the critical load for nitrogen deposition (Bobbink et al. 2010). N deposition during drought may not always be detrimental and alleviate some of the impacts of drought. Due to a potential shortage of available nutrients, we

expect the response of forest GPP to drought to be more severe in forests that experience very low levels of N deposition than in forest with intermediate levels of N deposition. At high N deposition levels, on the other hand, we expect that biomass partitioning and the anatomical and physiological development in trees plays a more dominant role in drought impact. As forest ecosystems under chronic, elevated N deposition levels may have reduced amounts of root biomass, we expect a more severe response of forest GPP to drought, especially for longer-lasting droughts.

5.2 Datasets and model

5.2.1 FLUXNET2015 data

The FLUXNET2015 dataset provides ecosystem-scale data on CO_2, water, and energy exchange between the biosphere and the atmosphere, as well as other meteorological and biological measurements (Pastorello et al., 2020). The eddy covariance technique measures land-atmosphere energy and greenhouse gas fluxes at an ecosystem level at a high temporal resolution of 30 minutes. High frequency (10-20 Hz) measurements of the vertical wind velocity and scalar variables (e.g. CO_2, temperature) are used to provide an estimate of the net exchange of that scalar variable over a footprint area around the point of measurement (Aubinet et al., 2012). The measured NEE is partitioned into the GPP and R_{eco} using the night-time method (Reichstein et al., 2005). In this study, we use estimates of the daily and monthly GPP and R_{eco}, as well as some other meteorological observations.

We selected forest sites in Europe with at least 6 years of observations left after the application of a pre-processing filter (see Methods section). An overview of the used sites including auxiliary information is given in Table S5.1 and S5.2 in the supplement. The locations of the selected sites are shown in Fig. 5.1.

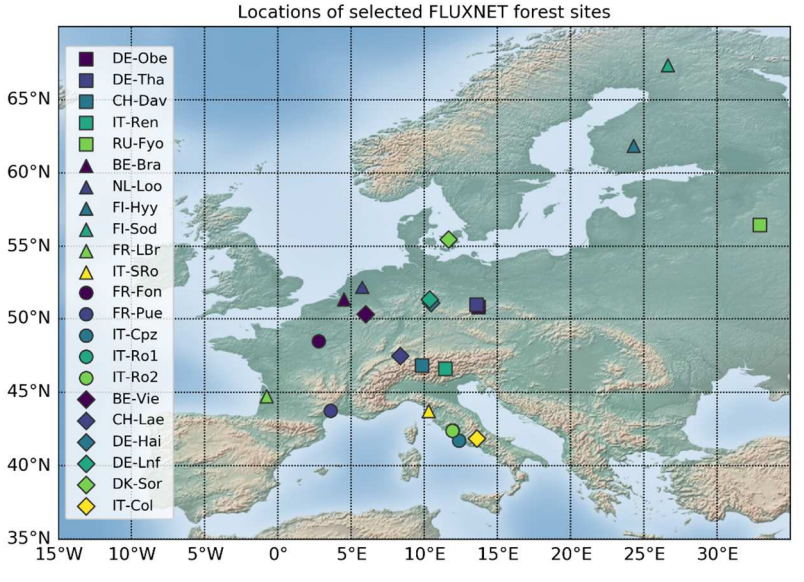

Figure 5.1. *Locations of the selected European FLUXNET forest sites.*

5.2.2 Soil type

The physical properties of the soils on which the forests are growing are obtained from the European Soil Data Centre (ESDAC) Topsoil physical properties for Europe (based on LUCAS topsoil data) (Ballabio et al., 2016). This dataset includes the percentage of clay, silt and sand in the topsoil layer (upper 20 cm), and is based on interpolation of around 20.000 survey points all over Europe from the LUCAS topsoil database using Multivariate Additive Regression Splines.

5.2.3 Drought characterization

5.2.3.1 Standardized Precipitation Evapotranspiration Index (SPEI)

The Standardized Precipitation Evapotranspiration Index (SPEI) is a drought index that takes into account both precipitation and potential evapotranspiration (Vicente-Serrano et al., 2010). The SPEI has been widely used because it allows the comparison among sites with contrasting climates and accounts for droughts at different time scales. The SPEI index is a standardized variate, i.e. a z-value, and expresses deviations from the current climatic balance (precipitation minus evapotranspiration potential) in respect to the long-term balance. Positive and negative SPEI values correspond to relatively wet and dry conditions, respectively. The SPEI values are computed globally on a grid for different time scales, depending on the time window that is used to calculate the SPEI values of the previous *n* months. Here, monthly SPEI values were obtained from the SPEIbase v.2.5, with 1-, 3-, 6- and 12- month time windows and a spatial resolution of 0.5º.

5.2.3.2 Soil volumetric water layer (swvl)

The soil volumetric water layer is the volume of water present in the total volume of soil (m^3/m^3), divided into different soil layers. Compared to the SPEI which is a statistical metric, the soil volumetric water layer is a soil physical variable which is related to plant available soil water. The volumetric soil water layer is a product of the European Centre for Medium-Range Weather Forecasts (ECMWF) ERA5-Land reanalysis (Copernicus Climate Change Service, 2019) and is associated with soil texture, soil depth and the underlying groundwater level. The model used by ECMWF has a four-layer representation of soil: the first layer extending from 0 to 7 cm depth, the second layer from 7 to 28 cm, the third layer from 28 to 100 cm and finally the fourth layer from 100 to 289 cm depth. Here, the same partitioning is kept.

5.2.4 N deposition fields

The N deposition fields used in this study are modelled using the LOTOS-EUROS chemical transport model (Manders et al., 2017). LOTOS-EUROS is an Eulerian chemistry transport model that simulates air pollution in the lower atmosphere. For this study, we used the mixed layer approach version of the model. We used a five-layer grid that extends up to 5 km vertically. The bottom layer is the surface layer that has a fixed thickness of 25 meters. This layer is followed by a mixing layer, which is in turn followed by two dynamic reservoir layers of equal thickness and finally a top layer that extends up to 5 km. The model performs hourly calculations using ECMWF meteorology (ECMWF, 2016), and uses the TNO CBM-IV gas-phase chemistry scheme (Schaap et al., 2009). The anthropogenic emissions are taken from CAMS-REG-AP (Copernicus Atmospheric Monitoring Services Regional Air Pollutants) emissions dataset v2.2 (Granier et al., 2019). The wet deposition computation simulates both in-cloud and below-cloud scavenging and is based on the CAMx approach (Banzhaf et al., 2012). The dry deposition flux is computed using the DEPAC3.11 (Deposition of Acidifying Compounds) module (Van Zanten et al., 2010). This module follows the resistance approach, in which the exchange velocity is equal to the reciprocal

sum of the aerodynamic, quasi-laminar and canopy resistance. A canopy compensation point for NH_3 is implemented in this routine, allowing bi-directional fluxes. The model uses the CORINE/Smiatek land use map to compute exchange velocities for different land use classes. In this study, we computed 12 years (2003 – 2014) of land use specific fluxes for deciduous and coniferous forest in Europe (35ºN to 70ºN, 15ºW to 35ºE). We used a horizontal resolution of 0.50º longitude by 0.25º latitude, corresponding to approximately 28 by 28 km^2. We match the modelled deposition flux with the FLUXNET sites based on their plant functional type. For mixed forest, the average flux for deciduous and coniferous forest is computed.

5.3 Methods

5.3.1 Deviations from reference GPP values

To quantify the response of forest GPP to drought, the observed daily GPP values are first compared to two types of reference GPP cycles, which we assume are "expected" or default GPP values at a specific day on the long term. The deviations from these reference cycles are then computed and matched with drought indices to quantify the response of forest GPP to a specific drought. Here, two types of reference cycles are defined: (1) the detrended daily mean and maximum GPP values, and (2) the modelled daily GPP values, estimated from the observed meteorological variables at the same location using multiple regression analysis. The daily deviations are computed and then accumulated over a month or season (spring and summer), so that they can be linked to the monthly drought indices. The two types of reference GPP cycles are explained in more detail in the sections below.

5.3.1.1 Mean and maximum daily GPP values

The first method directly uses the daily FLUXNET measurement of the GPP. For each site, the mean and maximum GPP values are computed for each day of the year and used as GPP reference cycles. For the computation of the daily mean GPP value, all measurements with a medium- to high-quality indication are used (NEE_VUT_REF_QC > 0.5). For determining the daily maxima, only observations with a high-quality flag indication (NEE_VUT_REF_QC > 0.9) were used to avoid the inclusion of outliers. The monthly accumulated deviations from the daily mean GPP values will be referred to as δGPP_1.

5.3.1.2 Modelled daily GPP values

In the second method, the reference GPP values are computed using multiple regression analysis. Here, daily FLUXNET observation of the ambient air temperature (T_{air}), incoming short-wave radiation (SW_{in}) and longwave radiation (LW_{in}), the sensible- (H) and latent (LE) heat flux and the vapor pressure deficit (VPD) are used. These parameters are used as predictors to estimate the expected daily GPP at a certain day of the year given the meteorological conditions. As most biochemical reactions follow a hyperbolic curve, the following multi polynomial regression model is fitted to the data in a least-squares sense:

$$GPP = a_1 {T_{air}}^2 + a_2 T_{air} + a_3 {SW_{in}}^2 + a_4 SW_{in} + a_5 {LW_{in}}^2 + a_6 LW_{in} + a_7 H^2 + a_8 H + a_9 LE^2 + a_{10} LE + a_{11} VPD^2 + a_{12} VPD + a_{13} t + a_{14} \quad \text{(Eq. 5.1)}$$

The relationship between these predictors and the GPP changes throughout the year and may be quite asymmetrical, especially for a deciduous forest. To avoid systematic over- or underestimations in specific months, we fit the model for two separate periods: a startup growing period and the remainder of the growing season. In the startup period, we commonly observe a delayed response of GPP to change in these predictors. After this period, the relationship stabilizes and can be modelled well with a single multi-regression fit (see Result section). For simplicity, the split is made at the beginning of May for sites with deciduous forests and at the beginning of June for sites with coniferous forests.

The monthly accumulated deviations from the daily modelled GPP values will be referred to as δGPP_2.

5.3.2 Detecting extreme drought events

Extreme droughts are detected using the following criterium: SPEI less than the 10^{th} percentile of the site-specific SPEI distribution. Here, only droughts that occur during spring and summer (March-August) are taken into account. The distribution of the different SPEI values (i.e., the monthly, 3-monthly, 6-monthly and 12-monthly) is computed at each forest site during the time the measurements took place and the months in the lower 10^{th} percentile are selected as drought events. The deviations from the reference cycles δGPP_1 and δGPP_2 during the months indicated as 'drought event' are then matched and (1) the distribution of δGPP_1 and δGPP_2 values and (2) the most extreme (negative) δGPP_1 and δGPP_2 values in the corresponding months are computed.

5.3.3 Comparison to N deposition, climate zone, soil type and forest age

After the deviations from the reference cycles δGPP_1 and δGPP_2 were computed and matched with the SPEI indices, they were compared to climatic and edaphic variables and N deposition estimates at each site. As a way of standardizing across forest sites, the δGPP_1 and δGPP_2 values are expressed as a percentage of the monthly mean GPP. As forest located in different climate zones respond differently to droughts of different durations, we determine which SPEI time window (1-,3-,6- or 12- months) shows the largest negative median δGPP_1 and δGPP_2 values at each site. The median and the largest negative, i.e., most severe, $\delta GPP_{1,2}$ values corresponding to the SPEI with this time window are compared to the average amount of N deposition, the mean annual temperature (MAT), the mean annual precipitation (MAP), the age of the forest, and the percentage of clay and sand in the soil.

5.3.4 Detecting low soil moisture content

The soil volumetric water layer is used to look at the direct effect of soil water deficits on forest GPP during spring and summer. The analysis is as follows: first, the weighted averages of the soil volumetric water layer in the upper three layers (up to 1 m depth) at each site are computed. The weighted values are normalized so that 1 corresponds to the wettest- and 0 to the driest soil conditions occurring at that site, respectively. Subsequently, for each year the average weighted soil volumetric water layer during the spring (March-May) and summer (June-August) is computed, which we call the "$swvl_{WA}$". Here, the daily maximum GPP values are used as reference values. For each year, the observed, total GPP during spring and summer is divided by the maximum GPP values during the same season, which we will refer to as "$fGPP_{max}$". The $swvl_{WA}$ during spring and summer are then plotted against the corresponding $fGPP_{max}$ values. A simple

linear regression model is fitted to all points and the slope and correlation coefficient are calculated. The computed slope and correlation coefficients are then compared to the average amount of N deposition, the mean annual temperature (MAT), the mean annual precipitation (MAP), the age of the forest, and the percentage of clay and sand in the soil for all sites simultaneously.

5.4 Results

5.4.1 Relationship between N deposition and GPP and Reco fluxes

First, the yearly N deposition at each forest site is directly compared to the corresponding gross primary production (GPP) and ecosystem respiration (R_{eco}) values. The annual GPP values show a clear dependence on the annual N deposition values, increasing linearly at first, and peaking at approximately 10-15 kg N ha^{-1} yr^{-1} and 2000 gC m^{-2} yr^{-1} (Fig. 5.2). For higher N deposition values (>15 kg N ha^{-1} yr^{-1}) a decrease in annual GPP is observed. This is in correspondence with the previously reported growth optimum related to N deposition. The relationship between R_{eco} and N deposition shows more inter-site variability but follows a similar pattern. The optimum again lies around 10-15 kg N ha^{-1} yr^{-1} and around 1500 gC m^{-2} yr^{-1}. The modelled N deposition is then split up into NO_y and NH_x deposition. The breakdown of the N deposition into NO_y versus NH_x components at each FLUXNET site is shown in Fig. S5.1. The yearly NO_y and NH_x deposition are compared to the corresponding GPP values in Fig. 5.3. For the individual components, a similar relationship to GPP is observed. The optima for each component, however, lie at different values. The optimum GPP for NO_y occurs around 8 kg N ha^{-1} yr^{-1}, while the optimum GPP for NH_x lies around 12 kg N ha^{-1} yr^{-1}. Beyond these optima, the GPP decreases at different rates. Here, the decrease is particularly strong for NO_y deposition values above 8 kg N ha^{-1} yr^{-1}, and relatively steeper than for NH_x.

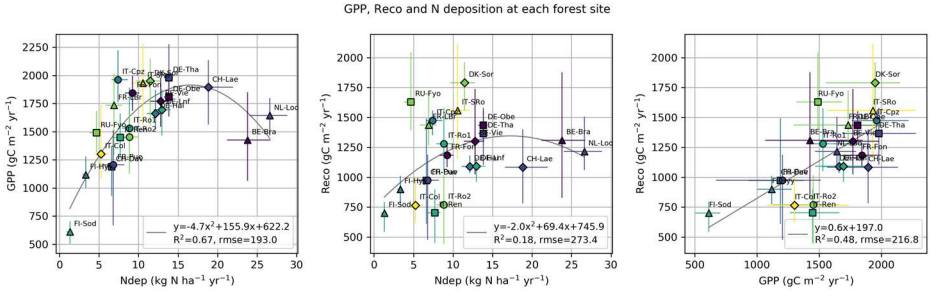

***Figure 5.2**. Yearly observed gross primary production (GPP) and ecosystem respiration (R_{eco}) plotted against modelled N deposition for each European FLUXNET forest site. The symbols indicate different sites, as in Figure 5.1. The colored lines indicate the entire range (minimum – maximum) of the GPP, R_{eco} and N deposition values at each site.*

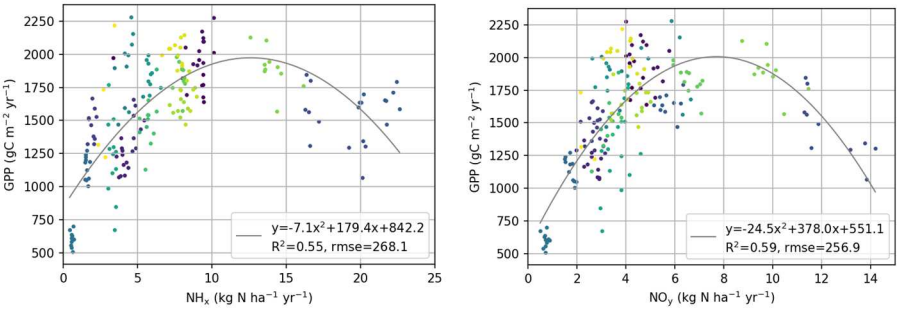

Figure 5.3. *Relationship between yearly GPP and NH_x* ***(left)*** *and NO_y* ***(right)*** *deposition. Only years with GPP values of quality flag 0.8 or higher are plotted. Each dot represents a single year and the colors represent different FLUXNET sites as in Figure 5.1. The grey lines represent the best least-squares polynomial fit through all points.*

5.4.2 Changes in GPP during extreme droughts

The mean and maximum GPP cycles at each of the FLUXNET forest sites, that are used as reference values, are shown in Fig. 5.4. The GPP cycle of the forest sites with *Picea abies* as dominant species is the most symmetrical throughout the year and the least variable across sites. Forest sites with predominant deciduous broadleaved species, e.g., with *Quercus* and *Fagus sylvatica* as dominant species, show the most asymmetrical GPP cycles, as was expected. The GPP cycles of most forest sites with *Quercus* subspecies as dominant forest type are twofold, with a large initial peak during spring- and summertime followed by a smaller peak during autumn. Moreover, a clear dependence on climate is observed. Forest located in colder climates, for instance in Finland (Fi-Sod, Fi-Hyy), have a relatively short growing season. For forests in Mediterranean climates (e.g., IT-Cpz), on the other hand, an early onset of the growing season, as well as relatively high GPP values in wintertime (Fig. 5.4c) are observed.

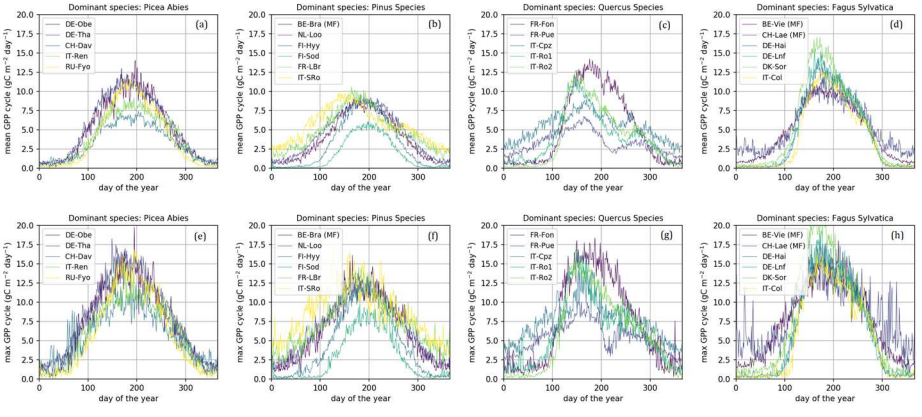

Figure 5.4. *The mean* ***(a,b,c,d)*** *and maximum* ***(e,f,g,h)*** *daily GPP cycle at each FLUXNET forest site.*

The distribution of the computed δGPP_1 and δGPP_2 values during months indicates as droughts are shown in Fig. S5.2. Table S5.1 shows an evaluation of the polynomial regression model per site, which includes the root-mean-squared deviation (RMSD), the mean absolute deviation

(MAD), Pearson's correlation coefficient r and the slope between the measured and modelled daily GPP values. First of all, the spread of the δGPP_1 and δGPP_2 values plotted in Fig. S5.2 varies quite a lot across sites. There seems to be significant variability in the GPP responses to different drought durations as well. For example, there are more frequent, negative GPP responses corresponding to longer-lasting droughts in sites with *Pinus* spp. as dominant tree species (e.g. *FI-Hyy, FI-Sod, FR-LBr*), as well as sites dominated by *Quercus* spp. (*FR-Pue, IT-Cpz, IT-Ro2*). The difference between δGPP_1 and δGPP_2 values indicates to what extent the response of forest GPP to drought can be explained by the weather conditions. Some forest sites for instance strongly respond to high ambient air temperatures in combination with high vapor pressure deficit values with a consistent decrease in GPP, which could indicate direct stomatal closure at these conditions. This is visible for forest sites with *Quercus* species as dominant forest type in particular (i.e. *FR-Fon, FR-Pue, IT-Cpz, IT-Ro1, IT-Ro2).*

In the following section, only months identified as 'extreme droughts' that correspond to negative impacts on GPP are considered. Fig. 5.6 shows the most negative response in δGPP_1 and δGPP_2 at each forest site plotted against the mean N deposition, the MAT and the MAP, the forest age and the sand and clay content of the soil. Fig. S5.2 shows the same information but grouped by dominant tree species. The largest negative δGPP_1 and δGPP_2 values differ the most for relatively young forest (< 80 years), young forest having a relatively larger negative response in δGPP_1. This indicates that young forests tend to respond more rapidly and consistently to changes in weather conditions. At first sight, there is a decreasing response in forest GPP to drought with increasing N deposition values, which levels off around 15 kg N ha^{-1} yr^{-1}. However, the variation is large and the R^2 values of the best fitting curves are relatively small (R^2=0.15 and R^2=0.39). In general, no clear pattern for all sites in relation to either MAT or MAP, or sand or clay content is observed. Here, too, the relationships are rather weak.

Fig. 5.7 shows the mean negative response in δGPP_1 and δGPP_2 per drought event at each forest site plotted against the mean N deposition, the MAT and the MAP, the forest age and the sand and clay content of the soil. Fig. S5.3 shows the same information but grouped by dominant tree species. In these figures, the values are plotted in g C m^{-2} per drought event, which corresponds to the mean decrease in GPP in one month identified as extreme drought (<10th percentile) by the used SPEI indices. First of all, all plotted relationships are rather weak. The mean negative response in forest GPP to drought increases with increasing MAT values, which indicates that forest sites located in warmer climates experience relatively strong GPP reductions during extreme droughts. Despite significant uncertainties, there appear to be some detectable relationships in forest sites with the same dominant tree taxa. For example, at forest sites with *Pinus* spp. as dominant species there seems to be a linear relationship between the mean negative δGPP_1 and the mean annual temperature and precipitation. Furthermore, in oak forests (*Quercus* ssp.), and to a lesser extent in spruce forests (*Picea* ssp.), linear relationships between the mean negative δGPP_1 and the soil sand and clay content can be observed at each site. In these forests, the response of forest GPP to drought seems to become more severe with decreasing soil sand content and increasing clay content. This suggests that *Quercus* ssp. are in general more sensitive to changes in soil water content and that *Quercus* ssp. forests on sandy soils are generally less susceptible to droughts than those on clayey soils.

5.4.3 Effect of soil volumetric water layer on seasonal GPP

Fig. 5.8 shows the slope and the correlation between the $svwl_{WA}$ and $fGPP_{max}$ during spring and summer at each forest site. Positive slopes and correlation coefficients represent a positive relationship between the $svwl_{WA}$ and $fGPP_{max}$, e.g., increasing GPP with increasing soil volumetric water layer. In general, GPP in most forest sites benefits from relatively low soil moisture levels during spring, and relatively high soil moisture levels during summer.

The highest correlations between $svwl_{WA}$ and $fGPP_{max}$ in spring are found for sites with *Fagus sylvatica* as dominant species (diamond). The growth during the beginning of the growing season is thus highly dependent on the amount of available soil water at sites with *Fagus sylvatica* as the dominant tree species. Generally, the soil volumetric water content in the topmost layer (> 1 meter below the surface) decreases gradually from wintertime towards the summer as accumulated evaporation becomes higher than accumulated precipitation. As a result, trees are thus less likely to experience serious water shortages during spring. Moreover, as the start of the growing season seems to be fairly consistent at these sites (see Fig. 5.5), the apparent positive effect of low soil moisture conditions on GPP in spring is likely caused by favorable meteorological conditions, such as higher air temperatures and higher amounts of incoming short-wave radiation, and not low soil moisture conditions.

During summertime, the relationship between $svwl_{WA}$ and $fGPP_{max}$ is mainly dependent on the mean annual temperature (MAT) and the forest age. The slope and correlation coefficient increase with increasing MAT values, indicating that forest sites located in warm climates are relatively sensitive to changes in soil moisture. The slope and the correlation coefficients decrease with increasing forest age, suggesting that the GPP in younger forests is more sensitive to changes in soil moisture compared to older forests. This is in line with the literature, as young forests have less developed root systems. In general, there are no clear pattern in relation to N deposition.

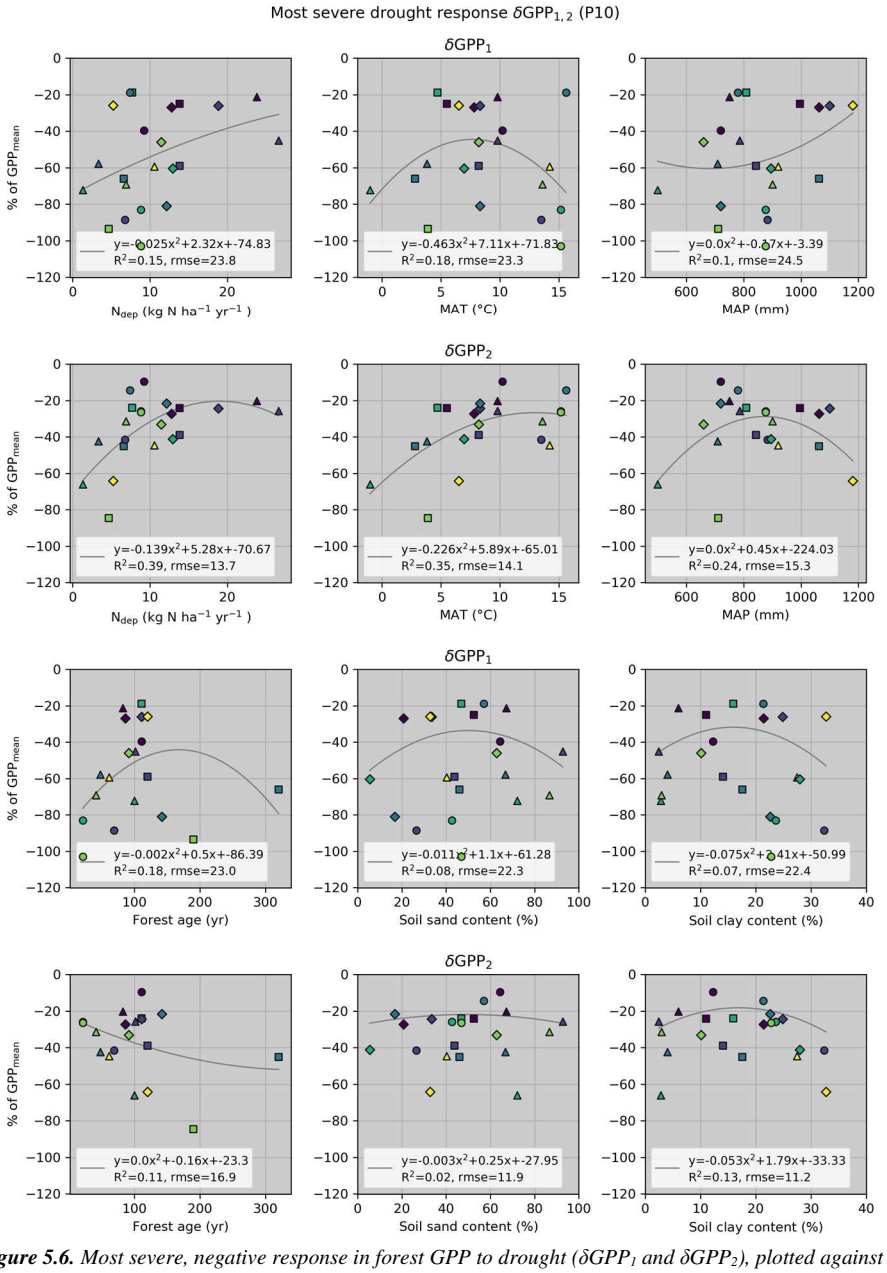

Figure 5.6. *Most severe, negative response in forest GPP to drought (δGPP_1 and δGPP_2), plotted against the mean N deposition (N_{dep}), mean annual temperature (MAT) and mean annual precipitation (MAP), the forest age and the soil sand and clay content. The δGPP_1 and δGPP_2 values are plotted as percentage of the monthly mean GPP at each site, and represents the most negative δGPP_1 or δGPP_2 value out of the all values computed with 1-, 3-, 6- and 12- monthly SPEI values. The symbols represent the dominant forest types at each site. The gray lines represent the best fitting polynomial function using least-squares optimization.*

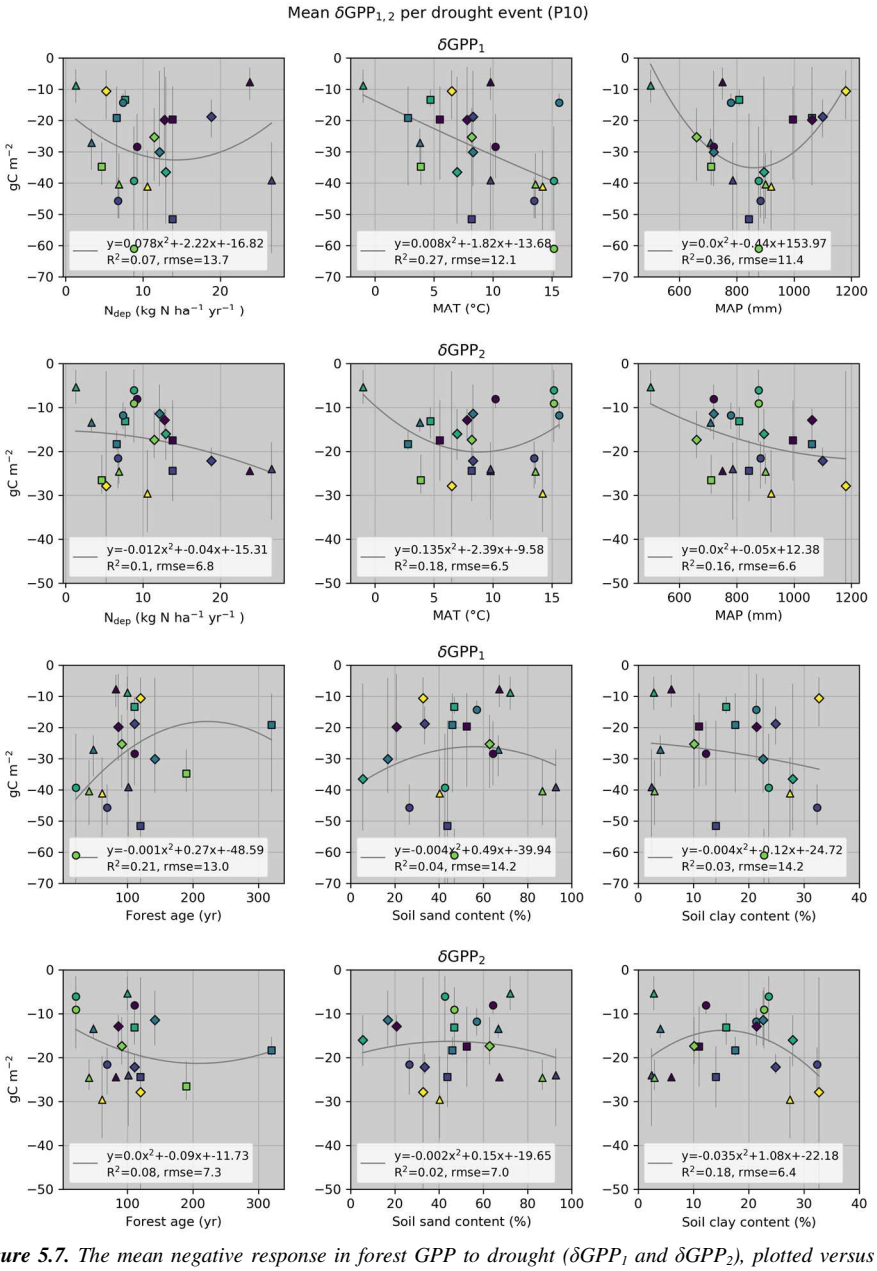

Figure 5.7. *The mean negative response in forest GPP to drought (δGPP_1 and δGPP_2), plotted versus the amount of N deposition (N_{dep}), the mean annual temperature (MAT) and the mean annual precipitation (MAP), the forest age and the soil clay and sand content. The GPP response per drought event is computed by summing all negative δGPP_1 and δGPP_2 values and then dividing that by the number of drought events per SPEI index (1-, 3-, 6- and 12- monthly). The gray lines indicate the spread in outcomes using different SPEI indices. The symbols represent the dominant forest types at each site.*

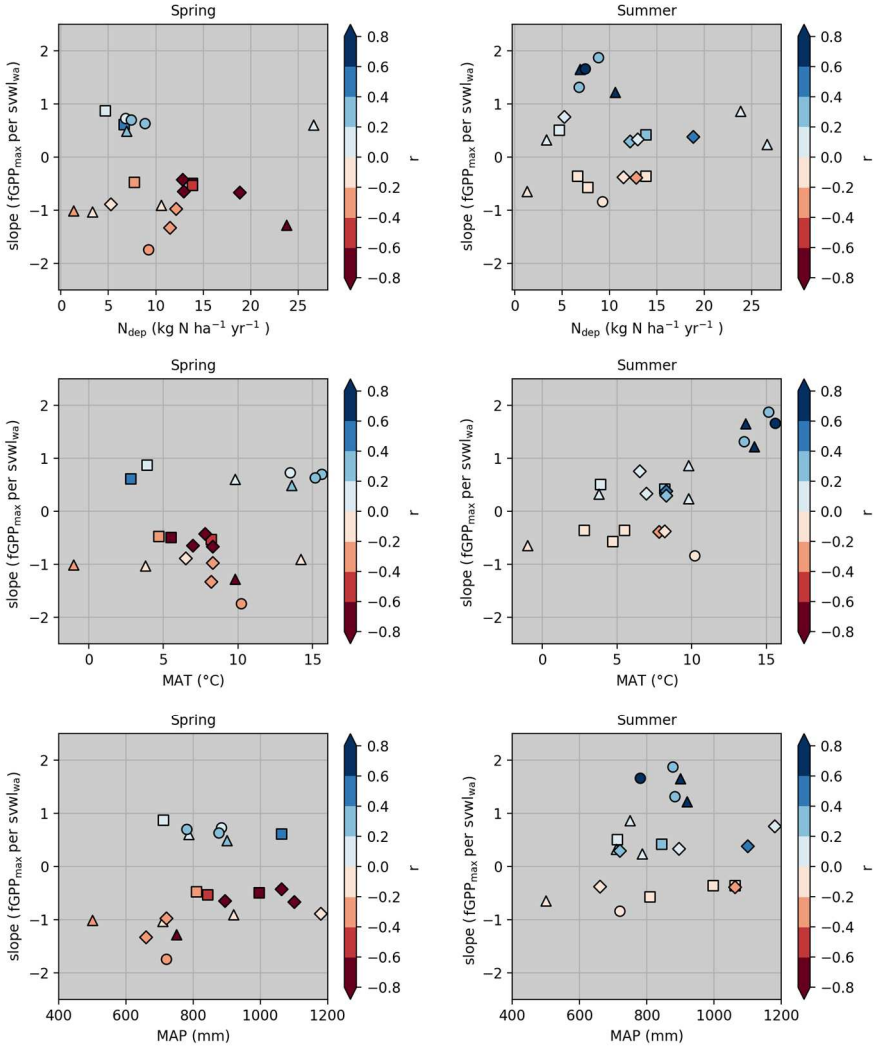

Figure 5.8. *The slope and the correlation coefficient between the weighted average normalized soil volumetric water layer ($swvl_{WA}$) and the fraction of the maximum GPP ($fGPP_{max}$) during spring and summer at all forest sites, plotted against the amount of N deposition (N_{dep}), the mean annual temperature (MAT) and the mean annual precipitation (MAP). Negative slopes and r values (red) indicate a preference for drier soil conditions, whereas positive slopes and r values (blue) indicate a preference for wetter soil conditions. The symbols represent the dominant forest types at each site. The slope and correlation coefficients are obtained by fitting a simple linear regression using least-squares optimization…*

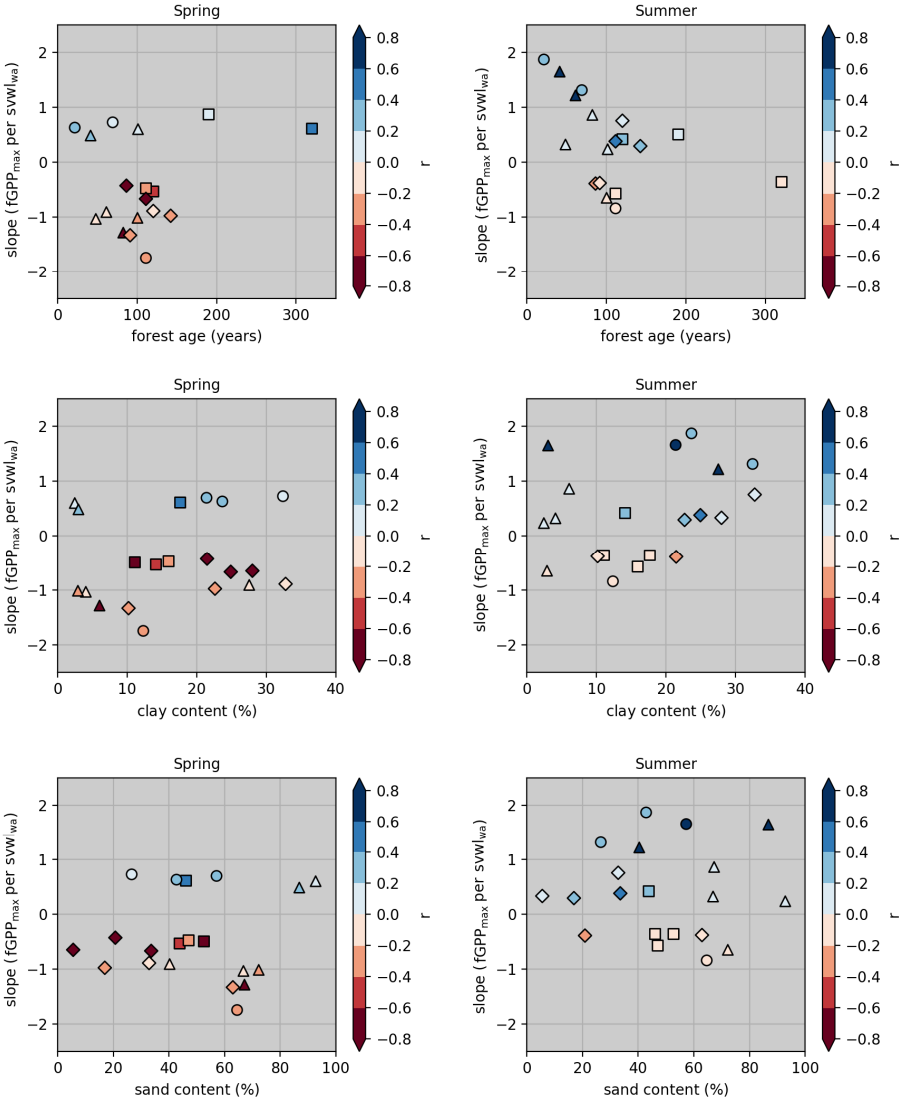

Figure 5.8. *…continued for the forest age and the soil sand and clay content.*

5.4.4 Case study: N deposition and drought interactions in pine forest (*Pinus* ssp.)

The results from the previous sections suggest that there is a differential response of forest GPP to drought across FLUXNET sites, seemingly independent from N deposition. However, by grouping sites with the same dominant tree taxa, some patterns could be distinguished. In this section, the group of sites located in pine forests (*Pinus spp.*) is studied in more detail. These pine forest sites (*FI-Hyy, FI-Sod, IT-SRo, FR-LBr, NL-Loo, BE-Bra*) showed the strongest relationship between the response in forest GPP to drought and the MAT, MAP and forest age. Moreover, the largest variation in N deposition levels is observed across these sites.

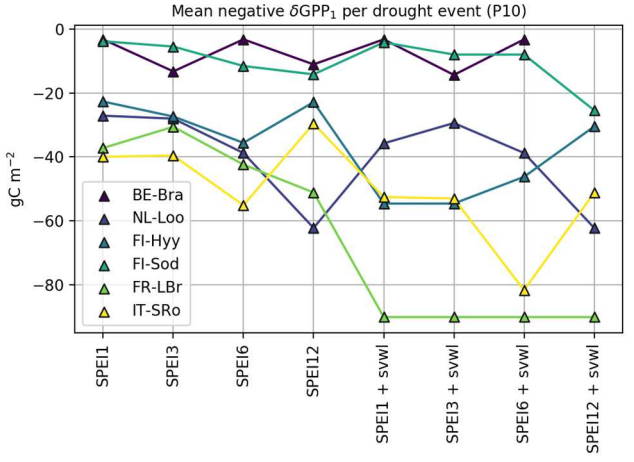

Figure 5.10. *The mean negative response in forest GPP (δGPP_1) per drought event identified by different drought indices. A specific month is classified as drought if the used drought index is below its 10th percentile value. The soil volumetric water layer (svwl) values are standardized.*

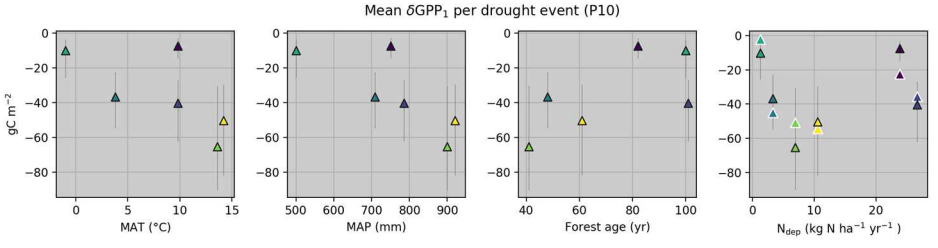

Figure 5.11. *The mean negative response in GPP (δGPP_1) per drought month in relation to the mean annual temperature (MAT), the mean annual precipitation (MAP), the forest age and the N deposition. Each triangle stands for one forest site, and the grey lines indicate the spread in outcomes using different SPEI values. The triangles with the white outline are the modelled δGPP_1 values, using a multi-linear regression fitted to the MAT, MAP and forest age (δGPP_1= 6.29*MAT - 0.35*MAP - 0.02*forest age + 183.43,* R^2 = 0.76, rmse = 10.0).

Fig. S5.5 shows the time series of the daily and monthly summed GPP deviations (δGPP_1). At some sites, there are consistently higher or lower GPP values throughout the entire year (*IT-SRo, FR-LBr, FI-Sod*). Other sites, on the other hand, show much more intra-annual variability (*NL-Loo, FI-Hyy*).

Fig. 5.10 shows the mean negative response in forest GPP (δGPP_1) per drought event identified by different drought indices. Here, the normalized soil volumetric water layer (*svwl*) values at each forest site is used as an additional drought indicator. Most sites respond more severely to longer-lasting droughts, except for *BE-Bra*. The addition of the *svwl* did not lead to a more severe response in forest GPP to drought at all sites. *BE-Bra, NL-Loo* and *FI-Sod* are insensitive to *svwl* as an additional drought indicator.

Fig. 5.11 shows the mean negative response in forest GPP (δGPP_1) per drought event, in relation to the MAT, MAP, forest age and the amount of N deposition. Overall, the response in GPP increases with increasing MAT and MAP values and decreasing with increasing forest age. To extract the influence of the MAT, MAP and forest age, a multi-linear regression was fitted. The resulting, modelled δGPP_1 are plotted in white in relation to N deposition, alongside the initial δGPP_1 values. From our hypothesis, we expect the response in forest GPP to drought to be more severe at forest sites with very low levels of N deposition (*FI-Hyy and FI-Sod*), and with very high levels of N deposition (*BE-Bra and NL-Loo*). At forest sites with intermediate levels of N deposition (*IT-SRo and FR-LBr*), N deposition is expected to alleviate the drought response in GPP. The fitted δGPP_1 values, however, at different levels of N deposition, are both higher and lower than the observed δGPP_1 values. Moreover, the response of forest GPP to drought was modelled with another multi-linear regression, this time including the amount of N deposition. The resulting fitted model (δGPP_1= 5.26*MAT - 0.38*MAP - 0.41*forest age +1.13*N_{dep} + 225.36) improved slightly, but not significantly (R^2 = 0.85, *RMSE* = 8.1) and shows that N deposition only explains another ~10% of the variation in the data. These results suggest that there is no consistent nor significant effect of N deposition on the response of forest GPP to drought in these pine forest sites and therefore do not support our hypothesis.

5.5 Discussion

This study discusses various pathways in which N deposition and drought can interact as co-stressors on forest productivity in European forest ecosystems. Based on the literature, our initial hypothesis was that the response of forest GPP to drought is relatively small in forest ecosystems that experience intermediate levels of N deposition (5-10 kg ha^{-1} yr^{-1}). Productivity in forest ecosystems with either very low N deposition levels (<5 kg ha^{-1} yr^{-1}) or higher N deposition levels approaching N saturation (>10 kg ha^{-1} yr^{-1}) was expected to show a relatively large magnitude response to drought. Due to a differential response to the used drought indices, we were unable to isolate a clear, overall dependence of the response of forest GPP to drought on N deposition. This, in part, results from the large inter-site variability in dependencies of the response of forest GPP to drought on varying physiological, climatic and edaphic conditions. Grouping sites with the same dominant tree species enabled us to extract some of these dependencies, such as the sensitivity of drought response to soil texture in oak (*Quercus* ssp.) forests. Furthermore, the GPP response to drought within the group with the largest variation in N deposition (*Pinus* ssp.) could be predicted using the site mean annual temperature and precipitation and the age of the forest (R^2 = 0.76, RMSE = 10.0). However, after extracting the contribution of these most prominent parameters, the variability in drought responses remained too large to substantiate any hypothesized N deposition effects.

We were unable to draw any generalized conclusions regarding the impact of N deposition on the response of GPP to drought in European forest ecosystems. In addition to the large inter-site variability in physiological, climatic and edaphic conditions in general, another limiting factor in this study setup was the low variation in N deposition levels within some groups of dominant forest species (e.g. *Quercus* ssp. or *Fagus sylvatica*). Moreover, even though the FLUXNET2015 dataset contains the most extensive network of eddy-covariance measurements to date, this study is limited by the relatively short time series at some forest sites. As a result, some forest sites for instance only experienced a handful of months indicated as severe droughts. As we established that for example both frequency and severity of a particular drought event play an important role in the forest response, it is especially hard to generalize the response with only a few droughts occurring. Moreover, a relatively short time series of GPP observations could result in a bias in the mean GPP cycle and therefore the drought-induced anomalies in GPP. For example, if the majority of the years with measurements at a particular site were relatively warm and dry, the difference in GPP with a classified drought period would be smaller than if these years were relatively cold and wet. Also, longer time series would allow us to look at the impact of re-occurring or longer-lasting droughts, and the impact of severe drought on the long-term C cycling in forest ecosystems.

A recent review by Speich et al., 2018 found that, for temperate forests, drought indices accounting for evaporative demand performed better than indices based on precipitation alone. The SPEI index used here does account for both precipitation and evaporative demand, but does not include any additional levels of information. The results showed that not all month indicated as extreme droughts by the SPEI-indices correspond to negative responses in GPP (Fig. S5.2). This is likely because the SPEI index does not account for soil moisture storage, the ease of soil water extraction by plant roots, or water table depth. Therefore, the first couple of months of drought, with possibly sufficient water availability coming from deeper soil layers, were included in the analysis. As long as tree root systems have access to sufficient amounts of soil water, favorable meteorological conditions during drought, such as higher incoming solar radiation, could even result in a relative increase of GPP. This illustrates that using the 10th percentile of the SPEI index as a definition of extreme drought conditions, as was done in this study, does not necessarily only include impactful droughts. Using a more applied drought index that uses more site-specific variables (e.g., soil moisture storage, stand properties, physiological thresholds) could potentially improve the selection of droughts.

Other factors contributing to the uncertainty in our analyses are related to the modelling of N deposition. The modelled N deposition fields used in this study have a relatively large uncertainty. N deposition measurements, both the dry and wet component of the deposition fluxes, at the same locations as the FLUXNET sites could help to improve on this and would allow us to represent the current N deposition levels per site more accurately. At the same time, most of these forests are around a 100 years old, and better estimates or measurements of current N deposition levels are, therefore, not necessarily correlated with historic N deposition levels. Here, we used a relatively long time-series (12 years) of modelled N deposition and assumed that these N deposition levels represent the N availability in these forests as a whole relatively well. N retention and allocation in forest ecosystems is, however, not only influenced by the current level of N deposition, but also by the accumulated N deposition that a forest ecosystem has received (De Vries et al., 2014). Using additional measurements of N in plant and soil pools could help us to get a better grip of the accumulated N in different forest compartments and herewith the historic N deposition levels.

Nutrient availability in general is a key regulator of the forest carbon balance. Not only N limitation plays a role in forest productivity, but also the availability of other nutrients (e.g., potassium, phosphorus, calcium, magnesium) (Fernandez-Martinez et al., 2014). For a more complete analysis, not only N availability but also other potentially limiting nutrients such as phosphorus (P) or other cations (Mg, Ca and K) could be considered. Moreover, surface ozone (O_3) also plays a critical role in forest growth and drought response (e.g. (Karlsson et al., 1997, Kronfuβ et al., 1998)). In the current study setup, however, adding more variables (for instance O_3 surface concentrations) would likely result in an even greater divergence in conditions between the FLUXNET forest sites. To effectively isolate N deposition-drought interactions, an extensive measurement network in forests with similar edaphic, physiological and climatic conditions is needed. To get more insight into N deposition – drought interactions for specific tree species, one could for instance set up N addition experiments in a managed forest. Another option would be to do measurements for the same type of trees in regions with strong, local N deposition gradients.

This is the first study to examine both the effects of modelled N deposition on forest productivity across the European FLUXNET sites and the possible effects of N deposition on the magnitude of a productivity response to drought. We find good agreement across the FLUXNET sites in the dependence of GPP to N deposition and its component (NO_y and NH_x), with an initial strong increase in GPP at low N deposition levels followed by a slow decline, and even a decrease at high N deposition levels. However, the effect of N deposition on the magnitude of the forest productivity response to drought could not be isolated. These results suggest that, while N deposition might play a critical role in the response of forest productivity to drought within specific forest ecosystems, N deposition does not seem to be a major or consistent driver of the magnitude of the GPP response to drought across a diverse set of FLUXNET forest sites in Europe.

Acknowledgements. The authors acknowledge the Nederlandse Organisatie voor Wetenschappelijk Onderzoek (NWO). This project was funded by the NWO under project number ALW-GO/16-05. This work used eddy covariance data acquired and shared by the FLUXNET community, including these networks: AmeriFlux, AfriFlux, AsiaFlux, CarboAfrica, CarboEuropeIP, CarboItaly, CarboMont, ChinaFlux, Fluxnet-Canada, GreenGrass, ICOS, KoFlux, LBA, NECC, OzFlux-TERN, TCOS-Siberia, and USCCC. The FLUXNET eddy covariance data processing and harmonization was carried out by the ICOS Ecosystem Thematic Center, AmeriFlux Management Project and Fluxdata project of FLUXNET, with the support of CDIAC, and the OzFlux, ChinaFlux and AsiaFlux offices.

Chapter 6: Synthesis

6.1 Overview

The human modification of the global nitrogen cycle has led to enhanced losses of reactive nitrogen (N_r) to the environment, exceeding many thresholds for human and ecosystem health. Excess atmospheric deposition of N_r on natural ecosystems causes soil acidification, eutrophication, and ultimately biodiversity loss. Moreover, nitrogen deposition may exacerbate the impact of climate change, for instance, by affecting vegetation growth and carbon exchange in case of drought (De Vries et al., 2011). So far, the coupling of nitrogen deposition and drought has been hampered by the relatively high uncertainty of the modelled nitrogen deposition estimates. To tackle this, the main goal of this PhD thesis was to improve nitrogen deposition estimates from chemical transport models (CTMs) through the integration and assimilation of different types of satellite observations. Furthermore, the effects of drought and nitrogen deposition on gross primary production in European forest ecosystems were studied using high-quality measurements from the FLUXNET database.

This PhD research was funded by the Netherlands Organization for Scientific Research (NWO) under project number ALW-GO/16-05. At the start of this PhD, satellite retrievals of atmospheric NH_3 concentrations from the Infrared Atmospheric Sounding Interferometer (IASI) and the Cross-track Infrared Sounder (CrIS) had recently been developed (IASI: Clarisse et al., 2009, Van Damme et al., 2014, CrIS: Shephard and Cady-Pereira, 2015) and validated (Dammers et al., 2016, Dammers et al., 2017ab). The NH_3 observations provided by these instruments could be used to reduce the large uncertainties that exist in the atmospheric budget and distribution of NH_3. In Chapter 2 of this thesis (van der Graaf et al., 2018), the IASI-NH_3 product, the product with the longest time series, was used in combination with information from the LOTOS-EUROS chemical transport model to derive dry deposition fluxes of NH_3. Here, we illustrated that the direct use of satellite data following the approach by Nowlan et al., 2014 did not provide any added value for directly constraining NH_3 fields in Europe. The validation of the results with in-situ measurements also emphasized the need for better, more robust methods for deriving large-scale deposition fluxes. The sensitivity study that was conducted in this chapter and a direct comparison of the satellite and model NH_3 distributions identified two important areas for improvements: the modelled deposition velocities and the input emissions for NH_3. Aiming to improve the surface characterization in LOTOS-EUROS, and herewith the deposition velocities, high resolution satellite observations were used to derive more realistic, dynamic input parameters for the deposition parameterization. The results of this study are presented in Chapter 3 (van der Graaf et al., 2020). The inclusion of the satellite-derived parameters led to significant changes in the modelled nitrogen deposition fields for specific land use types. These changes, however, were difficult to validate with the available set of in-situ observations.

Next, our focus shifted towards improving the spatiotemporal distribution of the NH_3 input emissions, and to achieve this a data assimilation study was performed. The results are presented in Chapter 4 of this work (van der Graaf et al., 2021a). Here, the CrIS-NH_3 product was used to derive NH_3 time factors and adjust NH_3 emissions with a Local Ensemble Transform Kalman Filter (LETKF) approach. Because of the lack of averaging kernels in the IASI-NH_3 product, the decision was made to switch to the CrIS-NH_3 products for a fairer comparison with the modelled NH_3 concentrations. In the meantime, a study was started to look at nitrogen deposition and drought interactions at European FLUXNET sites. Around this time, the new regional CAMS emission inventories became available for LOTOS-EUROS, which allowed us to model ecosystem-specific

nitrogen deposition fluxes for a long time period at an improved spatial resolution compared to existing deposition estimates. The results of this study are presented in Chapter 5 (van der Graaf et al., 2021b).

In the next sections of this concluding chapter, the main results of this thesis are summarized following the four research questions formulated in Chapter 1. Finally, the results are briefly discussed and prospects for future research are proposed.

6.2 Research questions

- How can NH_3 dry deposition estimates be improved through synergistic use of the LOTOS-EUROS model and NH_3 satellite observations?

A combination of NH_3 total column observations from IASI and modelled NH_3 concentration and dry deposition fields from LOTOS-EUROS were used to compute satellite-derived NH_3 surface concentrations and dry deposition (hereafter referred to as the IASI-derived surface concentrations and dry deposition). The IASI-derived NH_3 surface concentrations were used to identify regions with large model-satellite discrepancies. In these regions, systematic over-, or underestimations in modelled NH_3 concentrations were observed, potentially indicating errors in the current emission inventories for NH_3. The validation of the IASI-derived NH_3 surface concentrations and dry deposition fluxes was, however, hampered by the limited amount, and uneven distribution, of available in-situ measurements. A comparison to the available set of NH_3 surface concentrations measurements in Europe showed no significant or consistent improvement in the IASI-derived NH_3 surface concentrations compared to the originally modelled NH_3 surface concentrations from LOTOS-EUROS. The derivation of NH_3 surface concentrations and dry deposition fluxes from IASI satellite observations using some form of inferential modelling (incorporated in CTMs or standalone) could be very useful in remote regions or regions where NH_3 emissions estimates are highly uncertain or even lacking. Otherwise, these methods might not be viable at this time, particularly due to the relatively low sensitivity to near-surface NH_3 of the IASI instrument and the high uncertainty in surface-atmosphere exchange schemes for NH_3.

- How does the integration of satellite-derived LAI and z_0 values improve modelled N_r deposition fields in LOTOS-EUROS?

Several satellite products were used to derive more realistic, dynamic input values for the roughness length (z_0) and the leaf-area-index (LAI) values, to be used in the computation of the deposition fluxes in LOTOS-EUROS instead of fixed, land-use specific values. The monthly LAI input values were computed with the MODIS-LAI product (MCD15A2H). For short vegetation types (e.g., grass, arable land), the monthly z_0 input maps were a function of the MODIS-NDVI (MYD13A3) product. For forest, a combination of satellite-derived forest canopy heights and MODIS-LAI were used. The default and satellite-derived z_0 values were compared to z_0 values computed at FLUXNET sites. Overall, the root-mean-squared-difference (RMSD) decreased from 0.76 (default z_0) to 0.60 (satellite-derived z_0). The largest improvements were found for forests. Here, the RMSD decreased from 1.23 (default z_0) to 0.96 (satellite-derived z_0). The satellite-derived z_0 values for forests showed the most spatial variation. For example, a clear latitudinal

gradient with increasing z_0 values towards the south of Germany was observed, which is related to the relatively tall trees here. The integration of these satellite-derived LAI and z_0 input maps in LOTOS-EUROS led to distinct changes in the modelled total N_r deposition of up to ∼30 % compared to the default runs and an overall shift from wet to dry deposition. The N_r deposition fields were especially sensitive to changes in the LAI input values. The largest impacts were observed in the modelled land-use-specific N_r deposition fields. The changes in modelled total N_r deposition for forests ranged for instance from approximately −3 up to +2 kg N ha^{-1} yr^{-1} for deciduous forests and even over −3 kg N ha^{-1} yr^{-1} for coniferous forests. To conclude, the use of satellite products to derive LAI and z_0 values is a promising way to represent the surface characterization in CTMs more accurately, which is a step towards better N_r deposition estimates from CTMs by reducing the uncertainty related to the used input parameters.

- How can integration and assimilation of NH_3 satellite observations improve the spatio-temporal distribution of modelled NH_3 fields in LOTOS-EUROS?

To improve the modelled spatio-temporal distributions of the modelled NH_3 fields, CrIS-NH_3 satellite observations were integrated into the LOTOS-EUROS chemistry transport model in two different ways. The first method directly used NH_3 surface concentrations from CrIS to fit spatially varying NH_3 emission time factors, that were used to redistribute the model input NH_3 emissions over the year. Comparison to in-situ observations (NH_3 surface concentrations, NH_4^+ wet deposition) showed that this relatively simple, ad-hoc method can improve the temporal distribution of NH_3 input emissions locally. This method is especially useful in agricultural-intensive regions during spring (March to May), where it can be successfully used to estimate the onset and duration of the NH_3 spring peak. The second method used column concentrations from CrIS in a top-down approach to adjust the model input NH_3 emissions through a Local Ensemble Transform Kalman Filter (LETKF). The strength of this method primarily lies in fine-tuning pre-existing NH_3 emission patterns, and in that way improving the spatial distribution of the modelled NH_3 fields. The two methods were also combined in a two-step approach, i.e., first rescaling the NH_3 time factors before assimilating the CrIS-NH_3 columns. This setup enhanced the adaptability of the LETKF and led to the most significant improvements compared to the in-situ observations. To conclude, integration and data assimilation of the CrIS-NH_3 product with the methods presented here improved the temporal representativity of modelled NH_3 fields in LOTOS-EUROS. This led to better constraints on the N_r budget, especially in agricultural areas.

- What is the effect of nitrogen deposition on the drought response of gross primary production at European FLUXNET forest sites?

The response of gross primary production (GPP) to drought at European FLUXNET forest sites was quantified using different soil water availability indicators (e.g., Standardized Precipitation Evapotranspiration Index (SPEI), soil volumetric water). A differential response in the used drought indicators across forest sites with different dominant species was observed. Moreover, the variation in nitrogen deposition levels at similar forest sites (e.g., with the same dominant tree species) was very limited. The group of FLUXNET forest sites with *Pinus* trees as dominant species had the largest variation in nitrogen deposition. At these sites, the GPP drought response

could be predicted with the mean annual temperature (MAT), the mean annual precipitation (MAP), and the forest age. The effect of nitrogen deposition, however, could not be isolated. Although the effect of nitrogen deposition on forest GPP in itself was very apparent and coherent, no consistent or significant relationship between nitrogen deposition and the drought response of forest GPP arose from our analysis. To conclude, nitrogen deposition is a clear driver of forest GPP. However, because of the differential response of forest types to drought and the limited variation in nitrogen deposition levels at the European FLUXNET sites, no consistent positive nor negative nitrogen deposition effects on the drought response of GPP were observed.

6.3 Discussion and outlook

Most of this thesis (Chapter 2, 3 and 4) was devoted to reducing the uncertainty in nitrogen deposition estimates through synergetic use of satellite observations and CTMs. In addition, the effect of nitrogen deposition on the drought response of gross primary production at European FLUXNET forest sites was studied (Chapter 5). Here, the results are discussed and suggestions for follow-up research are given.

Uncertainties in modelled N_r fields

The two most important sources of uncertainty in the deposition computation in CTMs are the input emissions and the process descriptions. The emissions used in CTMs are a source of substantial uncertainties (Reis et al., 2009; Behera et al., 2013). Due to the large spatiotemporal variability and the diverse nature of agricultural sources, the uncertainty of NH_3 emissions is relatively high compared to other trace gases. The reported uncertainty of the European national annual total NH_3 emissions is estimated to be at least around ±30 %, versus ±10 % for SO_2 emissions and ±20 % for NO_x emissions (Kuenen et al., 2014, EMEP, 2016). Many counties, however, have limited research on their national emission inventory and the uncertainty can therefore be much larger. National emission inventories may for instance be incomplete and miss emissions from certain sources. In addition, emissions at a single point in space and time have a much larger uncertainty due to assumptions made in the spatio-temporal redistribution of the national emissions. Several studies have indicated an overall underestimation of both anthropogenic and natural NH_3 emissions in the current inventories (e.g., see Dammers et al., 2019). Globally, satellite-derived emissions of large agricultural and industrial NH_3 point sources are for instance estimated to be ~2.5 times higher than the reported emissions (Dammers et al., 2019).

Satellite observations of NH_3 concentrations from CrIS and IASI can help to improve the spatial distribution of the NH_3 input emissions. They can for instance be used to detect missing NH_3 point sources and to identify regions with large model-satellite discrepancies. In these regions, structural differences are likely attributed to under- or overestimations in NH_3 emissions. The methods presented in Chapter 2 and 4 of this work involved identifying systematic errors in the NH_3 emissions using these satellite products. Data assimilation algorithms can correct NH_3 emissions according to satellite observations within the uncertainty limits of a CTM. In Chapter 4 of this work, the NH_3 emissions in LOTOS-EUROS were constrained by assimilation of CrIS-NH_3 observations using a Local Ensemble Transform Kalman Filter (LETKF) approach. Our results, however, illustrated that data assimilation algorithms similar to the LETKF alone cannot sufficiently correct for missing NH_3 emission sources, given the current set of observations. This method proved to be mainly useful for refining existing NH_3 patterns in regions where the spatial

distribution of the NH_3 emissions is relatively well known, such as the Netherlands. For better results, a two-step approach with an initial scaling of the NH_3 base emissions could be tested in areas with systematic under- or overestimations in modelled NH_3 distributions. Another method would be to first identify missing or incorrect NH_3 emission sources with source-fitting methods (like Van Damme et al., 2018, Dammers et al., 2019) and include those in the existing NH_3 emissions before data assimilation.

Our results showed that the annual averages of the modelled and the observed NH_3 concentrations and wet deposition in Europe agree fairly well in background situations, but show larger discrepancies in intensive agriculture areas (see Chapter 2 and 4). In western Europe (the Netherlands, Belgium and Germany), the spatial distribution of the NH_3 concentrations observed by IASI and CrIS roughly coincide with the modelled concentrations when averaged over longer periods. However, these satellite observations point out several regions with large underestimations in modelled NH_3 concentrations, likely due to missing NH_3 emission sources. Moreover, in the majority of the regions with similar long-term spatial patterns, these satellite instruments observe higher NH_3 concentrations. Here, too, there appears to be an underestimation in modelled NH_3 emissions. Looking at the temporal distribution, the differences between the observed and modelled NH_3 concentrations become even larger. In this aspect there is still a lot of room for improvement. For one, the assumed annual time factors of the modelled NH_3 emissions seem to be incorrect. Our results for instance showed that the spring peak of agricultural NH_3 emissions is too steep in LOTOS-EUROS. For another, the NH_3 time profiles in CTMs are typically static and spatially invariant. Chapter 4 illustrated that the temporal distribution of NH_3 emissions in CTMs can be improved using satellite observed NH_3 concentrations. Because of the satellite footprint of the current NH_3 observing instrument, however, this method can only be used when modelling at a relatively coarse spatial resolution. Also, it does not provide much insight into the time profiles of individual sources. Another way to improve the temporal distribution of NH_3 emissions is the use of dynamic time profiles that are linked to different agricultural practices (see Ge et al., 2020). This would be especially advantageous for higher resolution modelling in CTMs. Moreover, detailed information from satellites can be utilized to refine bottom-up NH_3 emission inventories. Satellite observations could for instance potentially improve NH_3 emissions by providing information about meteorological circumstances (e.g., temperature, wind speed, precipitation) or the soil conditions. Observations from recent satellite missions like Sentinel-2 provide high-resolution land cover and crop type maps. These maps could for example be of use to CTMs to represent the surface or to estimate NH_3 emissions related to certain agricultural practices (Ge et al., 2021, submitted).

On the larger scale, the uncertainty in the emissions likely dominates the uncertainty in the modelled deposition. The total emissions of a certain trace gas on a country level are for example more or less equivalent to its deposition, particularly for large countries. Further away from source regions, or in regions with relatively good emission estimates, the uncertainty in the model process descriptions becomes increasingly important. For modelled deposition fields, this uncertainty largely stems from the used deposition schemes. The differences between NH_3 deposition schemes in CTMs are large and the complexity is typically low compared to the current level of process understanding (Flechard et al., 2013). Several multi-model studies have for instance illustrated large discrepancies between deposition fields (e.g., Flechard et al., 2011, Colette et al., 2017; Vivanco et al., 2018), with differences in dry deposition fluxes as large as a factor 2-3 (Flechard

et al., 2011). The computed deposition velocities for NH_3 may vary tremendously for certain land use categories, for instance for coniferous and mixed forests (Schrader and Brummer, 2014). In addition, the compensation point for NH_3 is regularly overlooked and not implemented.

Another source of uncertainty are the input parameters used in the deposition schemes, as was the focus of Chapter 3. Here, we illustrated that the modelled N_r deposition can already vary with up to ~30% as a result of using satellite-derived LAI and z_0 input values. For land use specific fluxes, the spatial differences were even larger. Chapter 3 illustrated that satellite observations can be used for a more realistic surface representation in CTMs, which in turn could lead to better local and land use specific N_r deposition estimates. In addition to this, further detailing of deposition schemes such as DEPAC could significantly improve deposition estimates, especially for certain ecosystem- or land use types. The DEPAC module currently only includes 9 land use categories, while land cover classification maps (e.g., CORINE, ESA CCI) typically have many more. As a result, a lot of information is lost in the translation. An improved distinction between ecosystem types in deposition modelling would also be beneficial for studying the effects of N_r deposition on an ecosystem level, as described in Chapter 5. A combination of further detailing of deposition schemes and the integration of satellite-derived input parameters would add a lot of spatial and temporal variation to vegetation and surface characteristics in CTMs that is not yet captured at this time.

To effectively utilize high resolution information from satellites and to further improve existing deposition schemes, however, more research is needed. Future research could focus on data-assimilation of several satellite products at once. Furthermore, different types of observations, such as ground observations of NH_3 concentrations or deposition measurements could be used in a data assimilation setting. In the end, when it comes to N_r, all processes in the nitrogen cascade are relevant and need to be better quantified. To this end, the alignment of atmospheric observations of different trace gases (e.g., NO_2 and SO_2 from TROPOMI) for simultaneous data assimilation in CTMs could also be helpful. As NH_3 plays a major role in the formation of secondary aerosols, assimilation of aerosol satellite products (e.g., aerosol optical depth (AOD)) can also help to improve modelled N_r fields.

Scarceness of available ground level observations

The scarceness of available in-situ observations is a recurring topic in this thesis. The number of available in-situ observations is especially limited for NH_3. One reason for this is that measuring NH_3 is challenging due to the high reactivity and sticky nature of the molecule. Several field campaigns have shown that the existing instruments have a relatively large uncertainty and bias (e.g., von Bobrutzki et al., 2010, Puchalski et al., 2011). In addition to this, the cost for obtaining, maintaining and operating the instruments can be high, especially for flux measurements. Such measurements, however, are vital for the validation of existing models, and importantly, to improve our understanding of ongoing processes.

To improve our understanding of the processes that govern the surface-atmosphere exchange of NH_3 as well as other N_r components, continuous micrometeorological flux measurements are needed (e.g., using the eddy-covariance technique or other techniques with high temporal resolution). Even though flux measurement networks for non-reactive greenhouse gases are common and already operational on a continental scale, flux measurements of N_r components are

still largely experimental with limited campaign durations (e.g., Zöll et al., 2016; Schrader et al., 2018, Moravek et al., 2019, Wintjen et al., 2020). A larger database of flux measurements could advance the development of surface-atmosphere exchange schemes and enable us to better validate existing inferential models. The high temporal resolution of eddy-covariance measurements (<1s) allows to identify and quantify processes taking place on short time scales, such as the bi-directional exchange of NH_3. In addition, simultaneous measurements of several N_r components at once would improve insight into other complex processes, e.g., chemistry, soil emissions or the quantification of direct N_r losses after field management.

The monitoring of NH_3 surface concentrations is relatively more common. However, from a global perspective, the number of available observations is still very limited, and the distribution is uneven. Even the Dutch network, one of the most extensive networks worldwide, cannot sufficiently capture the spatial and temporal variability in the NH_3 concentrations. The observations from the LML (Landelijk Meetnet Luchtkwaliteit) network have the temporal resolution needed to accurately monitor the variability of NH_3 concentrations in time. However, due to the small number of sites, this network is not representative of large regions. The MAN (Meetnet Ammoniak in Natuurgebieden) network, on the other hand, is very extended but misses much of the temporal variability of the NH_3 concentration because of its monthly resolution. Moreover, the spatial representativeness of the available observations is usually limited. NH_3 concentrations are highly variable in space and time and the observed NH_3 concentrations are therefore typically only representative for a relatively small, homogenous area. The MAN network, for example, only measures NH_3 concentrations in nature areas. The Dutch landscape, however, is very heterogeneous and nature areas are relatively small and scattered. Further extension of the Dutch network, for example also more MAN sites outside nature areas in agricultural or in urban areas, could improve its overall representativeness.

This would also lead to a fairer comparison to satellite observed or modelled NH_3 concentrations. The footprints of the atmospheric sounders used in this thesis (CrIS ~14km, IASI ~ 12km) are relatively coarse and satellite observations therefore miss the local, sub-footprint variability in the NH_3 concentrations, especially over heterogeneous terrain. The same applies to modelled concentrations. Here, too, the spatial resolution almost always exceeds the footprint of individual in-situ measurements by far.

Deriving NH_3 surface concentrations and fluxes from satellites

In Chapter 2 of this work, a method to infer NH_3 surface concentrations and dry deposition fluxes from IASI-NH_3 satellite observations was presented. Over the past years, several studies have presented comparable methods for directly deriving dry deposition fluxes from satellite NH_3 concentrations, from either IASI or CrIS, using inferential modelling (e.g., Kharol et al., 2018, Lui et al., 2020). While a part of the uncertainty in this method is related to the uncertainty in the surface-atmosphere exchange parameterization, another part is due to the relatively low near-surface sensitivity of the current satellite instruments. Because of this, NH_3 surface concentrations estimates from satellites often heavily rely on assumptions. Compared to the IASI instrument, the CrIS instrument has lower instrumental noise and increased vertical sensitivity for near-surface NH_3. Still, the amount of independent information at the Earth's surface is limited and the retrieved NH_3 concentrations from the CrIS-NH_3 product contain a lot of information from a-priori profiles. The a-priori profiles used in the NH_3 retrieval algorithms often come either from CTMs or from

field campaigns. The vertical NH_3 profiles from CTMs, however, may be inaccurate due to, among other things, uncertainties in the underlying NH_3 emissions, the vertical mixing and horizontal transport of atmospheric NH_3. Vertical profile assumptions based on field campaigns may, on the other hand, not be representative for other regions. In the future, more field campaigns aimed at measuring the vertical distribution of atmospheric NH_3 should be organized to reduce this uncertainty.

Harmonizing existing NH_3 satellite products

Further research should focus on the simultaneous use of existing NH_3 satellite products, for instance IASI and CrIS. The two instruments have different overpass times (IASI in the morning, CrIS in the afternoon), making them ideal for complementary use. The IASI-NH_3 and CrIS-NH_3 products, however, use different retrieval strategies for NH_3. To maximize their scientific return, more research is needed to compare and harmonize the used NH_3 satellite retrievals. The intercomparison of the NH_3 satellite retrievals can be useful to map and potentially solve under- and overestimations in the existing NH_3 products. Moreover, harmonization of the NH_3 satellite products could help to minimize biases in retrieved NH_3 concentrations. First, this would lead to an increased number of available observations and higher spatial coverage, which would be advantageous in data assimilation applications. Second, several harmonized observations at different times of the day could be used to study the diurnal cycle of atmospheric NH_3. And lastly, it would lead to a longer, consistent time series of NH_3 concentrations, which could be used for trend analysis. Harmonizing several NH_3 satellite products could also be beneficial for methods presented in Chapter 4. The alignment of multiple datasets could for instance facilitate the fitting of local NH_3 time factors and could allow for further refinement of NH_3 emissions through data assimilation.

Future developments in NH_3 observing satellites

In the future, satellite instruments and retrievals are expected to further improve, and more accurate and higher resolution information from satellites will become available. Enhanced identification of NH_3 emission sources and emission strength with future satellites would be very helpful for improving the current NH_3 emission inventories. Future satellite instruments are expected to have a lower instrumental noise and a higher spectral resolution, which would improve the sensitivity to near-surface NH_3 and the overall accuracy of satellite-derived NH_3-products. The next generation IASI instrument, the IASI-NG instrument on board of the Metop-SG satellite to be launched in 2022, will for example have half the spectral resolution and spectral noise of the current IASI instruments. Like the instrumental characteristics (i.e., lower instrumental noise and higher spectral resolution), the footprints of future satellites are also expected to improve. Atmospheric sounders aboard geostationary satellites could for instance take more frequent observations over smaller areas, which could enhance the identification of NH_3 points sources and give more insight into the diurnal and seasonal cycle and atmospheric lifetime of NH_3. An example is for instance the MTG-S satellite that will be launched in 2022. This satellite will be the first to carry a hyperspectral infrared sounder (IRS) into a geostationary orbit, providing NH_3 observations at a high spatial (~4 by 4 km) and temporal (~hourly) resolution over Europe.

Nitrogen deposition – drought interactions in forests

In the previous chapter (Chapter 5), the influence of nitrogen deposition and drought on gross primary production in forest ecosystems was studied. Our results showed a differential response

of different forest types to drought, with no consistent positive nor negative nitrogen deposition effects. The main reasons for this were the large inter-site variability and the limited variation in nitrogen deposition levels at the European FLUXNET sites.

The interactions between nitrogen deposition and drought are regulated by many complex interactions that are determined by local factors. For the quantification of these interactions, it is relevant to have the right data representing these local scales. This thesis shows that there are limitations to the nitrogen deposition estimates and therefore most attention was given to improve these in this thesis. Furthermore, drought indices and carbon exchange data also yield uncertainty. The effect of drought varies tremendously depending on the type of forest, climatic conditions and edaphic conditions, and because of this, the choice for a drought index was difficult. The Standardized Precipitation Evapotranspiration Index (SPEI) used in our study is a statistical measure that expresses drought in terms of a departure from long-term conditions. This drought index accounts for precipitation and evaporative demand and is suitable for comparisons across different climatic zones. Furthermore, the main advantages of this product are its global coverage, needed for eventual upscaling, and its flexible temporal scale, allowing us to account for variable drought durations. However, it does not account for soil moisture storage, which is why the soil volumetric water layer was introduced in our study. Before arriving at this choice, two other global drought indices that do include the influence of soil moisture storage, the Palmer Drought Severity Index (PDSI) and the self-calibrating Palmer Drought Severity Index (scPDSI), were tested. However, using these indices, we also saw a similar, differential response in the gross primary production. To shed more light on the influence of the type of forest, drought indices from water balance models that account for variations in physiological and stand properties could be used (e.g., relative extractable water (REW), ratio of actual to potential transpiration (AT/PT ratio)). These indices contain information about the surface or vegetation properties and would represent the water balance at each forest site more realistically. However, these types of indices are more site-specific and therefore less suitable when comparing the effect of drought across sites with varying meteorological conditions. Moreover, these indices are more difficult to compute for larger scales and therefore less suitable for upscaling.

The gross primary production is studied as the response variable to drought in Chapter 5. The measurements at the FLUXNET sites represent the carbon exchange of the area surrounding the flux towers. The gross primary production therefore includes carbon uptake from trees, but also from other vegetation. Moreover, the gross primary production may also contain effects of other external factors that interact with drought stress, for instance insects and pathogens infestations, forest fires, species competition or forest management.

Furthermore, to effectively isolate nitrogen deposition-drought interactions, a more extensive measurement network of forests with similar edaphic, physiological and climatic conditions is needed. More nitrogen addition experiments in managed forest or measurements in forests with strong, local nitrogen deposition gradients could for example help us to get more insight into nitrogen deposition – drought interactions. In addition, to fully understand the availability of N_r in specific ecosystems, more observations of N_r in plant and soil pools are needed. For instance, more observations of the N_r content in soils or leaves could help us to get a better grip of the accumulated N_r in different forest compartments and could give more insight into the historic nitrogen deposition levels a forest has received.

In the current study setup, there is quite a mismatch in spatial representativeness between the FLUXNET observations and the used drought and nitrogen deposition estimates. The flux footprints are in the order of tens to hundreds of meters (Burba, 2001), whereas the modelled nitrogen deposition fields have a spatial resolution of tens of kilometers. To represent the nitrogen deposition levels more accurately, local, high-resolution observations at the same locations as the FLUXNET sites are needed. Another possibility to overcome this would be to repeat our analysis with large-scale carbon exchange estimates, for example from FLUXCOM (Jung et al., 2020), instead.

6.4 Summary

6.4.1 English summary

The nitrogen cycle has been severely disturbed by human activity. Reactive nitrogen emissions have tremendously increased in the last century, leading to increased amounts of nitrogen deposition on natural ecosystems. Several studies have demonstrated the influence of nitrogen deposition on growth, and vegetation responses to drought in natural ecosystems. The coupling of nitrogen deposition to carbon exchange and drought, however, is currently hampered by the relatively large uncertainty of the nitrogen deposition estimates. With the scarceness of available observations, nitrogen deposition estimates usually come from models, such as chemical transport models. These models, however, are known to involve relatively large uncertainties stemming from, among other things, used parameterization and input data (e.g., emissions, land surface input parameters). Satellite observations may help to improve nitrogen deposition estimates from models. In this thesis, we aim to improve modelled nitrogen deposition estimates from the LOTOS-EUROS chemical transport model by integration and assimilation of different types of satellite measurements. Several approaches to use atmospheric satellite observations of NH_3 concentrations and satellite-derived land surface parameters (leaf-area-index, roughness length) for nitrogen deposition modelling are presented.

In the first study, presented in Chapter 2, NH_3 total column observations from the IASI satellite instrument are used in combination with information from LOTOS-EUROS to compute satellite-derived NH_3 surface concentration and dry deposition fields. The IASI-derived NH_3 surface concentrations were used to identify regions with systematic over-, or underestimations in modelled NH_3 concentrations, indicating potential errors in the current emission inventory for NH_3. The comparison with available in-situ observations in Europe, however, showed no significant or consistent improvement in the IASI-derived concentrations compared to the originally modelled concentrations from LOTOS-EUROS. Here, our study illustrated that the application of this method might not be viable at this time, particularly due to the relatively low near-surface sensitivity of the current NH_3 observing instruments and the uncertainty in surface-atmosphere exchange schemes for NH_3.

In the second study, presented in Chapter 3, several satellite products were used to derive more realistic, dynamic input values for the roughness length (z_0) and the leaf-area-index (LAI) values. The satellite-derived z_0 values were validated with z_0 values at FLUXNET sites, showing an overall improvement compared to the default values used in LOTOS-EUROS. The z_0 and LAI values were integrated in LOTOS-EUROS for the computation of deposition fluxes, instead of the fixed and land-use specific default values. Compared to the default model runs, this led to distinct changes in the modelled total N_r deposition of up to ~30 % and an overall shift from wet to dry deposition. Our results illustrated that the N_r deposition fields were especially sensitive to changes in the LAI input values. The changes for land use specific deposition fluxes were even greater, with particularly large changes in the modelled deposition fluxes over coniferous and deciduous forests.

In the third study, presented in Chapter 4, CrIS-NH_3 satellite observations were integrated into LOTOS-EUROS in two different ways. In the first method, the NH_3 surface concentrations from CrIS were used to fit spatially variant NH_3 emission time factors. This method proved to be especially useful in agricultural-intensive regions during spring, where it can be successfully used

to estimate the onset and duration of the NH_3 spring peak. In the second method, the NH_3 input emissions were refined in a top-down approach, using a Local Ensemble Transform Kalman Filter (LETKF) as data assimilation algorithm. The strength of this method primarily lies in fine-tuning existing NH_3 emission patterns, and in that way improving the spatial distribution of the modelled NH_3 fields. Both these methods, especially when combined, led to distinct improvements in the comparison with in-situ observations and showed strong potential to improve the NH_3 input emissions, and herewith modelled nitrogen deposition.

Lastly, in the fourth study, presented in Chapter 5, long-term, land-use specific, modelled nitrogen deposition estimates from LOTOS-EUROS were used to examine the interaction of nitrogen deposition and drought as co-stressors on gross primary production (GPP) at European FLUXNET forest sites. Our results showed that nitrogen deposition is a clear driver of GPP in forests. However, due to the differential response of various dominant forest types to drought and the limited variation in nitrogen deposition levels found at the FLUXNET sites, no consistent positive nor negative nitrogen deposition effects on the drought response of GPP could be isolated.

6.4.2 Dutch summary

De stikstofcyclus is ernstig verstoord door menselijk handelen. De afgelopen decennia zijn de emissies van reactief stikstof enorm toegenomen, wat heeft geleid tot meer stikstofdepositie op de natuur. Verschillende studies hebben aangetoond dat stikstofdepositie invloed heeft op vegetatiegroei, en de invloed van droogte hierop. De koppeling van stikstofdepositie aan koolstofuitwisseling, specifiek tijdens droogte, wordt echter bemoeilijkt door de relatief hoge onzekerheid van de huidige stikstofdepositieschattingen. Doordat er weinig waarnemingen beschikbaar zijn, zijn stikstofdepositieschattingen meestal afkomstig van modellen, bijvoorbeeld chemische transport modellen. Deze modellen brengen echter de nodige onzekerheid met zich mee, die onder meer voortvloeit uit de gebruikte procesbeschrijvingen en invoergegevens (bijvoorbeeld gebruikte emissies of landoppervlakte gegevens). Satellietwaarnemingen kunnen wellicht gebruikt worden om de stikstofdepositieschattingen van modellen te verbeteren. In dit proefschrift proberen wij gemodelleerde stikstofdepositieschattingen van het LOTOS-EUROS chemische transportmodel te verbeteren door integratie en assimilatie van verschillende soorten satellietmetingen. Wij presenteren verschillende manieren om gebruik te maken van atmosferische satellietwaarnemingen van ammoniakconcentraties en landoppervlaktegegevens van satellieten voor stikstofdepositiemodellering.

In het eerste onderzoek, beschreven in Hoofdstuk 2, werden NH_3 totale kolom waarnemingen van het IASI instrument gecombineerd met informatie van LOTOS-EUROS om satelliet afgeleide NH_3 grondconcentraties en droge depositievelden te bepalen. De IASI-afgeleide grondconcentraties werden vervolgens gebruikt om gebieden met systematische onder- of overschattingen in de gemodelleerde NH_3 concentraties te identificeren, wat wijst op mogelijke fouten in de gebruikte emissie inputdatabase voor NH_3. De vergelijking met beschikbare grondmetingen in Europa toonde echter aan dat er geen significante of consistente verbeteringen waren vergeleken met de oorspronkelijk gemodelleerde concentraties van LOTOS-EUROS. Ons onderzoek liet zien dat de toepassing van deze methode voor Europa op dit moment niet werkbaar is, voornamelijk door de relatief lage gevoeligheid van de huidige satellietinstrumenten voor NH_3 op grondniveau en de onzekerheid in de oppervlakte-atmosfeer uitwisselingsschema's voor NH_3.

In het tweede onderzoek, beschreven in Hoofdstuk 3, werden verschillende satellietproducten gebruikt om realistische, dynamische invoerwaarden voor de ruwheidslengte (z_0) en de bladoppervlakte-index (LAI) af te leiden. De satelliet afgeleide z_0 en de LAI waarden werden gevalideerd met z0 waarden van FLUXNET locaties. Dit liet een algehele verbetering zien ten opzichte van de standaard invoerwaarden gebruikt in LOTOS-EUROS. De z_0 en LAI waarden werden vervolgens geïntegreerd in LOTOS-EUROS voor de berekening van depositievelden. In vergelijking met de standaardversie van LOTOS-EUROS leidde dit tot veranderingen in de gemodelleerde stikstofdepositievelden van maximaal ~30% en een algehele verschuiving van natte naar droge depositie. Onze resultaten lieten zien dat de stikstofdepositie bijzonder gevoelig is voor veranderingen in LAI invoerwaarden. De veranderingen in landgebruikspecifieke depositievelden waren nog groter, met name boven naald- en loofbossen.

In het derde onderzoek, gepresenteerd in Hoofdstuk 4, werden NH_3 satelliet observaties van CrIS geïntegreerd in LOTOS-EUROS op twee verschillende manieren. In de eerste methode werden grondconcentraties van NH_3 van CrIS gebruikt om ruimtelijke variërende NH_3 emissietijdsfactoren te bepalen. Deze methode bleek vooral nuttig in regio's met intensieve landbouw in het voorjaar, waar het gebruikt kan worden om het begin en de duur van de NH_3 voorjaarsemissiepiek te schatten. In de tweede methode werden de NH_3 invoeremissies aangepast aan de hand van een Local Ensemble Transform Kalman Filter. De kracht van deze methode ligt in het verfijnen van bestaande emissiepatronen, waarmee de ruimtelijke verdeling van de gemodelleerde NH_3 velden verbeterd kan worden. De grootste verbetering in de vergelijking met gronddata was zichtbaar wanneer beide methoden gecombineerd werden.

In het vierde onderzoek, beschreven in hoofdstuk 5, hebben wij tenslotte de interactie tussen stikstofdepositie en droogte op de productiviteit van Europese bossen onderzocht, gebruik makende van FLUXNET-locaties en landgebruik specifieke stikstofdepositieschattingen uit LOTOS-EUROS. Onze resultaten lieten een duidelijk verband zien tussen stikstofdepositie en gross primary production (GPP) in bossen. Onze analyse kon echter geen consistente positieve of negatieve stikstofeffecten in de reactie van de GPP op droogte isoleren door de gevarieerde reactie op droogte van verschillende boomsoorten en de beperkte variatie in stikstofdepositie bij de FLUXNET-boslocaties.

References

Aber, J., McDowell, W., Nadelhoffer, K., Magill, A., Berntson, G., Kamakea, M., McNulty, S., Currie, W., Rustad, L., and Fernandez, I.: Nitrogen saturation in temperate forest ecosystems: hypotheses revisited, BioScience, 48, 921-934, 1998.

Aber, J., McDowell, W., Nadelhoffer, K., Magill, A., Berntson, G., Kamakea, M., McNulty, S., Currie, W., Rustad, L., and Fernandez, I.: Nitrogen saturation in temperate forest ecosystems: hypotheses revisited, BioScience, 48, 921-934, 1998.

Abida, R., Attié, J.-L., El Amraoui, L., Ricaud, P., Lahoz, W., Eskes, H., Segers, A., Curier, L., de Haan, J., Kujanpää, J., Nijhuis, A. O., Tamminen, J., Timmermans, R., and Veefkind, P.: Impact of spaceborne carbon monoxide observations from the S-5P platform on tropospheric composition analyses and forecasts, Atmos. Chem. Phys., 17, 1081–1103, https://doi.org/10.5194/acp-17-1081-2017, 2017.

Adams, C., McLinden, C. A., Shephard, M. W., Dickson, N., Dammers, E., Chen, J., Makar, P., Cady-Pereira, K. E., Tam, N., and Kharol, S. K.: Satellite-derived emissions of carbon monoxide, ammonia, and nitrogen dioxide from the 2016 Horse River wildfire in the Fort McMurray area, Atmospheric Chemistry and Physics, 19, 2577-2599, 2019.

Adams, H. D., Zeppel, M. J., Anderegg, W. R., Hartmann, H., Landhäusser, S. M., Tissue, D. T., Huxman, T. E., Hudson, P. J., Franz, T. E., and Allen, C. D.: A multi-species synthesis of physiological mechanisms in drought-induced tree mortality, Nature ecology & evolution, 1, 1285-1291, 2017.

Albuquerque, W. G., Severino, L. S., BELTRAO, N. d. M., Azevedo, C. A., and Da Silva Filho, J. L.: Growth and biomass allocation of Jatropha curcas plants as influenced by nitrogen under different soil moisture regime, Embrapa Algodão-Artigo em periódico indexado (ALICE), 2013.

Ammann, C.: FLUXNET2015 CH-Oe1 Oensingen grassland, 2002–2008, Dataset, https://doi.org/10.18140/FLX/1440135, 2016.

Anderegg, W. R., Trugman, A. T., Badgley, G., Anderson, C. M., Bartuska, A., Ciais, P., Cullenward, D., Field, C. B., Freeman, J., and Goetz, S. J.: Climate-driven risks to the climate mitigation potential of forests, Science, 368, 2020.

Aubinet, M., Vesala, T., and Papale, D.: Eddy covariance: a practical guide to measurement and data analysis, Springer Science & Business Media, 2012.

Baker, I., Prihodko, L., Denning, A., Goulden, M., Miller, S., and Da Rocha, H.: Seasonal drought stress in the Amazon: Reconciling models and observations, Journal of Geophysical Research: Biogeosciences, 113, 2008.

Bala, G., Devaraju, N., Chaturvedi, R., Caldeira, K., and Nemani, R.: Nitrogen deposition: how important is it for global terrestrial carbon uptake?, Biogeosciences Discussions, 10, 2013.

Ballabio, C., Panagos, P., and Monatanarella, L.: Mapping topsoil physical properties at European scale using the LUCAS database, Geoderma, 261, 110-123, 2016.

Banzhaf, S., Schaap, M., Kerschbaumer, A., Reimer, E., Stern, R., Van Der Swaluw, E., and Builtjes, P.: Implementation and evaluation of pH-dependent cloud chemistry and wet deposition in the chemical transport model REM-Calgrid, Atmospheric Environment, 49, 378-390, 2012.

Barbu, A., Segers, A., Schaap, M., Heemink, A., and Builtjes, P.: A multi-component data assimilation experiment directed to sulphur dioxide and sulphate over Europe, Atmospheric Environment, 43, 1622-1631, 2009.

Bauer, S. E., Tsigaridis, K., and Miller, R.: Significant atmospheric aerosol pollution caused by world food cultivation, Geophys. Res. Lett., 43, 5394–5400, 2016.

Beer, R., Shephard, M. W., Kulawik, S. S., Clough, S. A., Eldering, A., Bowman, K. W., Sander, S. P., Fisher, B. M., Payne, V. H., and Luo, M.: First satellite observations of lower tropospheric ammonia and methanol, Geophysical Research Letters, 35, 2008.

Behera, S. N., Sharma, M., Aneja, V. P., and Balasubramanian, R.: Ammonia in the atmosphere: a review on emission sources, atmospheric chemistry and deposition on terrestrial bodies, Environ. Sci. Pollut. Res. Int., 20, 8092–8131, https://doi.org/10.1007/s11356-013-2051-9, 2013.

Behera, S. N., Sharma, M., Aneja, V. P., and Balasubramanian, R.: Ammonia in the atmosphere: a review on emission sources, atmospheric chemistry and deposition on terrestrial bodies, Environmental Science and Pollution Research, 20, 8092-8131, 2013.

Beirle, S., Borger, C., Dörner, S., Li, A., Hu, Z., Liu, F., Wang, Y., and Wagner, T.: Pinpointing nitrogen oxide emissions from space, Science advances, 5, eaax9800, 2019.

Berkhout, A. J., Swart, D., Volten, H., Gast, L. F., Haaima, M., Verboom, H., Stefess, G., Hafkenscheid, T., and Hoogerbrugge, R.: Replacing the AMOR with the miniDOAS in the ammonia monitoring network in the Netherlands, 2017.

Bernhofer, C., Grünwald, T., Moderow, U., Hehn, M., Eichelmann, U., and Prasse H.: FLUXNET2015 DE-Gri Grillenburg, 2004–2014, Dataset, https://doi.org/10.18140/FLX/1440147, 2016b.

Bernhofer, C., Grünwald, T., Moderow, U., Hehn, M., Eichelmann, U., and Prasse, H.: FLUXNET2015 DE-Kli Klingenberg, 2004–2014, Dataset, https://doi.org/10.18140/FLX/1440147, 2016c.

Bernhofer, C., Grünwald, T., Moderow, U., Hehn, M., Eichelmann, U., and Prasse, H.: FLUXNET2015 DE-Obe Oberbärenburg, 2008–2014, Dataset, https://doi.org/10.18140/FLX/1440151, 2016d.

Bernhofer, C., Grünwald, T., Moderow, U., Hehn, M., Eichelmann, U., and Prasse, H.: FLUXNET2015 DE-Tha Tharandt, 1996–2014, Dataset, https://doi.org/10.18140/FLX/1440152, 2016e.

Bernhofer, C., Grünwald, T., Moderow, U., Hehn, M., Eichelmann, U., Prasse, H., and Postel, U.: FLUXNET2015 DE-Akm Anklam, 2009–2014, Dataset, https://doi.org/10.18140/FLX/1440213, 2016a.

Berveiller, D., Delpierre, N., Dufrêne, E., Pontailler, J. Y., Vanbostal, L., Janvier, B., Mottet, L., and Cristinacce, K.: FLUXNET2015 FR-Fon Fontainebleau-Barbeau, 2005–2014, Dataset, https://doi.org/10.18140/FLX/1440161, 2016.

Bessagnet, B., Pirovano, G., Mircea, M., Cuvelier, C., Aulinger, A., Calori, G., Ciarelli, G., Manders, A., Stern, R., Tsyro, S., García Vivanco, M., Thunis, P., Pay, M.-T., Colette, A., Couvidat, F., Meleux, F., Rouïl, L., Ung, A., Aksoyoglu, S., Baldasano, J. M., Bieser, J., Briganti, G., Cappelletti, A., D'Isidoro, M., Finardi, S., Kranenburg, R., Silibello, C., Carnevale, C., Aas, W., Dupont, J.-C., Fagerli, H., Gonzalez, L., Menut, L., Prévôt, A. S. H., Roberts, P., and White, L.: Presentation of the EURODELTA III intercomparison exercise – evaluation of the chemistry transport models' performance on criteria pollutants and joint analysis with meteorology, Atmos. Chem. Phys., 16, 12667–12701, https://doi.org/10.5194/acp-16-12667-2016, 2016.

Blank, F. T.: Meetonzekerheid Landelijk Meetnet Luchtkwaliteit (LML), KEMA, 50050870-KPS/TCM 01-3063, 2001.

Bobbink, R., Hicks, K., Galloway, J., Spranger, T., Alkemade, R., Ashmore, M., Bustamante, M., Cinderby, S., Davidson, E., and Dentener, F.: Global assessment of nitrogen deposition effects on terrestrial plant diversity: a synthesis, Ecological applications, 20, 30-59, 2010.

Bobbink, R., Hicks, K., Galloway, J., Spranger, T., Alkemade, R., Ashmore, M., Bustamante, M., Cinderby, S., Davidson, E., Dentener, F., Emmett, B., Erisman, J. W., Fenn, M., Gilliam, F., Nordin, A., Pardo, L., and De Vries, W.: Global assessment of nitrogen deposition effects on terrestrial plant diversity: a synthesis, Ecol. Appl., 20, 30–59, https://doi.org/10.1890/08-1140.1, 2010b.

Bodelier, P. L., and Steenbergh, A. K.: Interactions between methane and the nitrogen cycle in light of climate change, Current Opinion in Environmental Sustainability, 9, 26-36, 2014.

Boggs, J. L., McNulty, S. G., Gavazzi, M. J., and Myers, J. M.: Tree growth, foliar chemistry, and nitrogen cycling across a nitrogen deposition gradient in southern Appalachian deciduous forests, Canadian Journal of Forest Research, 35, 1901-1913, 2005.

Bolle, H. and Streckenbach, B.: Flux estimates from remote sensing, The Echival Field Experiment in a Desertification Threatened Area (EFEDA), final report, 406–424, 1993.

Bonsall, M. B., Froyd, C. A., and Jeffers, E. S.: Resilience: nitrogen limitation, mycorrhiza and long-term palaeoecological plant–nutrient dynamics, Biology Letters, 16, 20190441, 2020.

Bouwman, L., Goldewijk, K. K., Van Der Hoek, K. W., Beusen, A. H., Van Vuuren, D. P., Willems, J., Rufino, M. C., and Stehfest, E.: Exploring global changes in nitrogen and phosphorus cycles in agriculture induced by livestock production over the 1900–2050 period, Proceedings of the National Academy of Sciences, 110, 20882-20887, 2013.

Brümmer, C., Lucas-Moffat, A. M., Herbst, M., and Kolle, O.: FLUXNET2015 DE-Geb Gebesee, 2001–2014, Dataset, https://doi.org/10.18140/FLX/1440146, 2016.

Brutsaert, W.: Evaporation into the atmosphere: theory, history and applications, Springer Science & Business Media, 2013.

Businger, J. A., Wyngaard, J. C., Izumi, Y., and Bradley, E. F.: Flux-profile relationships in the atmospheric surface layer, J. Atmos. Sci., 28, 181–189, 1971.

Butterbach-Bahl, K., Gundersen, P., Ambus, P., Augustin, J., Beier, C., Boeckx, P., Dannenmann, M., Sanchez Gimeno, B., Ibrom, A., and Kiese, R.: Nitrogen processes in terrestrial ecosystems, in: The European nitrogen assessment: sources, effects and policy perspectives, Cambridge University Press, 99-125, 2011.

Butterbach-Bahl, K., Nemitz, E., Zaehle, S., Billen, G., Boeckx, P., Erisman, J. W., Garnier, J., Upstill-Goddard, R., Kreuzer, M., and Oenema, O.: Nitrogen as a threat to the European greenhouse gas balance, in: The European nitrogen assessment: sources, effects and policy perspectives, Cambridge University Press, 434–462, 2011.

Buttlar, J. v., Zscheischler, J., Rammig, A., Sippel, S., Reichstein, M., Knohl, A., Jung, M., Menzer, O., Arain, M. A., and Buchmann, N.: Impacts of droughts and extreme-temperature events on gross primary production and ecosystem respiration: a systematic assessment across ecosystems and climate zones, Biogeosciences, 15, 1293-1318, 2018.

Cao, H., Henze, D. K., Shephard, M. W., Dammers, E., Cady-Pereira, K., Alvarado, M., Lonsdale, C., Luo, G., Yu, F., and Zhu, L.: Inverse modeling of NH3 sources using CrIS remote sensing measurements, Environmental Research Letters, 15, 104082, 2020.

Chapin, F. S., Woodwell, G. M., Randerson, J. T., Rastetter, E. B., Lovett, G. M., Baldocchi, D. D., Clark, D. A., Harmon, M. E., Schimel, D. S., and Valentini, R.: Reconciling carbon-cycle concepts, terminology, and methods, Ecosystems, 9, 1041-1050, 2006.

Chen, Q., Jia, L., Hutjes, R., and Menenti, M. Estimation of aerodynamic roughness length over oasis in the Heihe River Basin by utilizing remote sensing and ground data. Remote Sensing, 7(4), 3690-3709, 2015.

Clarisse, L., Clerbaux, C., Dentener, F., Hurtmans, D., and Coheur, P.-F.: Global ammonia distribution derived from infrared satellite observations, Nature Geoscience, 2, 479-483, 2009.

Claussen, M.: Area-averaging of surface fluxes in a neutrally stratified, horizontally inhomogeneous atmospheric boundary-layer, Atmos. Environ., 24, 1349–1360, 1990.

Clerbaux, C., Boynard, A., Clarisse, L., George, M., Hadji-Lazaro, J., Herbin, H., Hurtmans, D., Pommier, M., Razavi, A., Turquety, S., Wespes, C., and Coheur, P.-F.: Monitoring of atmospheric composition using the thermal infrared IASI/MetOp sounder, Atmos. Chem. Phys., 9, 6041–6054, https://doi.org/10.5194/acp-9-6041-2009, 2009.

Colette, A., Andersson, C., Manders, A., Mar, K., Mircea, M., Pay, M.-T., Raffort, V., Tsyro, S., Cuvelier, C., Adani, M., Bessagnet, B., Bergström, R., Briganti, G., Butler, T., Cappelletti, A., Couvidat, F., D'Isidoro, M., Doumbia, T., Fagerli, H., Granier, C., Heyes, C., Klimont, Z., Ojha, N., Otero, N., Schaap, M., Sindelarova, K., Stegehuis, A. I., Roustan, Y., Vautard, R., van Meijgaard, E., Vivanco, M. G., and Wind, P.: EURODELTA-Trends, a multi-model experiment of air quality hindcast in Europe over 1990–2010, Geosci. Model Dev., 10, 3255–3276, https://doi.org/10.5194/gmd-10-3255-2017, 2017.

Conn, A. R., Gould, N. I., and Toint, P. L.: Trust region methods, SIAM, 2000.

Copernicus Climate Change Service: ERA5-Land hourly data from 2001 to present [Data set]. ECMWF (Ed.), 2019.

Copernicus Climate Change Service: European State of the Climate (ESOTC): https://climate.copernicus.eu/ESOTC, access: 06-06-2021, 2021.

Curier, R., Kranenburg, R., Segers, A., Timmermans, R., and Schaap, M.: Synergistic use of OMI NO2 tropospheric columns and LOTOS–EUROS to evaluate the NOx emission trends across Europe, Remote Sens. Environ., 149, 58–69, 2014.

Dammers, E., McLinden, C. A., Griffin, D., Shephard, M. W., Van Der Graaf, S., Lutsch, E., Schaap, M., Gainairu-Matz, Y., Fioletov, V., Van Damme, M., Whitburn, S., Clarisse, L., Cady-Pereira, K., Clerbaux, C., Coheur, P. F., and Erisman, J. W.: NH3 emissions from large point sources derived from CrIS and IASI satellite observations, Atmos. Chem. Phys., 19, 12261–12293, https://doi.org/10.5194/acp-19-12261-2019, 2019.

Dammers, E., Palm, M., Van Damme, M., Vigouroux, C., Smale, D., Conway, S., Toon, G. C., Jones, N., Nussbaumer, E., Warneke, T., Petri, C., Clarisse, L., Clerbaux, C., Hermans, C., Lutsch, E., Strong, K., Hannigan, J. W., Nakajima, H., Morino, I., Herrera, B., Stremme, W., Grutter, M., Schaap, M., Wichink Kruit, R. J., Notholt, J., Coheur, P.-F., and Erisman, J. W.: An evaluation of IASI-NH3 with ground-based Fourier transform infrared spectroscopy measurements, Atmos. Chem. Phys., 16, 10351–10368, https://doi.org/10.5194/acp-16-10351-2016, 2016.

Dammers, E., Schaap, M., Haaima, M., Palm, M., Kruit, R. J. W., Volten, H., Hensen, A., Swart, D., and Erisman, J. W.: Measuring atmospheric ammonia with remote sensing campaign: Part 1-Characterisation of vertical ammonia concentration profile in the centre of The Netherlands, Atmos. Environ., 169, 97–112, https://doi.org/10.1016/j.atmosenv.2017.08.067, 2017a.

Dammers, E., Shephard, M. W., Palm, M., Cady-Pereira, K., Capps, S., Lutsch, E., Strong, K., Hannigan, J. W., Ortega, I., Toon, G. C., Stremme, W., Grutter, M., Jones, N., Smale, D., Siemons, J., Hrpcek, K., Tremblay, D., Schaap, M., Notholt, J., and Erisman, J. W.: Validation of the CrIS fast physical NH3 retrieval with ground-based FTIR, Atmos. Meas. Tech., 10, 2645–2667, https://doi.org/10.5194/amt-10-2645-2017, 2017b.

Davi, H., Soudani, K., Deckx, T., Dufrene, E., Le Dantec, V., and Francois, C.: Estimation of forest leaf area index from SPOT imagery using NDVI distribution over forest stands, Int. J. Remote Sens., 27, 885–902, 2006.

De Ligne, A., Manise, T., Heinesch, B., Aubinet, M., and Vincke, C.: FLUXNET2015 BE-Vie Vielsalm, 1996–2014, Dataset, https://doi.org/10.18140/FLX/1440130, 2016b.

De Ligne, A., Manise, T., Moureaux, C., Aubinet, M., and Heinesch, B.: FLUXNET2015 BE-Lon Lonzee, 2004–2014, Dataset, https://doi.org/10.18140/FLX/1440129, 2016a.

de Vries, W., and Schulte-Uebbing, L.: Impacts of nitrogen deposition on forest ecosystem services and biodiversity, in: Atlas of Ecosystem Services, Springer, 183-189, 2019.

de Vries, W., Du, E., and Butterbach-Bahl, K.: Short and long-term impacts of nitrogen deposition on carbon sequestration by forest ecosystems, Current Opinion in Environmental Sustainability, 9, 90-104, 2014.

de Vries, W., Solberg, S., Dobbertin, M., Sterba, H., Laubhann, D., Van Oijen, M., Evans, C., Gundersen, P., Kros, J., and Wamelink, G.: The impact of nitrogen deposition on carbon sequestration by European forests and heathlands, Forest Ecology and Management, 258, 1814-1823, 2009.

den Bril, B. V., Meremans, D., and Roekens, E.: A Monitoring Network on Acidification in Flanders, Belgium, TheScientificWorldJOURNAL, 11, 2358-2363, 2011.

Denier van der Gon, H. A. C., Hendriks, C., Kuenen, J., Segers, A., and Visschedijk, A.: Description of current temporal emission patterns and sensitivity of predicted AQ for temporal emission patterns, TNO Report, 2011.

Dentener, F., Drevet, J., Lamarque, J. F., Bey, I., Eickhout, B., Fiore, A. M., Hauglustaine, D., Horowitz, L. W., Krol, M., Kulshrestha, U. C., Lawrence, M., Galy-Lacaux, C., Rast, S., Shindell, D., Stevenson, D., Van Noije, T., Atherton, C., Bell, N., Bergman, D., Butler, T., Cofala, J., Collins, B., Doherty, R., Ellingsen, K., Galloway, J., Gauss, M., Montanaro, V., Muller, J. F., Pitari, G., Rodriguez, J., Sanderson, M., Solmon, F., Strahan, S., Schultz, M., Sudo, K., Szopa, S., and Wild, O.: Nitrogen and sulfur deposition on regional and

global scales: A multimodel evaluation, Global Biogeochem. Cy., 20, Gb4003, https://doi.org/10.1029/2005gb002672, 2006a.

Dentener, F., Stevenson, D., Ellingsen, K., van Noije, T., Schultz, M., Amann, M., Atherton, C., Bell, N., Bergmann, D., Bey, I., Bouwman, L., Butler, T., Cofala, J., Collins, B., Drevet, J., Doherty, R., Eickhout, B., Eskes, H., Fiore, A., Gauss, M., Hauglustaine, D., Horowitz, L., Isaksen, I. S. A., Josse, B., Lawrence, M., Krol, M., Lamarque, J. F., Montanaro, V., Muller, J. F., Peuch, V. H., Pitari, G., Pyle, J., Rast, S., Rodriguez, J., Sanderson, M., Savage, N. H., Shindell, D., Strahan, S., Szopa, S., Sudo, K., Van Dingenen, R., Wild, O., and Zeng, G.: The global atmospheric environment for the next generation, Environ. Sci. Technol., 40, 3586–3594, https://doi.org/10.1021/es0523845, 2006b.

DeSoto, L., Cailleret, M., Sterck, F., Jansen, S., Kramer, K., Robert, E. M., Aakala, T., Amoroso, M. M., Bigler, C., and Camarero, J. J.: Low growth resilience to drought is related to future mortality risk in trees, Nature communications, 11, 1-9, 2020.

Didan, K.: MYD13A3 MODIS/Aqua Vegetation Indices Monthly L3 Global 1 km SIN Grid V006, NASA EOSDIS LP DAAC, https://doi.org/10.5067/MODIS/MYD13A3.006, 2015.

Dolman, H., Hendriks, D., Parmentier, F. J., Marchesini, L. B., Dean, J., and van Huissteden, K.: FLUXNET2015 NL-Hor Horstermeer, 2004–2011, Dataset, https://doi.org/10.18140/FLX/1440177, 2016.

Drewniak, B., and Gonzalez-Meler, M. A.: Earth system model needs for including the interactive representation of nitrogen deposition and drought effects on forested ecosystems, Forests, 8, 267, 2017.

Dušek, J., Janouš, D., and Pavelka, M.: FLUXNET2015 CZ-wet Trebon (CZECHWET), 2006–2014, Dataset, https://doi.org/10.18140/FLX/1440145, 2016.

ECMWF: European Centre for Medium-Range Weather Forecasts Annual report, 2016.

EEA: European Union emission inventory report 1990–2014 under the UNECE Convention on Long-range Transboundary Air Pollution (LRTAP), EEA Report, 16, https://doi.org/10.2800/628267, 2016.

Ehtesham, E., and Bengtson, P.: Decoupling of soil carbon and nitrogen turnover partly explains increased net ecosystem production in response to nitrogen fertilization, Scientific reports, 7, 46286, 2017.

Elvir, J. A., Rustad, L., Wiersma, G. B., Fernandez, I., White, A. S., and White, G. J.: Eleven-year response of foliar chemistry to chronic nitrogen and sulfur additions at the Bear Brook Watershed in Maine, Canadian Journal of Forest Research, 35, 1402-1410, 2005.

Emberson, L., Simpson, D., Tuovinen, J., Ashmore, M., and Cambridge, H.: Towards a model of ozone deposition and stomatal uptake over Europe, EMEP MSC-W Note, 6, 1–57, 2000.

EMEP: The European Monitoring and Evaluation Programme EMEP Status Report, 2016.

Erisman, J. and Schaap, M.: The need for ammonia abatement with respect to secondary PM reductions in Europe, Environ. Pollut., 129, 159–163, 2004.

Erisman, J. W. and Draaijers, G. P. J.: Atmospheric deposition in relation to acidification and eutrophication, Elsevier, 1995.

Erisman, J. W., and Draaijers, G. P.: Atmospheric deposition: in relation to acidification and eutrophication, Elsevier, 1995.

Erisman, J. W., and Duyzer, J. A micrometeorological investigation of surface exchange parameters over heathland. Boundary-layer meteorology, 57(1-2), 115-128, 1991.

Erisman, J. W., Galloway, J., Dice, N. B., Sutton, M., Bleeker, A., Grizzetti, B., Leach, A., and de Vries, W.: Nitrogen: too much of a vital resource, Science Brief, WWF Netherlands, Zeist, The Netherlands, 2015.

Erisman, J. W., Galloway, J., Seitzinger, S., Bleeker, A., and Butterbach-Bahl, K.: Reactive nitrogen in the environment and its effect on climate change, Current Opinion in Environmental Sustainability, 3, 281-290, 2011.

Erisman, J. W., Sutton, M. A., Galloway, J., Klimont, Z., and Winiwarter, W.: How a century of ammonia synthesis changed the world, Nat. Geosci., 1, 636–639, https://doi.org/10.1038/ngeo325, 2008.

Erisman, J. W., Van Pul, A., and Wyers, P.: Parametrization of surface resistance for the quantification of atmospheric deposition of acidifying pollutants and ozone, Atmos. Environ., 28, 2595–2607, 1994.

Erisman, J. W.: Acid deposition to nature areas in the Netherlands: Part I Methods and results, Water Air Soil. Poll., 71, 51–80, 1993.

Erisman, J., and Schaap, M.: The need for ammonia abatement with respect to secondary PM reductions in Europe, Environmental Pollution, 129, 159-163, 2004.

Erisman, J., Bleeker, A., Galloway, J., and Sutton, M.: Reduced nitrogen in ecology and the environment, Environmental pollution, 150, 140-149, 2007.

Erisman, J.-W., Vermetten, A. W., Asman, W. A., Waijers-Ijpelaan, A., and Slanina, J.: Vertical distribution of gases and aerosols: the behaviour of ammonia and related components in the lower atmosphere, Atmospheric Environment (1967), 22, 1153-1160, 1988.

European Environment Agency: EMEP/EEA air pollutant emission inventory guidebook 2019. Technical guidance to prepare national emission inventories, 2019.

European Environmental Agency: Airbase dataset, available at: http://discomap.eea.europa.eu (last access: 1 March 2020), 2019.

European Environmental Agency: CLC2012 Addendum to CLC2006 Technical Guidelines, EEA Report, 2014.

Evangeliou, N., Balkanski, Y., Eckhardt, S., Cozic, A., Van Damme, M., Coheur, P.-F., Clarisse, L., Shephard, M., Cady-Pereira, K., and Hauglustaine, D.: 10-year satellite-constrained fluxes of ammonia improve performance of chemistry transport models, Atmospheric Chemistry and Physics, 21, 4431-4451, 2021.

Evans, J. R.: Photosynthesis and nitrogen relationships in leaves of C 3 plants, Oecologia, 78, 9-19, 1989.

Evensen, G.: The ensemble Kalman filter: Theoretical formulation and practical implementation, Ocean dynamics, 53, 343-367, 2003.

Fang, H., Wei, S., and Liang, S.: Validation of MODIS and CYCLOPES LAI products using global field measurement data, Remote Sens. Environ., 119, 43–54, 2012.

Farquhar, G. D., Firth, P. M., Wetselaar, R., and Weir, B.: On the gaseous exchange of ammonia between leaves and the environment: determination of the ammonia compensation point, Plant Physiology, 66, 710-714, 1980.

Fernández-Martínez, M., Vicca, S., Janssens, I. A., Sardans, J., Luyssaert, S., Campioli, M., Chapin III, F. S., Ciais, P., Malhi, Y., and Obersteiner, M.: Nutrient availability as the key regulator of global forest carbon balance, Nature Climate Change, 4, 471-476, 2014.

Fioletov, V., McLinden, C. A., Kharol, S. K., Krotkov, N. A., Li, C., Joiner, J., Moran, M. D., Vet, R., Visschedijk, A. J., and Denier van der Gon, H. A.: Multi-source SO2 emission retrievals and consistency of satellite and surface measurements with reported emissions, Copernicus GmbH, 2017.

Fisher, J. B., Badgley, G., and Blyth, E.: Global nutrient limitation in terrestrial vegetation, Global Biogeochemical Cycles, 26, 2012.

Flechard, C. R., Ibrom, A., Skiba, U. M., de Vries, W., van Oijen, M., Cameron, D. R., Dise, N. B., Korhonen, J. F. J., Buchmann, N., Legout, A., Simpson, D., Sanz, M. J., Aubinet, M., Loustau, D., Montagnani, L., Neirynck, J., Janssens, I. A., Pihlatie, M., Kiese, R., Siemens, J., Francez, A.-J., Augustin, J., Varlagin, A., Olejnik, J., Juszczak, R., Aurela, M., Berveiller, D., Chojnicki, B. H., Dämmgen, U., Delpierre, N., Djuricic, V., Drewer, J., Dufrêne, E., Eugster, W., Fauvel, Y., Fowler, D., Frumau, A., Granier, A., Gross, P., Hamon, Y., Helfter, C., Hensen, A., Horváth, L., Kitzler, B., Kruijt, B., Kutsch, W. L., Lobo-do-Vale, R., Lohila, A., Longdoz, B., Marek, M. V., Matteucci, G., Mitosinkova, M., Moreaux, V., Neftel, A., Ourcival, J.-M., Pilegaard, K., Pita, G., Sanz, F., Schjoerring, J. K., Sebastià, M.-T., Tang, Y. S., Uggerud, H., Urbaniak, M., van Dijk, N., Vesala, T., Vidic, S., Vincke, C., Weidinger, T., Zechmeister-Boltenstern, S., Butterbach-Bahl, K., Nemitz, E., and Sutton, M. A.: Carbon–nitrogen interactions in European forests and semi-natural vegetation – Part 1: Fluxes and budgets of carbon, nitrogen and greenhouse gases from ecosystem monitoring and modelling, Biogeosciences, 17, 1583–1620, https://doi.org/10.5194/bg-17-1583-2020, 2020.

Flechard, C. R., Nemitz, E., Smith, R. I., Fowler, D., Vermeulen, A. T., Bleeker, A., Erisman, J. W., Simpson, D., Zhang, L., Tang, Y. S., and Sutton, M. A.: Dry deposition of reactive nitrogen to European ecosystems: a comparison of inferential models across the NitroEurope network, Atmos. Chem. Phys., 11, 2703–2728, https://doi.org/10.5194/acp-11-2703-2011, 2011.

Flechard, C. R., Van Oijen, M., Cameron, D. R., de Vries, W., Ibrom, A., Buchmann, N., Dise, N. B., Janssens, I. A., Neirynck, J., and Montagnani, L.: Carbon-nitrogen interactions in European forests and semi-natural vegetation-Part 2: Untangling climatic, edaphic, management and nitrogen deposition effects on carbon sequestration potentials, Biogeosciences, 17, 1621-2020, 2020.

Flechard, C., Massad, R.-S., Loubet, B., Personne, E., Simpson, D., Bash, J., Cooter, E., Nemitz, E., and Sutton, M.: Advances in understanding, models and parameterizations of biosphere-atmosphere ammonia exchange, in: Review and Integration of Biosphere-Atmosphere Modelling of Reactive Trace Gases and Volatile Aerosols, Springer, 11–84, 2013.

Fleischer, K., Wårlind, D., Van der Molen, M. K., Rebel, K. T., Arneth, A., Erisman, J. W., Wassen, M. J., Smith, B., Gough, C. M., and Margolis, H. A.: Low historical nitrogen deposition effect on carbon sequestration in the boreal zone, Journal of Geophysical Research: Biogeosciences, 120, 2542-2561, 2015.

Fowler, D., Cape, J., and Unsworth, M.: Deposition of atmospheric pollutants on forests, Philosophical Transactions of the Royal Society of London. B, Biological Sciences, 324, 247-265, 1989.

Fowler, D., Coyle, M., Skiba, U., Sutton, M. A., Cape, J. N., Reis, S., Sheppard, L. J., Jenkins, A., Grizzetti, B., and Galloway, J. N.: The global nitrogen cycle in the twenty-first century, Philosophical Transactions of the Royal Society B: Biological Sciences, 368, 20130164, 2013.

Fowler, D., Coyle, M., Skiba, U., Sutton, M. A., Cape, J. N., Reis, S., Sheppard, L. J., Jenkins, A., Grizzetti, B., Galloway, J. N., Vitousek, P., Leach, A., Bouwman, A. F., Butterbach-Bahl, K., Dentener, F., Stevenson, D., Amann, M., and Voss, M.: The global nitrogen cycle in the twenty-first century, Philos. T. Roy. Soc. B, 368, 20130164, https://doi.org/10.1098/rstb.2013.0164, 2013.

Fowler, D., Duyzer, J., and Baldocchi, D.: Inputs of trace gases, particles and cloud droplets to terrestrial surfaces, Proceedings of the Royal Society of Edinburgh, Section B: Biological Sciences, 97, 35-59, 1990.

Fowler, D., Steadman, C. E., Stevenson, D., Coyle, M., Rees, R. M., Skiba, U. M., Sutton, M. A., Cape, J. N., Dore, A. J., Vieno, M., Simpson, D., Zaehle, S., Stocker, B. D., Rinaldi, M., Facchini, M. C., Flechard, C. R., Nemitz, E., Twigg, M., Erisman, J. W., Butterbach-Bahl, K., and Galloway, J. N.: Effects of global change during the 21st century on the nitrogen cycle, Atmos. Chem. Phys., 15, 13849–13893, https://doi.org/10.5194/acp-15-13849-2015, 2015.

Friedlingstein, P., Meinshausen, M., Arora, V. K., Jones, C. D., Anav, A., Liddicoat, S. K., and Knutti, R.: Uncertainties in CMIP5 climate projections due to carbon cycle feedbacks, Journal of Climate, 27, 511-526, 2014.

Gallagher, M., Nemitz, E., Dorsey, J., Fowler, D., Sutton, M., Flynn, M., and Duyzer, J.: Measurements and parameterizations of small aerosol deposition velocities to grassland, arable crops, and forest: Influence of surface roughness length on deposition, J. Geophys. Res.-Atmos., 107, AAC 8-1–AAC 8-10, https://doi.org/10.1029/2001JD000817, 2002.

Gallego, F. J.: A population density grid of the European Union, Popul. Environ., 31, 460–473, https://doi.org/10.1007/s11111-010-0108-y, 2010.

Galloway, J. N., Aber, J. D., Erisman, J. W., Seitzinger, S. P., Howarth, R. W., Cowling, E. B., and Cosby, B. J.: The nitrogen cascade, Bioscience, 53, 341–356, https://doi.org/10.1641/0006-3568(2003)053[0341:Tnc]2.0.Co;2, 2003.

Galloway, J. N., Dentener, F. J., Capone, D. G., Boyer, E. W., Howarth, R. W., Seitzinger, S. P., Asner, G. P., Cleveland, C. C., Green, P., and Holland, E. A.: Nitrogen cycles: past, present, and future, Biogeochemistry, 70, 153–226, 2004.

Galloway, J. N., Townsend, A. R., Erisman, J. W., Bekunda, M., Cai, Z. C., Freney, J. R., Martinelli, L. A., Seitzinger, S. P., and Sutton, M. A.: Transformation of the nitrogen cycle: Recent trends, questions, and potential solutions, Science, 320, 889–892, https://doi.org/10.1126/science.1136674, 2008.

Gessler, A., Schaub, M., and McDowell, N. G.: The role of nutrients in drought-induced tree mortality and recovery, New Phytologist, 214, 513-520, 2017.

Giannakis, E., Kushta, J., Giannadaki, D., Georgiou, G. K., Bruggeman, A., and Lelieveld, J.: Exploring the economy-wide effects of agriculture on air quality and health: evidence from Europe, Science of The Total Environment, 663, 889-900, 2019.

Gilberto, P., Trotta, C., Eleonora, C., Housen, C., Christianson, D., You-Wei, C., Poindexter, C., Chen, J., Abdelrahman, E., and Humphrey, M.: The FLUXNET2015 dataset and the ONEFlux processing pipeline for eddy covariance data, Scientific Data, 7, 2020.

González de Andrés, E.: Interactions between climate and nutrient cycles on forest response to global change: The role of mixed forests, Forests, 10, 609, 2019.

González de Andrés, E.: Interactions between climate and nutrient cycles on forest response to global change: The role of mixed forests, Forests, 10, 609, 2019.

Graaf, S. C., Dammers, E., Schaap, M., and Erisman, J. W.: How are NH 3 dry deposition estimates affected by combining the LOTOS-EUROS model with IASI-NH 3 satellite observations?, Atmospheric Chemistry and Physics, 18, 13173-13196, 2018.

Graf, A., van de Boer, A., Moene, A., and Vereecken, H. Intercomparison of methods for the simultaneous estimation of zero-plane displacement and aerodynamic roughness length from single-level eddy-covariance data. Boundary-layer meteorology, 151(2), 373-387, 2014.

Granier, C., Darras, S., van der Gon, H. D., Jana, D., Elguindi, N., Bo, G., Michael, G., Marc, G., Jalkanen, J.-P., and Kuenen, J.: The Copernicus Atmosphere Monitoring Service global and regional emissions (April 2019 version), 2019.

Hanson, P. J., and Weltzin, J. F.: Drought disturbance from climate change: response of United States forests, Science of the total environment, 262, 205-220, 2000.

Hanson, P. J., Tschaplinski, T. J., Wullschleger, S. D., and Auge, R. M.: The resilience of upland-oak forest canopy trees to chronic and acute precipitation manipulations, e-Gen. Tech. Rep. SRS–101. US Department of Agriculture, Forest Service, Southern Research Station: 3-2012, 2007.

Hatfield, J.: Large scale evapotranspiration from remotely sensed surface temperature, Planning Now for Irrigation and Drainage in the 21st Century, ASCE, 502–509, 1988.

Hendriks, C., Kranenburg, R., Kuenen, J. J. P., Van den Bril, B., Verguts, V., and Schaap, M.: Ammonia emission time profiles based on manure transport data improve ammonia modelling across north western Europe, Atmos. Environ., 131, 83–96, https://doi.org/10.1016/j.atmosenv.2016.01.043, 2016.

Hertel, D., Strecker, T., Müller-Haubold, H., and Leuschner, C.: Fine root biomass and dynamics in beech forests across a precipitation gradient–is optimal resource partitioning theory applicable to water-limited mature trees?, Journal of Ecology, 101, 1183-1200, 2013.

Hertel, O., Reis, S., Skjoth, C. A., Bleeker, A., Harrison, R., Cape, J. N., Fowler, D., Skiba, U., Simpson, D., and Jickells, T.: Nitrogen processes in the atmosphere, 2011.

Hertel, O., Skjøth, C., Reis, S., Bleeker, A., Harrison, R., Cape, J. N., Fowler, D., Skiba, U., Simpson, D., and Jickells, T.: Governing processes for reactive nitrogen compounds in the European atmosphere, Biogeosciences, 9, 4921-4954, 2012.

Högberg, P., Näsholm, T., Franklin, O., and Högberg, M. N.: Tamm Review: On the nature of the nitrogen limitation to plant growth in Fennoscandian boreal forests, Forest Ecology and Management, 403, 161-185, 2017.

Hörtnagl, L., Eugster, W., Buchmann, N., Paul-Limoges, E., Etzold S., and Haeni, M.: FLUXNET2015 CH-Lae Lägern, 2004–2014, Dataset, https://doi.org/10.18140/FLX/1440134, 2016c.

Hörtnagl, L., Feigenwinter, I., Fuchs, K., Merbold, L., Buchmann, N., Eugster, W., and Zeeman, M.: FLUXNET2015 CH-Cha Chamau, 2005–2014, Dataset, https://doi.org/10.18140/FLX/1440131, 2016a.

Hörtnagl, L., Feigenwinter, I., Fuchs, K., Merbold, L., Buchmann, N., Eugster, W., and Zeeman, M.: FLUXNET2015 CH-Fru Früebüel, 2005–2014, Dataset, https://doi.org/10.18140/FLX/1440133, 2016b.

Hörtnagl, L., Maier, R., Eugster, W., Buchmann, N., and Emmel, C.: FLUXNET2015 CH-Oe2 Oensingen crop, 2004–2014, Dataset, https://doi.org/10.18140/FLX/1440136, 2016d.

Houborg, R. and Boegh, E.: Mapping leaf chlorophyll and leaf area index using inverse and forward canopy reflectance modeling and SPOT reflectance data, Remote Sens. Environ., 112, 186–202, 2008.

Hunt, B. R., Kostelich, E. J., and Szunyogh, I.: Efficient data assimilation for spatiotemporal chaos: A local ensemble transform Kalman filter, Physica D: Nonlinear Phenomena, 230, 112-126, 2007.

Janssens, I., Dieleman, W., Luyssaert, S., Subke, J.-A., Reichstein, M., Ceulemans, R., Ciais, P., Dolman, A. J., Grace, J., and Matteucci, G.: Reduction of forest soil respiration in response to nitrogen deposition, Nature geoscience, 3, 315-322, 2010.

Janssens, I.: FLUXNET2015 BE-Bra Brasschaat, 1996–2014, Dataset, https://doi.org/10.18140/FLX/1440128, 2016.

Jonckheere, I., Fleck, S., Nackaerts, K., Muys, B., Coppin, P., Weiss, M., and Baret, F.: Review of methods for in situ leaf area index determination: Part I. Theories, sensors and hemispherical photography, Agr. Forest Meteorol., 121, 19–35, 2004.

Karlsson, P., Uddling, J., Braun, S., Broadmeadow, M., Elvira, S., Gimeno, B., Le Thiec, D., Oksanen, E., Vandermeiren, K., and Wilkinson, M.: New critical levels for ozone effects on young trees based on AOT40 and simulated cumulative leaf uptake of ozone, Atmospheric Environment, 38, 2283-2294, 2004.

Kharol, S. K., Shephard, M. W., McLinden, C. A., Zang, L., Sioris, C. E., O'Brien, J. M., Vet, R., Cady-Pereira, K. E., Hare, E., Siemons, J., and Krotkov, N. A.: Dry deposition of reactive nitrogen from satellite observations of ammonia and nitrogen dioxide over North America, Geophys. Res. Lett., 45, 1157–1166, https://doi.org/10.1002/2017GL075832, 2017.

Klatt, J., Schmid, H. P., Mauder, M., and Steinbrecher, R.: FLUXNET2015 DE-SfN Schechenfilz Nord, 2012–2014, Dataset, https://doi.org/10.18140/FLX/1440219, 2016.

Knohl, A., Tiedemann, F., Kolle, O., Schulze, E. D., Kutsch, W., Herbst, M., and Siebicke, L.: FLUXNET2015 DE-Hai Hainich, Dataset, https://doi.org/10.18140/FLX/1440148, 2016.

Kobayashi, H., Delbart, N., Suzuki, R., and Kushida, K.: A satellite-based method for monitoring seasonality in the overstory leaf area index of Siberian larch forest, J. Geophys. Res.-Biogeo., 115, G01002, https://doi.org/10.1029/2009JG000939, 2010.

Kronfuß, G., Polle, A., Tausz, M., Havranek, W., and Wieser, G.: Effects of ozone and mild drought stress on gas exchange, antioxidants and chloroplast pigments in current-year needles of young Norway spruce [Picea abies (L.) Karst.], Trees, 12, 482-489, 1998.

Kuenen, J. J. P., Visschedijk, A. J. H., Jozwicka, M., and Denier van der Gon, H. A. C.: TNO-MACC_II emission inventory; a multi-year (2003–2009) consistent high-resolution European emission inventory for air quality modelling, Atmos. Chem. Phys., 14, 10963–10976, https://doi.org/10.5194/acp-14-10963-2014, 2014.

Lamarque, J.-F., Dentener, F., McConnell, J., Ro, C.-U., Shaw, M., Vet, R., Bergmann, D., Cameron-Smith, P., Dalsoren, S., and Doherty, R.: Multi-model mean nitrogen and sulfur deposition from the Atmospheric Chemistry and Climate Model Intercomparison Project (ACCMIP): evaluation of historical and projected future changes, Atmospheric Chemistry and Physics, 13, 7997-8018, 2013.

Lankreijer, H., Hendriks, M., and Klaassen, W.: A comparison of models simulating rainfall interception of forests, Agr. Forest Meteorol., 64, 187–199, 1993.

Lelieveld, J., Evans, J. S., Fnais, M., Giannadaki, D., and Pozzer, A.: The contribution of outdoor air pollution sources to premature mortality on a global scale, Nature, 525, 367–371, 2015.

Lévesque, M., Rigling, A., Bugmann, H., Weber, P., and Brang, P.: Growth response of five co-occurring conifers to drought across a wide climatic gradient in Central Europe, Agricultural and Forest Meteorology, 197, 1-12, 2014.

Li, Y., Thompson, T. M., Van Damme, M., Chen, X., Benedict, K. B., Shao, Y., Day, D., Boris, A., Sullivan, A. P., Ham, J., Whitburn, S., Clarisse, L., Coheur, P.-F., and Collett Jr., J. L.: Temporal and spatial variability

of ammonia in urban and agricultural regions of northern Colorado, United States, Atmos. Chem. Phys., 17, 6197–6213, https://doi.org/10.5194/acp-17-6197-2017, 2017b.

Liu, L., Zhang, X., Xu, W., Liu, X., Wei, J., Wang, Z., and Yang, Y.: Global estimates of dry ammonia deposition inferred from space-measurements, Science of the Total Environment, 139189, 2020.

Liu, X., Fan, Y., Long, J., Wei, R., Kjelgren, R., Gong, C., and Zhao, J.: Effects of soil water and nitrogen availability on photosynthesis and water use efficiency of Robinia pseudoacacia seedlings, Journal of Environmental Sciences, 25, 585-595, 2013.

Lolkema, D. E., Noordijk, H., Stolk, A. P., Hoogerbrugge, R., van Zanten, M. C., and van Pul, W. A. J.: The Measuring Ammonia in Nature (MAN) network in the Netherlands, Biogeosciences, 12, 5133–5142, https://doi.org/10.5194/bg-12-5133-2015, 2015.

Lopez-Restrepo, S., Yarce, A., Pinel, N., Quintero, O., Segers, A., and Heemink, A.: Forecasting PM10 and PM2. 5 in the Aburrá Valley (Medellín, Colombia) via EnKF based data assimilation, Atmospheric Environment, 232, 117507, 2020.

Lu, M., Zhou, X., Luo, Y., Yang, Y., Fang, C., Chen, J., and Li, B.: Minor stimulation of soil carbon storage by nitrogen addition: a meta-analysis, Agriculture, ecosystems & environment, 140, 234-244, 2011.

Mailler, S., Menut, L., Khvorostyanov, D., Valari, M., Couvidat, F., Siour, G., Turquety, S., Briant, R., Tuccella, P., Bessagnet, B., Colette, A., Létinois, L., Markakis, K., and Meleux, F.: CHIMERE-2017: from urban to hemispheric chemistry-transport modeling, Geosci. Model Dev., 10, 2397–2423, https://doi.org/10.5194/gmd-10-2397-2017, 2017.

Majumdar, A. K. and Ricklin, J. C. (Eds.): Free-space laser communications: principles and advances, Vol. 2, Springer Science & Business Media, 2010.

Manders, A. M. M., Builtjes, P. J. H., Curier, L., Denier van der Gon, H. A. C., Hendriks, C., Jonkers, S., Kranenburg, R., Kuenen, J. J. P., Segers, A. J., Timmermans, R. M. A., Visschedijk, A. J. H., Wichink Kruit, R. J., van Pul, W. A. J., Sauter, F. J., van der Swaluw, E., Swart, D. P. J., Douros, J., Eskes, H., van Meijgaard, E., van Ulft, B., van Velthoven, P., Banzhaf, S., Mues, A. C., Stern, R., Fu, G., Lu, S., Heemink, A., van Velzen, N., and Schaap, M.: Curriculum vitae of the LOTOS–EUROS (v2.0) chemistry transport model, Geosci. Model Dev., 10, 4145–4173, https://doi.org/10.5194/gmd-10-4145-2017, 2017.

Manders, A., Builtjes, P., Curier, L., Denier Van Der Gon, H., Hendriks, C., Jonkers, S., Kranenburg, R., Kuenen, J., Segers, A., and Timmermans, R.: Curriculum vitae of the LOTOS–EUROS (v2. 0) chemistry transport model, Geosci. Model Dev., 10, 4145–4173. 2017.

Marécal, V., Peuch, V.-H., Andersson, C., Andersson, S., Arteta, J., Beekmann, M., Benedictow, A., Bergström, R., Bessagnet, B., and Cansado, A.: A regional air quality forecasting system over Europe: the MACC-II daily ensemble production, Geoscientific Model Development, 8, 2777-2813, 2015.

Martin-StPaul, N. K., Limousin, J. M., Vogt-Schilb, H., Rodríguez-Calcerrada, J., Rambal, S., Longepierre, D., and Misson, L.: The temporal response to drought in a Mediterranean evergreen tree: comparing a regional precipitation gradient and a throughfall exclusion experiment, Global change biology, 19, 2413-2426, 2013.

Mason, P.: The formation of areally-averaged roughness lengths, Q. J. Roy. Meteor. Soc., 114, 399–420, 1988.

Massad, R. S., Loubet, B., Tuzet, A., and Cellier, P.: Relationship between ammonia stomatal compensation point and nitrogen metabolism in arable crops: Current status of knowledge and potential modelling approaches, Environmental Pollution, 154, 390-403, 2008.

Maurer, K.D., Hardiman, B.S., Vogel, C.S. and Bohrer, G. Canopy-structure effects on surface roughness parameters: Observations in a Great Lakes mixed-deciduous forest. Agric. For. Meteorol, 177, 24–34, 2013.

McDowell, N., Pockman, W. T., Allen, C. D., Breshears, D. D., Cobb, N., Kolb, T., Plaut, J., Sperry, J., West, A., and Williams, D. G.: Mechanisms of plant survival and mortality during drought: why do some plants survive while others succumb to drought?, New phytologist, 178, 719-739, 2008.

McNaughton, K. G. and Van Den Hurk, B. J. J. M.: A “Lagrangian” revision of the resistors in the two-layer model for calculating the energy budget of a plant canopy, Bound.-Lay. Meteorol., 74, 261–288, https://doi.org/10.1007/bf00712121, 1995.

Meier, I. C., and Leuschner, C.: Belowground drought response of European beech: fine root biomass and carbon partitioning in 14 mature stands across a precipitation gradient, Global Change Biology, 14, 2081-2095, 2008.

Meyer-Grünefeldt, M., Calvo, L., Marcos, E., von Oheimb, G., and Härdtle, W.: Impacts of drought and nitrogen addition on Calluna heathlands differ with plant life-history stage, Journal of Ecology, 103, 1141-1152, 2015.

Moors, E. and Elbers, J.: FLUXNET2015 NL-Loo Loobos, 1996–2014, Dataset, https://doi.org/10.18140/FLX/1440178, 2016.

Moran, M. S.: A satellite-based approach for evaluation of the spatial distribution of evapotranspiration from agricultural lands, PhD thesis, University of Arizona, Tucson, USA, 1990.

Moravek, A., Singh, S., Pattey, E., Pelletier, L., and Murphy, J. G.: Measurements and quality control of ammonia eddy covariance fluxes: a new strategy for high-frequency attenuation correction, Atmos. Meas. Tech., 12, 6059–6078, https://doi.org/10.5194/amt-12-6059-2019, 2019.

Myhre, G., Samset, B. H., Schulz, M., Balkanski, Y., Bauer, S., Berntsen, T. K., Bian, H., Bellouin, N., Chin, M., and Diehl, T.: Radiative forcing of the direct aerosol effect from AeroCom Phase II simulations, Atmospheric Chemistry and Physics, 13, 1853-1877, 2013.

Myneni, R., Knyazikhin, Y., and Park, T.: MCD15A2H MODIS/Terra+Aqua Leaf Area Index/FPAR 8-day L4 Global 500m SIN Grid V006, NASA EOSDIS Land Processes DAAC, https://doi.org/10.5067/MODIS/MCD15A2H.006, 2015.

Nakai, T., Sumida, A., Daikoku, K. i., Matsumoto, K., van der Molen, M. K., Kodama, Y., Kononov, A. V., Maximov, T. C., Dolman, A. J., and Yabuki, H.: Parameterisation of aerodynamic roughness over boreal, cool-and warm-temperate forests, Agr. Forest Meteorol., 148, 1916–1925, 2008.

Nassar, R., Hill, T. G., McLinden, C. A., Wunch, D., Jones, D. B., and Crisp, D.: Quantifying CO2 emissions from individual power plants from space, Geophysical Research Letters, 44, 10,045-010,053, 2017.

Nemitz, E., Milford, C., and Sutton, M. A.: A two-layer canopy compensation point model for describing bi-directional biosphere-atmosphere exchange of ammonia, Quarterly Journal of the Royal Meteorological Society, 127, 815-833, 2001.

Nemitz, E., Sutton, M. A., Schjoerring, J. K., Husted, S., and Wyers, G. P.: Resistance modelling of ammonia exchange over oilseed rape, Agricultural and Forest Meteorology, 105, 405-425, 2000.

NOAA (National Oceanic and Atmospheric Administration): State of the Climate: Global Climate Report for Annual 2013, available at: https://www.ncdc.noaa.gov/sotc/global/201313, last access: 1 July 2018.

NOAA (National Oceanic and Atmospheric Administration): State of the Climate: Global Climate Report for Annual 2014, available at: https://www.ncdc.noaa.gov/sotc/global/201413, last access: 1 July 2018.

Nowlan, C. R., Martin, R. V., Philip, S., Lamsal, L. N., Krotkov, N. A., Marais, E. A., Wang, S., and Zhang, Q.: Global dry deposition of nitrogen dioxide and sulfur dioxide inferred from space-based measurements, Global Biogeochem. Cy., 28, 1025–1043, https://doi.org/10.1002/2014gb004805, 2014.

Oren, R., Ellsworth, D. S., Johnsen, K. H., Phillips, N., Ewers, B. E., Maier, C., Schäfer, K. V., McCarthy, H., Hendrey, G., and McNulty, S. G.: Soil fertility limits carbon sequestration by forest ecosystems in a CO 2-enriched atmosphere, Nature, 411, 469-472, 2001.

Paerl, H. W., Gardner, W. S., McCarthy, M. J., Peierls, B. L., and Wilhelm, S. W.: Algal blooms: noteworthy nitrogen, Science, 346, p. 175, 2014.

Palatova, E.: Effect of increased nitrogen depositions and drought stress on the development of Scots pine (Pinus sylvestris L.)–II. Root system response, J. For. Sci, 48, 237-247, 2002.

Pan, Y., Birdsey, R. A., Fang, J., Houghton, R., Kauppi, P. E., Kurz, W. A., Phillips, O. L., Shvidenko, A., Lewis, S. L., and Canadell, J. G.: A large and persistent carbon sink in the world's forests, Science, 333, 988-993, 2011.

Papale, D., Reichstein, M., Aubinet, M., Canfora, E., Bernhofer, C., Kutsch, W., Longdoz, B., Rambal, S., Valentini, R., and Vesala, T.: Towards a standardized processing of Net Ecosystem Exchange measured with eddy covariance technique: algorithms and uncertainty estimation, Biogeosciences, 3, 571-583, 2006.

Pastorello, G., Papale, D., Chu, H., Trotta, C., Agarwal, D., Canfora, E., Baldocchi, D., and Torn, M.: The FLUXNET2015 dataset: The longest record of global carbon, water, and energy fluxes is updated, EOS T. Am. Geophys. Un., 98, https://doi.org/10.1029/2017EO071597, 2017.

Picon, C., Guehl, J.-M., and Ferhi, A.: Leaf gas exchange and carbon isotope composition responses to drought in a drought-avoiding (Pinus pinaster) and a drought-tolerant (Quercus petraea) species under present and elevated atmospheric CO2 concentrations, Plant, Cell & Environment, 19, 182-190, 1996.

Plate, E. J.: Aerodynamic Characteristics of Atmospheric Boundary Layers, Argonne National Lab., Ill. Karlsruhe Univ., 1971.

Pope III, C. A., Ezzati, M., and Dockery, D. W.: Fine-particulate air pollution and life expectancy in the United States, New England Journal of Medicine, 360, 376-386, 2009.

Pregitzer, K. S., Burton, A. J., Zak, D. R., and Talhelm, A. F.: Simulated chronic nitrogen deposition increases carbon storage in Northern Temperate forests, Global change biology, 14, 142-153, 2008.

Raupach, M.: Simplified expressions for vegetation roughness length and zero-plane displacement as functions of canopy height and area index, Bound.-Lay. Meteorol., 71, 211–216, 1994.

Rees, W. G.: Physical principles of remote sensing, Cambridge university press, 2013.

Reichstein, M., Falge, E., Baldocchi, D., Papale, D., Aubinet, M., Berbigier, P., Bernhofer, C., Buchmann, N., Gilmanov, T., and Granier, A.: On the separation of net ecosystem exchange into assimilation and ecosystem respiration: review and improved algorithm, Global change biology, 11, 1424-1439, 2005.

Reis, S., Pinder, R. W., Zhang, M., Lijie, G., and Sutton, M. A.: Reactive nitrogen in atmospheric emission inventories, Atmos. Chem. Phys., 9, 7657–7677, https://doi.org/10.5194/acp-9-7657-2009, 2009.

Rijksdienst voor Ondernemend Nederland (RVO): Wanneer mest uitrijden: https://www.rvo.nl/onderwerpen/agrarisch-ondernemen/mest/gebruiken-en-uitrijden/wanneer-mest-uitrijden, access: 8th April, 2021.

Rijksinstituut voor Volksgezondheid en Milieu: Landelijk Meetnet Luchtkwaliteit, available at: http://www.lml.rivm.nl/, last access: 15 November 2017.

Rockstrom, J., Steffen, W., Noone, K., Persson, A., Chapin III, F. S., Lambin, E. F., Lenton, T. M., Scheffer, M., Folke, C., and Schellnhuber, H. J.: A safe operating space for humanity: identifying and quantifying planetary boundaries that must not be transgressed could help prevent human activities from causing unacceptable environmental change, argue Johan Rockstrom and colleagues, Nature, 461, 472-476, 2009.

Rodgers, C. D., and Connor, B. J.: Intercomparison of remote sounding instruments, Journal of Geophysical Research: Atmospheres, 108, 2003.

Rodgers, C.: Inverse methods for atmospheric sounding–Theory and practice, Ser. on Atmos. Oceanic and Planet, Phys, 2000.

Sala, A., Piper, F., and Hoch, G.: Physiological mechanisms of drought-induced tree mortality are far from being resolved, The New Phytologist, 186, 274-281, 2010.

Schaap, M., Banzhaf, S., Scheuschner, T., Geupel, M., Hendriks, C., Kranenburg, R., Nagel, H.-D., Segers, A. J., von Schlutow, A., Wichink Kruit, R., and Builtjes, P. J. H.: Atmospheric nitrogen deposition to terrestrial ecosystems across Germany, Biogeosciences Discuss., https://doi.org/10.5194/bg-2017-491, in review, 2017.

Schaap, M., Hendriks, C., Kranenburg, R., Kuenen, J., Segers, A., Schlutow, A., Nagel, H.-D., Ritter, A., and Banzhaf, S.: PINETI-3: Modellierung und Kartierung atmosphärischer Stoffeinträge von 2000 bis 2015

zur Bewertung der ökosystem-spezifischen Gefährdung von Biodiversität in Deutschland, Umweltbundesamt, 2018.

Schaap, M., Manders, A., Hendricks, J. M., Cnossen, A. J. S., Segers, H. A. C., Denier van der Gon, M., Jozwicka, M., Sauter, F., Velders, G., Matthijsen, J., and Builtjes, P.: Regional modelling of particulate matter for the Netherlands, Netherlands Research Program on Particulate Matter, 500099008, 2009.

Schaap, M., Manders, M., Hendriks, E., Cnossen, J., Segers, A., van der Gon, H. D., Jozwicka, M., Sauter, F., Velders, G., and Mathijssen, J.: Regional modelling of particulate matter for the Netherlands, Technical Report BOP, 2008.

Schaap, M., Manders, M., Hendriks, E., Cnossen, J., Segers, A., van der Gon, H. D., Jozwicka, M., Sauter, F., Velders, G., and Mathijssen, J.: Regional modelling of particulate matter for the Netherlands, Technical Report BOP, 2009.

Schaap, M., Timmermans, R. M., Roemer, M., Boersen, G., Builtjes, P., Sauter, F., Velders, G., and Beck, J.: The LOTOS? EUROS model: description, validation and latest developments, International Journal of Environment and Pollution, 32, 270-290, 2008.

Schaap, M., Wichink Kruit, R., Hendriks, C., Kranenburg, R., Segers, A., Builtjes, P., Banzhaf, S., Scheuschner, T., and Nagel, H.: Modelling and assessment of acidifying and eutrophying atmospheric deposition to terrestrial ecosystems (PINETI2)–Part I: Atmospheric deposition to German natural and seminatural ecosystems during 2009, 2010 and 2011, UBA-Project No.(FKZ), 3712, 240-241, 2017.

Scharnweber, T., Manthey, M., Criegee, C., Bauwe, A., Schröder, C., and Wilmking, M.: Drought matters–Declining precipitation influences growth of Fagus sylvatica L. and Quercus robur L. in north-eastern Germany, Forest Ecology and Management, 262, 947-961, 2011.

Schaudt, K. and Dickinson, R.: An approach to deriving roughness length and zero-plane displacement height from satellite data, prototyped with BOREAS data, Agr. Forest Meteorol., 104, 143–155, 2000.

Schimel, J., Balser, T. C., and Wallenstein, M.: Microbial stress-response physiology and its implications for ecosystem function, Ecology, 88, 1386-1394, 2007.

Schmidt, M. and Graf, A.: FLUXNET2015 DE-RuR Rollesbroich, 2011–2014, Dataset, https://doi.org/10.18140/FLX/1440215, 2016a.

Schmidt, M. and Graf, A.: FLUXNET2015 DE-RuS Selhausen Juelich, 2011–2014, Dataset, https://doi.org/10.18140/FLX/1440216, 2016b.

Schneider, K. and Schmidt, M.: FLUXNET2015 DE-Seh Selhausen, 2007–2010, Dataset, https://doi.org/10.18140/FLX/1440217, 2016.

Schrader, F. and Brummer, C.: Land Use Specific Ammonia Deposition Velocities: a Review of Recent Studies (2004–2013), Water Air Soil Poll., 225, 2114, https://doi.org/10.1007/s11270-014-2114-7, 2014.

Schrader, F., Brümmer, C., Flechard, C. R., Wichink Kruit, R. J., van Zanten, M. C., Zöll, U., Hensen, A., and Erisman, J. W.: Non-stomatal exchange in ammonia dry deposition models: comparison of two state-of-the-art approaches, Atmos. Chem. Phys., 16, 13417–13430, https://doi.org/10.5194/acp-16-13417-2016, 2016.

Schrader, F., Schaap, M., Zöll, U., Kranenburg, R., and Brümmer, C.: The hidden cost of using low-resolution concentration data in the estimation of NH 3 dry deposition fluxes, Scientific reports, 8, 1-11, 2018.

Schulte-Uebbing, L., and de Vries, W.: Global-scale impacts of nitrogen deposition on tree carbon sequestration in tropical, temperate, and boreal forests: A meta-analysis, Global Change Biology, 24, e416-e431, 2018.

Schulze, E.-D.: Air pollution and forest decline in a spruce (Picea abies) forest, Science, 244, 776-783, 1989.

Schwalm, C. R., Williams, C. A., Schaefer, K., Arneth, A., Bonal, D., Buchmann, N., Chen, J., Law, B. E., Lindroth, A., and Luyssaert, S.: Assimilation exceeds respiration sensitivity to drought: A FLUXNET synthesis, Global Change Biology, 16, 657-670, 2010.

Seinfeld, J. H.: ES&T books: atmospheric chemistry and physics of air pollution, Environmental science & technology, 20, 863-863, 1986.

Selman, M., Sugg, Z., and Greenhalgh, S.: Eutrophication and Hypoxia in Coastal Areas, 2008.

Sevanto, S., Hölttä, T., and Holbrook, N. M.: Effects of the hydraulic coupling between xylem and phloem on diurnal phloem diameter variation, Plant, Cell & Environment, 34, 690-703, 2011.

Shephard, M. W. and Cady-Pereira, K. E.: Cross-track Infrared Sounder (CrIS) satellite observations of tropospheric ammonia, Atmos. Meas. Tech., 8, 1323–1336, https://doi.org/10.5194/amt-8-1323-2015, 2015.

Shephard, M. W., Dammers, E., Cady-Pereira, K. E., Kharol, S. K., Thompson, J., Gainariu-Matz, Y., Zhang, J., McLinden, C. A., Kovachik, A., and Moran, M.: Ammonia measurements from space with the Cross-track Infrared Sounder: characteristics and applications, Atmospheric Chemistry and Physics, 20, 2277-2302, 2020.

Shephard, M., and Cady-Pereira, K.: Cross-track Infrared Sounder (CrIS) satellite observations of tropospheric ammonia, Atmospheric Measurement Techniques, 8, 2015.

Shin, S., Kang, J.-S., and Jo, Y.: The local ensemble transform Kalman filter (LETKF) with a global NWP model on the cubed sphere, Pure and Applied Geophysics, 173, 2555-2570, 2016.

Silva, J., Ribeiro, C., and Guedes, R.: Roughness length classification of Corine Land Cover classes, Proceedings of the European Wind Energy Conference, Milan, Italy, 710, p. 110, 2007.

Simard, M., Pinto, N., Fisher, J. B., and Baccini, A.: Mapping forest canopy height globally with spaceborne lidar, J. Geophys. Res.-Biogeo., 116, G04021, https://doi.org/10.1029/2011jg001708, 2011.

Simpson, D., Benedictow, A., Berge, H., Bergström, R., Emberson, L. D., Fagerli, H., Flechard, C. R., Hayman, G. D., Gauss, M., Jonson, J. E., Jenkin, M. E., Nyíri, A., Richter, C., Semeena, V. S., Tsyro, S., Tuovinen, J.-P., Valdebenito, Á., and Wind, P.: The EMEP MSC-W chemical transport model – technical description, Atmos. Chem. Phys., 12, 7825–7865, https://doi.org/10.5194/acp-12-7825-2012, 2012.

Sintermann, J., Dietrich, K., Häni, C., Bell, M., Jocher, M., and Neftel, A.: A miniDOAS instrument optimised for ammonia field measurements, Atmos. Meas. Tech., 9, 2721–2734, https://doi.org/10.5194/amt-9-2721-2016, 2016.

Skjøth, C. A., Geels, C., Berge, H., Gyldenkærne, S., Fagerli, H., Ellermann, T., Frohn, L. M., Christensen, J., Hansen, K. M., Hansen, K., and Hertel, O.: Spatial and temporal variations in ammonia emissions – a freely accessible model code for Europe, Atmos. Chem. Phys., 11, 5221–5236, https://doi.org/10.5194/acp-11-5221-2011, 2011.

Smil, V.: Enriching the earth: Fritz Haber, Carl Bosch, and the transformation of world food production, MIT press, 2001.

Smith, V. H., and Schindler, D. W.: Eutrophication science: where do we go from here?, Trends in ecology & evolution, 24, 201-207, 2009.

Søgaard, H. T., Sommer, S. G., Hutchings, N., Huijsmans, J., Bussink, D., and Nicholson, F.: Ammonia volatilization from field-applied animal slurry—the ALFAM model, Atmospheric Environment, 36, 3309-3319, 2002.

Someya, Y., Imasu, R., Shiomi, K., and Saitoh, N.: Atmospheric ammonia retrieval from the TANSO-FTS/GOSAT thermal infrared sounder, Atmospheric Measurement Techniques, 13, 309-321, 2020.

Soudani, K., François, C., Le Maire, G., Le Dantec, V., and Dufrêne, E.: Comparative analysis of IKONOS, SPOT, and ETM+ data for leaf area index estimation in temperate coniferous and deciduous forest stands, Remote Sens. Environ., 102, 161–175, 2006.

Speich, M. J.: Quantifying and modeling water availability in temperate forests: a review of drought and aridity indices, iForest-Biogeosciences and Forestry, 12, 1, 2019.

Spindler, G., Teichmann, U., and Sutton, M. A.: Ammonia dry deposition over grassland-micrometeorological flux-gradient measurements and bidirectional flux calculations using an inferential model, Q. J. Roy. Meteor. Soc., 127, 795–814, https://doi.org/10.1002/qj.49712757305, 2001.

Sutton, M. A., Bleeker, A., Howard, C., Erisman, J., Abrol, Y., Bekunda, M., Datta, A., Davidson, E., De Vries, W., and Oenema, O.: Our nutrient world. The challenge to produce more food & energy with less pollution, Centre for Ecology & Hydrology, 2013a.

Sutton, M. A., Erisman, J. W., Dentener, F., and Möller, D.: Ammonia in the environment: from ancient times to the present, Environmental Pollution, 156, 583-604, 2008.

Sutton, M. A., Oenema, O., Erisman, J. W., Leip, A., van Grinsven, H., and Winiwarter, W.: Too much of a good thing, Nature, 472, 159-161, 2011.

Sutton, M. A., Reis, S., Riddick, S. N., Dragosits, U., Nemitz, E., Theobald, M. R., Tang, Y. S., Braban, C. F., Vieno, M., and Dore, A. J.: Towards a climate-dependent paradigm of ammonia emission and deposition, Philosophical Transactions of the Royal Society B: Biological Sciences, 368, 20130166, 2013b.

Talhelm, A., Pregitzer, K., and Burton, A.: No evidence that chronic nitrogen additions increase photosynthesis in mature sugar maple forests, Ecological Applications, 21, 2413-2424, 2011.

Thomas, R. Q., Canham, C. D., Weathers, K. C., and Goodale, C. L.: Increased tree carbon storage in response to nitrogen deposition in the US, Nature Geoscience, 3, 13-17, 2010.

Tian, Y., Dickinson, R. E., Zhou, L., Zeng, X., Dai, Y., Myneni, R., Knyazikhin, Y., Zhang, X., Friedl, M., and Yu, H.: Comparison of seasonal and spatial variations of leaf area index and fraction of absorbed photosynthetically active radiation from Moderate Resolution Imaging Spectroradiometer (MODIS) and Common Land Model, J. Geophys. Res.-Atmos., 109, D01103, https://doi.org/10.1029/2003JD003777, 2004.

Tørseth, K., Aas, W., Breivik, K., Fjæraa, A. M., Fiebig, M., Hjellbrekke, A. G., Lund Myhre, C., Solberg, S., and Yttri, K. E.: Introduction to the European Monitoring and Evaluation Programme (EMEP) and observed atmospheric composition change during 1972–2009, Atmos. Chem. Phys., 12, 5447–5481, https://doi.org/10.5194/acp-12-5447-2012, 2012.

Toth, C., and Jóźków, G.: Remote sensing platforms and sensors: A survey, ISPRS Journal of Photogrammetry and Remote Sensing, 115, 22-36, 2016.

Troen, I. and Petersen, E. L.: European Wind Atlas. Risø National Laboratory, Roskilde, 656 pp., ISBN 87-550-1482-8, 1989.

Turner, D. P., Cohen, W. B., Kennedy, R. E., Fassnacht, K. S., and Briggs, J. M.: Relationships between leaf area index and Landsat TM spectral vegetation indices across three temperate zone sites, Remote Sens. Environ., 70, 52–68, 1999.

Van Damme, M., Clarisse, L., Dammers, E., Liu, X., Nowak, J. B., Clerbaux, C., Flechard, C. R., Galy-Lacaux, C., Xu, W., Neuman, J. A., Tang, Y. S., Sutton, M. A., Erisman, J. W., and Coheur, P. F.: Towards validation of ammonia (NH3) measurements from the IASI satellite, Atmos. Meas. Tech., 8, 1575–1591, https://doi.org/10.5194/amt-8-1575-2015, 2015.

Van Damme, M., Clarisse, L., Heald, C. L., Hurtmans, D., Ngadi, Y., Clerbaux, C., Dolman, A. J., Erisman, J. W., and Coheur, P. F.: Global distributions, time series and error characterization of atmospheric ammonia (NH3) from IASI satellite observations, Atmos. Chem. Phys., 14, 2905–2922, https://doi.org/10.5194/acp-14-2905-2014, 2014a.

Van Damme, M., Clarisse, L., Whitburn, S., Hadji-Lazaro, J., Hurtmans, D., Clerbaux, C., and Coheur, P.-F.: Industrial and agricultural ammonia point sources exposed, Nature, 564, 99-103, 2018.

Van Damme, M., Erisman, J. W., Clarisse, L., Dammers, E., Whitburn, S., Clerbaux, C., Dolman, A. J., and Coheur, P. F.: Worldwide spatiotemporal atmospheric ammonia (NH3) columns variability revealed by satellite, Geophysical Research Letters, 42, 8660-8668, 2015.

Van Damme, M., Kruit, R. J. W., Schaap, M., Clarisse, L., Clerbaux, C., Coheur, P. F., Dammers, E., Dolman, A. J., and Erisman, J. W.: Evaluating 4 years of atmospheric ammonia (NH3) over Europe using IASI satellite observations and LOTOS-EUROS model results, J. Geophys. Res.-Atmos., 119, 9549–9566, https://doi.org/10.1002/2014jd021911, 2014b.

Van Damme, M., Whitburn, S., Clarisse, L., Clerbaux, C., Hurtmans, D., and Coheur, P.-F.: Version 2 of the IASI NH3 neural network retrieval algorithm: near-real-time and reanalysed datasets, Atmos. Meas. Tech., 10, 4905–4914, https://doi.org/10.5194/amt-10-4905-2017, 2017.

Van der Swaluw, E., De Vries, W., Sauter, F., Aben, J., Velders, G., and Van Pul, A.: High-resolution modelling of air pollution and deposition over the Netherlands with plume, grid and hybrid modelling, Atmos. Environ., 155, 140–153, https://doi.org/10.1016/j.atmosenv.2017.02.009, 2017.

Van der Werf, G., Sass-Klaassen, U. G., and Mohren, G.: The impact of the 2003 summer drought on the intra-annual growth pattern of beech (Fagus sylvatica L.) and oak (Quercus robur L.) on a dry site in the Netherlands, Dendrochronologia, 25, 103-112, 2007.

van Grinsven, H. J., Rabl, A., and de Kok, T. M.: Estimation of incidence and social cost of colon cancer due to nitrate in drinking water in the EU: a tentative cost-benefit assessment, Environmental health, 9, 1-12, 2010.

van Zanten, M. C., Kruit, R. J. W., Hoogerbrugge, R., Van der Swaluw, E., and van Pul, W. A. J.: Trends in ammonia measurements in the Netherlands over the period 1993–2014, Atmos. Environ., 148, 352–360, https://doi.org/10.1016/j.atmosenv.2016.11.007, 2017.

van Zanten, M. C., Sauter, F. J., Wichink Kruit, R. J., van Jaarsveld, J. A., and van Pul, M. A. J.: Description of the DEPAC module: Dry deposition modelling with DEPAC_GCN2010, Rivm Report 680180001/2010, RIVM, Bilthoven, Netherlands, 2010.

Vicente-Serrano, S. M., Beguería, S., and López-Moreno, J. I.: A multiscalar drought index sensitive to global warming: the standardized precipitation evapotranspiration index, Journal of climate, 23, 1696-1718, 2010.

Vicente-Serrano, S. M., Camarero, J. J., and Azorin-Molina, C.: Diverse responses of forest growth to drought time-scales in the N orthern H emisphere, Global Ecology and Biogeography, 23, 1019-1030, 2014.

Vitousek, P. M., Cassman, K., Cleveland, C., Crews, T., Field, C. B., Grimm, N. B., Howarth, R. W., Marino, R., Martinelli, L., and Rastetter, E. B.: Towards an ecological understanding of biological nitrogen fixation, in: The nitrogen cycle at regional to global scales, Springer, 1-45, 2002.

Vivanco, M. G., Theobald, M. R., García-Gómez, H., Garrido, J. L., Prank, M., Aas, W., Adani, M., Alyuz, U., Andersson, C., Bellasio, R., Bessagnet, B., Bianconi, R., Bieser, J., Brandt, J., Briganti, G., Cappelletti, A., Curci, G., Christensen, J. H., Colette, A., Couvidat, F., Cuvelier, C., D'Isidoro, M., Flemming, J., Fraser, A., Geels, C., Hansen, K. M., Hogrefe, C., Im, U., Jorba, O., Kitwiroon, N., Manders, A., Mircea, M., Otero, N., Pay, M.-T., Pozzoli, L., Solazzo, E., Tsyro, S., Unal, A., Wind, P., and Galmarini, S.: Modeled deposition of nitrogen and sulfur in Europe estimated by 14 air quality model systems: evaluation, effects of changes in emissions and implications for habitat protection, Atmos. Chem. Phys., 18, 10199–10218, https://doi.org/10.5194/acp-18-10199-2018, 2018.

von Bobrutzki, K., Braban, C. F., Famulari, D., Jones, S. K., Blackall, T., Smith, T. E. L., Blom, M., Coe, H., Gallagher, M., Ghalaieny, M., McGillen, M. R., Percival, C. J., Whitehead, J. D., Ellis, R., Murphy, J., Mohacsi, A., Pogany, A., Junninen, H., Rantanen, S., Sutton, M. A., and Nemitz, E.: Field inter-comparison of eleven atmospheric ammonia measurement techniques, Atmos. Meas. Tech., 3, 91–112, https://doi.org/10.5194/amt-3-91-2010, 2010.

WallisDeVries, M. F.: Linking species assemblages to environmental change: Moving beyond the specialist-generalist dichotomy, Basic and Applied Ecology, 15, 279-287, 2014.

Wang, M., Shi, S., Lin, F., Hao, Z., Jiang, P., and Dai, G.: Effects of soil water and nitrogen on growth and photosynthetic response of Manchurian ash (Fraxinus mandshurica) seedlings in northeastern China, PloS one, 7, e30754, 2012.

Wang, Y., Woodcock, C. E., Buermann, W., Stenberg, P., Voipio, P., Smolander, H., Häme, T., Tian, Y., Hu, J., and Knyazikhin, Y.: Evaluation of the MODIS LAI algorithm at a coniferous forest site in Finland, Remote Sens. Environ., 91, 114–127, 2004.

Warner, J. X., Wei, Z., Strow, L. L., Dickerson, R. R., and Nowak, J. B.: The global tropospheric ammonia distribution as seen in the 13-year AIRS measurement record, Atmospheric Chemistry and Physics, 16, 5467, 2016.

Watson, D. J.: Comparative physiological studies on the growth of field crops: I. Variation in net assimilation rate and leaf area between species and varieties, and within and between years, Ann. Bot., 11, 41–76, 1947.

Wesely, M.: Parameterization of surface resistances to gaseous dry deposition in regional-scale numerical models, Atmos. Environ., 23, 1293–1304, 1989.

Whitburn, S., Van Damme, M., Clarisse, L., Bauduin, S., Heald, C. L., Hadji-Lazaro, J., Hurtmans, D., Zondlo, M. A., Clerbaux, C., and Coheur, P. F.: A flexible and robust neural network IASI-NH3 retrieval algorithm, J. Geophys. Res.-Atmos., 121, 6581–6599, https://doi.org/10.1002/2016jd024828, 2016.

Whitburn, S., Van Damme, M., Kaiser, J. W., van der Werf, G. R., Turquety, S., Hurtmans, D., Clarisse, L., Clerbaux, C., and Coheur, P.-F.: Ammonia emissions in tropical biomass burning regions: Comparison between satellite-derived emissions and bottom-up fire inventories, Atmospheric Environment, 121, 42-54, 2015.

Whitten, G. Z., Hogo, H., and Killus, J. P.: The Carbon-Bond Mechanism – a Condensed Kinetic Mechanism for Photochemical Smog, Environ. Sci. Technol., 14, 690–700, https://doi.org/10.1021/es60166a008, 1980.

Wichink Kruit, R. J., Schaap, M., Sauter, F. J., van Zanten, M. C., and van Pul, W. A. J.: Modeling the distribution of ammonia across Europe including bi-directional surface-atmosphere exchange, Biogeosciences, 9, 5261–5277, https://doi.org/10.5194/bg-9-5261-2012, 2012.

Wichink Kruit, R. J., van Pul, W. A. J., Otjes, R. P., Hofschreuder, P., Jacobs, A. F. G., and Holtslag, A. A. M.: Ammonia fluxes and derived canopy compensation points over non-fertilized agricultural grassland in The Netherlands using the new gradient ammonia – high accuracy – monitor (GRAHAM), Atmos. Environ., 41, 1275–1287, https://doi.org/10.1016/j.atmosenv.2006.09.039, 2007.

Wichink Kruit, R. J.: ECLAIRE model inter-comparison of atmospheric nitrogen deposition and concentrations over Europe, presentation at the ACCENT-Plus Symposium held in September in Urbino, Italy, 2013.

Wieringa, J.: Representative roughness parameters for homogeneous terrain, Bound.-Lay. Meteorol., 63, 323–363, 1993.

Wintjen, P., Ammann, C., Schrader, F., and Brümmer, C.: Correcting high-frequency losses of reactive nitrogen flux measurements, Atmos. Meas. Tech., 13, 2923–2948, https://doi.org/10.5194/amt-13-2923-2020, 2020.

Wu, Z., Schwede, D. B., Vet, R., Walker, J. T., Shaw, M., Staebler, R., and Zhang, L.: Evaluation and intercomparison of five North American dry deposition algorithms at a mixed forest site, J. Adv. Model. Earth Sy., 10, 1571–1586, 2018.

Xing, Q., Wu, B., Yan, N., Yu, M., and Zhu, W.: Evaluating the relationship between field aerodynamic roughness and the MODIS BRDF, NDVI, and wind speed over grassland, Atmosphere, 8, 16, https://doi.org/10.3390/atmos8010016, 2017.

Xu, B., Li, J., Park, T., Liu, Q., Zeng, Y., Yin, G., Zhao, J., Fan, W., Yang, L., and Knyazikhin, Y.: An integrated method for validating long-term leaf area index products using global networks of site-based measurements, Remote Sens. Environ., 209, 134–151, 2018.

Yan, K., Park, T., Yan, G., Liu, Z., Yang, B., Chen, C., Nemani, R. R., Knyazikhin, Y., and Myneni, R. B.: Evaluation of MODIS LAI/FPAR product collection 6. Part 2: Validation and intercomparison, Remote Sens., 8, 460, https://doi.org/10.3390/rs8060460, 2016.

Yang, R. and Friedl, M. A.: Determination of roughness lengths for heat and momentum over boreal forests, Bound.-Lay. Meteorol., 107, 581–603, 2003.

Yu, M., Wu, B., Yan, N., Xing, Q., and Zhu, W.: A method for estimating the aerodynamic roughness length with NDVI and BRDF signatures using multi-temporal Proba-V data, Remote Sensing, 9, 6, https://doi.org/10.3390/rs9010006, 2017.

Zavyalov, V., Esplin, M., Scott, D., Esplin, B., Bingham, G., Hoffman, E., Lietzke, C., Predina, J., Frain, R., and Suwinski, L.: Noise performance of the CrIS instrument, Journal of Geophysical Research: Atmospheres, 118, 13,108-113,120, 2013.

Zhang, L., Chen, Y., Zhao, Y., Henze, D. K., Zhu, L., Song, Y., Paulot, F., Liu, X., Pan, Y., and Lin, Y.: Agricultural ammonia emissions in China: reconciling bottom-up and top-down estimates, 2018.

Zhu, L., Henze, D., Cady-Pereira, K., Shephard, M., Luo, M., Pinder, R., Bash, J., and Jeong, G. R.: Constraining US ammonia emissions using TES remote sensing observations and the GEOS-Chem adjoint model, Journal of Geophysical Research: Atmospheres, 118, 3355-3368, 2013.

Zhu, L., Suomalainen, J., Liu, J., Hyyppä, J., Kaartinen, H., and Haggren, H.: A review: Remote sensing sensors, Multi-purposeful application of geospatial data, 19-42, 2018.

Zhu, X., Zhang, W., Chen, H., and Mo, J.: Impacts of nitrogen deposition on soil nitrogen cycle in forest ecosystems: A review, Acta Ecologica Sinica, 35, 35-43, 2015.

Zöll, U., Brümmer, C., Schrader, F., Ammann, C., Ibrom, A., Flechard, C. R., Nelson, D. D., Zahniser, M., and Kutsch, W. L.: Surface-atmosphere exchange of ammonia over peatland using QCL-based eddy-covariance measurements and inferential modeling, Atmos. Chem. Phys., 16, 11283–11299, https://doi.org/10.5194/acp-16-11283-2016, 2016.

Zwally, H., Schutz, B., Abdalati, W., Abshire, J., Bentley, C., Brenner, A., Bufton, J., Dezio, J., Hancock, D., and Harding, D.: ICESat's laser measurements of polar ice, atmosphere, ocean, and land, J. Geodyn., 34, 405–445, 2002.

Appendix

Supplementary materials for Chapter 3: Satellite-derived leaf area index and roughness length information for surface–atmosphere exchange modelling: a case study for reactive nitrogen deposition in north-western Europe using LOTOS-EUROS v2.0.

S3.1 Derivation of z_0 values from EC measurements

We used the regression method (e.g. Graf et al., 2014. Chen et al., 2015) to compute z_0 from several eddy covariance sites. A description of the methodology and the data processing is given in this section. The wind profile in the surface layer can be approximated by:

$$\ln\left(\frac{z-d}{z_0}\right) = \frac{k\,u(z)}{u^*} + \Psi_m\left(\frac{z-d}{L}\right) \qquad \text{(Eq. S3.1)}$$

here, z is the measurement height, d is the displacement height, z_0 is the aerodynamic roughness length, k is the Von-Karman constant (=0.4), $u(z)$ is the average wind speed, u^* is the friction velocity and Ψ_m is the integrated universal momentum function, also known as the stability correction term. Ψ_m is a function of L, the Monin-Obukhov length, which is defined as (e.g. Erisman and Duyzer, 1991):

$$L = -\frac{u_*^3\, T_a \rho c_p}{kgH} \qquad \text{(Eq. S3.2)}$$

where T_a is the air temperature, ρ the air density (= 1.2 kg m^{-3}), $c_p$the heat capacity at constant pressure (=1005 J kg^{-1} K^{-1}), g the acceleration due to gravity, and H the sensible heat flux. Stability correction term Ψ_m is in principle a non-linear function, however, for a certain stability range it can be approximated by a linear function. It is shown that for moderately stable conditions ($0 < \frac{z-d}{L} < 1$) stability correction term Ψ_m holds the following form:

$$\Psi_m\left(\frac{z-d}{L}\right) = -\beta * \left(\frac{z-d}{L}\right) \qquad \text{(Eq. S3)}$$

where β is a constant. We consider a simple linear regression with offset parameter a and slope parameter b. If we assume that Ψ_m is linear, we can rewrite Eq. S3.1 in the following form:

$$\frac{k\,u(z)}{u^*} = a + b\left(\frac{z-d}{L}\right) \qquad \text{(Eq. S3.4)}$$

Now a provides an estimate of $\ln(z-d)/z_0$, and we can directly compute z_0 from $(z-d)/\exp(a)$. We use observations from 2014 only, unless stated otherwise in Table 1. For forest we assume that $d = (2/3) * h$ (Maurer et al., 2013), and we use the forest canopy height derived from GLAS. For short vegetation we assume that displacement height d is negligible, that is, $d = 0$. Graf et al., 2014 illustrated that the linearity approximation of Ψ_m is valid for small negative values of $(z-d)/L$, so we first select all points where $-0.1 < (z-d)/L < 1$. We filter out observation during rainfall and where $u^* < 0.15$, as presented in Chen et al., 2015. We split our data into a group with stable conditions ($L > 0$) and with unstable conditions ($L < 0$). We assume that the z_0 is more or less constant over a period of 5 days. For each 5-day period we plot $ku(z)/u^*$ against $(z-d)/L$ and fit a simple line function using linear least-squares. The z_0 values

are then computed from offset parameter a. We compute the mean, median, standard deviation and the range of the all computed z_0 values in one year. If the computed z_0 values for stable and unstable conditions in one 5-day period differ more than 50% from their arithmetic mean they are filtered out.

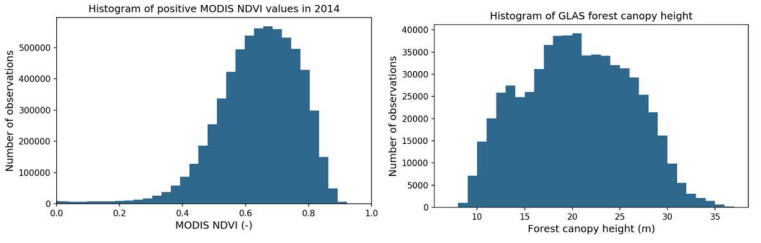

Figure S3.1. *Histogram of all positive MODIS NDVI values* ***(left)*** *and the forest canopy height derived from GLAS* ***(right)****.*

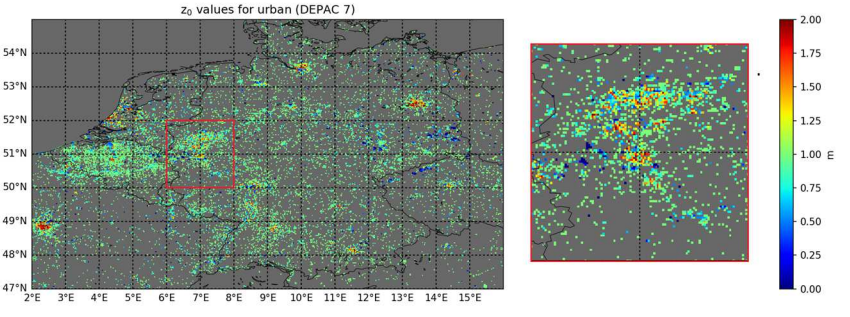

Figure S3.2. *Map of the updated z_0 values for urban areas, with a zoom-in of the Ruhr-valley* ***(right)****.*

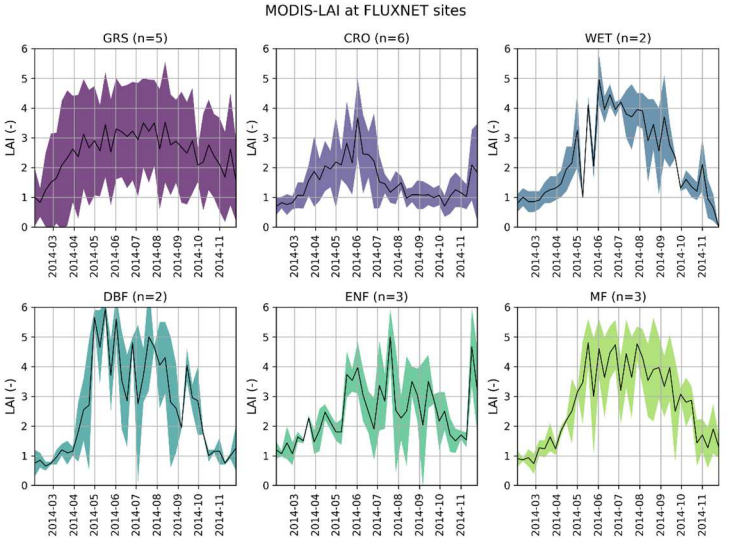

Figure S3.3. *Seasonal variation of the MODIS-LAI at FLUXNET sites with different land use classifications. The black line represents the mean MODIS-LAI value per land use and the ranges represent the mean plus and minus the standard deviation.*

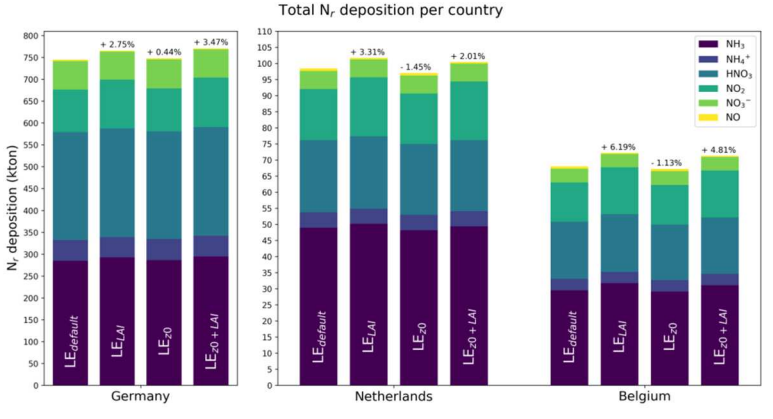

Figure S3.4. *The total N_r deposition (kton) per country for each of the model runs, and the division into different N_r component. The colours depict the part of the total deposition each individual N_r component comprises. The numbers above the individual bars indicate the change in the total N_r deposition for each of the runs.*

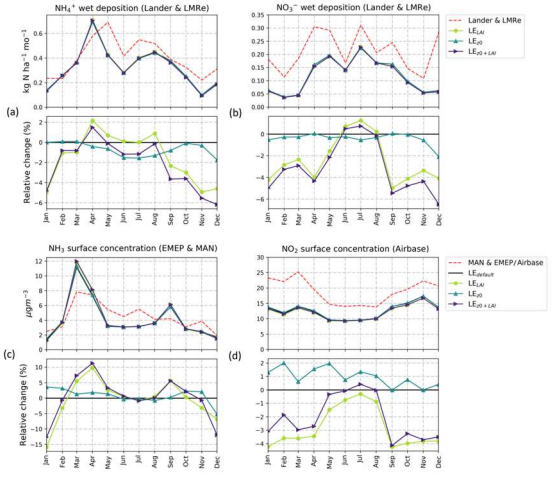

Figure S3.5. *The absolute* ***(top)*** *and the relative* ***(bottom)*** *changes in monthly mean NH_4^+* ***(a)*** *and NO_3^-* ***(b)*** *wet deposition and NH_3* ***(c)*** *and NO_2* ***(d)*** *surface concentrations w.r.t. the default model run induced by the inclusion of the MODIS-LAI and the updated z_0 values. The dotted red line represents the corresponding observations as measured by the in-situ networks.*

Table S3.1. *Correlation coefficient r, root-mean-square difference, slope and intercept of the different in-situ networks in comparison with the corresponding values from the different model runs.*

	Network	*Run ID*	*r*	*RMSD*	*Slope*	*Intercept*
NH_4^+ wet deposition	UBA n = 139	$LE_{default}$	0.38	0.30	0.75	0.03
		LE_{z0}	0.38	0.30	0.74	0.03
		LE_{LAI}	0.38	0.31	0.77	0.02
		LE_{z0+LAI}	0.38	0.31	0.76	0.02
	LMRe n = 7	$LE_{default}$	0.67	0.25	0.87	-0.01
		LE_{z0}	0.67	0.25	0.87	-0.01
		LE_{LAI}	0.66	0.26	0.89	-0.03
		LE_{z0+LAI}	0.66	0.25	0.89	-0.03
NO_3^- wet deposition	UBA n = 173	$LE_{default}$	0.41	0.17	0.53	0.01
		LE_{z0}	0.41	0.17	0.53	0.01
		LE_{LAI}	0.40	0.17	0.53	0.00
		LE_{z0+LAI}	0.40	0.17	0.53	0.00
	LMRe n = 7	$LE_{default}$	0.78	0.15	0.60	-0.04
		LE_{z0}	0.78	0.15	0.61	-0.04
		LE_{LAI}	0.78	0.15	0.61	-0.04
		LE_{z0+LAI}	0.78	0.15	0.61	-0.04
NH_3 surface concentration	MAN n = 239	$LE_{default}$	0.60	3.13	1.18	-1.17
		LE_{z0}	0.60	3.15	1.19	-1.17
		LE_{LAI}	0.61	3.34	1.30	-1.62
		LE_{z0+LAI}	0.61	3.35	1.31	-1.62
	EMEP n = 20	$LE_{default}$	0.81	1.38	1.08	-0.03
		LE_{z0}	0.82	1.36	1.10	-0.07
		LE_{LAI}	0.81	1.45	1.15	-0.13
		LE_{z0+LAI}	0.82	1.44	1.16	-0.16
NO_2 surface concentration	Airbase n = 333	$LE_{default}$	0.75	8.83	0.78	-2.22
		LE_{z0}	0.75	8.76	0.79	-2.41
		LE_{LAI}	0.75	9.14	0.74	-1.93
		LE_{z0+LAI}	0.75	9.08	0.76	-2.09

Table S3.2. *Pearson's correlation coefficient and root-mean-square difference computed for stations located on specific land use classes. The stations are co-located with the CORINE/Smiatek land cover map used in LOTOS-EUROS, and then translated to DEPAC classes and grouped. Statistics are computed when at least 10 sites per land use class were left.*

	Land use type		Grass		Arable land		Coniferous forest		Deciduous forest		Urban	
			r	RMSD	r	RMSD	r	RMSD	r	RMSD	r	RMSD
NH_4^+	UBA											
		n	19		74		72		43		96	
		$LE_{default}$	0.49	0.29	0.37	0.32	0.40	0.28	0.21	0.32	0.44	0.30
		LE_{z0}	0.49	0.29	0.37	0.32	0.40	0.28	0.21	0.32	0.44	0.30
		LE_{LAI}	0.49	0.29	0.37	0.32	0.40	0.29	0.21	0.32	0.44	0.30
		LE_{z0+LAI}	0.49	0.29	0.37	0.32	0.40	0.29	0.21	0.32	0.44	0.30
NO_3^-	UBA											
		n	18		44		97		39		3	
		$LE_{default}$	0.45	0.14	0.54	0.13	0.43	0.18	0.27	0.18	-	-
		LE_{z0}	0.45	0.14	0.54	0.13	0.43	0.18	0.27	0.18	-	-
		LE_{LAI}	0.45	0.14	0.52	0.14	0.42	0.18	0.26	0.18	-	-
		LE_{z0+LAI}	0.45	0.14	0.52	0.14	0.42	0.18	0.26	0.18	-	-
NH_3	MAN											
		n	98		64		24		38		10	
		$LE_{default}$	0.61	3.25	0.65	3.09	0.60	2.89	0.49	3.33	0.65	2.92
		LE_{z0}	0.62	3.25	0.65	3.08	0.59	2.95	0.49	3.42	0.66	2.84
		LE_{LAI}	0.61	3.49	0.66	3.40	0.62	3.06	0.50	3.43	0.66	2.93
		LE_{z0+LAI}	0.62	3.50	0.66	3.38	0.61	3.12	0.50	3.50	0.67	2.83
NO_2	Airbase											
		n	23		86		33		24		166	
		$LE_{default}$	0.71	6.50	0.72	7.61	0.78	6.13	0.81	5.53	0.69	10.49
		LE_{z0}	0.71	6.49	0.72	7.61	0.78	6.14	0.82	5.50	0.69	10.38
		LE_{LAI}	0.71	6.62	0.72	7.87	0.78	6.29	0.81	5.73	0.69	10.88
		LE_{z0+LAI}	0.71	6.60	0.71	7.87	0.78	6.31	0.82	5.72	0.69	10.78

Table S3.3. *Comparison of the forest canopy heights at FLUXNET forest sites. Hmax is the maximum forest canopy height found in (Flechard et al., 2019).*

Site ID	*Hmax (m)* [1]	*Hcanopy GLAS (m)*
BE-Bra	21	18
BE-Vie	30	22
DE-Hai	23	26
DE-Tha	27	23
NL-Loo	18	17
CH-Lae	30	28

Supplementary materials for Chapter 4: Data assimilation of CrIS-NH_3 satellite observations for improving spatiotemporal NH_3 distributions in LOTOS-EUROS.

S4.1 Local Ensemble Transform Kalman Filter setting experiments

Two experiments were performed to study the effect of the LETKF filter settings in more detail. In the first experiment homogeneous NH_3 emission fields were used to study the possible emission adjustments that can be achieved by the LETKF. In this experiment, the NH_3 base emissions at every grid cell were set to two times the mean NH_3 emissions in the Netherlands. The NH_3 time factors were kept time-invariant, i.e., set to 1 throughout the year. For different LETKF filter settings, the obtained emission perturbation factors β are shown in Fig. S4.22 and Fig. S4.23. The experiment shows that increasing temporal length scale τ, i.e., prolonging the time an emission update computed by the LETKF is kept in the model, leads to a larger distribution of computed β factors. Imposing more noise on the ensemble members, i.e., a σ value to 1 instead of 0.5, also leads to a larger distribution in β factors, as well as an overall increase in β factors. The average computed β factors illustrate those large-scale spatial patterns in NH_3 concentrations, as observed by the CrIS instrument, can be resolved. The distribution of the obtained β factors is, except for March, very similar throughout the year. This illustrates that the LETKF is unable to resolve temporal patterns well without sensible initial inputs. In the second experiment the effect of temporal length scale τ is studied in more detail. In this experiment, our initial model setup was kept, but the temporal length scale is extended to τ = 10 days and τ = 14 days. The obtained β factors are shown in Fig. S4.24 and Fig. S4.25. The spatial pattern of the obtained β factors remained very similar in all model runs, however, the range in β factors increased with increasing τ. Moreover, as patterns of the CrIS-NH_3 observations is followed more strongly with increasing τ values, the obtained spatial variation in β factors became more distinct.

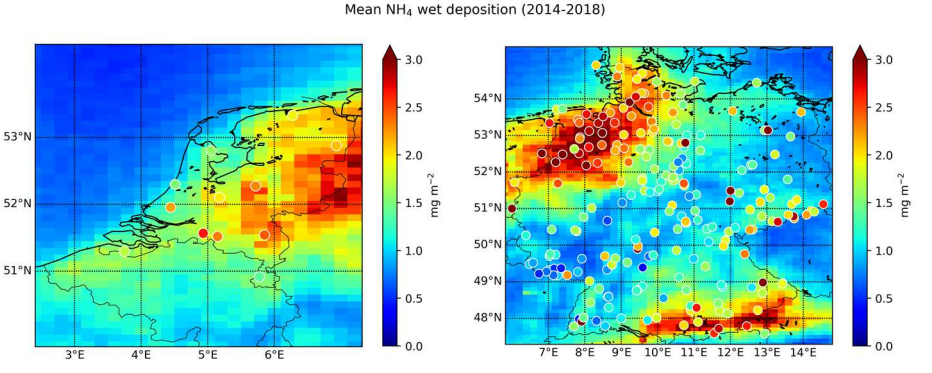

Figure S4.1. *Locations of the wet-only samplers used in this study, plotted on top of the modelled mean NH_4 wet deposition in 2014 to 2018.*

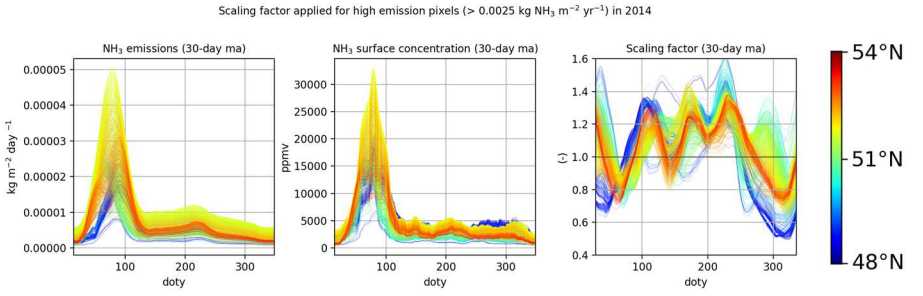

Figure S4.2. *Example of the calculated scaling factors applied to correct for NH_3 surface concentration to NH_3 emission ratios in 2014.*

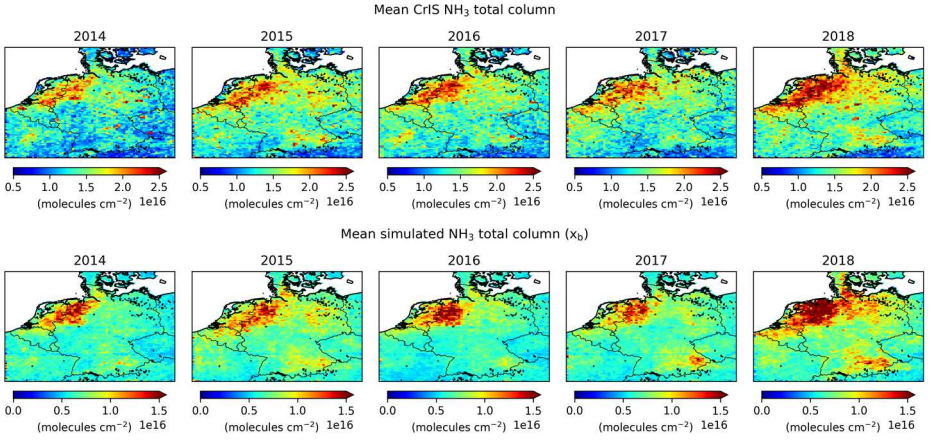

Figure S4.3. *Retrieved* ***(top)*** *and simulated* ***(bottom)*** *NH_3 total column per year.*

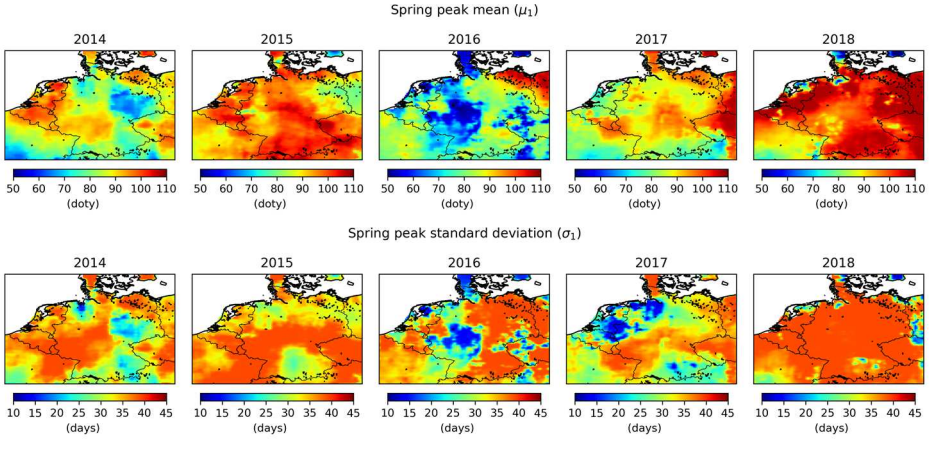

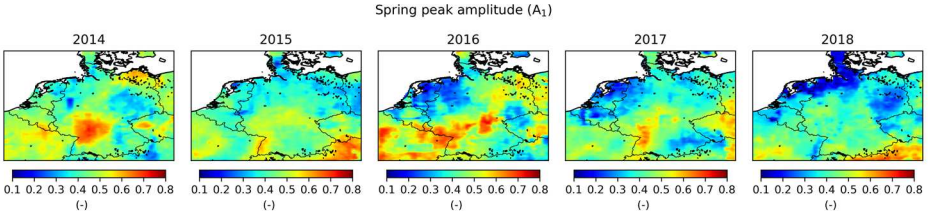

Figure S4.4. *The fitted spring peak parameters (μ_1, σ_1 and A_1) per year.*

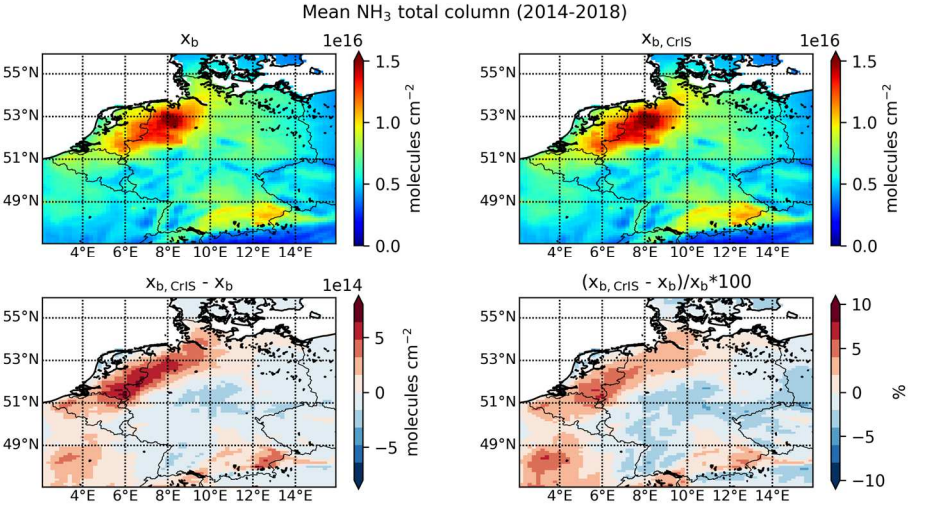

Figure S4.5. *The mean NH_3 total column over 2014 to 2018 from the **(top left)** default background run (x_b) and the **(top right)** background run with CrIS-based NH_3 time factors ($x_{b,CrIS}$) and their **(bottom left)** absolute and **(bottom right)** relative difference.*

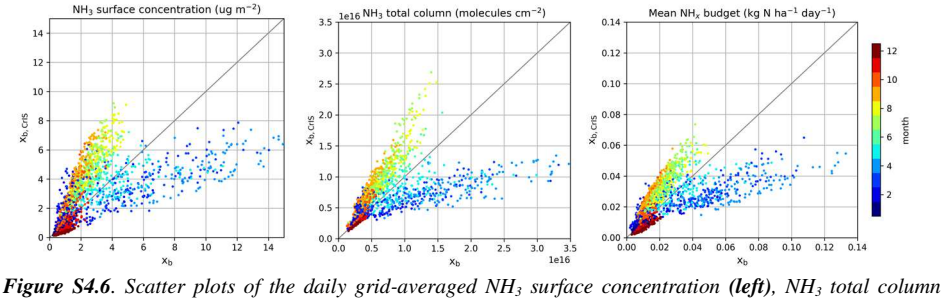

Figure S4.6*. Scatter plots of the daily grid-averaged NH_3 surface concentration **(left)**, NH_3 total column **(center)** and NH_x deposition **(right)** colored per month. x_b represents the default LOTOS-EUROS background run and $x_{b,CrIS}$ the LOTOS-EUROS background run with CrIS-based NH_3 time factors.*

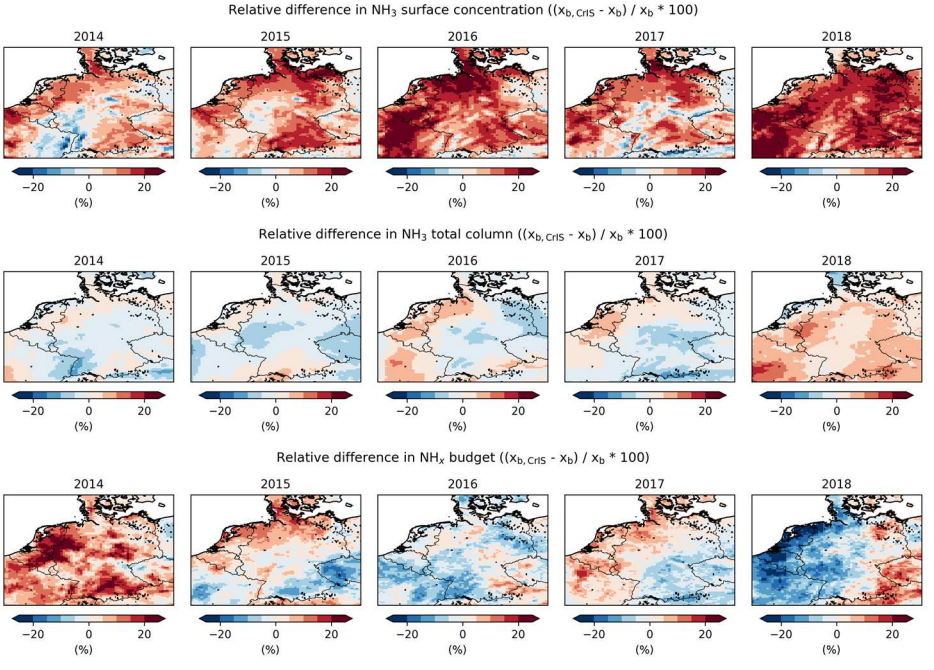

Figure S4.7. *Relative difference in mean NH_3 surface concentrations* ***(top)****, total column concentrations* ***(center)*** *and total NH_x deposition* ***(bottom)*** *per year following the inclusion of the CrIS-based NH_3 time factors in LOTOS-EUROS. x_b represents the default LOTOS-EUROS background run and $x_{b,CrIS}$ the LOTOS-EUROS background run with CrIS-based NH_3 time factors.*

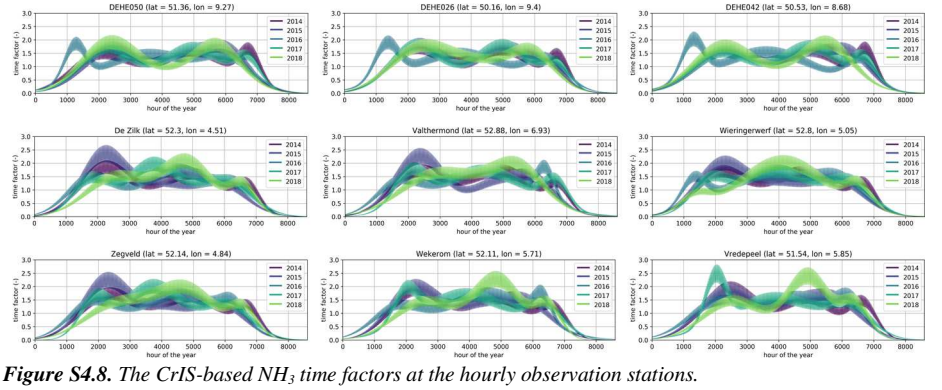

Figure S4.8. *The CrIS-based NH_3 time factors at the hourly observation stations.*

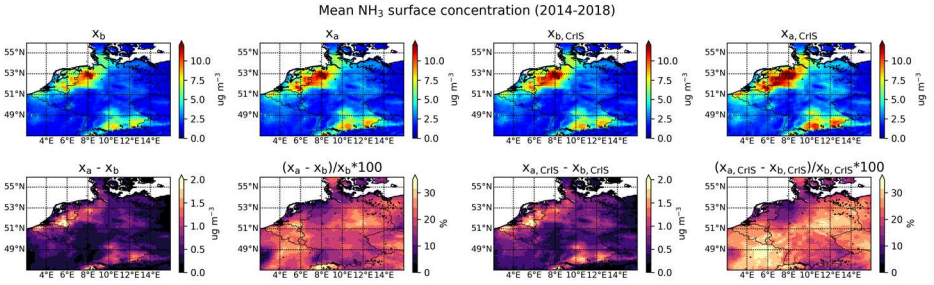

Figure S4.9. *Mean NH_3 surface concentration in 2014-2018 in the background runs x_b and $x_{b,\ CrIS}$ and in analysis runs x_a and $x_{a,CrIS}$* ***(top panels)****, as well as their absolute and relative difference* ***(bottom panels)****.*

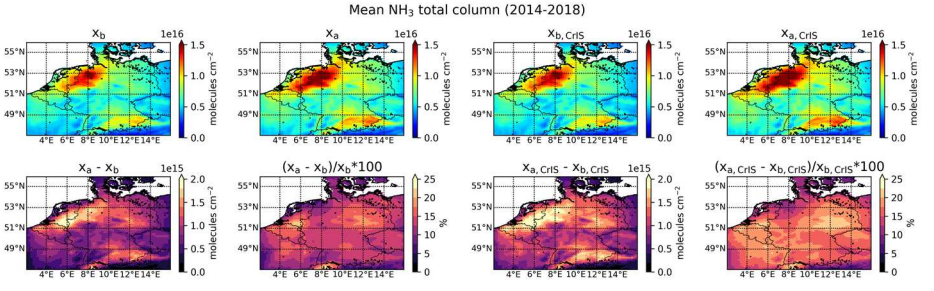

Figure S4.10. *Mean NH_3 total column concentration in 2014-2018 in the background runs x_b and $x_{b,\ CrIS}$ and in analysis runs x_a and $x_{a,CrIS}$* ***(top panels)****, as well as their absolute and relative difference* ***(bottom panels)****.*

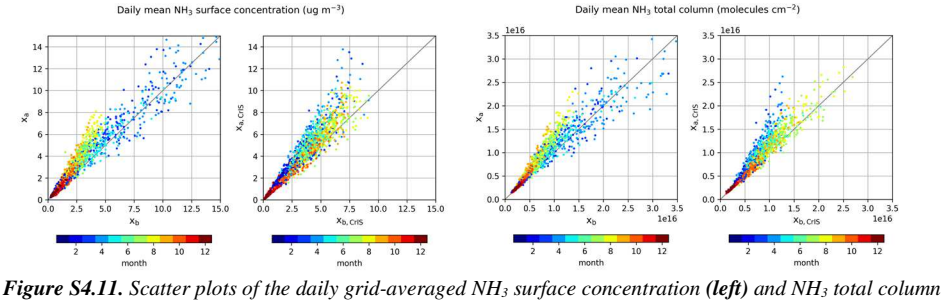

Figure S4.11. *Scatter plots of the daily grid-averaged NH_3 surface concentration* ***(left)*** *and NH_3 total column concentration* ***(right)*** *in 2014-2018 from the background runs x_b and $x_{b,\ CrIS}$ versus analysis runs x_a and $x_{a,CrIS}$ in LOTOS-EUROS, colored per month.*

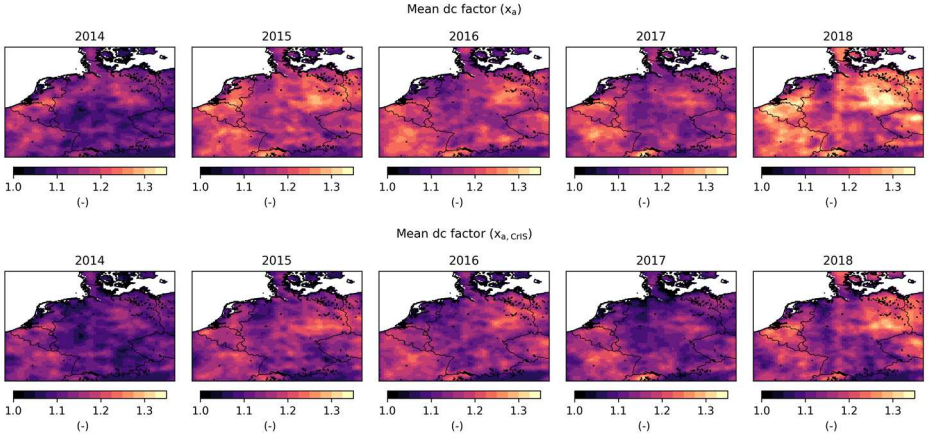

Figure S4.12. *Mean emission perturbation factors (β) per year for* ***(top)*** *LOTOS-EUROS runs with default NH_3 emission time factors and* ***(bottom)*** *LOTOS-EUROS runs with CrIS-based NH_3 time factors.*

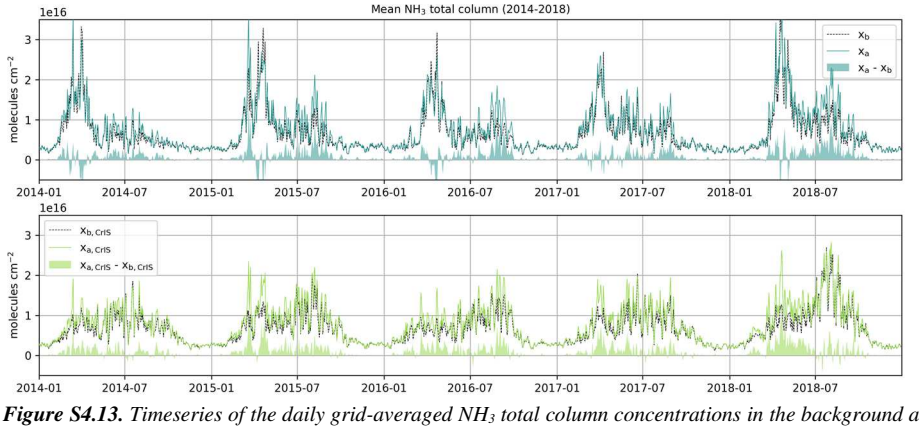

Figure S4.13. *Timeseries of the daily grid-averaged NH_3 total column concentrations in the background and analysis runs, and their absolute difference. The top figure (blue) represents the default background (x_b) and analysis run (x_a). The bottom figure (green) the background ($x_{b,CrIS}$) and analysis run ($x_{a,CrIS}$) with the CrIS-based NH_3 time factors.*

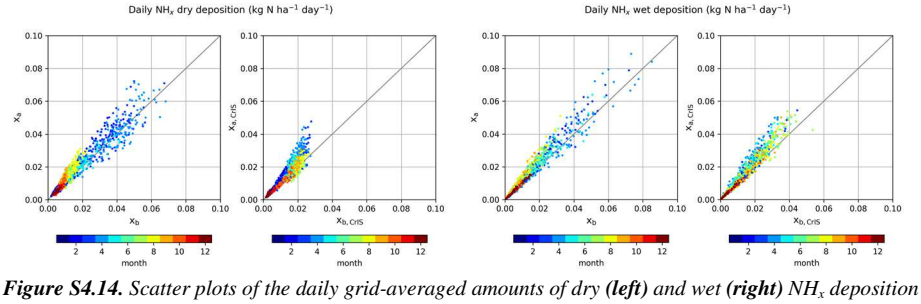

Figure S4.14. *Scatter plots of the daily grid-averaged amounts of dry* ***(left)*** *and wet* ***(right)*** *NH_x deposition in 2014-2018 from the background (x_b and $x_{b,CrIS}$) versus the analysis (x_a and $x_{a,CrIS}$) model runs in LOTOS-EUROS, colored per month.*

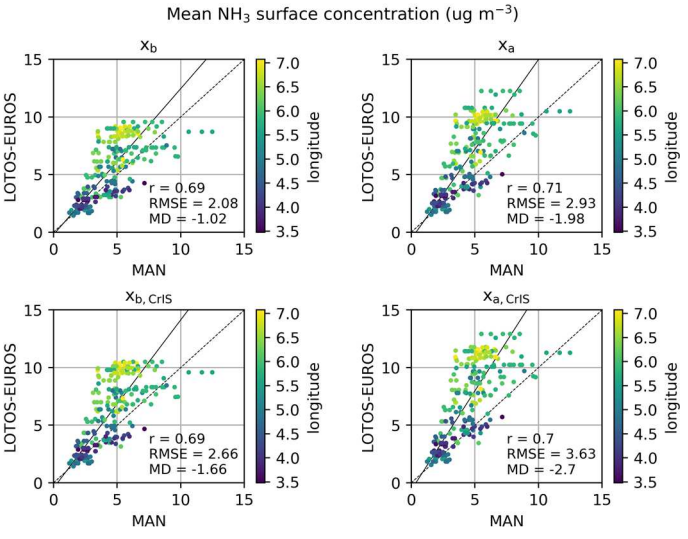

Figure S4.15. *Mean NH_3 surface concentrations (2014-2017) as observed by the Dutch MAN stations and the matching modelled values. The upper figures represent the matching mean NH_3 surface concentrations from the default version of LOTOS-EUROS: x_b the background run and x_a the analysis run. The lower figures represent the matching values from the LOTOS-EUROS run with the CrIS-based NH_3 time factors: $x_{b,CrIS}$ the background run and $x_{a,CrIS}$ the analysis run.*

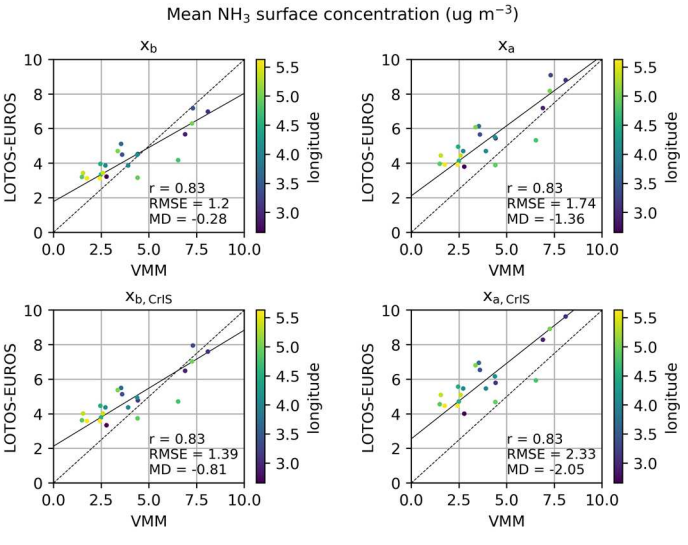

Figure S4.16. *Mean NH_3 surface concentrations (2014-2018) as observed by the Belgium VMM stations and the matching modelled values. The upper figures represent the matching mean NH_3 surface concentrations from the default version of LOTOS-EUROS: x_b the background run and x_a the analysis run. The lower figures represent the matching values from the LOTOS-EUROS run with the CrIS-based NH_3 time factors: $x_{b,CrIS}$ the background run and $x_{a,CrIS}$ the analysis run.*

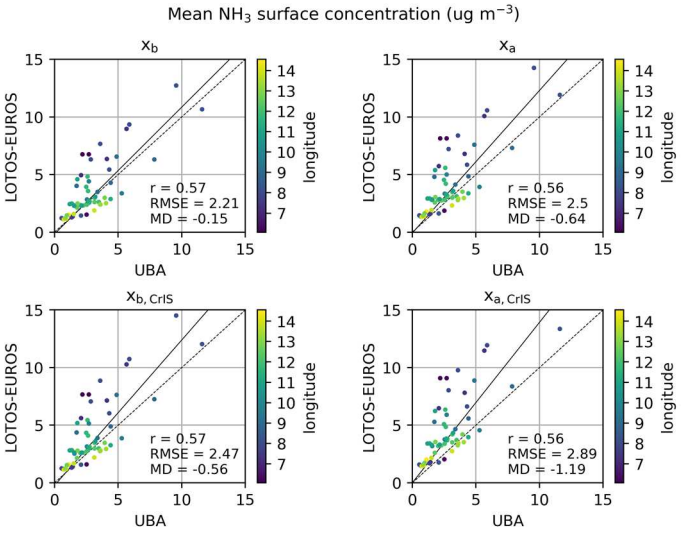

Figure S4.17. *Mean NH_3 surface concentrations (2014-2018) as observed by the German passive sampler stations and the matching modelled values. The upper figures represent the matching mean NH_3 surface concentrations from the default version of LOTOS-EUROS: x_b the background run and x_a the analysis run. The lower figures represent the matching values from the LOTOS-EUROS run with the CrIS-based NH_3 time factors: $x_{b,CrIS}$ the background run and $x_{a,CrIS}$ the analysis run.*

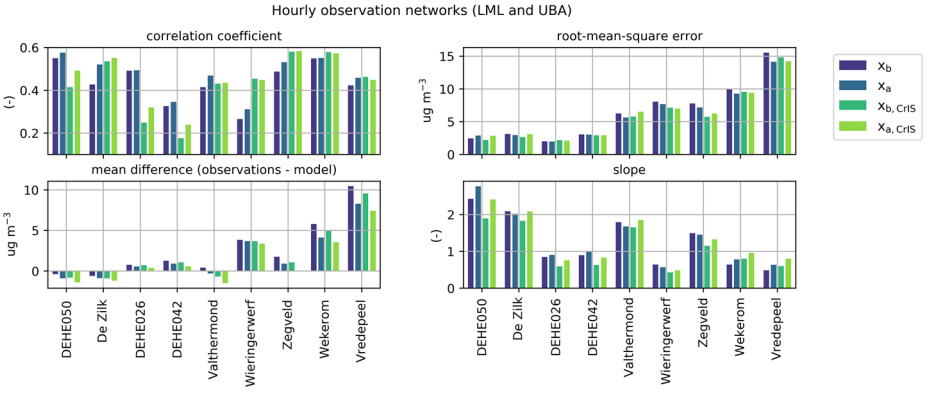

Figure S4.18. *Correlation coefficient r, root-mean-square error, differences in means, slope and intercept between the observed and modelled NH_3 surface concentrations. The stations are sorted by increasing mean NH_3 surface concentration. The colors of the bars represent the different background (x_b and $x_{b,CrIS}$) and analysis (x_a and $x_{a,CrIS}$) runs.*

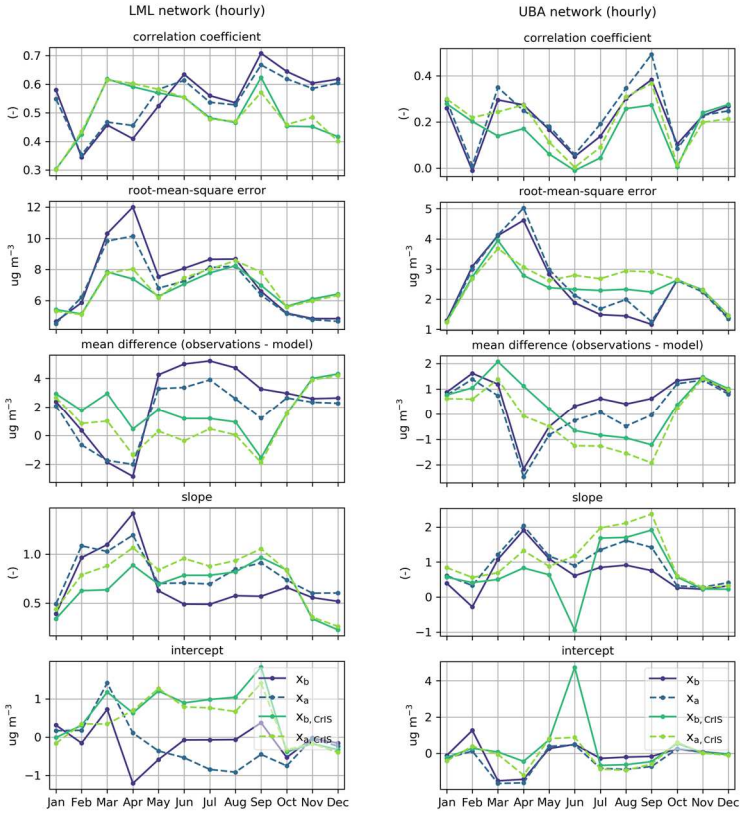

Figure S4.19. *Monthly comparison of the observed and modelled NH_3 surface concentrations per hourly observation network. From top to bottom, the Pearson's correlation coefficient r, the root-mean-square error, the differences in means, the slope and the intercept are plotted. The purple lines represent the default version of LOTOS-EUROS (x_b being the background run, x_a the analysis run) and the green lines the version of LOTOS-EUROS with the CrIS-based NH_3 time factors ($x_{b,CrIS}$ the background run, $x_{a,CrIS}$ the analysis run).*

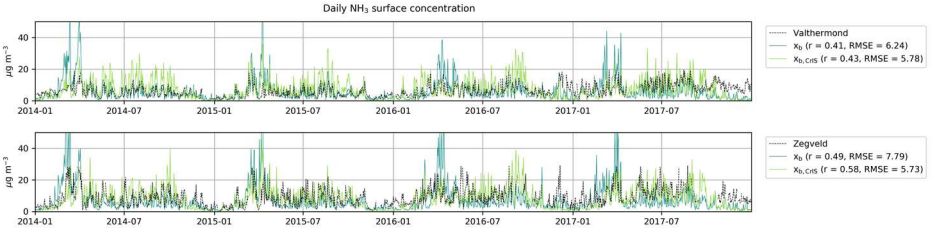

Figure S4.20. *Example of the observed and modelled daily NH_3 surface concentrations at LML stations Valthermond and Zegveld. x_b represents the default LOTOS-EUROS background run and $x_{b,CrIS}$ the LOTOS-EUROS background run with CrIS-based NH_3 time factors.*

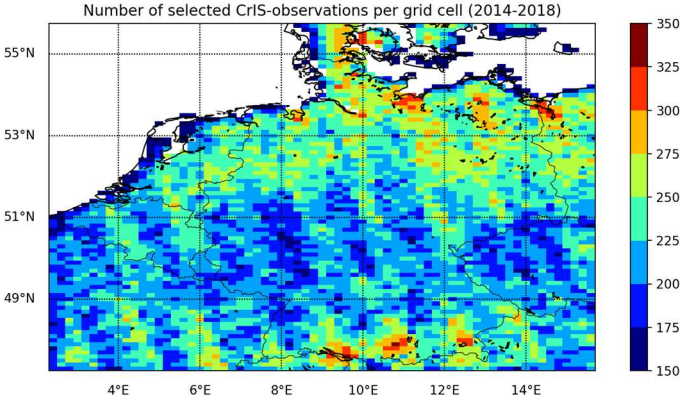

Figure S4.21. *Number of selected CrIS-NH_3 observations per grid cell.*

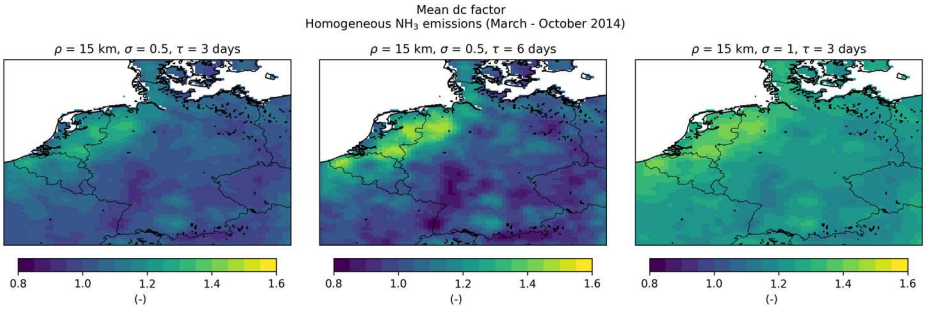

Figure S4.22. *Mean emission perturbation factors (β) from March to October 2014 for model runs with initially homogeneous NH_3 emissions, using different local Ensemble Kalman filter settings.*

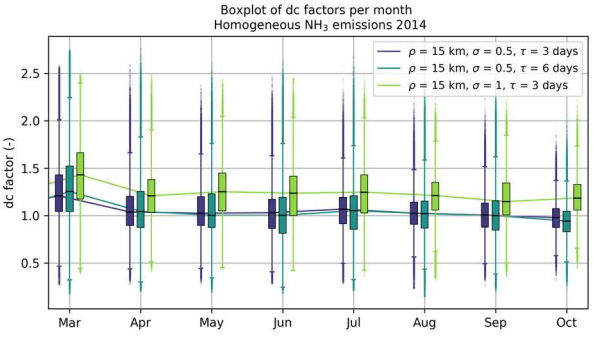

Figure S4.23. *Distribution of emission perturbation factors (β) per month for model runs with initially homogeneous NH_3 emissions, using different local Ensemble Transform Kalman filter settings.*

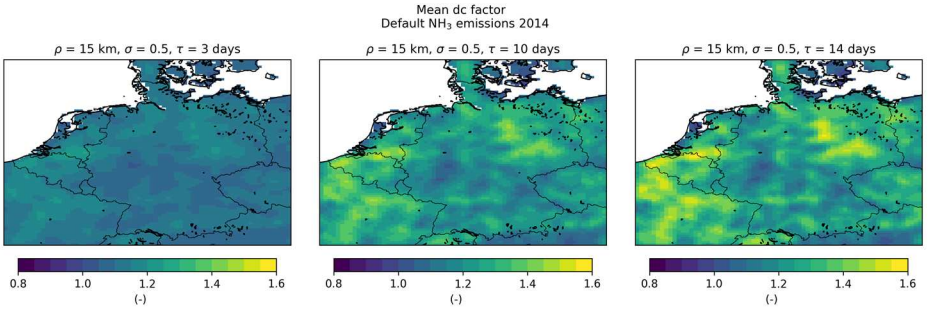

Figure S4.24. *Mean emission perturbation factors (β) in 2014 for model runs with default NH_3 emissions with varying temporal correlation length τ values.*

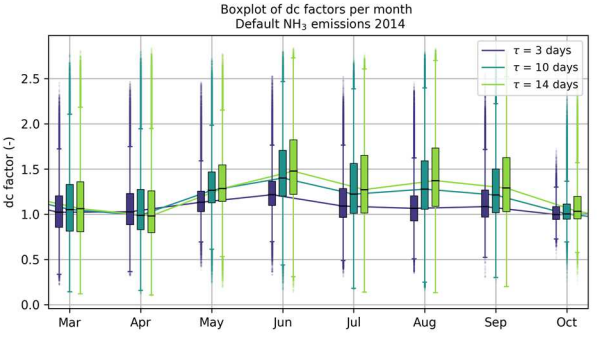

Figure S4.25. *Distribution of emission perturbation factors (β) per month for model runs with default NH_3 emissions, using different values for temporal correlation length τ.*

Supplementary materials for Chapter 5: Nitrogen deposition shows no consistent negative nor positive effect on the response of forest productivity to drought across European FLUXNET forest sites.

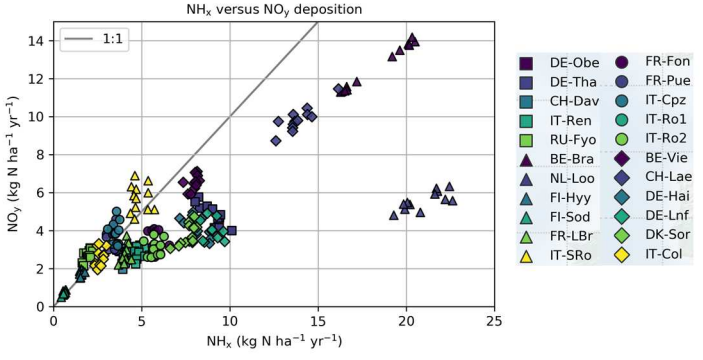

Figure S5.1. *Modelled NO_y and NH_x deposition at each FLUXNET forest sites.*

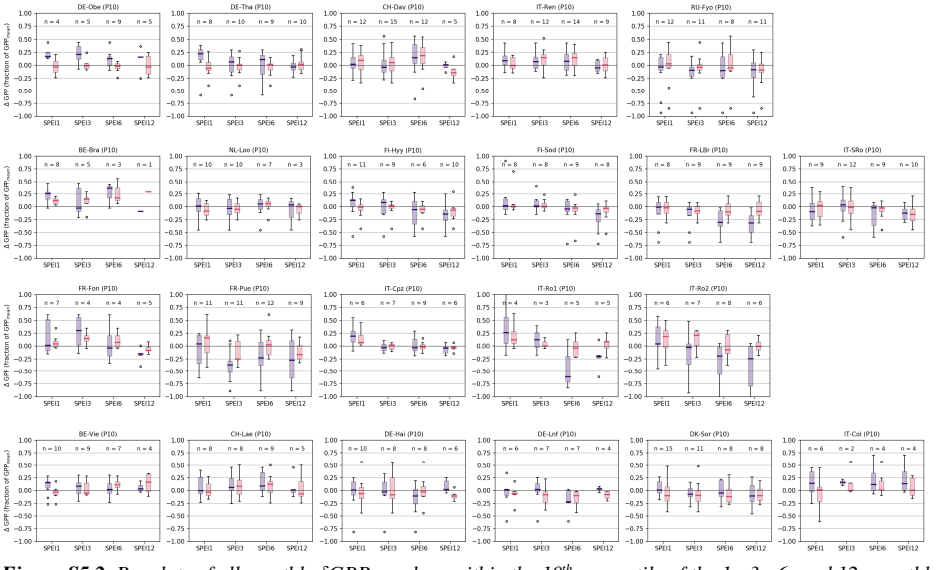

Figure S5.2. *Boxplots of all monthly $\delta GPP_{1,2}$ values within the 10^{th} percentile of the 1-, 3-, 6- and 12- monthly SPEI values, respectively, at each European FLUXNET forest site. The values in purple represent the monthly deviations in GPP with respect to the mean GPP cycle. The red values represent he residuals of the multi polynomial regression.*

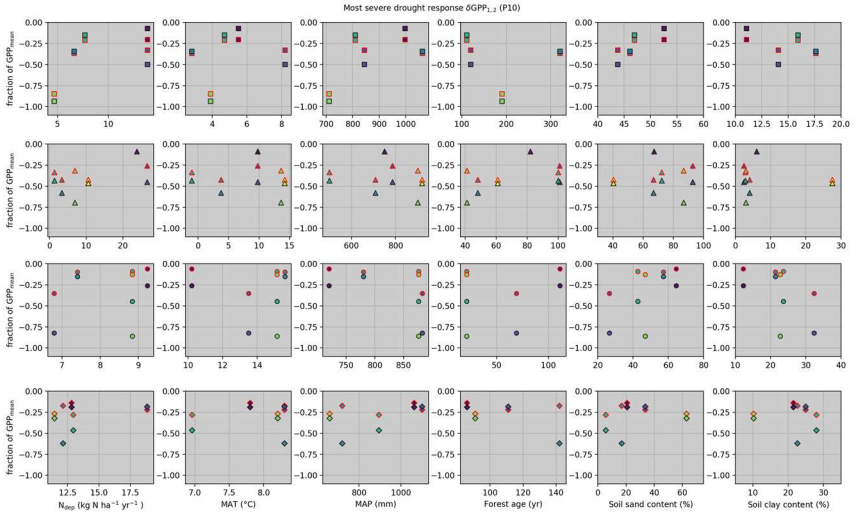

Figure S5.3. *Most severe negative response in δGPP_1 (black outline) and δGPP_2 (red outline) for each group of sites with the same dominant forest type, plotted against the mean N deposition (N_{dep}), mean annual temperature (MAT), mean annual precipitation (MAP), the forest age and the sand and clay content. The minimum $\delta GPP_{1,2}$ is plotted as the fraction of the monthly mean GPP at each site, and represents the most negative $\delta GPP_{1,2}$ out of the values computed with 1-, 3-, 6- and 12- monthly SPEI values. The symbols represent the dominant forest types at each site.*

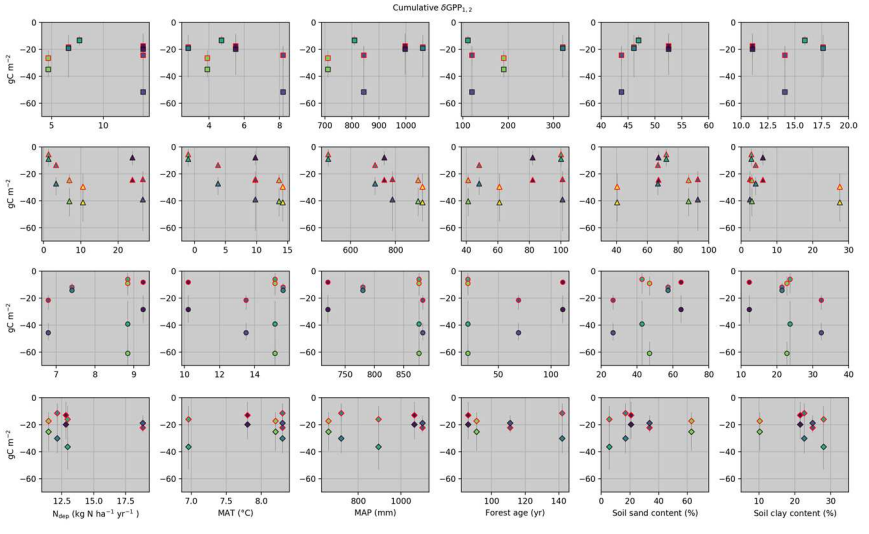

Figure S5.4. *The mean negative response of δGPP_1 (black outline) and δGPP_2 (red outline) per drought event for each group of sites with the same dominant forest type, plotted versus the amount of N deposition (N_{dep}), the mean annual temperature (MAT), the mean annual precipitation (MAP), forest age and sand and clay content. The response per drought event is computed by summing all negative $\delta GPP_{1,2}$ and then dividing that by the number of drought events per SPEI index (1-, 3-, 6- and 12- monthly). The gray lines indicate the spread in outcomes using different SPEI indices. The symbols represent the dominant forest types at each site.*

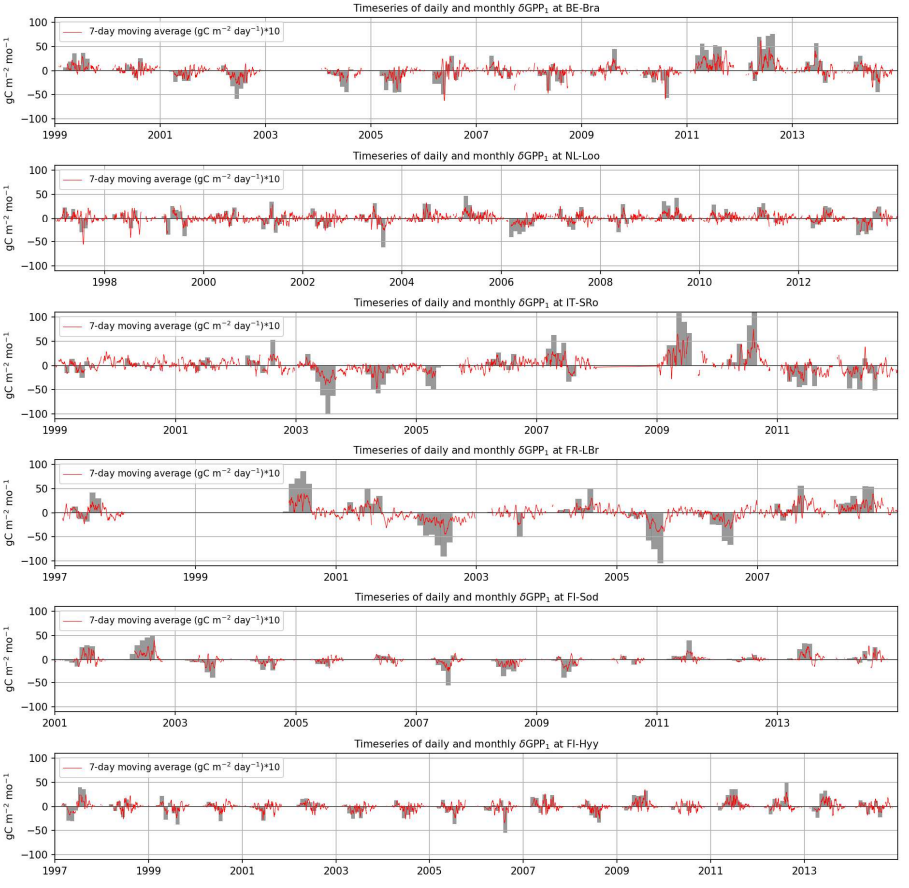

Figure S5.5. *Timeseries of the daily and monthly summed variations in GPP (δGPP_1) with respect to the mean GPP cycle at all FLUXNET forest sites with Pinus ssp. as dominant forest type. Years with less than 200 full days of observations are filtered out.*

Table S5.1. *FLUXNET2015 forest sites used in this study. [1]Plant functional type. ENF = evergreen needle leaf forest, EBF = evergreen broadleaf forest, DBF = deciduous broadleaf forest, MF = mixed forest. [2]Köppen-Geiger climate classification. Cfa = Warm temperate fully humid with hot summer, Cfb = Warm temperate fully humid with warm summer, Csa = Warm temperate with dry, hot summer, Dfb = Snow fully humid warm summer, Dfc = Snow fully humid cool summer, ET = Polar tundra.*

Site id	*Location*	*PFT[1]*	*Dominant species*	*Forest age*	*Climate zone[2]*	*FLUXNET2015 DOIs*
DE-Obe	Oberbärenburg, Germany	ENF	*Picea abies*	-	Cfb	10.18140/FLX/1440151
DE-Tha	Tharandt, Germany	ENF	*Picea abies*	120	Cfb	10.18140/FLX/1440152
CH-Dav	Davos, Switzerland	ENF	*Picea abies*	240 – 400	ET	10.18140/FLX/1440132
IT-Ren	Renon, Italy	ENF	*Picea abies*	111	Dfc	10.18140/FLX/1440173
RU-Fyo	Fyodorovskoye, Russia	ENF	*Picea abies*	190	Dfb	10.18140/FLX/1440183
BE-Bra	Brasschaat, Belgium	MF	*Pinus sylvestris*	82	Cfb	10.18140/FLX/1440128
NL-Loo	Loobos, the Netherlands	ENF	*Pinus sylvestris*	101	Cfb	10.18140/FLX/1440178
FI-Hyy	Hyytiälä, Finland	ENF	*Pinus sylvestris*	48	Dfc	10.18140/FLX/1440158
FI-Sod	Sodankylä, Finland	ENF	*Pinus sylvestris*	100	Dfc	10.18140/FLX/1440160
FR-LBr	Le Bray, France	ENF	*Pinus pinaster*	41	Cfb	10.18140/FLX/1440163
IT-SRo	San Rossore, Italy	ENF	*Pinus pinaster*	61	Csa	10.18140/FLX/1440176
FR-Fon	Fontainebleau, France	DBF	*Quercus robur, Quercus petraea*	111	Cfb	10.18140/FLX/1440161
FR-Pue	Puechabon, France	EBF	*Quercus ilex*	69	Csa	10.18140/FLX/1440164
IT-Cpz	Castelporziano, Italy	EBF	*Quercus ilex*	-	Csa	10.18140/FLX/1440168
IT-Ro1	Roccarespampani, Italy	DBF	*Quercus cerris*	21	Csa	10.18140/FLX/1440174
IT-Ro2	Roccarespampani, Italy	DBF	*Quercus cerris*	21	Csa	10.18140/FLX/1440175
BE-Vie	Vielsalm, Belgium	MF	*Fagus sylvatica, Pseudotsuga menziessii*	86	Cfb	10.18140/FLX/1440130
CH-Lae	Laegern, Switzerland	MF	*Fagus sylvatica, Picea abies*	111	Cfb	10.18140/FLX/1440134
DE-Hai	Hainich, Germany	DBF	*Fagus sylvatica*	142	Cfb	10.18140/FLX/1440148
DE-Lnf	Leinefelde, Germany	DBF	*Fagus sylvatica*	113	Cfb	10.18140/FLX/1440150
DK-Sor	Sorø, Denmark	DBF	*Fagus sylvatica*	91	Cfb	10.18140/FLX/1440155
IT-Col	Collelongo, Italy	DBF	*Fagus sylvatica*	120	Cfa	10.18140/FLX/1440167

Table S5.2. *Additional information per site.*

Site id	*Location*	*Start*	*End*	*Latitude*	*Longitude*	*Elevation (m)*	*MAT (ºC)*	*MAP (mm)*
DE-Obe	Oberbärenburg, Germany	2008	2014	50.78666	13.72129	734	5.5	996
DE-Tha	Tharandt, Germany	1996	2014	50.96235	13.56516	385	8.2	843
CH-Dav	Davos, Switzerland	1997	2014	46.81533	9.85591	1639	2.8	1062
IT-Ren	Renon, Italy	1998	2013	46.58686	11.43369	1730	4.7	809.3
RU-Fyo	Fyodorovskoye, Russia	1998	2014	56.46153	32.92208	265	3.9	711
BE-Bra	Brasschaat, Belgium	1996	2014	51.30761	4.51984	16	9.8	750
NL-Loo	Loobos, the Netherlands	1996	2014	52.16658	5.74356	25	9.8	786
FI-Hyy	Hyytiälä, Finland	1996	2014	61.84741	24.29477	181	3.8	709
FI-Sod	Sodankylä, Finland	2001	2014	67.36239	26.63859	180	-1	500
FR-LBr	Le Bray, France	1996	2008	44.71711	-0.7693	61	13.6	900
IT-SRo	San Rossore, Italy	1999	2012	43.72786	10.28444	6	14.2	920
FR-Fon	Fontainebleau, France	2005	2014	48.47636	2.7801	103	10.2	720
FR-Pue	Puechabon, France	2000	2014	43.7413	3.5957	270	13.5	883
IT-Cpz	Castelporziano, Italy	1997	2009	41.70525	12.37611	68	15.6	780
IT-Ro1	Roccarespampani, Italy	2000	2008	42.40812	11.93001	235	15.15	876.2
IT-Ro2	Roccarespampani, Italy	2002	2012	42.39026	11.92093	160	15.15	876.2
BE-Vie	Vielsalm, Belgium	1996	2014	50.30496	5.99808	493	7.8	1062
CH-Lae	Laegern, Switzerland	2004	2014	47.47808	8.3650	689	8.3	1100
DE-Hai	Hainich, Germany	2000	2012	51.07917	10.4530	430	8.3	720
DE-Lnf	Leinefelde, Germany	2002	2012	51.32822	10.3678	451	6.96	894.6
DK-Sor	Sorø, Denmark	1996	2014	55.48587	11.64464	40	8.2	660
IT-Col	Collelongo, Italy	1996	2014	41.84936	13.58814	1560	6.5	1180

***Table S5.3**. Evaluation of the polynomial multi regression model at each FLUXNET forest site. The units of the root-mean-squared deviation (RMSD) and the mean absolute deviation (MAD) are given in gC m^{-1} day^{-1}.*

	All year				*Spring*				*Summer*			
	RMSD	MAD	r	slope	RMSD	MAD	r	slope	RMSD	MAD	r	slope
DE-Obe	1.38	1.03	0.95	0.94	1.24	0.98	0.93	0.91	1.76	1.31	0.84	0.85
DE-Tha	1.34	1.01	0.95	0.94	1.44	1.1	0.90	0.91	1.70	1.33	0.78	0.83
CH-Dav	1.45	1.11	0.79	0.79	1.38	1.07	0.75	0.75	1.69	1.3	0.44	0.56
IT-Ren	1.47	1.13	0.88	0.87	1.44	1.14	0.84	0.82	1.67	1.29	0.63	0.63
RU-Fyo	1.60	1.17	0.91	0.91	1.37	1.05	0.86	0.86	2.11	1.66	0.67	0.72
BE-Bra	1.08	0.80	0.94	0.94	1.07	0.82	0.9	0.89	1.38	1.04	0.82	0.89
NL-Loo	0.98	0.75	0.95	0.95	1.09	0.83	0.87	0.85	1.18	0.92	0.8	0.83
FI-Hyy	0.90	0.68	0.96	0.96	0.82	0.63	0.92	0.91	1.13	0.9	0.84	0.92
FI-Sod	0.83	0.60	0.93	0.92	0.57	0.44	0.89	0.87	1.09	0.85	0.72	0.76
FR-LBr	1.35	1.02	0.89	0.89	1.25	0.95	0.84	0.82	1.66	1.33	0.81	0.82
IT-SRo	1.44	1.06	0.86	0.86	1.53	1.14	0.81	0.8	1.87	1.39	0.7	0.65
FR-Fon	1.64	1.21	0.94	0.94	1.54	1.11	0.94	0.92	2.06	1.61	0.67	0.86
FR-Pue	0.85	0.65	0.90	0.90	0.85	0.68	0.87	0.86	1.07	0.81	0.89	0.86
IT-Cpz	1.31	0.99	0.82	0.82	1.31	0.98	0.71	0.70	1.65	1.28	0.66	0.63
IT-Ro1	1.28	0.93	0.93	0.93	1.40	1.04	0.95	0.85	1.55	1.19	0.89	0.93
IT-Ro2	1.38	1.00	0.94	0.94	1.45	1.02	0.96	0.88	1.61	1.24	0.88	0.94
BE-Vie	1.34	0.99	0.94	0.93	1.38	1.05	0.87	0.87	1.72	1.35	0.74	0.85
CH-Lae	2.15	1.61	0.84	0.84	2.15	1.65	0.79	0.76	2.33	1.79	0.64	0.74
DE-Hai	1.44	1.03	0.96	0.95	1.49	1.02	0.94	1.06	1.70	1.34	0.82	0.96
DE-Lnf	1.63	1.2	0.95	0.94	1.59	1.15	0.92	0.95	2.03	1.64	0.77	0.9
DK-Sor	1.79	1.27	0.95	0.94	1.76	1.21	0.94	0.94	2.46	1.97	0.77	0.88
IT-Col	1.74	1.27	0.93	0.92	1.59	1.07	0.91	0.93	2.19	1.74	0.62	0.83

Dankwoord

Het zit erop! Na bijna vijf jaar is deze thesis dan eindelijk af. Het was een periode met de nodige ups en downs, maar al met al kijk ik terug op een positieve, leuke en leerzame tijd. In dit dankwoord wil ik alle mensen bedanken die direct of indirect hebben meegewerkt aan het tot stand komen van deze thesis.

Allereerst wil ik mijn eerste promotor Jan Willem Erisman bedanken. Jan Willem, bedankt voor alle begeleiding, expertise en hulp van de afgelopen jaren. Je stond altijd voor mij klaar, ook nadat je bent gewisseld van baan en bij de universiteit van Leiden aan de slag ging, en dat waardeer ik heel erg. Jouw enthousiasme voor dit onderwerp, en eigenlijk voor alles rondom stikstof, heeft mij door de jaren heen flink gemotiveerd en motiveert mij nu nog steeds om door te gaan met onderzoek naar stikstof. Dan wil ik mijn tweede promotor Martijn Schaap bedanken voor zijn begeleiding. Martijn, bedankt dat ik de afgelopen jaren te gast mocht zijn bij jouw groep bij TNO in Utrecht. Ik heb bij jullie onwijs veel geleerd en het erg naar mijn zin gehad.

Dan wil ik ook meteen de rest van mijn collega's bij TNO bedanken, bedankt voor al jullie hulp en daarnaast ook voor alle gezelligheid! In het bijzonder wil ik Arjo en Richard bedanken voor al hun praktische hulp met LOTOS-EUROS en de vele modelaanpassingen die zij met mij en voor mij hebben doorgevoerd. Ook wil ik natuurlijk Enrico bedanken. Enrico, je voorspelling is uitgekomen, tijdens deze PhD heb ik min of meer non-stop vragen jouw kant op geslingerd, zelfs toen je in Canada was. Je hebt mij onwijs veel geholpen en dat waardeer ik heel erg, bedankt!

Furthermore, I would like to thank my colleagues at the VU. Thank you all for all the nice chats and fruitful discussions, the many coffee breaks and occasional drinks, you made my time at the office a fun and successful one! Kanayim, I want to thank you in particular for being a friend to me these past few years. I am thankful for all the great years we had sharing an office at the VU. We really had some fun times and you made coming to our office worthwhile.

Thomas, bedankt voor het beantwoorden van mijn vele bomen- en niet-bomen-gerelateerde vragen. Anne, bedankt voor alle gezelligheid! Sander, bedankt dat je de laatste jaren bij de VU een soort van "stand-in supervisor" voor mij was en dat ik deel uit mocht maken van jouw atmospheric modelling group. Dit was voor mij erg leuk en leerzaam. En tenslotte wil ik Fenny bedanken voor alle hulp met praktische zaken.

Daarnaast wil ik iedereen uit mijn promotiecommissie bedanken voor de tijd en aandacht die zij aan mijn proefschrift hebben geschonken. Bedankt heren!

Ik wil ook mijn familie en vrienden bedanken. In bijzonder mijn ouders, Henk en Trudy. Lieve pap en mam, bedankt dat jullie altijd voor mij klaar staan. Jullie hebben mij altijd gemotiveerd om door te groeien en mezelf te blijven ontwikkelen. Niet alleen op intellectueel niveau, maar ook als persoon. Zonder jullie liefde en steun was ik niet de persoon die ik vandaag de dag ben. En natuurlijk ook bedankt voor de oppas op Liam de afgelopen maanden, dankzij jullie hulp is dit boekje af! Ook wil ik mijn zusjes bedanken. Gwendolynn en Megan, jullie hebben de afgelopen jaren eindeloze verhalen over mijn promotie moeten doorstaan. Ik kan altijd bij jullie terecht, voor een leuk uitje samen of gewoon om even gezellig te (video)bellen als ik om een praatje verlegen zit. Jullie zijn naast mijn zusjes stiekem ook mijn beste vriendinnen. Kortom, ik kan niet zonder

jullie! Dan wil ik mijn zoontje Liam bedanken. Liam, je kan dit voorlopig nog niet lezen, maar jouw komst was echt een stok achter de deur om mijn thesis af te ronden. Mijn leven is zo veel mooier met jou erin. Bedankt dat je er bent, lief ventje!

Als laatste wil ik mijn vriend Nick bedanken. Nick, wat hebben wij een bijzonder jaar achter de rug. De geboorte van Liam, en dan nu de afronding van mijn proefschrift. Het voelt echt als de start van een nieuwe fase in ons leven. Bedankt voor al jouw liefde, steun en interesse de afgelopen jaren, het heeft mij enorm geholpen. Met name het laatste jaar van mijn promotie waren wij flink op elkaar aangewezen. Bijna een jaar thuis(werken), en daarbij ook nog zwanger zijn. Het was voor mij niet altijd even gemakkelijk en je hebt mij er soms echt doorheen moeten sleuren. Je bent echt mijn rots in de branding en je kan me altijd weer opvrolijken als het even tegenzit. Nick, je bent mijn beste vriend. Ik hou van jou!